Green Energy and Technology

Pasquale Corbo
Fortunato Migliardini
Ottorino Veneri

Hydrogen Fuel Cells for Road Vehicles

Springer

Green Energy and Technology

For further volumes:
http://www.springer.com/series/8059

Pasquale Corbo · Fortunato Migliardini ·
Ottorino Veneri

Hydrogen Fuel Cells for Road Vehicles

Springer

Dr. Pasquale Corbo
Istituto Motori
National Research Council of Italy
Via Marconi, 8
80125 Naples
Italy
e-mail: p.corbo@im.cnr.it

Dr. Ottorino Veneri
Istituto Motori
National Research Council of Italy
Via Marconi, 8
80125 Naples
Italy
e-mail: o.veneri@im.cnr.it

Dr. Fortunato Migliardini
Istituto Motori
National Research Council of Italy
Via Marconi, 8
80125 Naples
Italy
e-mail: f.migliardini@im.cnr.it

ISSN 1865-3529 e-ISSN 1865-3537

ISBN 978-0-85729-135-6 e-ISBN 978-0-85729-136-3

DOI 10.1007/978-0-85729-136-3

Springer London Dordrecht Heidelberg New York

British Library Cataloging in Publication Data
A Catalogue record for this book is available from the British Library

Cover design: eStudio Calamar, Berlin/Figueres

Printed on acid-free paper

Springer is part of Springer Science+Business Media (www.springer.com)

Preface

In recent years the concept of a fuel cell propulsion system has gained in attention as a result of the need to reduce the fossil fuel consumption and greenhouse gas emissions. Since the fuel cells suitable for vehicle application (polymeric electrolyte membrane fuel cells) are fuelled by hydrogen, and deliver power as long as fuel and air are supplied, they potentially can provide the range capabilities of an internal combustion engine when used in a power system, but with clean and quiet operation. Therefore, the fundamental benefit of this type of propulsion consists in the possibility to adopt pollution-free electric drive-trains, without the drive range limitations typical of traditional electric vehicles.

A fuel cell propulsion system operates in hybrid configuration with an electric energy storage system (batteries and/or supercapacitors), in order to take advantage of the best attributes of both power sources. In fact, against the driving range capabilities of fuel cells, batteries and supercapacitors are characterized by defined and limited energy storage, but are able to deliver large peak current without the limitations due to the dynamic behavior of auxiliary sub-systems of the fuel cell generator. Fuel cells and storage systems, therefore, complement each other in a hybrid configuration where they supply the electric drive through an electric parallel connection. Suitable management strategies have to be implemented to optimize the energy flows within the overall power train, as function of power size and road mission of the vehicle, with the goal of achieving peak acceleration power, long range and recharge capabilities.

This book is organized to provide a general view of the present status of this moving field, taking into account that the study of a propulsion system using hydrogen as a fuel, an electric drive train for traction and electrochemical systems as power sources requires some basic knowledge in different scientific disciplines. The text is aimed at undergraduate or graduate-level students, and has been structured in a theoretical part, dealing with the fundamental concepts involved in the study of a fuel cell power train, and in a final practical section where the principles previously illustrated are applied in design, realization and experimental characterization of two real fuel cell propulsion systems.

The introduction in Chap. 1 tackles the problem of energy strategies and their implications in the transportation sector. Future availability of fossil sources, potentialities of alternative sources, well-to-wheel analysis of conventional and innovative propulsion systems are discussed in relation to their impact on the future feasibility of efficient and carbon-free transportation means.

Hydrogen production, onboard storage and distribution technologies are reviewed in Chap. 2, while basic concepts of electrochemistry are recalled in Chap. 3, with an assessment of the state of development of fuel cells for automotive applications, in terms of performance and durability.

The analysis of the main aspects to be faced in design and realization of a fuel cell system as power source of an electric drive train is described in Chap. 4. Here the problems connected to the choice of auxiliary components, their energy consumption and integration in the overall system are discussed, paying particular attention to the management of membrane humidification, hydrogen purge and air supply as a way to optimize system efficiency and reliability.

The general theme of electric vehicles is covered in Chap. 5, with particular reference to hybrid vehicles that adopt both fuel cells and batteries/supercapacitors as power sources. The analysis of possible hybrid configurations is presented together with a review of different types of electric energy storage systems.

Chapters 6 and 7 refer to two practical case studies, in particular two fuel cell propulsion systems of different size. Here the technical characteristics of all individual components are described, and the results of an experimental characterization carried out on laboratory dynamic test benches are discussed. The findings of these two chapters evidence the limitations and potentialities of fuel cell power trains at the present state of development, in terms of performance, efficiency, environmental impact and durability.

Naples, April 2010

Dr. Pasquale Corbo
Dr. Fortunato Migliardini
Dr. Ottorino Veneri

Contents

Chapter 1
Possible Routes Towards Carbon-Free Vehicles

It is widely documented that the continuously increasing energy consumption is linked to population and economic growth. Industry, domestic and transportation sectors augment their share of primary energy use, with a consequent higher standard of living. The annual report of International Energy Agency (IEA), World Energy Outlook 2008, gives some forecasts about the future primary energy demands based on a Reference Scenario, which considers the effects of government measures adopted up to mid-2008 [1]. Table 1.1, which summarizes these previsions by fuel starting from 2006 until 2030, evidences that world energy demands in the Reference Scenario should rise of about 45% in the period considered (with an average of 1.6% per year), with fossil sources (coal, oil and natural gas) accounting of most overall increase (>80%). About half of the projected increase is attributed to the emerging giants in the global economy (China and India), which have to be considered as energy wasting countries due to their enormous population, huge market size and lasting economic growth.

The relation between energy demand, population increase and continuous amelioration of economic conditions is strictly connected to some crucial issues regarding the human impact on the environment and the reserves of primary energy resources. These questions are the basis of the worldwide diffused awareness that concomitant growth of human population, economic prosperity and energy demand, may not be sustainable far into the future without any modification of the present model of economic and social development.

The main environmental concern is related to the increasing concentration of carbon dioxide (CO_2) in the atmosphere (with consequent enhanced greenhouse effect), which is attributed to the combustion of carbon-containing fossil fuels and considered responsible of the global climate change observed in recent years. According to forecasts of World Energy Outlook 2008 (Table 1.2), the world energy-related carbon dioxide emissions was about 28 billion tons in 2006, and should increase up to about 42 billion tons in 2030 in the Reference Scenario, considering both OECD and non-OECD countries. The percentage of these emissions due to the transportation sector was about 18% in 2006, and represents a

P. Corbo et al., *Hydrogen Fuel Cells for Road Vehicles*,
Green Energy and Technology, DOI: 10.1007/978-0-85729-136-3_1,

Table 1.1 Previsions of IEA for world energy demand by fuel until 2030

Fuel	2006	2010	2020	2030
		Mtoe[a]		
Oil	4000	4200	4700	5100
Coal	3100	3500	4300	4900
Natural gas	2500	2750	3150	3750
Biomass	1150	1250	1500	1650
Nuclear	750	800	850	900
Hydro	250	270	300	400
Other renewables	40	90	150	250

Adapted from Ref. [1]
[a]Million tons of oil equivalent (one TOE = 11630 kWh)

Table 1.2 Previsions of IEA for world energy-related CO_2 emissions until 2030

Country	2006	2010	2020	2030
		Billion tonnes		
OECD	13	15	14	16
Non-OECD	15	16	23	26
World total	28	31	37	42

Adapted from Ref. [1]

very significant fraction if compared to the contribution of other economic sectors, such as power generation (37%) and industry (17%) [1].

On the other hand, when environmental issues due to the human mobility are considered, the specific aspect of global CO_2 emissions cannot be disjoined by the evaluation of other environmental impacts at local level (especially in metropolitan areas, as well documented worldwide) connected to pollutant emissions typical of the internal combustion engines, which represent the current and mature technology the road transportation means are almost totally based on.

The question of primary energy reserves is of fundamental importance not only from the general point of view of energy supply necessary to the economic growth, but also for the transportation sector, which is strongly dependent on fossil fuels availability. Both spark and compression ignition engines are currently fueled with carbon-containing fuels deriving from fossil sources (oil or natural gas), and are continuously improved in order to meet the always more stringent legislative limit on pollutant emissions.

However, the above-mentioned significant contributions to the greenhouse effect of the transportation sector, the always present environmental issues in urban areas, and the foreseeable scarcity of fossil fuels in some decades, strongly drive the interests of private and governmental research centers towards the study of novel propulsion systems, able to face the cited problems.

The next paragraphs in this chapter will examine in detail the issues anticipated in these preliminary remarks, paying particular attention to the driving forces towards the possible affirmation of hydrogen as an energy carrier in incoming years: (i) the limitation of oil reserves, (ii) the necessity of ulterior reduction in pollutant emissions from road vehicles to meet the more and more severe legislative limits, (iii) the need of lowering the CO_2 emissions to control the greenhouse effect.

1.1 Mobility Demands and Primary Energy Resources

Everywhere in the world, the acceleration of industrialization and economic growth is accompanied by an increase of mobility demand, in particular in most of the developing countries the requirements of mobility solutions able to drive the pressing economic growth continues to outpace supply. In the last 20 years, the number of cars and other vehicles is massively grown in many developed countries, while the vehicle ownership is rising at a rate of 15–20% annually in great part of the developing world. Some recent projections show that some regions such as Eastern Europe and Former Soviet Union are likely to reach OECD levels of private transport by 2050, while China and Latin America will reduce the divide significantly. Other regions, such as Africa, Middle East and rest of Asia should see only small increase in their rates of personal mobility [2].

The worldwide increasing diffusion of environmental consciousness has favored the affirmation of the sustainable mobility concept. This can be regarded as the capability of a transportation system to meet the need of society to move freely, improving the access of people to work, education and services, without causing damages to the environment, as these could offset the socio-economic benefits of accessibility improvements. This goal requires the development of new strategies for enabling access to safer, cleaner and more efficient motorized vehicles, public transit systems and transport infrastructures. All the concerns which should be taken into account for the evaluation of sustainable mobility, including the definition of a number of different indicators, have been the object of specific programs, involving many worldwide automotive and energy companies [2], and they will not reiterated here. This chapter will be instead focused on issues directly connected to propulsion system technologies, starting in this paragraph from a discussion on impact of increasing mobility demand on supply of transport-related energy, in the context of overall primary energy availability.

Figure 1.1 shows the distribution of world energy consumption by sources in 2007 [3], it can be noticed that fossil sources represent the largest fraction of the utilized sources (88%), with 36% for petroleum, followed by coal (28%) and natural gas (24%). As almost 90% of the whole energy currently used in the transportation sector derives from crude oil (petroleum), and about 65% of this raw material is converted to fuels (the remainder goes to electric energy, building heating, asphalts and chemicals), the main concerns regarding the availability and environmental impacts of this fundamental primary energy resource have to be discussed.

Petroleum has accompanied the industrial growth and the development of the automotive market in the twentieth century. The reasons which have favored its diffusion in substitution of coal are the higher energy density on mass basis (about 25% higher than coal) and its liquid state (easier and cheaper handling and transportation). Until 1970s, the price of oil did not represent a problem, on the contrary, it was an additional factor for affirmation of petroleum as energy source. The first oil crisis at the beginning of 1970s brought out to attention of the great

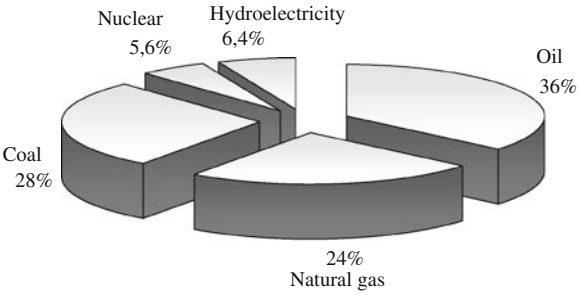

Fig. 1.1 World primary energy consumptions 2007 (total = 11099 Mtoe) [3]

mass of people some limitations until then ignored: geopolitical and financial involvements, depletion of available reserves, environmental impact. The first concern, with its implications on oil price jumps, is not a topic of this book and can be examined closely starting from other publications [4–8], while the environmental impact related to the use of oil-derived hydrocarbons as current transportation fuels will be addressed in next paragraphs. Due to the crucial dependence of transportation means on this resource, some considerations about the controversial problem of future oil availability are presented here.

The limited availability of petroleum is not questionable, because of its fossil nature, then exhaustible and not renewable (millions of years have been necessary to form the oil today extracted, a period of time not comparable to that of its utilization, which is restricted in few decades). The critical issues regard the amount actually still present in the ground and the real possibility and convenience of extracting it. The question of the existing reserves is not easy to be cleared, because of a number of reasons: many oil producers may declare major reserves than those really available in order to obtain financial or political credits, the search of new oil-fields requires new prospecting technologies still under development, any new technology which could favor an increase of production from either existing or new oil-well imposes significant investments (today about 40% of each well is exploited, and higher percentage would possible by more costly technologies). However, a famous model, proposed by the geologist Hubbert on 1949 [9], can be used as basis for estimations about the petroleum left for the future. The Hubbert theory analyzed the ultimate recoverable reserves of crude oil in USA, and was based on the historical annual production data cumulated over the total period of extraction, and on extrapolation of these data to the ultimate extractable amount of petroleum. Applying this model, the oil production curve results "bell shaped" and approximately symmetric, with an early period of exponential growth of the production rate, followed by a maximum value and successive diminution as the integrated production reaches the total amount of the resource. The application of the Hubbert model predicted in the mid 1950s that oil production of USA would reach a peak between 1965 and 1970 [10]. This prediction turned out to be very close to the mark, in fact oil production of USA reached a maximum in 1971, and after then they are importing petroleum with a production reduced to about half than that of 1960. The peak oil theory has been

widely re-proposed and discussed in recent years [11–14], and applied to world oil production for incoming years. The results, in spite the above pointed out difficulties of this type of prediction, converge towards the conclusion that oil worldwide production peak should be reached around 2020 [15–17]. Without considering here neither the apocalyptic scenarios of oil peak theory upholders, nor the skepticism of its deniers, it is possible to observe that there is a virtual agreement among geologists that world production of conventional oil will peak at some point in a not too distant future. On the other hand, considering the other fossil sources, natural gas (only marginally used in the transportation sector) will see its production peak some years later than oil, while for coal (mainly used worldwide for electric energy generation) this will occur some decades later. Natural gas is directly usable as fuel for road vehicles (see Sect. 1.2), while coal should be before converted to syngas ($CO + H_2$) and subsequently to liquid hydrocarbons by the Fischer–Tropsch process [18]; however, these solutions can give benefits in terms of mitigation of the current dependence of transportation sector on petroleum, but do not represent a solution for the problem of CO_2 emissions (see Sect. 1.3). On the other hand, the use of biofuels for vehicles could help to reduce the global CO_2 emissions, but issues regarding efficiency of the production process limit them at a niche sector (see Sects. 1.2 and 1.3). These considerations, together with the well-ascertained fact that energy and mobility demand will only grow over time, and the diffused awareness about climate change problem, appear as sufficient motivations to stimulate policy makers and governments to plan effective implementation of alternative non-fossil energy resources. The link between the development of different energy resources and the decoupling of transports from petroleum consists in the possibility to exploit in this field energy carriers alternatives to conventional fossil fuels, i.e. electricity and hydrogen. This can be realized by a widespread diffusion of electric vehicles, which could adopt two different solutions regarding the supply of energy to the electric drive (see Chap. 5): electric energy storage systems (battery electric vehicles, BEV) or electric energy generation systems, such as hydrogen fuel cells, in hybrid configuration with batteries (hydrogen fuel cell electric vehicles, HFCEV).

The interest of using hydrogen as fuel in the transportation sector is based not only on its very high specific energy (see Sect. 1.2), but above all on its unique characteristic of not emitting any carbonaceous emission during its utilization for energy production, being water its only oxidation product. However, like electricity, it is not an energy source, but rather an energy carrier. In fact, although hydrogen is the most abundant chemical element in the universe (about 80%, the remainder being mostly helium) and the third most diffused element on earth after oxygen and silicon, it is not significantly present on our planet in the free state directly usable for energy production (diatomic gaseous molecule), but only in its compounds. Therefore, hydrogen has to be generated from primary sources (water and fossil hydrocarbons can be considered the most commune hydrogen sources), and this conversion can be performed by several processes (see Sect. 2.1). However, it appears obvious that if the fundamental advantage of hydrogen

(lack of carbonaceous emissions associated with its utilization) has to be maintained at a global level, the development of economically viable production methods starting from carbon-free primary sources is mandatory (as discussed in Sect. 2.1 the technologies for carbon capture and sequestration are far to be practically exploited). At the present state of technology, this means starting from water as primary resource, and using non-fossil electricity to dissociate water in H_2 and O_2, according to electrolysis process (see Sect. 2.1.2).

This immediately raises a problem of comparison in terms of well-to-wheels efficiency between electricity and hydrogen, i.e., between BEVs and HFCEVs, which will be faced later (see Sect. 1.3). The crucial aspect to be stressed here is that both electricity and hydrogen can be considered as clean and sustainable energy carriers only if they are produced by non-fossil sources, in particular if hydrogen is derived from water by electrolysis using electricity generated by renewable energy, the entire system from fuel production to end use on vehicles has the potential to be "zero emission", in terms of both greenhouse gases and local pollution.

Figure 1.1 shows that 6.4% of the energy consumed worldwide is produced from conventional renewable sources (hydroelectric), while only a marginal fraction is generated from new renewable energy sources (about 0.4%, not reported in Fig. 1.1). According to the most commonly accepted definition, a renewable resource is one that can be replenished over a relatively short timescale or is essentially limitless in supply. The new renewable resources—essentially solar, wind and biomass, being tidal and geothermal very far from a commercial exploitation—are worthy being greatly promoted because they constitute an important alternative to fossil fuels. At this regards recent decisions of the European Union (Decision N. 1639/2006/EC of the European Parliament, [19]) go in this direction. The target is to reach a 20% share of energy from renewable sources in the overall mix, focusing efforts on electricity, heating, and biofuels.

The main renewable source is the direct solar radiation, which can be exploited for both direct and indirect electricity production. The power of the energy flow coming from the sun depends on a number of parameters, such as season, latitude, longitude, altitude, orientation, and inclination of the receiving surface, and at sea level can reach the maximum value of about 1000 W/m^2. It can be converted in heat energy, which is either directly used in producing hot water or house heating (solar thermal energy), or concentrated by mirror systems and then used for steam production and consequent electricity by expansion in turbines (solar thermodynamic energy). Moreover, the solar energy can be directly converted in electric energy by using photovoltaic cells. These devices are composed by two thin layers of semiconductors materials (*n*- and *p*-types, negative and positive, respectively), between them an electric field is present due to the different nature of the two materials (solar photovoltaic energy) [20]. The absorption of incident photons (sunlight) generates an electron–hole pair, and when an external circuit is connected to the cell, the electron and hole are separated by the structure of the device (electrons to the negative terminals and holes to the positive terminal) thus generating electric power. The most mature solutions regarding the material used to

generate the photovoltaic effect are based on silicon cells. Advanced designs have achieved conversion efficiencies (defined as ratio between power of solar radiation to maximum power supplied by the device) of almost 30% in laboratory conditions, while efficiencies of 10–15% are available on current commercial devices [21]. Research in this field is being also conducted in order to produce competitive organic photovoltaic cells with significantly lower costs than silicon cells. As the voltage obtainable from a single photovoltaic cell is too low for the most common applications (about 0.5 V), the connection in series of several cells is necessary, realizing arrays of cells usually installed in metallic frames and covered by anti-reflection glass (photovoltaic modules for different applications).

Wind energy is currently proposed in the contest of new renewable sources for the direct production of electricity by wind generators, with power capability ranging from few Watts to Megawatts. The possibility to exploit the wind energy in a specific geographic place depends on three main parameters: intensity, direction and velocity of the wind in that particular site. Turbines are generally spaced approximately three blade diameters apart, in all directions, leaving significant area of land still available to be exploited for other purposes. Wind generators with blades of 50 cm diameter are used as battery rechargers, while those with blades of about 50 m can be used for electric energy production up 2 MW. The most diffuses types of wind generators adopt two or three blades of about 30 m, and are capable to generate an electric power of about 1500 kW. The wind generators are connected each other to realize the so-called *wind farm*. Wind energy is classified according to the range 1–5, corresponding to the average wind velocity in a site, where 5 is the strongest. Typical output power densities for class 5 sites range from 3.2 to 5.7 W/m^2 [22]. As wind change and variability is caused by uneven heating of the ground by the sun, the power of the wind can be considered as a form of solar power. Assuming an average solar power density of 200 W/m^2, the output power density of 5.7 W/m^2 before considered corresponds to an efficiency of 2.85% for a wind generator. This efficiency, although not directly dependent on solar radiation as for photovoltaic, permits a comparison between the two renewable resources. Wind power efficiencies are lower than photovoltaic of about one order of magnitude, but whereas a solar photovoltaic array requires 100% of the land on which the modules are placed, a wind farm occupies only a small fraction of the land for the base of the turbine and access roads.

Biomass can be defined as any organic material available on a recurring base, which can be transformed in a variety of products, such as energy, chemicals and biomaterials, a possibility which has led in recent years to the concept of *biorefinery*. The most obvious types of biomass are wood and crops, which are considered to be renewable as they can be continually regenerated by taking up carbon dioxide from atmosphere during growth (through photosynthesis). In addition also many types of organic wastes (forestry residues, straw, food waste, manure, etc.) can be considered as biomass. At the end of their utilization biomass resources return to the air, so creating a closed loop cycle. This evidences that also biomass, like wind, can be regarded as a form of solar energy, which is transformed by living organisms through their normal functions of growth and metabolism.

A part from the physical upgrading of biomass for obtaining solid renewable fuels (such as wood power, briquette and pellets), the energy production from biomass can be realized by two basic types of processes: microbiological and thermochemical methods. The choice of the specific process is effected evaluating the characteristics of the initial biomass, in particular its carbon and nitrogen content (C/N ratio) and humidity. A high nitrogen content implies green vegetable material, more suitable for biochemical reactions, whereas a high carbon content indicates that the biomass can be usefully exploited by combustion. Microbiological processes are involved in obtaining a number of biofuels from different types of starting biomaterials: bioethanol by alcoholic fermentation from any carbohydrate-containing materials, biodiesel from plant oils or algae after transesterification of triglycerides with methanol, biogas (a mixture of methane and carbon dioxide with traces of hydrogen, nitrogen and hydrogen sulfide) by anaerobic digestion of complex organic materials, such as animal dejections and by-products of several cultivations (C/N 15–30, humidity higher than 50%), biohydrogen by conversion of protons to hydrogen gas occurring during metabolism of many types of micro-organisms (hydrogenases) [23].

Unlike microbiological methods, the thermochemical processes permit the dry biomass to be transformed, preferably with high C/N ratio, not only to chemicals and fuels but also directly in heat and electricity, and can be divided in the following groups: combustion, pyrolysis, and gasification. Combustion in the presence of air is obviously the most simple and diffused method for converting chemical energy in biomass to power (thermal and electric), being usually carried out in furnaces, boilers, steam turbines and turbo-generators starting from dry materials with humidity grade <50%. The other two methods are capable to supply a variety of products as function of the operative conditions. Pyrolysis is the incomplete thermal degradation in the absence of oxygen of any carbon-containing material, it can occur already at temperatures lower than 400–500°C providing products containing carbonaceous residues, gaseous compounds but mainly bio-oil (or pyrolysis oil), a liquid mixture of different substances, such as alcohols, aldehydes, ketones, esters and phenolic compounds. At temperatures higher than 800°C in the presence of air and water the complete gasification of biomass can be observed. Coal or carbohydrates of different molecular length from biomass can react with oxygen and steam to generate CO and H_2 (bio-syngas), which can be directly used in gas turbines for power generation or converted to different fuels in the presence of catalysts and at different operative conditions. In this contest the Fischer–Tropsch process, based on the reaction between CO and H_2 to give water and alkanes, in the presence of Fe based catalysts at 200–350°C and 10–40 bar, represents a possibility to produce biodiesel starting from biomass. Finally, another route to obtain hydrogen from biomass is constituted by the transformation of biogas (biomethane), deriving from anaerobic digestion, in bio-syngas by the steam reforming or partial oxidation reactions (see Sect. 2.1).

Electricity production from biomass (direct combustion or derived by biofuels) presents some advantages: very low cost of the starting material with respect to fossil fuels, zero net CO_2 emissions, security of supply and reduction of transport distances when electricity is produced close to the biomass production site.

However, from the efficiency point of view, it has to be considered that the biomass formation always requires the conversion of solar energy to some type of biomaterial, and this can be realized only by the photosynthesis process, whose energy efficiency is lower than 1% (see Sect. 1.3).

The well-known limits of new renewable energies reside in their low energy density (all of them), intermittency (solar, wind) and not always reliable predictability (wind). For this reason in recent years the debate on nuclear energy has seen a renewed interest, especially in countries where its utilization has not yet accepted or widely diffused. In 2007 about 6% of the total world energy usage is produced from nuclear (Fig. 1.1), in over 400 current operating nuclear plants. Several recent publications analyze the main issues and last advances associated with nuclear power [24–28], here limits and potentialities of this technology are briefly described, in relation to the usage of electricity and hydrogen as energy carriers on transportation means [29–33].

The commercial nuclear technology is still based on *fission* of isotope 235 of uranium (^{235}U). This is defined as fissile material since it is capable to absorb neutrons of any kinetic energy (also low energy "thermal" neutrons). Uranium is mainly present in natural deposits as U_3O_8, where 0.7% of uranium is constituted by ^{235}U, the remainder being ^{238}U. In order to have an amount of fissile nuclei sufficient for reactor operation all fission reactors are fueled with uranium which has been enriched to about 4% in the fissile ^{235}U. High energy neutrons produced by the fission of ^{235}U can be absorbed by other ^{235}U nuclei, so continuing the reaction. The fission of one nucleus of ^{235}U produce about 200 MeV of usable energy, to be compared with 4 eV produced by the oxidation of one C atom. During the overall process, a huge amount of heat is produced through a controlled nuclear chain reaction in a critical mass of fissile material. Potential future developments (fission in *fast neutron reactors* (*breeders*), also known as *fourth generation nuclear*, which could use ^{238}U, much more abundant than ^{235}U, and *nuclear fusion*) are decades away from their practical utilization for producing energy.

The risks associated with highly radioactive spent fuel wastes, with the uncertainties regarding the stability of the geological repositories for the required length of time (about 200,000 years), and the not eliminable possibility of accidents in plants, constitute fundamental causes of intense opposition to the current nuclear technology. Another critical aspect is connected to the ascertained reserves of uranium, which could not be sufficient to fuel over 400 already existing nuclear reactors (65,000 tons/year consumed) plus possible future plants. The world reserves of uranium, as estimated by IAEA (International Atomic Energy Agency) as function of market price and with reference to the current uranium production, should be sufficient for about 100 years at 100 USD/kg U_3O_8 (approximately equal to the average price at the beginning of 2010). However, this evaluation considers not only the reasonably assured resources, but also the estimated additional ones, deduced from exploration data relative to known deposits [34]. This problem could make impracticable a substantial expansion of nuclear energy in next years, in particular the requirements of uranium coming from strategically influent countries would

create a competition for uranium provisions, compromising the nuclear plans of the weaker countries. Other aspects of nuclear energy which could limit its further development consist in very high investment costs and the feature of guarantee the maximum efficiency only producing electric energy at constant power, which would not be compatible with the typical absorption fluctuations of the electric grid if electricity was totally produced by nuclear.

In comparison with the above critical concerns, the main advantages of nuclear energy are constituted by very high specific energy (1 ton of U_3O_8 can produce about the same electricity obtainable from 14,000 tons of coal) and the substantial absence of greenhouse gas emissions, even if some CO_2 generation has to be considered for other operations connected to working of a nuclear plant, such as extraction of uranium from U_3O_8 ore and plant fabrication. These significant advantages could better express their potentialities if nuclear power generation was integrated with energy storage systems based on hydrogen as energy carrier. While thermochemical routes to produce hydrogen from water feedstock by using nuclear-produced heat have not yet reached the prototype phase, the electrolysis process based on low-cost nuclear electricity appears in the short term as the best approach to store the surplus of energy produced by the reactor and not required by grid in the same site of the nuclear plant [34], so permitting overcoming of one of the limitations of nuclear reactors for electricity generation, i.e. the working at constant power in proximity of the *base load*. In the long term, high temperature electrolysis could be coupled to thermochemical water splitting, both enabled by nuclear heat (see Sect. 2.1). Regarding the transportation sector, recent studies have compared different possibilities of using nuclear energy for production of energy carriers for vehicles, i.e. electricity, hydrogen, and liquid fuels (both synthetic and biofuels) [31]. In this case, the role of the nuclear energy in the production of liquid fuels would consist in supplying heat and/or electrolitycal hydrogen for the coal gasification and Fischer–Tropsch processes. These analysis have evidenced that the availability of low cost and carbon-free energy carriers, such as electricity and hydrogen nuclear-derived, could reduce the CO_2 emissions in the production of liquid fuels by eliminating the combustion of fossil materials for the required heat supplying and would be essential for the future development of both solutions before considered as zero emission vehicles, i.e. BEVs and HFCEVs.

Regarding the economic implications of the different energy supply processes before considered, in recent years the approach based on Energy Return On Investment (EROI) is gaining always growing assents [35–37]. Expressed as function of time the EROI can be defined as the ratio of the delivered end-user energy, $E_o(t)$, to the energy invested for its delivery, $E_c(t)$ (all energy costs associated with the fabrication of the plant, its management and dismantling), both quantities being cumulative for the specified time t: EROI $(t) = E_o(t)/E_c(t)$. Assuming the time t equal to the whole life cycle of the plant, $E_o(t)$ can be calculated with sufficient reliability and data are readily available, while $E_c(t)$ needs an approach based on the *life cycle analysis* (LCA), which is often object of estimates not convergent. On the other hand, although in societies based on free market the correlation between money and energy should be always verified, it is unavoidable that some distortions

Table 1.3 Estimations of energy return on investment (EROI) ratios for different energy processes

Fuel supply technology	EROI
Oil and gas (wellhead) 1940s	>100
Oil and gas (wellhead) 1970s	8
Coal (mine mouth) (1950s)	80
Coal (mine mouth) (1970s)	30
Ethanol (sugarcane)	0.8–1.7
Coal to electricity	9.0
Hydropower to electricity	11.2
Nuclear to electricity (light water reactors)	4.0
Solar Photovoltaic to electricity	1.7–10

Adapted from reference [39]

can be introduced by extra-market interventions, such as governmental incentives in favor of a particular technology [38]. For this reason, in spite of uncertainties about the LCA evaluations, the EROI method appears more reliable than money-based assessments, and data ranges present in literature are sufficient for an useful comparison between different energy supply processes. Some estimates based on reference [39] are reported in Table 1.3, where any value of EROI <1 implies a net loss of energy, that is more energy has been consumed with respect to that produced during the life cycle of the plant, while the higher EROI is, the more convenient the production process results in energetic terms. It can be noticed that EROI for oil and gas was very high (>100) before 1970, after then it rapidly decreased due to the exhausting of the largest and cheapest wells. EROI of coal for electricity production is still quite high (about 9), but this technology produces the highest CO_2 emissions at parity of electric energy produced. Among carbon-free resources the EROI of nuclear power to electricity is lower than fossil resources and comparable to that of solar photovoltaics (about 1.7–10).

The EROI approach suggests that, in spite of the limitations of new renewable energy resources above considered, the significant potentialities not yet entirely exploited offered by these alternative technologies should convince scientists and politicians to make any possible effort aimed at their widespread diffusion, in order to limit the future necessity to resort to fossil or nuclear sources. In particular, electricity produced by renewable resources can be used for decentralized production of hydrogen, with a strong interaction between these two *clean* energy carriers, which could be extended to the transportation sector.

1.2 Internal Combustion Engines and Their Impact on Air Quality

Motor vehicles are a key factor affecting both economy and lifestyle of populations in rich countries, and are gaining the same role in emerging nations. Thus, the growth in human mobility demand is expected to continue, intensifying the negative impact of transportation means on environment.

The dominant technology used for almost two centuries to power both light and heavy duty vehicles is based on internal combustion engines, that generate power by converting chemical energy of the burning fuel into heat and then into mechanical work, an energy transformation realized by either Otto or Diesel thermodynamic cycle.

For a deep analysis of all issues regarding the internal combustion engines and for a comprehensive examination of energy sources for transportation, which are outside the scope of this book, other monographs are recommended [40, 41]. The discussion of this section will be subsequently focused on interactions engine-fuel and their effects on local and global environmental issues.

In the Otto cycle engine, the air–fuel mixture is burnt by using a timed ignition generated by an external electric source (SI, Spark Ignition engine). This principle can be practically realized in two different basic ways, reciprocating engine with four or two strokes, and rotary engines. The four-stroke reciprocating engine is the most frequently used in both light and heavy duty vehicles, and utilizes four strokes for gas exchange processes, controlled by valves (during one working stroke the crankshaft turns twice): air–fuel mixture intake, compression and timed ignition shortly before the piston has reached the top dead center, working stroke (combustion and expansion), exhaust of combusted gases. In the more recent development of spark ignition engines (SIDI, Spark Ignition Direct Injection), the air flow is regulated by a throttle valve and is compressed in the cylinder, while the fuel, managed by electronic injection systems, is added to the compressed air inside the cylinder. This system ensures more accurate control of air–fuel mixture in terms of homogeneity and carburation, with consequent benefits for fuel consumption, performance and response in transient phases. After ignition induced by the spark plug, combustion must develop in a controlled way under all operative conditions, without autoignition phenomena. These occur if ignition quality of the fuel does not meet that required by the engine, provoking very sharp increase of temperature and pressure (*knocking combustion*) with consequent damages to the engine. A retarded ignition could avoid knocking also with poor quality fuels, but would imply higher exhaust gas temperature with efficiency losses. The ignition quality of the gasoline is described by the *octane number*, which is determined by comparing in a reference engine the ignition characteristics of a gasoline to those of isooctane (2,2,4-trimethylpentane) and heptane. Isoctane is assigned octane number of 100, due to its prerogative to burn smoothly with little knock, while heptane is given an octane number of zero because of its bad knocking properties.

Two stroke Otto engines, in which a working cycle is achieved with each rotation of the crankshaft, can be smaller and lighter with respect to four stroke ones, and are used almost exclusively on small motorcycle, due to unsolved problems regarding fuel consumption and emissions. The rotary engine (or Wankel engine) can be considered a variant of the four-stroke reciprocating engine, from which it differs for its rotary piston and for the use of ports instead of valves for gas exchange phases. This type of engine is not diffused on modern vehicles due to its relatively high fuel consumption and exhaust gas emissions.

In principle also Diesel engines can operate either with two or four strokes, but in practice, while the four-stroke Diesel engines are present on the vast majority of vehicles, the two stroke ones have some application only on large ships. The modern four-stroke direct injection Diesel engine (CIDI, Compression Ignition Direct Injection) differs from the SIDI Otto engine for the self ignition of the fuel and more heterogeneous air–fuel mixture. The air intake is unthrottled and the fuel/air ratio varies with the quantity of fuel injected. The energy required for ignition comes from the high temperature of air compressed in the cylinder, which determines the self-ignition of the fuel just before the end of the compression stroke. This implies the adoption of very high compression ratios to reach the temperatures necessary to ignition. The ignition delay (time between injection and start of combustion) is necessary to be tuned in order to assure optimal engine operation, with high efficiencies and low consumptions, exploiting the fuel self-ignition properties. Too long ignition delay implies a steep pressure rise in the combustion chamber, with consequent increase in noise and nitrogen oxides emissions. The self-ignition properties of the Diesel fuel are quantified by the *cetane number*, which is defined as volume percentage of cetane (hexadecane) in α-methylnaphthalene. A cetane number of 100 is attributed to *n*-hexadecane, a compound characterized by very high ignition quality, while a value of zero is given to α-methylnaphthalene, with very low ignition properties. These engines must operate in lean conditions (i.e. with air/fuel ratio higher than stoichiometric requirements), in order to reach the complete combustion of the heterogeneous mixture, with benefits in terms of efficiency and torque, but less power with respect to SIDI engine of comparable size. The more recent versions of CIDI engines use turbochargers to assure additional power (by feeding larger amounts of fuel and air into the cylinders), and the so-called multi-jet common rail technology, which permits reaching of very high injection pressures inside the combustion chamber and utilizes sequential electronically controlled multi-injections of fuel, with benefits on emissions, fuel consumption and noise. The CIDI engines reach higher efficiencies when compared to SIDI engines, because of high compression ratios and lean air–fuel mixtures.

Homogeneous charge compression ignition (HCCI) engines have received much attention in recent years and are today becoming an industrial reality. They combine the essential characteristics of Otto and Diesel engines; in particular, a premixed homogeneous and lean air–fuel charge is compressed to the autoignition point, permitting low NO_x and particulate emissions, and efficiency values comparable to Diesel engines [42].

Nearly all motor vehicles today are propelled by either gasoline (Otto engines) or gasoil (Diesel engines), which are carbon-containing liquids derived from a non-renewable resource, such as crude oil. These fuels have been always considered particularly suitable for vehicles because of their availability, ease of use and high energy density. Because of different types of combustion occurring in Otto and Diesel engines, completely different characteristics are required for gasoline and gas oil, which are described in detail in the reference [41].

Gasoline is produced by fractional distillation of crude oil. It is a complex mixture of about 500 hydrocarbons in the C_4–C_{12} range, belonging to four compound groups: alkanes, cycloalkanes, alkenes, and aromatics. Straight chain or branched alkanes are present in greatest amounts (about 50%), with smaller quantities of cyclic alkanes and aromatics and trace amounts of alkenes. The most important motor properties of a gasoline are its octane quality, which is responsible for its resistance to autoignition, and volatility. This is expressed by distillation behavior and vapor pressure, and permits obtaining of an ignitable air–fuel vapor in the combustion chamber in all operative conditions, but can also affect exhaust gas and evaporative emissions. Benzene and lead additives were formerly used to control antiknocking properties of gasolines, but because of their toxicity they are today substituted by isomerate higher aromatics, ethers (methyl *tert*-butyl ether), alcohols.

Gasoline should be ideally converted to water and carbon dioxides during combustion, however, also undesired compounds are present in engine exhaust gas because of different phenomena occurring in the combustion chamber [40]. These compounds can be grouped as total unburned hydrocarbons (THC), non-methane unburned hydrocarbons (NMHC), carbon monoxide (CO), nitrogen oxides (NO_x), and particulate matter (PM). While improved engine technology has led to some reduction in exhaust emissions, their dramatic reduction has been possible, thanks to the introduction of exhaust gas treatment catalytic systems. Actually, more than 95% of these pollutants are converted (oxidized or reduced) on three-way catalytic converters currently installed into the exhaust system of gasoline vehicles [43], while their residual concentration can be affected by fuel reformulation in the refinery. Several studies have been carried out about the effect of alternative reformulations of gasoline on air quality; in particular the reduction of total aromatics and sulfur has been successfully investigated [41].

The gasoil for Diesel engines derives from the middle distillate fraction of crude oil distillation. Unlike gasoline, it need to be easily decomposed at temperature and pressure values reached in the combustion chamber, as a consequence its composition is mainly based on alkanes and cycloalkanes (about 80–90%), while the presence of different unsaturated compounds (aromatics and olefins) permits other engine requirements to be met, such as low temperature behavior and heating value. A high cetane number is beneficial not only for self-ignition and starting behavior, but also for emission reduction and noise. As sulfur in the fuel increases the emissions of sulfur dioxide and particulate matter, its content in commercial Diesel fuels has been limited at very low levels (50 ppm in Europe since 2005) and tends to be almost completely eliminated (10 ppm in Europe since 2009). Apart from the direct benefits on particulate emissions a sulfur content reduction from 50 to 10 ppm could also increase the performance and durability of oxidizing catalytic converters and give benefits in the form of reduced sulfur-induced corrosion and slower acidification of engine lubricating oil. Regarding the effect of gasoil hydrocarbon composition on exhaust emissions the correlation between mutagenicity of exhaust gas and aromatic content has been also assessed [44].

Although air quality has improved over the last 20–30 years, there are still significant pollution problems throughout industrialized and emerging countries, especially in urban areas and densely populated regions. At this regard, the research in the field of new engine and fuel technologies has been mainly forced by legislators, rather than by marketplace. Governmental legislators are mandating increasingly stringent standards for pollutant emissions from vehicles' exhaust, with a general warning also about fuel economy issues and lowering of greenhouse gas emissions. In particular, reduced emissions from road transport are seen as an important factor to improve air quality, particularly because the share of Diesel vehicles in the overall sales of light duty vehicles is increasing. In the European Union the Euro 5 and Euro 6 emission standards for cars have been fixed by the introduction of Regulation (EC) N. 715/2007 [45] and it's implementing regulation (EC) N. 692/2008 [46]. These regulations revise the current emission limits for motor vehicles (the Euro 4 standards, in force since 1, January 2005), and their technical requirements take effect in two stages, with Euro 5 emission limits coming into force since 1, September 2009, and Euro 6 emission limits since 1, September 2014. The main effect of Euro 5 is to reduce the emissions of particulate matter from Diesel cars from 25– 5 mg/km. This will make the introduction of particle filters for Diesel car mandatory. Euro 6 limits mainly reduce the emissions of nitrogen oxide from Diesel cars further, from 180 mg/km to 80 mg/km. As the introduction of new technologies implies additional costs and determines an increase in consumer prices of new vehicles, the new emission limit values of Euro 5 and Euro 6 have been calculated in order to ensure a benefit in air quality standards without compromising affordability of cars for the consumers.

The necessity to meet the always more severe emission limits imposed by regulators, together with concerns about the extent of crude oil reserves and excessive dependence on oil-producing countries, have favored in the past decades a strong interest towards the possibility of using alternative fuels to propel road vehicles.

Natural gas is a fossil fuel very abundant in nature, but, at variance of crude oil, whose reserves are located prevalently in the Middle East (about 65%), it is evenly distributed around the world, with the largest known reserves in the areas of ex-Soviet Union (35%) and Middle East (40%), followed by Asia, Africa, America and Western Europe. It is mainly constituted by methane (85–99%, in dependence of its source), with other compounds present in much lower concentrations: heavier hydrocarbons (ethane, propane, butane, and their isomers), inert gases (nitrogen and carbon dioxide), sulfur compounds (hydrogen sulfide, carbonyl sulfide, mercaptans), traces of noble gas and water. This composition is responsible for the main advantage of natural gas with respect to gasoline and gas oil from an environmental point of view, in fact natural gas vehicle have much lower non-methane hydrocarbon and particulate matter emissions, but higher methane emissions, which imply less toxicity of the engine exhaust gas [47]. However, also natural gas vehicles need the adoption of three-way catalytic converters (with enhanced reactivity with respect to those designed for gasoline vehicles, due to the higher chemical stability of methane) and modern electronic fuel control systems

in order to meet the severe regulations on pollutant emissions. Furthermore, since natural gas contains only 75% carbon by mass versus 86–88% for gasoline and gasoil, less CO_2 per unit of energy released is present in the exhaust gas (comparable to CO_2 emissions from a Diesel vehicle, which operates with lean air–fuel mixture and higher efficiency). Regarding the motor characteristics, the methane has a very high resistance to autoignition, which means high potential for use in a high compression engine, and wider flammability range than other hydrocarbons, allowing the engine to operate lean (but the need of using three-way catalyst imposes a working in stoichiometric conditions). On the other hand, the volume of the gas reduces the air breathing capacity of the engine, with diminution of engine performance, which could be partially recovered by increasing the compression ratio. However, as the majority of natural gas vehicles are bi-fuels aftermarket-converted gasoline vehicles, then designed for specific antiknocking characteristics typical of gasoline, the entire potential of methane cannot be exploited on these vehicles. The low energy density of natural gas also causes storage problems on board of vehicles, due to the pressurized cylinders necessary to store the gaseous fuel, and consequent driving range limitations, especially for passenger cars. Although a large amount of both light- and heavy-duty vehicles propelled with methane are running in many countries, the main obstacles to widespread diffusion of natural gas vehicles are still the absence of transportation and storage infrastructure.

Liquid petroleum gas (LPG) is separated from natural gas by extraction of heavier liquid hydrocarbons, removed before gas distribution, or derived by processing of crude oil in refineries. It is constituted mainly by propane, and at lower extension by butane, isobutane, propene, and butenes, in dependence of the production method. In addition to these components, other species may be present in trace amounts, such as sulfur compounds, water and tars. The major producers and exporters of LPG are the Middle East, Canada, North Africa and the Far East, while the main consumers are USA, Japan and Western Europe (about 10% in the transportation sector). Presently, LPG supply exceeds demand in most petroleum-refining countries, so its price is low compared to other hydrocarbons. It has good fuel properties (higher octane rating and wider flammability limits than gasoline), and as a fuel for spark ignition engines it presents many of the advantages as natural gas, with the useful additional characteristic of being easier to store on board of a vehicle, thanks to its liquid form at room temperature and low pressure (8–10 bar). Also, emissions characteristics are similar to those of natural gas vehicles, with differences regarding hydrocarbon composition at the exhaust, which is depending on fuel composition (propane/butane mixture instead of methane, with lower H/C ratio). The transformation of vehicles to operate with LPG is made either by the user by retrofitting after vehicle purchasing, or by the manufacturer before sailing. The LPG transformation kit interfaces with the standard vehicle electronic control unit, so that all emission control systems are fully employed. LPG is considered both as an alternative fuel and as an intrinsically clean fuel by many governmental agencies, with consequent tax incentives or exemption from no thoroughfare in some historical centers, which have promoted its diffusion.

Methanol is currently produced from natural gas by steam reforming process and is distributed primarily as an industrial chemical, but it could be produced also by any carbonaceous material including biomass. It has many desirable combustion and emissions characteristics, such as higher octane number and wider flammability limits (lean combustion capability) than gasoline, in addition being a liquid its storage and handling are much simpler than gaseous fuels. Light duty methanol vehicles have NO_x and CO emissions similar to gasoline vehicles, while light hydrocarbons emissions are about half those gasoline vehicles. Emissions of formaldehyde (a primary combustion product of methanol) are much higher with respect to those of vehicles fueled by gasoline or other alternative fuels, but can be easily controlled by exhaust catalytic converters. Its H/C ratio is higher than gasoline or Diesel fuel, therefore it produces less CO_2 when burned. However, methanol presents some serious limitations as motor fuel, in particular it is highly toxic and corrosive, its energy density is lower than that of gasoline due to the high atomic weight of the oxygen contained in its molecule, its mass heating energy is about half with respect to gasoline. The most common methanol fuel is the blend M85, containing 15% of gasoline, which solves the cold start problems of methanol, due to its volatility.

Since oil crisis of 1970, the potential use of fuels deriving from renewable sources has been studied and proposed. In this perspective ethanol produced by biomass (bioethanol) has received the major attention. Due to the fact that bioethanol is produced from plants, its burning would lead to a complete recyclable carbon dioxide. It can be obtained by fermentation techniques from any carbohydrate-containing materials, in particular from several types of cereals, sugarcane, sugarbeet, and wood. Brazil and USA are the largest producers of ethanol (two-third of the total worldwide production), obtained from sugarcane and corn, respectively, while the contribution of Europe is lower than 10% (mainly from sugarbeet). About 80% of the ethanol produced worldwide is utilized in the transportation sector, where it is most commonly used as an oxygenate in blends with gasoline, which can be burned in conventional spark ignition engines, while specialized engines would be necessary to burn pure ethanol. In Brazil, the proportion of bioethanol in gasoline is about 25% ("gasohol"), while in USA and Europe concentrations of 10 and 5% are admitted, respectively. The main effect of using ethanol in blend with gasoline consists in slightly lower emissions of light hydrocarbons and CO. The possibility of using much higher concentrations of ethanol has been permitted by the recent developments of the so-called "flexible fuel vehicles" (FFVs), which are able to run with any mixture of gasoline and ethanol up to a concentration of 85% ethanol (E85 fuel). In these vehicles, the oxygen content of the fuel is monitored by sensors, in order to adjust all engine parameters accordingly. As ethanol has no lubricant properties, its use as stand alone fuel requires the adoption of additives to ensure the necessary lubricity of the fuel. These vehicles have reached a large diffusion in Brazil, where about 80% of new cars utilize the FFV technology. A large use of bioethanol in FFVs could enable several countries to achieve their targets for CO_2 emission reduction, however, since ethanol is mainly derived from grains and sugars, its production for

transportation use is in direct competition with food production in most countries, keeping ethanol price relatively high and discouraging its use as a motor fuel except where it is strongly subsidized, such as in Brazil and USA. From this point of view, ethanol produced from lignocellulosic feedstocks (woody and herbaceous biomass) could represent a more suitable source of this renewable fuel.

Biodiesel is a renewable Diesel fuel substitute. Generally, it can be considered as a Diesel fuel derived from any biomass; however, its current production method is based on the transesterification reaction (or alcoholysis) of triglycerides by methyl alcohol (methanol), to obtain a product known as fatty acid methyl ester (FAME). Triglycerides can be contained in different fatty biomaterials, such as vegetable oils and animal fats. In the European Union, world leader in production and consumption of biodiesel, it is mainly derived from rapeseed and sunflowers, while in USA, the predominant source is the soybean oil. The European Union is expected to continue to be the main producer of biodiesel, thanks to the introduction in 2003 of European Directive 2003/30/CE, which requires that 5.75% of conventional fossil fuels will have to be substituted by biofuel. Triglycerides are esters of three fatty acids and one glycerol, with the type of fatty acid depending on the nature of the bio-source. FAME is regarded as "first generation" biofuel as it is produced by only a small fraction of the crop (the oil extracted from the sees of the plant), while second and third-generation biofuels will use the whole crop thanks to new technology under development. In principle, vegetable oils could be directly used in Diesel engines; however, some of their characteristics would cause several problems in vehicle applications. In particular, the viscosity of vegetable oils is about 10–20 times higher than that of petroleum Diesel fuel, which implies very different injection and atomization characteristics. As fuel injection systems of modern Diesel engines are very sensitive to viscosity change, the problem deriving by the direct use of vegetable oils has been avoided by the transesterification with methyl alcohol. However, the use of methyl alcohol implies the introduction into the production process of an additional fossil energy (methyl alcohol is produced by natural gas via syngas), which partially compromises the closed-loop carbon dioxide circle regarded as the main environmental advantage of using plants as energy sources. Biodiesel can be used in Diesel engines neat or blended with petroleum Diesel fuel, and its beneficial properties with respect to the conventional fuel include higher cetane number, zero sulfur and aromatics content, lower particulate matter, CO and polycyclic aromatic hydrocarbons (PAH) emissions (higher emissions of aldehydes can be controlled by exhaust catalytic converters). While the use of FAME as a component of blended Diesel fuels is commercially increasing (blend B20, containing 20% of biodiesel), the neat FAME biodiesel is present only in niche market. Similarly to any other fuel derived from plants (i.e. bioethanol) the worldwide limited landscape surface for cultivation, with the consequent competition with food production, is a key concern which strongly hinders the biomass fuel diffusion. Although the second and third-generation biofuels promise to utilize the whole crop of non-edible plants, land exploitation issues will remain of fundamental importance for all fuels derived from biomass, especially if the very low efficiency (<1%) of the natural

process converting solar energy in vegetable material is taken into account (see Sect. 1.3). Recent studies have evidenced that the global potential for biomass energy production could substitute not more than a few percent of current fossil fuel usage [48].

Hydrogen is a fuel much different from those above considered, due to its nature of carbon-free fuel, which implies obvious benefits in terms of exhaust emissions. However when combustion is used as an oxidation process to provide energy, NO_x emissions are unavoidable, together with traces of hydrocarbons and CO deriving from engine lubricant. A part from the absence of carbonaceous emissions, the great interest towards hydrogen as a transportation fuel is based on its thermal properties. Its specific energy is about three times higher with respect to both conventional liquid fuels (gasoline and Diesel fuel) and natural gas; however, its volumetric energy density at atmospheric pressure is more than three times lower than natural gas. This implies that if hydrogen has to be used in automobile fuel tanks, it needs to be compressed at very high pressure (at least 700 bar) to ensure a driving range per refill comparable to that of conventional vehicles, or stored as a liquid in cryogenic cylinders (see Sect. 2.3). Regarding its utilization in internal combustion engines for road vehicles, hydrogen presents some beneficial characteristics, such as very higher octane number and wider flammability than gasoline. While low ignition energy and high flame speed can cause self-ignition phenomena or flame flash-back during mixture preparation, the wider ignition range permits very lean air/fuel mixtures to be burnt, giving a way of controlling the NO_x emissions. Recent developments of BMW have led to the seven series H_2 prototype [49], with liquid hydrogen on board and an electronic fuel mixture system, able to exactly regulate the hydrogen intake. The combustion on this prototype is generally lean, with reduced NO_x emissions, while the insulation system of the cryogenic tank ensures loss-free storage of hydrogen for about 3 days with a refilling time of about three minutes.

If the aspect of vehicle exhaust emissions is considered as a priority, the above considerations show that hydrogen is the most suitable fuel for the technology currently adopted to power most of today vehicles (i.e. internal combustion engines). However, other critical issues related to usage of this energy carrier, in particular production and storage methods, besides the need of dedicated infrastructures (see Chap. 2), suggest to evaluate the convenience of its utilization in a wider context, taking into account atmospheric emissions at global level, and estimations of well-to-wheels efficiencies.

1.3 Climate Change and Carbon-Free Fuel Chance

The greenhouse effect is a natural process which helps to regulate the earth's temperature, avoiding planet freezing. About half of the visible radiation coming from sun pass freely through the atmosphere and is transformed in heat when

absorbed by earth's surface. Because of its temperature, the earth's surface returns this energy back to atmosphere in the form of infrared radiation. Some gaseous species present in the atmosphere are capable to absorb and trap as heat a fraction of the infrared energy emitted from earth's surface after this has been heated by the sun. Thanks to this natural phenomenon the average planet temperature is about 15°C, instead of −19°C which would be observable in the absence of natural greenhouse effect. The most abundant *natural* greenhouse gases are water vapor (mainly coming from ocean evaporation), carbon dioxide (derived from plant and animal respiration) and methane (produced by anaerobic degradation of organic materials), whereas other gases present in the atmosphere and able to absorb terrestrial infrared radiation are removed in very short times and do not accumulate in significant concentrations. For average survival times of 1 year or longer, the greenhouse gas released at earth's surface can be spread by the winds thorough the atmosphere and may absorb infrared radiation at all latitudes and longitudes. Human activities can further contribute to the presence of greenhouse gases in the atmosphere, not only regarding the above-mentioned water vapor, carbon dioxide, and methane (mainly derived from combustion of fossil fuels including natural gas), but also with emissions of nitrous oxide (N_2O, coming from use of fertilizers in agriculture) and synthetic halocarbons (mainly uses as solvents, pesticides and refrigerants). While it is not questionable that human activities have been causing a concentration increase of greenhouse gases in the atmosphere, an intense scientific debate is currently focused on alterations that this increase can determine on earth's natural equilibrium, enhancing the natural greenhouse effect and provoking dangerous climate changes by the undesired earth's global warming.

Table 1.4 shows a comparison between different greenhouse gases in terms of removal times from atmosphere, climate forcing capability, and global warming potential. According to IPCC 2007 Report [50], a *climate forcing* can be defined as an imposed perturbation of earth's energy balance, typically expressed in watts per square meter (W/m^2), whereas the *global warming potential* (GWP) of a gaseous specie in the atmosphere is proposed as a measure of how much a given mass of that gas is estimated to contribute to global warming. It essentially depends on both the absorbance of the molecule with respect to infrared radiation and its time removal, and is measured relative to the same amount of CO_2 for a specific timescale (GWP of CO_2 is by definition 1). Table 1.4 evidences the effect of

Table 1.4 Removal times, climate forcing capability and global warming potential for the main greenhouse gases

Chemical species	Removal times	Climate forcing values (W/m^2)	GWP, 20 years time horizon	GWP, 100 years time horizon
Water vapor	Some days	–	–	–
Carbon dioxide	>100 years	1.3–1.5	1	1
Methane	12 years	0.5–0.7	72	25
Nitrous oxide	114 years	0.1–0.2	289	298
Hydrofluorocarbon	270 years	0.01	12000	14800

Adapted from reference [50]

removal times on GWP especially for methane when time horizon is increase from 20 to 100 years, and the very high GWP of nitrous oxides and halocarbons for both time horizons considered. On the other hand, though water vapor is very significant in terms of infrared radiation absorbance (its contribution to the natural greenhouse effect is preponderant, in the order of 60–80% of the total natural greenhouse gases), climate forcing and GWP values are not reported for this molecule. This is due to an important distinction which has to be taken into account between climate forcing agents, able to create an initial change in the climate, and feedback agents, responsible for amplifying the initial forcing. This difference is connected to the removal times of chemical species from the atmosphere, which results to be too short for water vapor (in the order of some days), with respect to removal times of several years for the other species. Due to its short atmospheric lifetime water vapor cannot force an initial climate change, but its concentration in atmosphere can increase as a consequence of temperature increase caused by long-lived climate forcing agents (other compounds in Table 1.4). Additional water evaporation due to this temperature increase contributes to the greenhouse effect generating further global warming, then acts as amplifying agent of initial forcings, in a loop called *positive feedback* of water vapor.

Considering only the species able to act as climate forcing, since the contribution to the greenhouse effect by a specific gas is affected not only by the characteristics of the gas (time removal, climate forcing capability and GWP) but also by its abundance, among gases reported in Table 1.4 carbon dioxide is regarded as the most important greenhouse agent produced by human activities because of high removal times (>100 years), significant climate forcing value, and elevated concentration levels in the atmosphere (at least three order of magnitude higher than methane and nitrous oxide, and six order of magnitude higher with respect to halocarbons). Even if natural sources of carbon dioxide are about 20 times higher than those anthropogenic, over long periods (from years up to centuries) natural sources enter into the natural carbon cycle (absorption by oceans, photosynthesis, weathering of rocks). Then the problem of carbon dioxide as regard climate change issues is connected to its additional release derived by human activities, which is essentially constituted by fossil fuels burnings, and made worse by deforestation. For this reason in recent years, the attention of climate experts and intergovernmental organisms has been paid to the problem of atmospheric CO_2 concentration increase and to possible effects on earth's global warming.

As mentioned before the link between greenhouse gases increase and global warming is cause of strong disagreement in the scientific debate, in particular the large uncertainty level regarding natural variability and time history of the most important climate forcing agents makes that linkage very difficult to be unequivocally established. In fact, the observation that the magnitude of the global warming registered in the last decades is too large when compared to natural variability can only suggest the validity of the relationship between greenhouse gas concentration increase and climate change, but does not constitute a scientific demonstration.

In spite of these considerations, the following facts can be evidenced, according to data reported in [50]:

(1) warming of the climate system is unequivocal, as shown by increases of average air and ocean temperatures, rising of average sea level and widespread of ice. In the period 1995–2006, 11 years out of 12 have resulted the warmest years since 1850. The linear warming trend over the 50 years in the period 1956-2005 (0.13°C/decade) is nearly twice that of the period 1906–2005 (100 years). This increase is extremely significant, especially if compared with the temperature rise which caused the end of the Glacial Period (about 1.5°C in more than 5000 years). Furthermore, since 1961, the temperature of average global ocean has increased at depths of at least 3000 m, while average sea level has risen of 1.8 mm/year in the period 1961–2003, and of 3.1 mm/year in the period 1993–2003. Satellite data since 1978 show that annual average Arctic sea ice has shrunk by 2.7%/decade.
(2) many natural systems of both continents and oceans are being affected by regional temperature increases. Observations since 1980 evidence earlier "greening" of vegetation in the spring and several changes in marine and freshwater biological systems.
(3) annual emissions of the most important anthropogenic greenhouse gas (CO_2) have grown by about 80% in the period 1970–2004, from 21 to 38 gigatons, and represent 77% of the total anthropogenic greenhouse gases emissions in 2004, mostly due to energy supply, transport and industry (see Table 1.2 for percentage data of CO_2 emissions). The global atmospheric concentration of CO_2 has increased from a pre-industrial value of about 280 ppm to 379 ppm in 2005. The annual CO_2 concentration growth rate was larger during the period 1995–2005 (average of 1.9 ppm/year) with respect to the whole period of observation available (1960–2005, with an average of 1.4 ppm/year).
(4) global atmospheric concentration of other most important greenhouse gases (CH_4 and N_2O) has increased as a result of human activities since 1750 and is now much higher than pre-industrial values. Methane has increased from a pre-industrial value of about 715–1732 ppb in the early 1990, and was 1774 ppb in 2005. Nitrogen oxide concentration increased from a pre-industrial value of about 270–319 ppb in 2005. Many halocarbons, which were practically absent in the atmosphere in pre-industrial era, has increased up to values in the order of hundreds of ppt.
(5) anthropogenic contributions to aerosol emissions (sulfate, particulate carbon, nitrate and dust) can produce an appreciable but not determinant cooling effect.
(6) feedback agents can amplify the response to a given climate forcing agent. The role of water vapor as a positive feedback agent has already been examined before, but another positive feedback can be produced by CO_2, in fact warming reduces both terrestrial and ocean CO_2 uptake, leaving higher concentration of this gas in the atmosphere for a given emission scenario.

The conclusions drawn by the experts of IPCC, based on the facts above reported and on statistical analysis, is that the observed increase in global average

temperatures since the mid-twentieth century is *very likely* due to the observed increase in anthropogenic greenhouse gases, with an assessed probability of occurrence >90%, while high grades of probability and confidence are also attributed to the effect of global warming on ecosystems, economic sectors and geographical regions [50].

The estimation of future climate changes is also object of debate, and has been analyzed by IPCC on the base of different emission scenarios. The results of these analysis evidence that if carbon dioxide emissions will continue to increase at the current growth rate for anthropogenic causes (about 3%/year) its atmospheric concentration will reach about 1100 ppm by 2100 (and in this case there will remain few doubts about the severe negative effects on climate), while if CO_2 emissions will be controlled maintaining the current annual level, they will be about 520 ppm in the atmosphere by 2100. In the contest of these scenarios, many climate models have been used to individuate an *acceptable* value for CO_2 atmospheric concentration, i.e. a value compatible with the forecasts regarding population and energy demand increase. A part from the different values proposed as CO_2 concentration level to be stabilized (ranging from 450 to 550 ppm by 2050), there is agreement among researchers that this stabilization cannot be achieved only by the improvement of current energy technologies, prevalently based on fossil sources, although they are becoming continuously more efficient. On the other hand, some proposed solutions about the possibility to solve the problem of CO_2 emissions by *sequestration* of this gas in "safe" sites, such as disused mines or oil wells and seabeds, are very energy demanding and still in an initial stage of development [51]. As a consequence, it is a generally established opinion that an acceptable value of CO_2 concentration in the atmosphere can be reached by the mid-21st century only thanks to the implementation of energy carriers generated from nuclear or renewable resources.

It has been already discussed before that electricity and hydrogen, produced by carbon-free resources, can be regarded as clean energy carriers to be used in both stationary and mobile applications. In particular, BEVs and HFCEVs represent the fundamental instruments towards the implementation of alternative energy carriers in a key sector such as that of transportation means. However, as any evaluation regarding the employment of alternative energy sources cannot leave efficiency issues out of consideration, the potential of BEVs and HFCEVs has to be assessed and compared in terms of global efficiency, i.e. by "well-to-wheels" analysis, with the two types of vehicles using fossil fuels—internal combustion vehicles (ICVs) and hybrid thermal electric vehicles (HTEVs). In the latter, thanks to hybridization, the internal combustion engine can be designed for the mean power of a typical driving cycle instead of the maximum power required, allowing the engine to operate in conditions closer to those of its optimal efficiency (details on working characteristics of vehicles using electric drives are discussed later, in Chap. 5). When this evaluation is effected for vehicles powered by different energy carriers, it is necessary to consider the primary energy utilization efficiency as a measure of comparison, in order to take into account the entire amount of energy involved from the "well" to the "wheels". Starting from an amount of any primary energy (the

"well") the following energy losses have to be considered to evaluate the final energy usable for traction: (i) losses due to fuel production and distribution, in order to attain the actual energy entering the vehicle, (ii) losses due to vehicle on road management (conditioning, lighting) to draw the net energy entering the powertrain, (iii) losses due to road load and heat lost by the engine, to obtain the remaining energy actually available for the "wheels". These evaluations are very complex as involve several assumptions on the long-term development of technologies which can present very different progress trends; however, quite a few results regarding this type of comparison based on different primary resources are present in scientific literature [52–54], and the results up today available seem to converge towards some general conclusions. Tables 1.5 and 1.6 report the results of such evaluations effected for the different types of vehicles above mentioned, with reference to fossil and renewable energy resources, respectively. These data are based on the comprehensive analysis reported in [52] and other references therein.

Table 1.5 evidences that well-to-wheels efficiencies of fossil resources are approximately comprised between 20 and 30%, with a maximum value of 31% estimated for BEVs using electricity derived by natural gas. The minimum well-to-wheels efficiency is obtained for Diesel vehicles, in spite of the very high efficiency of carrier production (95%), this is due to the lower efficiency of the internal combustion powertrain with respect to electric or hybrid thermal-electric ones (internal combustion engines could work at their maximum efficiency comprised between 35 and 40% only in conditions close to their maximum power, while all vehicles efficiencies in Table 1.5 are estimated on US Federal Test Procedure driving cycle, characterized by a mean power very lower than the maximum power of the vehicle). HTEVs present a very interesting well-to-wheels efficiency, thanks to the higher vehicle efficiency if compared to ICVs. The primary energy efficiency evaluated for HFCEVs is also quite elevated (25%), but hydrogen is considered deriving from natural gas by catalytic reforming processes (see Sect. 2.1), then its production is accompanied by carbon dioxide emissions.

Table 1.5 Well to wheels percentage efficiencies for different types of vehicles starting from fossil primary energy resources

Primary energy	Energy carrier	Type of vehicle	Primary energy to energy carrier % eff.[a]	Vehicle % eff.[b]	Well-to-wheels % eff.
Coal	Electricity	BEV	37	61	22
Natural gas	Electricity	BEV	51	61	31
Natural gas	Hydrogen	HFCEV	73 (350 bar)	34	25
Crude oil	Diesel oil	ICV	95	20	19
Crude oil	Diesel oil	HTEV	95	29	27

Adapted from Ref. [52]

[a]Includes carrier distribution efficiency (93% for electricity, 86% for compressed hydrogen, 99.8% for oil)

[b]Evaluated on US FTP driving cycle, NiMH batteries for electric drivetrains

Table 1.6 Well to wheels percentage efficiencies for different types of vehicles starting from non-fossil primary energy resources

Primary energy	Energy carrier	Type of vehicle	Primary energy to energy carrier % eff.[a]	Vehicle % eff.[b]	Well-to-wheels % eff.
Nuclear	Electricity	BEV	28[c]	61	17
Nuclear	Hydrogen	HFCEV	28 to electricity[c] 47 for electrolysis[c]	34	4.5
Photovoltaic	Electricity	BEV	11[c]	61	6.7
Photovoltaic	Hydrogen	HFCEV	11 to electricity[c] 47 for electrolysis[c]	34	1.8
Biomass	Electricity	BEV	1 for photosynthesis[d] 42 for biomass to electricity[c]	61	0.26
Biomass	Hydrogen	HFCEV	1 for photosynthesis[d] 59 for biomass to H_2[c]	34	0.20

[a]Include carrier distribution efficiency (93% for electricity, 86% for compressed hydrogen [52])
[b]Taken from Ref. [52], evaluated on US FTP driving cycle, NiMH batteries for electric drive-trains
[c]Taken from Ref. [54] and corrected for footnote a
[d]Generally considered as comprised between 0.1 and 1% [55]

Table 1.6 refers only to non-fossil primary energy resources, and presents a comparison between BEVs and HFCEVs, i.e., between electricity and hydrogen as energy carriers for transportation sector, since both these two energy carriers can be produced starting from several carbon-free resources, such as nuclear and renewable. The well-to-wheels efficiencies show that only starting from nuclear and producing electricity for direct use on BEVs, it is possible to obtain a primary energy utilization comparable to that of fossil resources (17%), while very low values can be estimated for solar biomass (0.26% for BEVs), mainly because of low efficiency of the photosynthesis process (the efficiency of the natural process which converts the energy of light—photons, electromagnetic waves—into chemical potential energy stored in organic structures such as plants is generally considered comprised between 0.1 and 1% [55]).

The overall well-to-wheels efficiencies for BEVs and HFCEVs starting from solar biomass evidence that this path cannot be considered as a massive solution for application of biofuels to electric vehicles, unless biomass is not obtained from already existing organic wastes (forestry residues, straw, food waste, manure, etc.).

The comparison between electricity and hydrogen is more significant when nuclear and solar photovoltaic are considered as primary resources. It is possible to notice from Table 1.6 that for both these primary resources the well-to-wheels efficiency of BEVs results about four times higher than of HFCEVs.

This is not only due to the higher efficiency of battery powered vehicles, but also to the lower efficiency of the overall process necessary to assure hydrogen feeding to fuel cells, i.e., production of electricity starting from the primary resource plus hydrogen production by electrolysis (13% from nuclear and 5% from photovoltaic, to be compared with values corresponding to electricity production

Table 1.7 Well to wheels percentage efficiencies for internal combustion vehicles fueled with hydrogen produced from different primary energy resources

Primary energy	Energy carrier	Type of vehicle	Primary energy to energy carrier % eff.[a]	Vehicle % eff.[b]	Weel-to-wheels % eff.
Natural gas	Hydrogen	ICV	73 (350 bar)	20	15
Nuclear	Hydrogen	ICV	28 to electricity[c] 47 for electrolysis[c]	20	2.6
Photovoltaic	Hydrogen	ICV	11 to electricity[c] 47 for electrolysis[c]	20	1.0
Biomass	Hydrogen	ICV	1 for photosynthesis[d] 59 for biomass to H_2[c]	20	0.1

[a]Includes carrier distribution efficiency (93% for electricity, 86% for compressed hydrogen, 99.8% for oil [52])
[b]Taken from Ref. [52], evaluated on US FTP driving cycle for Diesel vehicle and attributed to H_2 vehicle
[c]Taken from Ref. [54] and corrected for footnote a
[d]Generally considered as comprised between 0.1 and 1% [55]

for direct use on BEVs, 28 and 11% from nuclear and photovoltaic, respectively). The hydrogen produced by electricity is then converted back to electricity by fuel cells in HFCEVs, leading to the expectable conclusion of well-to-wheels efficiencies lower than BEVs (4.5 and 1.8% starting from nuclear and photovoltaic, respectively, to be compared with 17 and 6.7%).

The option of using hydrogen in conventional internal combustion engines is analyzed in Table 1.7 in terms of well-to-wheels efficiency. These data show that also attributing to hydrogen ICVs the same high vehicle efficiency of Diesel vehicles (20%, Table 1.5), only producing hydrogen from natural gas (with carbon dioxide emissions) it is possible to reach a primary energy efficiency comparable to that of other conventional fuels for ICVs (19% for Diesel vehicles, Table 1.5). On the other hand, if hydrogen is produced from nuclear or renewable resources, the well-to-wheels efficiency for ICVs results always lower than the corresponding efficiencies estimated for paths involving fuel cells and electric drivetrains (HFCEVs, Table 1.6), with the additional drawback of NO_x emissions at the engine exhaust associated with hydrogen combustion.

The well-to-wheels analysis can give useful indications regarding the potential of a specific technology in terms of primary energy utilization efficiency, but is not sufficient to point to one technology or energy carrier as the best option. In fact, the high well-to-wheels efficiency obtained for BEVs, especially starting from a primary resource at high energy density such as nuclear, has to be weighed in the light of indispensable requisites which road vehicles must have to be compatible with their practical usage. Among these characteristics the driving range still represents, on the base of current technology, the main limit to a widespread diffusion of battery powered vehicles, essentially due to not yet satisfactory performance of electric energy storage systems in terms of specific energy per weight/volume of the storage. In particular, some evaluations based on the current technologies [56] have evidenced that also with the most advanced Li/ion batteries

the driving range obtainable with BEVs is about half with respect to that of vehicles fueled with compressed hydrogen (both 250 and 600 bar) with severe penalties in terms of vehicle weight, while very lower range values could be reached with Pb/acid and NiMH systems. Then the problem of developing new batteries characterized by specific energy comparable to that of conventional fuels or compressed hydrogen appears to be the key factor towards the successful introduction of electric vehicles in the consumer market and for their affirmation as future transportation means at high efficiency.

The analysis of the different types of energy storage systems for electric vehicles will be effected later (see Sect. 5.1), meanwhile in this paragraph, the main functional parameters which characterize the performance of these systems, i.e. storage capability and output voltage, are examined for different electrochemistry pairs, in order to highlight the current status of developing of BEVs and give further indications useful to compare electricity and hydrogen as future energy carriers in the transportation sector. In Table 1.8, the open circuit voltage and specific energy are summarized for some today available batteries (Pb/acid, Ni/Cd, NiMH) and other systems still under study (lithium and metal/air) [57–60].

The theoretical values of open circuit voltage (OCV) represent the electrochemical potentials of the single cell reaction, while the theoretical specific energies are calculated applying the Faraday law.

When a practical battery is assembled, the weights of inactive components (current collectors, electrolyte, binders, packaging) add to the total weight of the battery without contributing to energy, then the actual values for both parameters are also reported in Table 1.8 to take into account the characteristics and/or limitations of the real systems and the possible variations among different battery manufacturers [61]. In different countries, various organizations have been funded with the aim of promoting research activities in this field, with the final goal of developing new types of batteries characterized by improved cycle life, safety, reliability and cost, but overall by a major breakthrough as regard the energy

Table 1.8 Open circuit voltage (OCV) and specific energy values for different types of battery. Specific energy values for USABC and gasoline

Battery	Theoretical OCV, V	Actual OCV, V	Theoretical specific energy, Wh/kg	Actual specific energy, Wh/kg
Pb/acid	2.1	2.0	252	30–45
Ni/Cd	1.35	1.2	244	40–51
NiMH	1.35	1.2	206	50
Li/ion	4.1	4.1	410	150
Li/polymer (MnO_2)	3.5	3.0	1000	120
Zn/air	1.65	1.5	1350	200–300
Al/air	2.7	1.6	8140	300–500
USABC	–	–	–	200
Gasoline	–	–	–	13000

Adapted from Ref. [57–60]

storage capacity. All these organizations have individuated goals to be met by the innovative batteries in order to fulfil the requirements of electric vehicles acceptable by the market. As an example, in the United States the Advanced Battery Consortium (USABC), founded in 1995 by Ford, General Motors and Chrysler in cooperation with Department of Energy (DOE) have proposed that a BEV battery should be able to store at least 200 Wh/kg to afford the vehicle an acceptable driving range [59], and this value is generally accepted as term of progress for battery development programs worldwide. For comparison the specific energy value established by USABC for future acceptable batteries and the value for gasoline are also reported in Table 1.8. The actual specific energy data evidence in detail the fundamental problem of today battery vehicles, i.e. the driving range connected to limited specific energy of the currently available batteries (maximum 50 Wh/kg for NiMH, and lower values for Pb/acid). On the other hand, also with lithium systems, which are the presently more promising batteries still under development, storage capabilities compatible with transportation applications are not reached (maximum 150 Wh/kg for lithium/ion). The data of Table 1.8 show also the very significant potentialities of metal air systems (also regarded as semi-fuel cells, since the oxidant is supplied from outside), in particular Al/air batteries offer a theoretical specific energy of almost the same order of magnitude than gasoline, and an actual value about two times higher with respect to USABC target. However, while lithium systems are in phase of advanced development [62], the metal/air batteries require intense efforts of basic research since they still present important limitations which affect not only actual OCV and specific energy values, but also power capabilities and durability [58].

The electric drivetrain is the common denominator for alternative propulsion systems able to favor the introduction of carbon-free energy resources into the transport sector, but the possibility to follow for these systems the most efficient well-to-wheels path is based on the widespread diffusion of BEVs. Since these types of electric vehicles are totally dependent on batteries as on board energy source, and the electric storage systems require significant improvements far to be reached, the extensive affirmation of BEVs appears as a long-term solution. On the other hand, the urgency of giving fast and reliable answers to the problem of anthropogenic greenhouse effect imposes scientists and policy makers to suggest ways practicable on near and mid-term.

In this view, the approach of energy saving should be properly considered as the first goal to be pursued by any energy policy, independently of nature of the primary resource. At this regard an estimation of IPCC has argued that by the end of this century at least 30% of worldwide energy demand could be satisfied by the consequences of energy saving policies, rather than by novel clean technologies [50]. The concept of energy saving should be applied to any type of technology involved in human activities, such as buildings, industries, production processes, but above all to the transport sector, with obvious reductions of emissions and crude oil usage when conventional vehicles are considered. The examination of Table 1.5, 1.6, and 1.7 clearly evidences which are the paths able to favor the introduction of more efficient transport solutions on near-term, without completely

abandon the already available technologies. After the most efficient option represented by the path natural gas–electricity–BEVs (31%), other two very convenient possibilities, in terms of well-to-wheels efficiency, are the hybrid thermal electric vehicles (HTEV, 27%) using Diesel oil or gasoline as energy carriers, and hydrogen fuel cell vehicles (HFCEVs, 25%) adopting hydrogen produced from natural gas with commercial processes (see Sect. 2.1). While the first option is already object of some commercial realizations, and permits a not negligible reduction in pollutant emissions and fuel consumption with respect to internal combustion vehicles, the second solution has to face the same technological issues of all fuel cell vehicles, but the utilization of mature and available processes for hydrogen production would have the advantage to favor its rapid introduction into the world energy system.

The further development and diffusion of these technologies, coupled to a convinced policy of governmental incentives for high efficiency vehicles, could give research makers and car manufacturers enough time to overcome technical problems of totally carbon-free alternatives, such as HFCEVs and BEVs powered by energy carriers deriving from nuclear and renewable resources (see Sect. 2.1.2 and Sect. 3.4). In particular, the hydrogen fuel cell vehicles, adopting non-fossil hydrogen as on board energy carrier and fuel cells to generate electric energy, even if represent a less efficient solution in terms of well-to-wheels analysis with respect to BEVs and any other fossil-based technology, could become a proper answer to the requirements of carbon-free transport systems on mid-term.

The Fig. 1.2 reports the carbon and hydrogen contents for some fuels which have been adopted by humanity in the last three centuries. Starting from wood (C/H = 9), which was the main fuel available before the industrial revolution, the

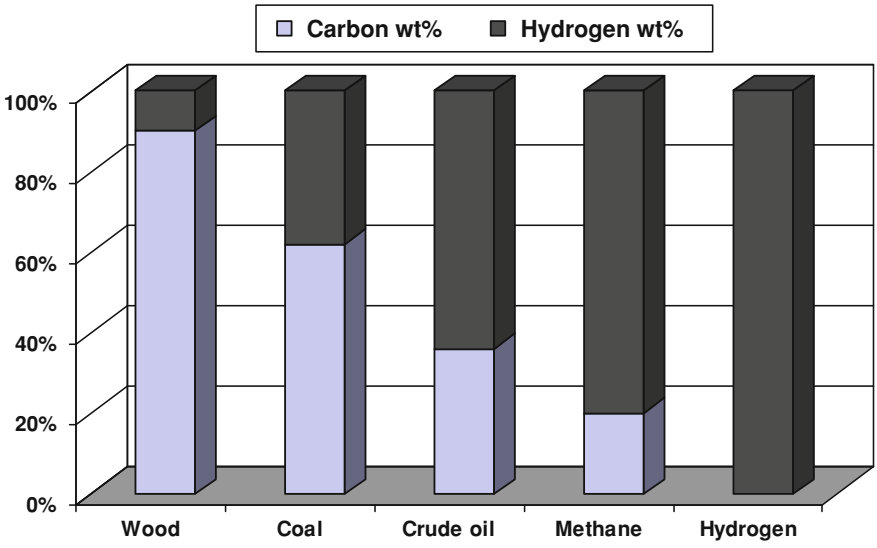

Fig. 1.2 Carbon and hydrogen contents for different fuels

C/H ratio has steeply decreased passing to coal (C/H = 1.63), oil (C/H = 0.56) and methane (C/H = 0.25). In this perspective, hydrogen (C/H = 0) can be regarded as the final step in continue research of abundant, easy to use and clean fuels. However, the lack of hydrogen fuel infrastructure and the necessity to produce it from carbon-free primary energy sources imply that only a strong co-operation between legislators, vehicle manufacturers and energy companies could favor the widespread diffusion of hydrogen as an economically feasible fuel for future transportation systems.

References

1. International Energy Agency (2008) World energy outlook 2008. OECD Publishing, Paris
2. World Business Council for Sustainable Development (WBCSD). Mobility 2030: meeting the challenges to sustainability. http://www.wbcsd.org/plugins/DocSearch/details.asp?type=DocDet&ObjectId=NjA5NA. Accessed 2 Feb 2010
3. BP Statistical Review of World Energy June 2008
4. Askari H, Krichene N (2008) Oil price dynamics (2002–2006). Energ Econ 30(5):2134–2153
5. Kaufmann RK, Bradford A, Belanger LH, Mclaughlin JP, Miki Y (2008) Determinants of OPEC production: Implications for OPEC behavior. Energ Econ 30:333–351
6. Wirl F (2008) Why do oil prices jump (or fall)? Energy Policy 36:1029–1043
7. Hirsch RL (2008) Mitigation of maximum world oil production: Shortage scenarios. Energy policy 36:881–889
8. Nel WP, Cooper CJ (2008) A critical review of IEA's oil demand forecast for China. Energy Policy 36:1096–1106
9. Hubbert MK (1949) Energy from fossils fuels. Science 109:103–109
10. Hubbert MK (1956) Nuclear energy and the fossil fuels. In: Presented before the Spring Meeting of the Southern District. American Petroleum Institute, Plaza Hotel, San Antonio, Texas, March 7–9, 1956. http://www.hubbertpeak.com/hubbert/1956/1956.pdf. Accessed 02 Feb 2010
11. Wilkinson P (2008) Peak oil: threat, opportunity or phantom? Public Health 122:664–666
12. Lea R (2008) The days of cheap oil have gone, but the peak oil theory is far too bleak. Public Health 122:667–668
13. Meng QY, Bentley RW (2008) Global oil peaking: responding to the case for 'abundant supplies of oil'. Energy 33:1179–1184
14. Hanlon P, McCartney G (2008) Peak oil: Will it be public health's greatest challenge? Public Health 122:647–652
15. Leder F, Shapiro JN (2008) This time is different: an inevitable decline in world petroleum production will keep oil product prices high, causing military conflicts and shifting wealth and power from democracies to authoritarian regimes. Energy Policy 36(8):2850–2852
16. Brecha RJ (2008) Emission scenarios in the face of fossil-fuel peaking. Energy Policy 36:3492–3504
17. Kaufmann RK, Shiers LD (2008) Alternatives to conventional crude oil: when, how quickly, and market driven? Ecol Econ 67(3):405–411
18. Abu-Jrai A, Rodríguez-Fernández J, Tsolakis A, Megaritis A, Theinnoi K, Cracknell RF, Clark RH (2009) Performance, combustion and emissions of a diesel engine operated with reformed EGR. Comparison of diesel and GTL fuelling. Fuel 88(6):1031–1041
19. Official Journal of the European Union (2006) L310/15. http://eur-lex.europa.eu/LexUriServ/LexUriServ.do?uri=OJ:L:2006:310:0015:0040:EN:PDF. Accessed 02 Feb 2010

20. Markvart T, Castaner L (2003) Principles of solar cell operation. In: Markvart T, Castaner L (eds) Practical handbook of photovoltaics. Fundamental and applications. Elsevier, Kidlington
21. Landsberg PT, Markvart T (2003) Ideal efficiencies. In: Markvart T, Castaner L (eds) Practical handbook of photovoltaics. Fundamental and applications. Elsevier, Kidlington
22. Pro BH, Hammerschlag R, Mazza P (2005) Energy and land use impacts of sustainable transportation scenarios. J Clean Prod 13:1309–1319
23. Arshadi M, Sellstedt A (2008) Production of energy from biomass. In: Clark J, Deswarte F (eds) Introduction to chemical from biomass. Wiley, Chichester
24. Abu-Khader MM (2009) Recent advances in nuclear power: a review. Prog Nucl Energy 51(2):225–235
25. Fthenakis VM, Kim HC (2007) Greenhouse-gas emissions from solar electric- and nuclear power: a life-cycle study. Energy Policy 35:2549–2557
26. Lenzen M (2008) Life cycle energy and greenhouse gas emissions of nuclear energy: a review. Energy Convers Manage 49:2178–2199
27. Manheiemr W (2006) Can fusion and fission breeding help civilization survive? J Fusion Energy 25(3/4):121–139
28. Dean SO (2007) Fusion: pathways to the future. J Fusion Energy 26:283–292
29. Duffey RB (2005) Sustainable futures using nuclear energy. Prog Nucl Energy 47(1–4): 535–543
30. Lewis D (2008) Hydrogen and its relationship with nuclear energy. Prog Nucl Energy 50:394–401
31. Hori M (2008) Nuclear energy for transportation: paths through electricity, hydrogen and liquids fuels. Prog Nucl Energy 50:411–416
32. Forsberg CW (2009) Sustainability by combining nuclear, fossil and renewable energy sources. Prog Nucl Energy 51(1):192–200
33. Kato Y, Otsuka K, Ryu J (2008) Carbon recycle nuclear hydrogen carrier system for transportation field. Prog Nucl Energy 50:417–421
34. Kruger P (2006) Alternative energy resources: the quest for sustainable energy. Wiley, Hoboken
35. Cleveland CJ, Kaufmann RK, Stern DI (2000) Aggregation and the role of energy in the economy. Ecol Econ 32:301–317
36. Cleveland CJ (2005) Net energy from the extraction of oil and gas in the United States. Energy 30:769–782
37. Gately M (2007) The EROI of U.S. offshore energy extraction: a net energy analysis of the Gulf of Mexico. Ecol Econ 63:355–364
38. Faundez P (2008) Renewable energy in a market-based economy: how to estimate its potential and choose the right incentives. Renew Energy 33:1768–1774
39. Cleveland CJ, Costanza R, Hall CAS, Kaufmann R (1984) Energy and U.S. economy: a biophysical perspective. Science 225:890–897
40. Heywood JB (1988) Internal combustion engines fundamentals. McGraw-Hill, Singapore
41. Dabelstein W, Reglitzky A, Schtze A, Reders K (2008) Automotive fuels. In: Elvers B (ed) Handbook of fuels. Wiley-VCH, Weinheim
42. Yao M, Zheng Z, Liu H (2009) Progress and recent trends in homogeneous charge compression ignition (HCCI) engines. Prog Energy Combust 35(5):398–437
43. Eastwood P (2000) Critical topics in exhaust gas aftertreatment. Research Studies Press Ltd., Baldock, Hertfordshire
44. Crebelli R, Conti L, Crochi B, Carere A, Bertoli C, Del Giacomo N (1995) The effect of fuel composition on the mutagenicity of diesel engine exhaust. Mutat Res Lett 346(3): 167–172
45. Official Journal of the European Union (2007) L 171/1. http://eur-ex.europa.eu/LexUriServ/LexUriServ.do?uri=OJ:L:2007:171:0001:0016:EN:PDF. Accessed 02 Feb 2010
46. Official Journal of the European Union (2008) L 199/1. http://eur-lex.europa.eu/LexUriServ/LexUriServ.do?uri=OJ:L:2008:199:0001:0136:EN:PDF. Accessed 02 Feb 2010

47. Turrio-Baldassarri L, Battistelli CL, Conti L, Crebelli R, De Berardis B, Iamiceli AL, Gambino M, Iannaccone S (2006) Evaluation of emission toxicity of urban bus engines: Compressed natural gas and comparison with liquid fuels. Sci Total Environ 355:64–77
48. Field CB, Campbell JE, Lobell DB (2007) Biomass energy: the scale of the potential resource. Trends Ecol Evol 23(2):65–72
49. Schuers A, Abel A, Artmann R, Fickel X, Preis M (2002) 12-cylinder hydrogen engine in the BMW 750hL. Motortechnische Zeitschrift 63(2):98–105. http://www.bmw.com/com/en/insights/technology/efficient_dynamics/phase_2/clean_energy/bmw_hydrogen_7.html. Accessed 02 Feb 2010
50. Intergovernmental Panel on Climate Change (2007–2008) Fourth assessment report: climate change 2007. Cambridge University Press, Cambridge
51. Gerard D, Wilson EJ (2009) Environmental bonds and the challenge of long-term carbon sequestration. J Environ Manage 90:1097–1105
52. Ahman M (2001) Primary energy efficiency of alternative powertrains in vehicles. Energy 26:973–989
53. Rand DAJ, Dell RM (2005) The hydrogen economy: a threat or an opportunity for lead-acid batteries? J Power Sources 144:568–578
54. Van Mierlo J, Maggetto G, Lataire P (2006) Which energy source for road transport in the future? A comparison of battery, hybrid and fuel cell vehicles. Energy Convers Manage 47:2748–2760
55. Vallentyne J (1965) Net primary productivity and photosynthetic efficiency in the biosphere. In: Goldman C (ed) Primary productivity in aquatic environments. University of California Press, Berkeley
56. Jorgensen K (2008) Technologies for electric, hybrid and hydrogen vehicles: electricity from renewable energy sources in transport. Util Policy 16:72–79
57. Linden D, Reddy TB (2001) Handbook of batteries, 3rd edn. McGraw-Hill, New York
58. Yang S, Knickle H (2002) Design and analysis of aluminium/air battery system for electric vehicles. J Power Sources 112:162–173
59. Li Q, Bjerrum NJ (2002) Aluminium as anode for energy storage and conversion: a review. J Power Sources 110:1–10
60. Chan CC, Sun L, Liang R, Wang Q (2007) Current status and future trends of energy storage system for electric vehicles. J Asian Electr Veh 5(2):1055–1060
61. Chan CC (2004) The state of the art of electric vehicles. J Asian Electr Veh 2(2):579–600
62. Chalk SG, Miller JF (2006) Key challenges and recent progress in batteries, fuel cells and hydrogen storage for clean energy systems. J Power Sources 159:73–80

Chapter 2
Hydrogen as Future Energy Carrier

In the view of a desirable and drastic reduction of both world-wide greenhouse gas emissions and not-renewable resource exploitation, the utilization of sustainable energy sources, such as solar, wind, hydro, or biomass are a mandatory option as well as the use of alternative fuels in the transportation field. In the context of new advanced energy conversion technologies, since 1990s a strong interest of international scientific and industrial community has been addressed towards the possible development of a global 'hydrogen economy' based on the hypothesis that hydrogen could play a basilar role as future energy carrier [1–3], in particular as innovative fuel in automotive field, where it could flank or, in a long-term scenario, replace the traditional oil-derived liquid mixtures in passenger cars. Hydrogen is the most common element in the universe, and its molecule (H_2) has the highest energy content per unit weight of any known fuel, but it never occurs by itself on earth, as it always combines with other elements such as oxygen (to form water as molecule) or carbon (to form hydrocarbons and coal). Thus, it needs to be produced and for this reason it is not a primary source, but only an energy carrier, which could be used in combination with electricity in an innovative overall energy system.

In this chapter, the state of art on the main technologies for hydrogen production, distribution and storage is detailed and analysed evidencing the technical potentialities of this fuel and the barriers which hinder its massive diffusion in automotive field. The key factor for a large utilization of hydrogen not only in transportation sector but also in all the other energy markets is represented by cost and efficiency of production technologies. In the first paragraph the technical issues of the main hydrogen production methods are discussed taking into account that hydrogen can be produced starting from a large variety of primary resources. Moreover, the application of hydrogen in the transportation sector introduces additional problems correlated to the creation of a large infrastructure network for fuel utilization, strictly related to the selected production technologies. The development of specific on-board storage technologies is necessary to match the

P. Corbo et al., *Hydrogen Fuel Cells for Road Vehicles*,
Green Energy and Technology, DOI: 10.1007/978-0-85729-136-3_2,

high energy densities typical of the traditional liquid fuels (gasoline, diesel, LPG) used to feed internal combustion engines in passenger cars. Hydrogen infrastructure scenarios are briefly reported in Sect. 2.2, while Sect. 2.3 analyses the potentialities of different on-board storage technologies.

2.1 Hydrogen Production

One of the advantages of using hydrogen as energy carrier is that all primary resources such as fossil fuels, renewable energy sources (solar, wind, hydro, geothermic, biomass) and nuclear power could be used for its production [4]. In particular, it can be extracted from any substance containing hydrogen atoms, such as hydrocarbons, water and even some organic matter. Thus, the different technologies utilize mainly these compounds as starting materials for the final H_2 molecule formation. In addition it can be readily produced from synthesised hydrogen carriers such as methanol, ammonia and synthetic fuels.

In Table 2.1, the contributions of the different sources to the current worldwide hydrogen production are summarized, together with the available technologies used for each raw material.

Almost half of the hydrogen used worldwide comes from steam reforming (SR) of natural gas (48%), as it is the most economical route from hydrocarbon feedstock. The other contributions to hydrogen production are based mainly on partial oxidation of refinery oil (about 30%) and coal gasification (18%), whereas only 4% of the produced hydrogen derives by water electrolysis. The hydrogen is mainly used to make ammonia for fertilizers, in refineries to make reformulated gasoline, and also in the chemical, food and metallurgical industries.

The pathways involving fossil fuels (natural gas, refinery oil and coal) that provide for almost 96% of the total production of hydrogen, release carbon dioxide in the atmosphere.

Innovative strategies able to capture and sequestrate carbon dioxide emissions, so-called Carbon Capture and Sequestration (CCS) technologies, are the object of several analysis and heated debate. CCS technologies should be applied for an environmental-friendly diffusion of fossil fuel-based H_2 production methods, but they are presently in the embryonic stage of development and certainly would involve a great growth of costs.

Table 2.1 World hydrogen production capacity from different sources

Raw material	Technology	%
Natural gas	Catalytic steam reforming	48
Refinery oil	Partial oxidation	30
Coal	Gasification	18
Water	Electrolysis	4

Adapted from [5]

On the other hand, water electrolysis, which is an intrinsic carbon-free method as it involves splitting water into its component parts, hydrogen (H_2) and oxygen (O_2), is strongly limited because of the present high costs of electricity generation. Thus, the costs will certainly represent one of the most important barriers to be overcome for a sustainable massive production of hydrogen.

An overview of the strategies for hydrogen manufacture is reported in Fig. 2.1, where all likely production technologies are related to the different resource options.

The different methods could be classified as: (i) thermal, (ii) electrolytic or (iii) photolytic processes, they will be all detailed in this Section.

The heart of the thermal processes consists of using the energy associated with chemical reactions to obtain directly hydrogen (see Sect. 2.1.1). Hydrocarbon reforming reactions as well as coal gasification are part of this type of processes. In natural gas SR the fuel reacts with steam at relatively high temperature, producing hydrogen and carbon dioxide [5]. In partial oxidation and gasification processes the fuels react with a controlled oxidant mixture (air or/and oxygen, and steam) producing similar product mixtures. A further method that should be considered as 'thermal' is the technology based on thermochemical cycles involving different

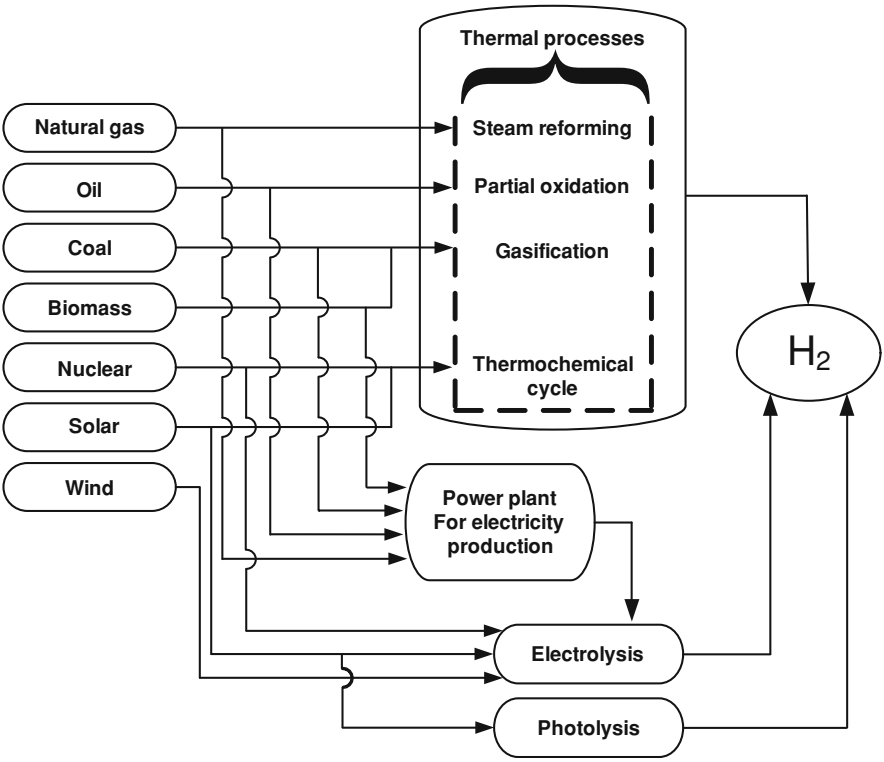

Fig. 2.1 Flowsheet of the main hydrogen production technologies

chemical reagents [4]. In these processes hydrogen is extracted from water thanks to heat combined with closed-chemical cycles, necessary to reduce the very high water decomposition temperatures (>2500°C), difficult to be reached for heavy limitations due to materials and heat source.

Electrolysis uses electricity to split water into hydrogen and oxygen by means of an electrochemical approach (see Sect. 2.1.2). Hydrogen produced via electrolytic processes can result in zero greenhouse gas emissions, depending on the selected primary source of the electricity. In addition to renewable and nuclear power, fossil fuels or biomass could be also used in stationary power plants to produce electricity for water electrolysis (see Fig. 2.1).

The analysis of photolytic methods (see Sect. 2.1.3) completes the discussion about hydrogen production. They use sunlight energy to split water into hydrogen and oxygen by photo-electrochemical and photo-biological approaches. These *direct sunlight*-based processes are currently in the very early stages of research, but could offer long-term potential for sustainable hydrogen production with low environmental impact.

2.1.1 Thermal Processes

The thermal processes require the use of thermal energy to favour the advance of chemical reactions providing hydrogen as direct product. Thermal approaches involve, as reactants, various resources which contain hydrogen atoms as part of their molecular structure, such as hydrocarbons or water, and the conversion advance aimed at directly obtaining high hydrogen yield can be further improved by catalyst addition (hydrocarbon reforming) or should require chemical compound usage (water splitting by thermochemical cycles).

Natural gas SR, hydrocarbon partial oxidation or coal gasification are all examples of 'thermal' methods and they are described in Sects. 2.1.1.1, 2.1.1.2 and 2.1.1.4, respectively. The theoretical possibility to overcome the problem of carbon dioxide emissions without using the CCS technology is based on other possible 'thermal' methods, such as the hydrocarbon cracking (see Sect. 2.1.1.3), or gasification of biomass-derived fuels (see Sect. 2.1.1.5). Also the thermal production of hydrogen based on thermochemical cycles appears quite promising (see Sect. 2.1.1.6), being its overall reaction based on the decomposition of water aided by intervention of chemicals, anyway completely recycled.

2.1.1.1 Natural Gas SR

SR of hydrocarbons, in particular of Natural Gas (NG), is still today the major industrial process for the manufacture of hydrogen [6–8].

This process was introduced in Germany at the beginning of the twentieth century to produce hydrogen for ammonia synthesis, and it was further developed

in the 1930s when NG and other hydrocarbon feedstocks such as naphtha became available on large scale. H_2 is currently produced from NG in large quantities in mixtures with nitrogen or carbon oxides for manufacture of ammonia, alcohols (mainly methanol) and for Gas to Liquid (GTL) processes [6]. In particular, SR produces a mixture of H_2 and CO (synthesis gas or syngas) that could be used directly for the synthesis of methanol or higher alcohols, and for Fischer–Tropsch synthesis.

Natural Gas feedstock is mainly constituted by methane molecule (CH_4), which represents the hydrocarbon with the highest H/C ratio. The composition of the NG could slightly change in dependence of the geographic region where it is extracted, but generally the mixture contains mainly small amounts of light hydrocarbons (C_2–C_4). The compound present in the highest concentration is the ethane (C_2H_6) that can reach in some mixtures a volumetric concentration of 5%. Not negligible traces of sulphur are often detectable in the hydrocarbon mixture.

A simplified scheme of methane SR is shown in Fig. 2.2, which includes all main process steps involved in hydrogen production plants based on the SR reaction [8].

Two units remove the sulphur concentrations (ppm), added to natural gas as an odorant for safety detection, or present in higher hydrocarbon feedstocks, to protect downstream catalysts (sulphur is a poison for SR catalysts) and process equipment. In particular, the organo-sulphur species are converted to H_2S at pressures exceeding about 500 psig and temperatures higher than 350°C by catalytic hydrodesulphurisation (HDS unit), and Co and Mo alumina-based particulates are used as catalysts. This step is not required for methanol but would be necessary for any sulphur-containing petroleum-based fuels. A second unit permits the H_2S produced in the first step to be removed by a particulate bed of ZnO. When necessary a further step for chloride removal should be included (not reported in Fig. 2.2).

The third step is the heart of the process (steam reformer). Ni-based (Ni-Al_2O_3) catalysts, loaded in tubular reactors, favour the advancement of the following reactions:

$$CH_4 + H_2O \leftrightarrows CO + 3H_2 \quad \Delta H = +206 \text{ kJ/mol} \tag{2.1}$$

or for higher hydrocarbons:

$$C_nH_m + nH_2O \leftrightarrows nCO + (m + 2n)/2\, H_2 \tag{2.2}$$

Simultaneously in high- and low-temperature shift reactors, the so-called water gas shift reaction produces further H_2 according to the exothermic equation:

$$CO + H_2O \leftrightarrows CO_2 + H_2 \quad \Delta H = -41 \text{ kJ/mol} \tag{2.3}$$

Thus SR process is highly energy intensive as the Eqs. 2.1 or 2.2 are highly endothermic and requires high energy inputs, in dependence of the fuel. SR is normally carried out at 800–900°C and about 0.1–0.3 MPa. Expensive alloy reaction tubes have to be used to withstand the severe operating conditions.

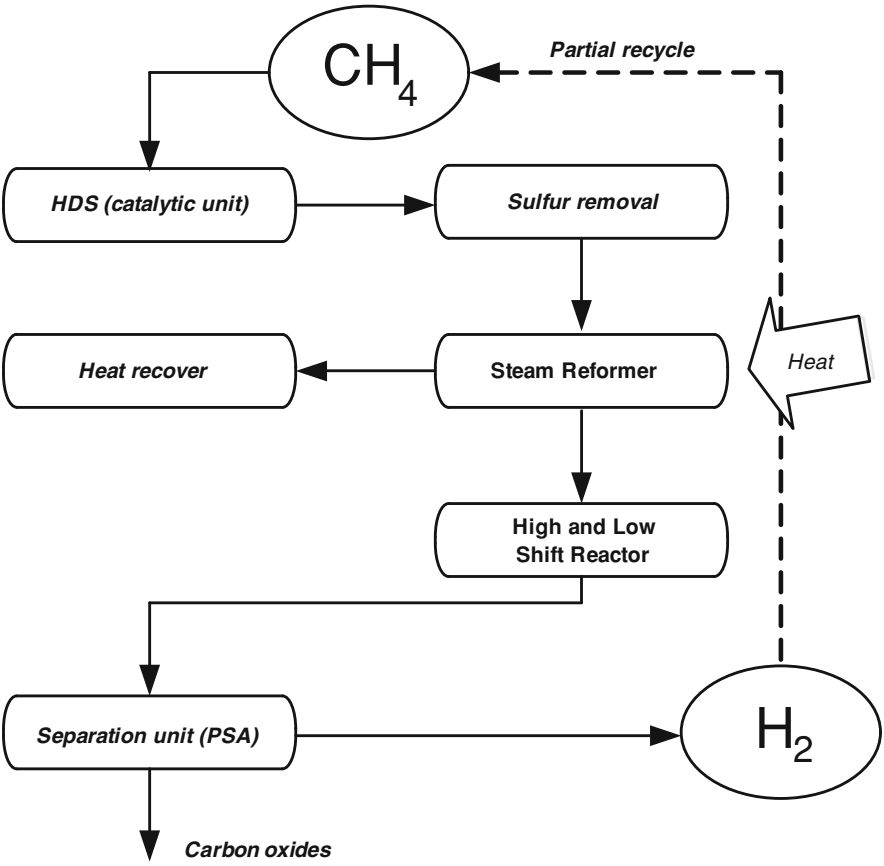

Fig. 2.2 Simplified scheme including all main process steps involved in hydrogen production plants based on methane SR

The array of tubes filled with the catalyst is suspended in a furnace that supplies heat for the highly endothermic reforming reactions.

In some cases carbon dioxide may replace steam to give a more favourable H_2/CO ratio for subsequent reactions of the products [8]:

$$CH_4 + CO_2 \leftrightarrows 2CO + 2H_2 \quad \Delta H = +247 \text{ kJ/mol} \tag{2.4}$$

The product selectivity for all these reactions is controlled predominantly by thermodynamics, i.e. the final product composition can be foreseen by multi-component chemical equilibria calculations.

When other hydrocarbons (for example propane) are used as feedstocks, CH_4 is the favoured product at lower temperatures, while hydrogen is preferred at temperatures superior to 700–800°C [6], then the product gas leaves the tubular reactor at temperatures between 700 and 950°C, in dependence of the particular application. The necessity to operate at these temperatures introduces several

potential problems. In particular, the thermal stability of catalysts needs to be carefully verified [9], because steam tends to favour catalyst and support sintering [10]. However, the major problem lies in the formation of coke, according to the following thermodynamically possible reactions:

$$CH_4 \leftrightarrows C + 2H_2 (\text{methane decomposition}) \quad \Delta H = +74.7 \text{ kJ/mol} \tag{2.5}$$

or for higher hydrocarbons:

$$C_nH_{2n+2} \leftrightarrows nC + (n+1)\ H_2 \tag{2.6}$$

$$2CO \leftrightarrows C + CO_2 (\text{Boudouard equilibrium}) \quad \Delta H = -173 \text{ kJ/mol} \tag{2.7}$$

$$CO + H_2 \leftrightarrows C + H_2O \quad \Delta H = -131 \text{ kJ/mol} \tag{2.8}$$

The coke can affect the performance of active sites of SR catalysts [11, 12], determining their partial deactivation, with progressive loss of selectivity towards synthesis gas production, blockage of reformer tubes and increasing pressure drop.

The above reactions are in equilibrium and the formation of coke via reactions (2.7) and (2.8) becomes less favoured as the temperature increases. However, coke formation via reactions (2.5) or (2.6) becomes increasingly important at higher temperatures and, depending on the nature of the feed, can rapidly deactivate the SR catalyst and block the reactor [12].

Therefore, the minimization of coking is one of the major factors controlling the industrial application of SR. The thermodynamic of the process dictates reaction conditions that favour coke formation cannot be avoided, but operating conditions can be chosen to minimize coke. Temperature, pressure and feed composition must be carefully controlled to avoid catalysts deactivation due to coking. Perhaps, the most obvious way is to increase the steam to hydrocarbon ratio to favour the reverse of reaction (2.8). Rostrup-Nielsen et al. [13] have presented carbon limit diagrams which relate the propensity of the catalyst to coke formation as function of to the H/C and O/C ratios in the gas phase.

The outlet from the secondary reformer contains about 10–14% CO (dry gas) which is fed to a high-temperature water gas shift (WGS) reactor (Fig. 2.2), typically loaded with Fe or Cr particulate catalyst at about 350°C. This further increase the H_2 content lowering CO content to about 2% as governed by the thermodynamic and kinetics of the Eq. 2.3, that is an exothermic reaction. Water gas shift reaction equilibrium is sensitive to temperature with the tendency to shift towards products when temperature decreases.

Then the product gas is fed to a low-temperature reactor where a $Cu/Zn–Al_2O_3$ particulate WGS catalyst works at about 200°C. Outlet CO concentration is decreased to <0.5%, while the remaining CO, which can poison downstream ammonia or methanol synthesis catalysts, is removed by pressure swing adsorption (PSA) unit. This method exploits the adsorption capacity of different molecular sieves or active carbon, which selectively permit the crossover of hydrogen but not of the other compounds present in the effluents. This technology has been

introduced relatively few years ago (the industrial application started in the 1970s) and results highly reliable and flexible.

Starting exclusively from Eqs. 2.1 and 2.3, considering a stoichiometric mixture of CH_4 and H_2O completely converted to H_2 and CO_2, and taking into account the heat of reaction supplied by combustion of CH_4, it is possible to calculate the theoretical energy associated with lower heating value (LHV) of methane to produce H_2. The minimum energy consumption which can be reached by this process corresponds to 2.59 Gcal/1000 Nm^3 H_2 when starting from water vapour, and 2.81 Gcal/1000 Nm^3 H_2 when starting from liquid water, as the real process [6].

Hydrogen plants designed with conventional technology utilize reforming temperatures below 900°C and high steam to carbon ratios (>2.5), to limit coke formation problems. These plants are characterized by quite poor energy efficiency, as significant amounts of process steam have to be condensed by large air and water coolers. Moreover, investment costs are high, as large volumetric process flows have to be handled [6].

Modern hydrogen plants utilize the new developments in SR and shift technology, allowing apparatus to be designed with reforming temperatures above 900°C and steam to carbon ratios even lower than 2.0 [6]. These advanced SR plants have improved energy efficiency and reduced hydrogen production costs. Currently, the processes require about 2.98 Gcal/1000 Nm^3 H_2 implying that an advanced reforming technology consumes about 6% more energy than the theoretical minimum.

In recent years, new concepts to produce hydrogen by methane SR have been proposed to improve the performance in terms of capital costs reducing with respect to the conventional process. In particular, different forms of in situ hydrogen separation, coupled to reaction system, have been studied to improve reactant conversion and/or product selectivity by shifting of thermodynamic positions of reversible reactions towards a more favourable equilibrium of the overall reaction under conventional conditions, even at lower temperatures. Several membrane reactors have been investigated for methane SR in particular based on thin palladium membranes [14]. More recently, the sorption-enhanced steam methane reforming (Se-SMR) has been proposed as innovative method able to separate CO_2 in situ by addition of selective sorbents and simultaneously enhance the reforming reaction [15].

2.1.1.2 Hydrocarbon Partial Oxidation

An alternative route to produce synthesis gas starting from hydrocarbon feedstock is the partial oxidation reaction (POX) [16]. This reaction utilizes the oxygen in the air as oxidant and results moderately exothermic. The oxygen to carbon ratio is lower than that required by stoichiometric complete combustion.

The stoichiometric equation for methane conversion is:

$$CH_4 + {}^1/_2\,O_2 \rightarrow CO + 2H_2 \quad \Delta H = -35.6\ \text{kJ/mol} \tag{2.9}$$

or for higher hydrocarbons:

$$C_nH_m + {}^n/_2\,O_2 \rightarrow nCO + {}^m/_2\,H_2 \tag{2.10}$$

The theoretical H_2 to CO ratio results lower than that of SR (about 2/3), as the main oxidant is O_2 instead H_2O. However, a small amount of water is often added to the reactor feed, to better control reaction temperature and coke formation [16].

The reactions (2.9) or (2.10) are not the exclusive routes of the process as other stoichiometric equations are thermodynamically compatible with the mixture composition fed to the reactor. Equations 2.1–2.8 involved in hydrocarbon SR might occur also in partial oxidation, i.e. they are possible reaction pathways in addition to (2.9) or (2.10). On the other hand, it is necessary to consider that further equations related to several oxidation reactions could occur during fuel conversion:

$$CH_4 + 2O_2 \rightarrow CO_2 + 2H_2O \quad \Delta H = -801.6\ \text{kJ/mol} \tag{2.11}$$

$$CO + {}^1/_2\,O_2 \rightarrow CO_2 \quad \Delta H = -282.7\ \text{kJ/mol} \tag{2.12}$$

$$H_2 + {}^1/_2\,O_2 \rightarrow H_2O \quad \Delta H = -241.6\ \text{kJ/mol} \tag{2.13}$$

POX involves the combustion of hydrocarbon feedstock in a flame with less than stoichiometric oxygen required by complete combustion with production of carbon dioxide (CO_2) and water (H_2O), according to Eqs. 2.11–2.13, which in turn react with the unreacted hydrocarbon (Eqs. 2.1 and 2.4 in Sect. 2.1.1.1), to produce carbon monoxide and hydrogen. Usually a slight excess (20–30%) of oxygen with respect to the stoichiometric value required by equations (2.9) or (2.10) is fed to the system. The most recognized reaction mechanism hypothesis is that the highly exothermic total oxidation reaction consumes essentially all the available oxygen, and the large amount of thermal power produced by the combustion is exploited by endothermic reforming reactions. However, the POX process remains globally exothermic.

A non-catalytic partial oxidation process based on the above reactions has been largely used for the past five decades for a wide variety of feedstocks, in particular heavy fractions of refinery, such as naphtha, vacuum fuel oil, asphalt residual fuel oil, or even whole crude oil. The absence of catalysts implies that the operation of the production unit is simpler (decreased desulfurization requirement) but the working temperatures results higher than 1200°C. The high values of this parameter permit satisfactory yield to H_2 and CO to be obtained without using a selective catalyst.

A catalytic partial oxidation (CPO) reaction permits operation temperature to be lowered and meets the requirements of recently proposed decentralized applications based on small-scale reformer plants [17], better than the SR or the non-catalytic partial oxidation process. This evaluation is based on the dependence of costs associated with both SR and CPO manufacture and management plants by

power size. The potentialities of small-scale plants suggest a deeper discussion about hydrogen distribution network scenarios that is carried out in Sect. 2.2.

The scientific community interest has been focused in recent years especially on H_2 catalytic production by partial oxidation of methane, due to the large diffusion of natural gas as primary feedstock. Coke formation and its deposition on catalyst active sites represent, as well as for SR process, the main barrier to be abated for a practical utilization of CPO in hydrogen production plants.

Methane CPO has been intensively studied to select new advanced catalysts able to maximize hydrocarbon conversion, hydrogen yield and especially to control catalytic deactivation phenomena, strictly connected to coke deposition problem, similar to SR process [18–23]. The role of transition metal-based catalysts in methane CPO reaction mechanism has been detailed [24], evidencing that fuel dissociation step is crucial for a viable overall process rate at reasonable temperatures, as expected taking into account the stability of methane molecule.

LPG could be another favourable feedstock for distributed hydrogen production since it is easy to store and transport. Furthermore, LPG and NG appear attractive because hydrocarbon mixtures with short aliphatic chains (C_1–C_4) and no-sulphur or other electronegative atoms (Cl, P) could limit carbon deposition and catalyst poisoning. Commercial Ni catalysts used for SR plants have resulted very active also for CPO of methane and propane, but deactivation resistance due to coke is not yet acceptable [25–28]. Ni-based catalyst modification with rare-earth metal oxide La_2O_3 can reduce the Lewis acidity of the catalyst surface and enhance its ability to suppress carbon deposition [29], while among the various noble metal catalysts Rh has been reported as active and stable [30]. Bi-metallic Ni–Pt catalysts supported on Al_2O_3 result very promising if compared with monometallic catalytic solids [31]. Mixed oxides containing Ce seem useful to formulate a catalyst suitable for a durable hydrogen production, in particular CeO_2 is known to be an oxy-transporter, i.e. it is capable to oxidize deposited carbon particles and to actively participate in mechanism of redox catalytic reactions [32]. On the other hand, the incorporation of ZrO_2 into CeO_2 lattice promotes the CeO_2 redox properties, increasing the oxygen mobility within the solid solution formed [33].

If the water quantity added as feed increases up to a value corresponding to neutral energetic balance between exothermic and endothermic reaction steps, the overall process is denominated autothermal reformer (ATR). This approach combines both SR and POX catalytic processes and it has been recently proposed to optimize the performance in terms of compactness and efficiency of small-medium production plants. This technology could permit a compromise between the good efficiency of SR and the fast start up of POX. However, it needs a careful control of in going mass stream [6, 7].

2.1.1.3 Hydrocarbon Decomposition

The direct thermal decomposition of methane or higher hydrocarbons represents the unique approach for a theoretical direct decarbonization strategy [34, 35].

Equation 2.5, moderately endothermic, already involved in SR or partial oxidation processes as secondary undesired reaction, written for a general hydrocarbon

$$C_nH_m \rightarrow nC + {}^1/_2\, mH_2 \tag{2.14}$$

evidences that theoretically hydrogen produced by this route results carbon dioxide emission-free, with the additional potentiality of producing a valuable carbon material.

The non-catalytic route, as for the other fuel processing processes, requires a too high temperature (1300–1600°C) to obtain high reactant conversions, while a catalytic approach would permit the working temperature to be lowered to more practical values. Various Ni-supported catalysts [36–38], and more recently innovative systems doped with other transition metals such as Fe and Co [39, 40], greatly reduce the working temperature, but fast deactivation occurs, due to carbon deposition. The activity loss strongly limits both efficiency and environmental benefits, as catalyst regeneration is necessary, consuming additional energy and producing carbon dioxide emissions.

Carbon-based catalysts and in particular their kinetics have been intensively studied [41–43], because they should reduce the disadvantages related to metal-based catalysts. Carbon materials are more available, have the potential of cost reduction, do not require periodic regeneration because it is not necessary to separate the carbon-product from the catalyst. The fluidised bed reactor technology represents the optimal choice for this kind of hydrocarbon cracking process as it can withdraw the carbon particles evermore, permitting a reliable storage of produced carbon for further use [44–46]. A novel technological solution aimed to improve activity and stability of carbon catalysts has been recently proposed [47]. The presence of small amount of O_2 in an autothermal approach seems to be the best solution to minimize CO_2 emissions in the overall process.

Plasma technology has been proposed as alternative solution to be used in different fuel processing pathways [4, 35, 48, 49]. Similar to catalysis, the plasma approach could drastically increase the rate of the key reaction steps, mainly related to fuel molecule dissociation, abating the activation barrier for the advance of the overall decomposition reaction. The most common method utilizes a high electric discharge produced by two electrodes (‘arc’), which determines intense heat, and breaks down organic molecules into their elemental atoms. However, this kind of processes suffers by many limitations, in particular the electricity cost impact on overall efficiency needs to be accurately verified for a transition to large-scale hydrogen production.

Recently, a laboratory atmospheric pressure microwave plasma reactor has demonstrated to be useful for a single-stage, non-catalytic dry methane thermolysis, resulting active and selective towards hydrogen production [50]. Similarly, another novel process proposed for thermo-catalytic decomposition, based on plasma generation of catalytically active carbon aerosol particles, has provided very high efficiency (higher than 80%) at working temperatures below 1000°C [51].

2.1.1.4 Coal Gasification

Another important thermal method is based on the gasification process, currently used on industrial scale essentially to generate electricity.

This technology is also the oldest method for hydrogen production and could convert any type of organic material, such as coal and other petroleum or biomass-derived mixtures. The interest towards this approach comes from the practical possibility of using coal as fuel that is the most world-wide available and relative cheap fossil fuel [52].

The gasification of coal or other carbonaceous substances was largely used in the past century especially for iron making. The process consists of a series of chemical reactions finally producing, similar to reforming reactions, carbon monoxide and hydrogen mixtures, also called 'town gas', which represented in the past century an important chemical feedstock in North American, Europe and China for domestic heating and lighting, public street lighting and domestic fertiliser industry. However, the popularity of town gas decreased significantly by the 1950s as natural gas became widely available. Gasification takes place at high pressure (up to 60 bar) and temperature superior to 700°C, with a controlled amount of oxygen and/or steam. Similar to hydrocarbon reforming-derived synthesis gas, the effluent mixture may be used to produce hydrogen or methanol, burned directly in internal combustion engines, or converted via the Fischer–Tropsch process into synthetic fuel [53].

Coal substances have complex chemical structures and their compositions are highly variable. For example a carbon/hydrogen composition in bituminous coal may be represented as about one atom of hydrogen per atom of carbon. For a generic gasification process based on the above coal feedstock, selected as reference carbonaceous fuel, the following (not balanced) overall chemical equation can be written as:

$$CH + O_2 + H_2O \leftrightarrows CO + CO_2 + H_2 + \text{other species} \tag{2.15}$$

The carbonaceous particles are heated and volatilized at temperatures ranging from 1000 to 1500°C producing carbon oxides and hydrogen gaseous mixtures and simultaneously char (pyrolysis).

A limited amount of oxidant (oxygen or air) is introduced into the reactor and is mixed with crushed/pulverized coal feed (either dry or as slurry) to allow volatile products and some of the char reacts with oxygen to form carbon dioxide and carbon monoxide. The basic reactions for the CO and CO_2 formation are the partial and total combustion of C, respectively

$$C + {}^1/_2\,O_2 \rightarrow CO \quad \Delta H = -110.4 \text{ kJ/mol} \tag{2.16}$$

$$C + O_2 \rightarrow CO_2 \quad \Delta H = -393.1 \text{ kJ/mol} \tag{2.17}$$

The exothermicity of the above reactions provides heat for the subsequent gasification reactions. The char (or other resulting hydrocarbons) reacts with steam

(but also with carbon dioxide) to produce carbon monoxide and hydrogen, according to the following equation that is the reverse of Eq. 2.8

$$C + H_2O \leftrightarrows CO + H_2 \quad \Delta H = +131 \text{ kJ/mol} \tag{2.18}$$

In addition, the reversible gas phase water gas shift reaction (2.3) reaches very fast equilibrium at temperatures typical of a gasifier. The above chemical equations balance all the product (CO, CO_2, H_2O, H_2) concentrations of the process.

Gasification process could be inserted in a Integrated Gasification Combined Cycle plant (IGCC) [54, 55] to improve the overall process efficiency. The syngas produced in the gasifier is used as fuel in the gas turbine generator of the integrated combined-cycle technology, which consists also of a heat recovery steam generator and a steam turbine/generator. A simplified scheme of a proposed gasification overall plant for generation of both electricity and hydrogen is reported in Fig. 2.3. The scheme evidences different steps to produce electricity and hydrogen. The heart of the overall process remains the gasifier. The coal fed to the reactor is

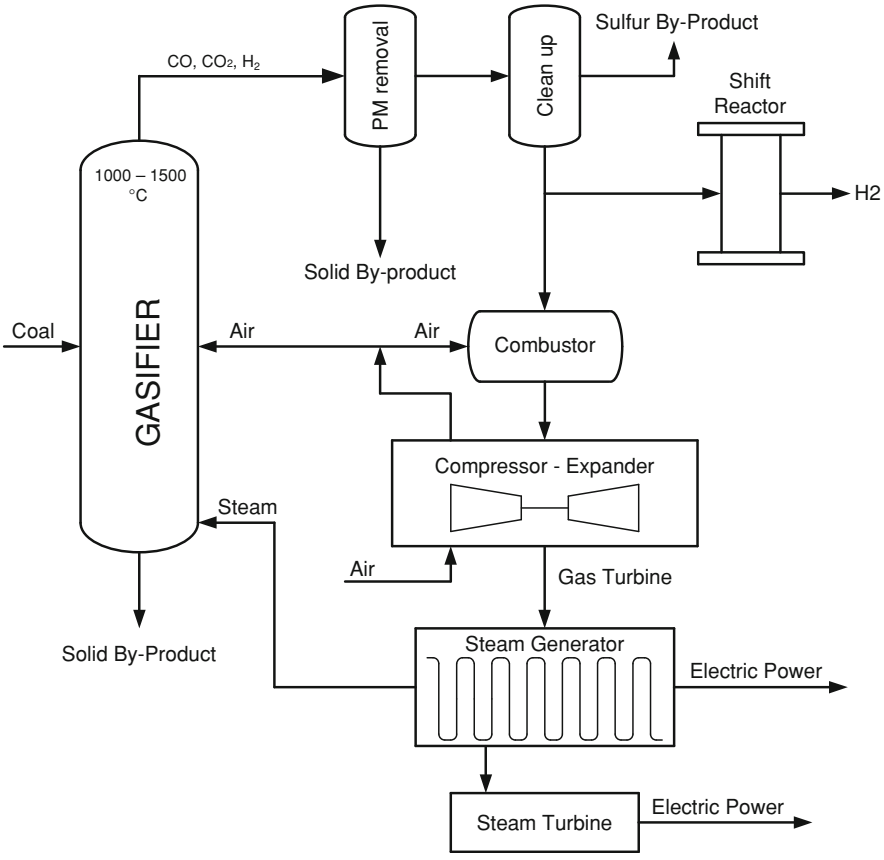

Fig. 2.3 Simplified scheme of an integrated gasification plant [54]

exposed to steam and carefully controlled amounts of air or oxygen under high temperatures and pressures. Sulphur is converted to hydrogen sulphide (clean-up reactor in Fig. 5.3) and can be captured by processes presently used in the chemical industry.

The exhaust heat from the combustion turbine is recovered in the heat recovery steam generator to produce steam. The waste heat is passed to a steam turbine system, while heat is recovered from both the gasification process and the gas turbine exhaust in advanced boilers producing steam. The steam is then used in steam turbines to produce additional electrical power, while the syngas mixture could also feed a fuel cell plant (IGFC).

A potential advantage of this technology is that carbon dioxide can be easily separated from the syngas and then captured, instead of being released into the atmosphere [56–58]. If oxygen is used in a coal gasifier instead of air, carbon dioxide is emitted as a concentrated gas stream in syngas at high pressure. In this form, it can be captured and sequestered more easily and at lower costs. Finally, plasma technology added to gasification plant has been recently proposed to improve energy performance and quality of product mixtures [59].

Hydrogen could be produced from coal gasification with near-zero greenhouse gas emissions only if CCS technology, in particular the crucial sequestration stage, will be successfully developed in the next decades. In this view, the coal gasification technology appears most appropriate for large-scale, centralized hydrogen production plants, where handling of large amounts of coal and CCS technologies could be more functionally managed. Significant technological efforts towards the development of an advanced apparatus capable to enhance efficiency, environmental performance and reliability appear necessary.

2.1.1.5 Biomass Gasification

The choice of a carbon neutral source class as feedstock for hydrogen production, such as biomass substances, could permit the problem of carbon dioxide emissions to be overcome.

In recent years, several methods for hydrogen production starting from biomass materials have been investigated [60–62], and great efforts have been addressed in particular in selecting advanced solutions for optimization of the previously analysed thermal processes, such as SR or gasification, by substituting the fossil fuel feedstocks (coal or petroleum-derived fuels) with different types of biomass-derived fuels.

In particular, biomass-derived materials could be converted in gasifiers, to obtain a gaseous mixture of hydrogen, carbon monoxide, carbon dioxide and other compounds, by applying heat under pressure in the presence of steam and a controlled amount of oxygen, very similar to coal gasification process. On the other hand, the produced syngas could be reformed to maximize hydrogen production but it may also feed an electrical power plant coupled to an electrolysis unit [63].

Typically, a biomass-derived material contains substances constituted by carbon, hydrogen and oxygen atoms. As an example, the simplified not balanced chemical equation representative of the overall gasification process for a reference substance such as glucose is:

$$C_6H_{12}O_6 + O_2 + H_2O \leftrightarrows CO + CO_2 + H_2 + \text{other species} \tag{2.19}$$

The exhaust gases contain CH_4, N_2, H_2O, tar, acidic and basic compounds (NH_3, HCN, H_2S) considered as impurities. Tar conversion has to be controlled to maximize the reliability of mechanical equipments and to assure the operation of the successive clean-up catalytic steps for final hydrogen separation and purification [64]. This step involves the utilization of additional steam and selective catalysts, affecting the overall efficiency of the process [65]. The operation with oxygen instead of air may improve the efficiency of the process but it suffers the costs associated with air liquefaction process, necessary for O_2/N_2 separation.

The current industrial concept for biomass gasification is conditioned by several problems, i.e. heterogeneity of material availability, relatively high costs of collection and transporting the feedstock, and a relatively low thermal efficiency due to the vaporization cost of the moisture contained in the biomass. In order to lower capital costs many efforts are addressed towards the development of advanced membrane technologies able to separate oxygen from air (when the gasifier utilizes oxygen), replacing the cryogenic process of air liquefaction, and separate and purify hydrogen from the produced gas stream [66].

Similar to coal, biomass gasification technology seems to be more appropriate for large-scale, centralized hydrogen production, due to the nature of handling large amounts of biomass and the required economy of scale for this type of process, and it may be relevant in specific geographic zones where this feedstock is readily available. However, it will be also useful to explore the future possibilities to use biomass for improving economics of distributed and/or semicentral reforming processes. In this respect, heterogeneous waste and in particular municipal rubbish could represent an important feedstock, if thermally pretreated, in medium-sized power plants.

2.1.1.6 Thermochemical Methods

The possibility to transform directly a high-temperature thermal source to chemical energy makes quite attractive the water thermolysis process. This approach represents a direct route for conversion of heat associated with a primary source into hydrogen without intermediate steps; the constraint is that theoretically attractive efficiency can be obtained only if primary sources producing high-temperature energy are used.

Severe engineering barriers are correlated to the very high temperatures necessary to split water exclusively by heat, together with the problems connected to heat extraction and thermal management. These problems require the practical

development of a more complex concept of water decomposition, based on multi-step thermochemical processes. This approach is founded on the characteristics of several chemical reagents, capable to lower the temperatures of water decomposition down to a commercially viable value, inferior to 1200°C.

A schematic overall process involves at least two steps:

$$H_2O + 2X \leftrightarrows 2XH + {}^1/_2O_2 \tag{2.20}$$

$$2XH \leftrightarrows 2X + H_2 \tag{2.21}$$

where *X* represents the generic chemical agent. Obviously the net balance reaction is the reverse of Eq. 2.13:

$$H_2O \leftrightarrows H_2 + {}^1/_2\,O_2 \quad \Delta H = +288\,\text{kJ/mol} \tag{2.22}$$

where ΔH is calculated considering the water in liquid form. The nature and the role of intermediate compounds (XH) are the key point for a successful process, strictly related to the reaching of the following targets [4]:

1. Gibbs free energy variation of all individual reaction steps must approach zero.
2. The different steps should be minimal.
3. Direct and reverse reaction rates of the different steps need to be very fast.

A lot of thermochemical cycles have been proposed in literature [4, 67, 68], potentially able to exploit the high-temperature energy coming from nuclear or concentrating solar plants (CSP).

In particular iodine–sulphur reaction results quite attractive [68]. It consists of three steps at different operation temperatures, which involve the H_2SO_4 and HI dissociation and the re-production of both acids starting from I, SO_2 and H_2O. Particular interest is also focused on CeO_2/Ce_2O_3 cycle, cerium–chlorine cycle (Ce–Cl), Zinc–zinc-oxide cycle (Zn/ZnO), but also on a Cu–Cl cycle, which is a cycle with an electrochemical step [69].

This technology appears really promising for a massive efficient hydrogen production but it is still far to be practically realized in few years, basically because of engineering and material constraints associated with high operation temperature (not inferior to 900–1000°C).

2.1.2 Electrolytic Processes

The possibility to store the surplus of electric energy produced by the power plants into a hydrogen carrier represents an attractive potential solution to optimize the overall efficiency of energy production and utilization. This idea requires a technology able to transform the excess of produced electric energy into the chemical energy of hydrogen molecule.

A well-known electro-chemical method to obtain hydrogen using electricity is the water electrolysis [70, 71], which permits the splitting of water molecule into H_2 and O_2 according to Eq. 2.22 reported in Sect. 2.1.1.6.

The galvanic cells produce electric energy via electro-chemical reactions, while electrolytic cells, such as those used in water electrolysis, are electrochemical cells in which a chemical reaction is forced by added electric energy.

The galvanic cells are based on a spontaneous overall reaction characterized by a negative value of the Gibbs free energy, which corresponds to the theoretical electric work (see details in Sect. 3.1). The electrolytic cells represent exactly the reverse of the galvanic process, then the overall reaction, characterized by a positive value of the Gibbs free energy, is not spontaneous, and needs an external energy resource to force the advance towards the products.

Different electrolysis technologies could be applied, from the commercially available method based on alkaline cells to the new advanced cells based on proton exchange membrane (PEM) and solid oxide mixtures as electrolytes. The basic schemes of these electrolysers are shown in Fig. 2.4.

The alkaline device utilizes a solution of potassium hydroxide (KOH) as electrolyte (Fig. 2.4a). The two semi-reactions of reduction (cathode side) and oxidation (anode side) that occur in alkaline solution are, respectively

$$2H_2O + 2e^- \rightarrow H_2 + 2OH^- \tag{2.23a}$$

$$2OH^- \rightarrow {}^1/_2\, O_2 + H_2O + 2e^- \tag{2.23b}$$

The sum of the two semi-reactions (2.23a) and (2.23b) gives the overall Eq. 2.22. Hydroxyl-ions represent the chemical species that close the electric circuit through the electrolyte. The alkaline solution contains about 30 wt% of potassium hydroxide and operates at about 80°C. Today, this technology gives

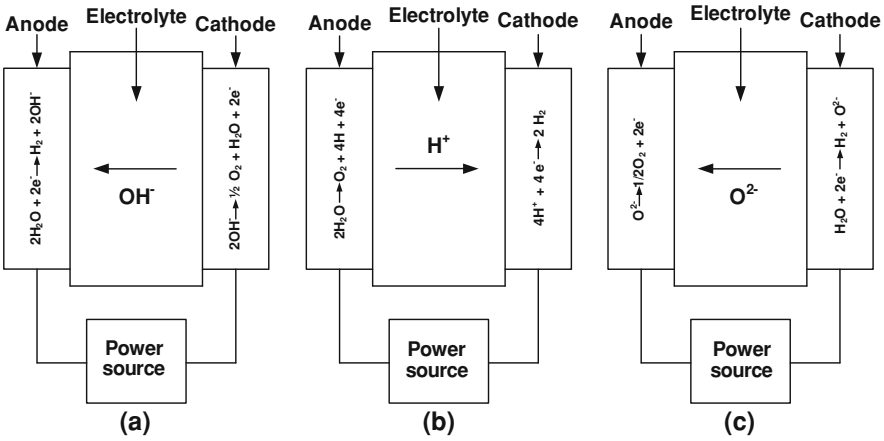

Fig. 2.4 Simplified principle scheme for alkaline (**a**), PEM (**b**) and solid oxide (**c**) cells for water electrolysis

a very low contribution to the worldwide hydrogen production (see Table 2.1), because of the high costs of electricity and the high but not complete conversion efficiency [72]. Furthermore, the KOH solution could limit the resistance of used materials because of corrosion phenomena. In the past years, many studies have been addressed towards a further improvement of catalysed electrodes to optimize the efficiency and reliability of the electrolytic process involving alkaline cells, but the results have not yet satisfactory [73–75].

New advances of the other two electrolytic cells reported in Fig. 2.4 have been recently encouraged to exploit the higher potentialities of PEM and solid oxide technologies, as electrolyser components to be integrated in plants based on wind and solar renewable sources [76, 77] or nuclear power [78], respectively.

As regarding electrolysis with PEM cells (scheme b of Fig. 2.4), which is just the reverse of fuel cell operation mode, the interest derives by greater energy efficiency, ecological cleanness, easy maintenance, smaller mass–volume characteristics and high degree of gases purity [79–81]. Furthermore, it is expected that future costs could be progressively reduced due to foreseeable technological advances of PEM devices working as electric power generation.

The two semi-reactions involved in the process are:

$$2H_2O \rightarrow O_2 + 4H^+ + 4e^- \tag{2.24a}$$

$$4H^+ + 4e^- \rightarrow 2H_2 \tag{2.24b}$$

Equations 2.24a and 2.24b are the oxidation and reduction steps, occurring at anode and cathode side, respectively, while the protons represent the ion species passing through the solid polymer electrolyte. However, the overall electrochemical reaction is the same of alkaline electrolysers.

Recent studies have been devoted to the optimization of the already existent PEM electrolysers, first exploring the possibilities to increase the working pressure. The high pressure electrolysis (HPE) should reduce significantly the energy costs for the successive fuel compression step. Currently, the on board-storage of hydrogen in fuel cell cars (see details in Sect. 2.3) requires a compression stage before feeding the vehicle, while the need for an external hydrogen compressor could be avoided by pressurising the hydrogen in the electrolyser. The energy required to produce high pressure hydrogen by high pressure water electrolysis is estimated to be about 5% less than that required for devices working in atmospheric conditions [82]. However, high pressure operation could affect the performance of existent Nafion electrolytic membranes [83] and yield additional problems regarding efficiency loss due to cross-permeation phenomena [81] that implies also relevant safety issues. On the other hand, the application of this technology for electrolytic hydrogen production is mainly related to costs of noble metals used in membrane electrode assembly (MEA, see Sect. 3.2) materials, requiring the development of new high performance and low cost materials [84].

PEM electrolysis process has been proposed especially for wind turbines or solar photovoltaic (PV) panel utilizations. In this case, the electrolysis represents

only a step in the overall hydrogen production process. Efficiency, reliability and costs of overall integrated plants have to be carefully analysed, in particular taking into account the typical intermittent operation mode of each renewable source. Several configurations of PV arrays or wind turbines connected to an electrolyser, based on PEM technology, have been considered evidencing the potentialities of each solution [76, 77]. A possible optimal option is to select the PV panels so that their voltage–current output matches the polarization curves of the electrolyser. Solar PV energy has shown good potentialities as an electricity source for water electrolysis but recent analysis related to environmental and economical issues evidence that wind energy seems to be, at least for the existent technological level, a more promising option to produce electrolytic hydrogen [85, 86].

The operative temperature could play a crucial role for the development of a very efficient electrolyser plant. Solid oxide cells (scheme c in Fig. 2.4) have been proposed for high temperature electrolysis (HTE), because of the strong resistance at high temperatures of the related electrolytes. With respect to traditional room-temperature electrolysis HTE modules presents two main advantages [87]:

1. electrical energy requirement is reduced because of better recover of residual heat, which is cheaper than electricity
2. the power generating cycle, including also electrolysis reaction, is more efficient at higher temperatures.

Currently yttria-stabilized zirconia and doped $LaGaO_3$ systems seem the most promising materials for developing high temperature (about or higher than 800°C) and intermediate temperature (between 400 and 800°C) electrolysis technologies, respectively [88].

This method could be used for nuclear, concentrating solar or geothermal power plants without carbon dioxide emissions.

The process is based on the following two electrochemical semi-reactions:

$$H_2O + 2e^- \rightarrow H_2 + O^{2-} \tag{2.25a}$$

$$O^{2-} \rightarrow {}^1/_2\, O_2 + 2e^- \tag{2.25b}$$

where the ionic species are oxygen anions. As for alkaline and PEM electrolyser technologies the overall reaction is Eq. 2.22.

In Fig. 2.5, a simplified scheme of a high-temperature electrolysis plant based on nuclear power is reported [89].

Water is warmed up by outer heat in the boiler of the nuclear reactor, before entering as steam into cathode side, where it decomposes according to Eq. 2.25a, hydrogen molecule is removed as product, and oxygen anion moves to anode through a solid oxide electrolyte with high oxygen ion conductivity. Oxygen ion, loosing electrons at the anode side, is the reactant of the oxidation semi-reaction, and is recovered as oxygen molecule, according to Eq. 2.25b.

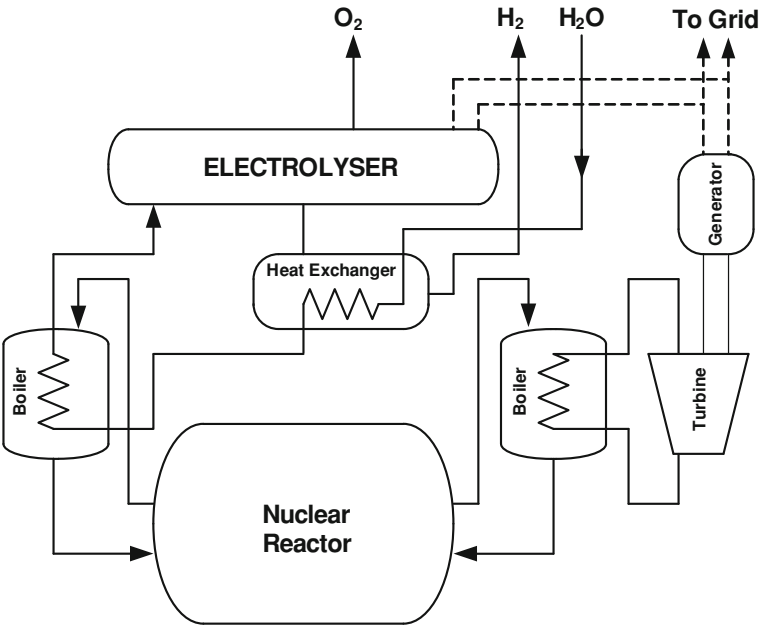

Fig. 2.5 Scheme of a HTE plant based on nuclear power [89]

The steam–hydrogen mixture exits from the electrolyser and the water/hydrogen gas mixture passes through a separator to obtain pure hydrogen, while a portion of the electricity produced by the reactor is used to feed the electrolyser.

Electrochemical oxidation of coal has been investigated at the beginning of 1980s [90] to evaluate the possibility to limit the high electric power required by H_2O electrolysis, simultaneously overcoming the limitations of the conventional hydrogen production starting from coal (see Sect. 2.1.1.4), related to the high costs due to working temperature and separation units. The electrolysis of coal takes place according to the following reactions:

$$C + 2H_2O \rightarrow CO_2 + 4H^+ + 4e^- \tag{2.26a}$$

$$4H^+ + 4e^- \rightarrow 2H_2 \tag{2.26b}$$

Coal is oxidized at the anode, while protons are reduced to form hydrogen molecule at the cathode. The low current densities achieved in the reaction (about 2.5 mA/cm^2 at 1 V) have discouraged further studies in the successive two decades, but recent works on the development of noble metal carbon fibre electrodes have demonstrated the possibility to improve their activity [91] justifying further experimental tests aimed at fabricating a coal electrolytic cell (CEC) operating at intermediate temperatures (40–108°C) [92]. Finally, another potential advantage of the coal electrochemical oxidation is that downstream separation of gases is not necessary as pure H_2 and CO_2 are generated in different compartments of the cell.

2.1.3 Photolytic Processes

The photolytic effect represents another technology able to directly exploit the sunlight, in addition to photovoltaic effect and concentrating solar technology. This process could be theoretically used to directly dissociate water molecules into hydrogen and oxygen [93]. The recent advances realized in this field [4, 94] encourage a wide research effort aimed at individuating technological pathways alternative to thermal, thermochemical and electrolytic approaches, for an useful contribution to medium–long term hydrogen production.

In particular, two kinds of processes are under investigation:

1. the photoelectrochemical (PEC) process that uses photoactive cells in which doped semiconductor electrodes are immersed in aqueous solutions or water;
2. the photobiological (PB) water splitting, related to the specific activity of specialized microorganisms.

In the PEC process, an electronic charge formed at the surface of the anode, radiated from solar energy, is able to generate an electron–hole pair. In the presence of an electric field, holes and electrons are forced to move in opposite directions determining the H_2O oxidation to oxygen at the anode side and the hydrogen ion reduction to molecular hydrogen at the cathode side. PEC research is mainly focused on finding reliable semiconductors able to split water in an energetically suitable way [95–97]. On the other hand, PB processes could exploit the potentialities of algae and bacteria in consuming water and produce hydrogen as a byproduct of their natural metabolic processes [98, 99]. This research is focused on the possibility of modifying or engineering them, addressing the solar energy selectively towards direct hydrogen production.

2.2 Hydrogen Distribution

The transition towards the so-called hydrogen economy requires the development of infrastructure plans. Currently, few limited networks for hydrogen utilization exist in the world, mostly concentrated in Europe (UK, Netherlands, Germany) and USA, and located close to refinery site for petrochemical or other industrial requirements.

A future massive network can be realized according to two possible scenarios:

1. a centralized management of the worldwide hydrogen production and distribution, corresponding to the existent energy production strategies
2. a distributed territorial production and utilization, for which H_2 is produced on-site at small–medium-scale filling station.

The analysis of the above strategies needs to include all the stages necessary to produce and distribute the fuel for a widespread use, and should benefit from the following two options for hydrogen transport and distribution:

1. delivery of compressed gas or liquid by tracks
2. gaseous pipelines.

The choice is strictly related to the above scenarios, and depends on the technologies and scale selected for hydrogen production [3, 100].

In Fig. 2.6, the most significant fuel supply options are represented, evidencing individual steps concurring to the realization of each production–distribution chain. The centralized manufacture of hydrogen requires means of transportation, as well as intermediate storage capabilities. In particular, the utilization of hydrogen produced as gas in centralized plants, located at sites quite far from the user points, would require a pipeline grid. Pipelines seem more indicated to transport large quantities of gaseous fuel, and to cover long distances. Road

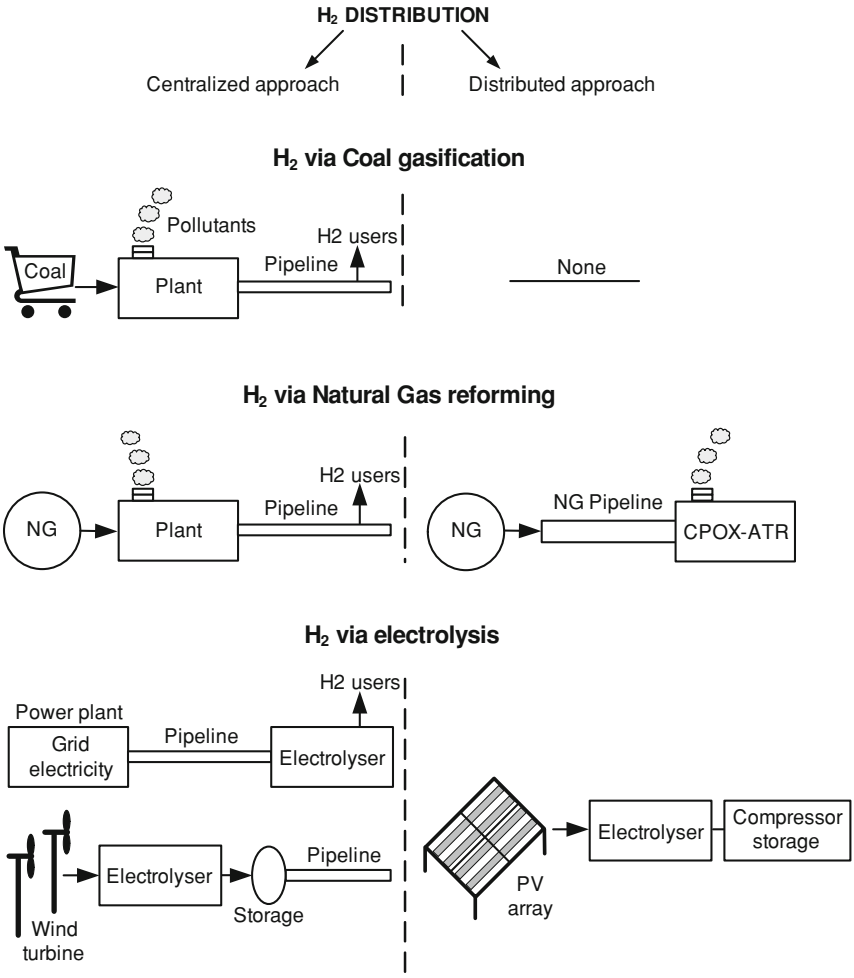

Fig. 2.6 H_2 supply options in centralized and distributed approaches

transportation by trucks, in both high-pressure gas and liquid, should become competitive to move only small quantities of hydrogen.

On the other hand, a distributed manufacture, based on either on-site small reforming plants or on small-size electrolyzers, would permit storage at the vehicle facility and strongly reduce the specific impact of fuel distribution and transport costs on a global techno-economic assessment.

Taking into account that hydrogen can be transported in pipelines similar to natural gas, it is interesting to verify if the existing pipeline infrastructure could be used, evaluating in particular the energetic limitations and the current performance of materials of construction and of shut techniques. This analysis first requires a comparison between the energy flows of hydrogen and methane. The volumetric flow rate through a pipeline can be calculated according to the following equation [101]:

$$Q = \mathrm{CD}^{2.5}\lambda\sqrt{\frac{(p_1 - p_2)^2}{dZTLf}} \tag{2.27}$$

where Q is the volumetric flow rate of the gaseous fuel (Nm^3/h), C is a proportionality constant (about 0.00013), D is the inner diameter (mm), λ is the pipeline efficiency, p_1 and p_2 are the inlet and outlet pressure, respectively (kPa), d is the relative density compared to air, Z is the compressibility factor, T is the absolute temperature, L the length (km) and f is the friction factor. In Fig. 2.7, a scheme of a section of pipeline is shown with the indication of main parameters affecting gas flow rate.

Considering the upper heating values of H_2 and CH_4 (12.8 and 40 MJ/Nm^3, respectively) as well as the wide difference in density values (0.09 for hydrogen and 0.68 kg/Nm^3 for methane, respectively), similar pressure drops have to be overcome to match the same energy demand. On the other hand, the accurate evaluation of compressibility and friction factor indicates that hydrogen is able to transport at least 80% of the energy carried by NG [102].

Also the aspects related to compression stage and pressure reduction stations need to be accurately considered. The performance of the centrifugal compressor, quite satisfactory for natural gas processing, becomes significantly limited when hydrogen is used, because of the need of higher rotational velocity, not compatible with material strength [101]. On the other hand, hydrogen fragileness [103] could represent a further problem for a sufficient reliability of the pipings and fixings

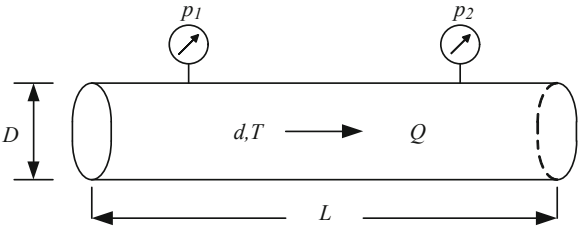

Fig. 2.7 Section of a pipeline with indication of the main parameters useful for volumetric flow rate calculation (Q)

during long-time operation, while hydrogen leakage, obviously higher with respect to methane, can be significantly limited, especially if polyethylene pipelines will be used for new hydrogen distribution infrastructures [101]. The transportation of hydrogen inside pipelines in liquid cryogenic forms theoretically should increase strongly the energy capacity, but it determines also a dramatic growth of capital costs and severe safety problems [101].

As regarding the transportation of hydrogen using the road, currently hydrogen travels mainly on trucks loaded inside high-pressure vessels (20 MPa). The overall transportation capacity utilizing liquid reservoirs should be higher than commercial vessels, in spite of much higher insulating and refrigeration costs that make them not yet satisfactory for a widespread transportation.

The above discussion suggests that the development of a hydrogen system concept based on distributed small-scale power plants should be easier. In this respect, the most appropriate hydrogen production technologies are based on PV-solar, natural gas reformer or wind-turbine resources, even if the last solution expects some infrastructure network to transport hydrogen from the production point to the user points.

The different pathways need to be environmental efficient and require a carefully evaluation of their impact not only on the costs but also on reliability, safety and social acceptance [104]. Since in a decentralized approach infrastructure cost related to hydrogen distribution is strongly reduced, a global economical evaluation related to both production and distribution has to accurately consider this perspective. On the other hand, the possibilities to lower the costs of centralized hydrogen production and to improve the technologies involved in the creation of a hydrogen transport and distribution infrastructure claim to be also carefully analysed. Optimization-based models capable to evaluate all these aspects for the development of a viable long-term plan has been recently presented, to aid the decision making process [105].

2.3 Hydrogen Storage

The storage capability of tanks is a crucial quality of fuels for road vehicles, because of the need to match the large driving range user demands. The mileage of conventional vehicles powered by liquid fuels reaches values clearly superior to those of battery powered electric vehicles. This is the main reason why the electric powertrain diffusion has been strongly limited up today. Hydrogen fuel cell powertrains could enter in a massive automotive market as potential competitor only overcoming successfully this important question.

The phase diagram for hydrogen is shown in Fig. 2.8, [106] while in Table 2.2 physical and thermodynamic data are reported for hydrogen in molecular form and for commercial liquid fuels, i.e. gasoline, diesel, LPG and liquid natural gas (LNG) that are high and low heating values, gravimetric density and volumetric energy

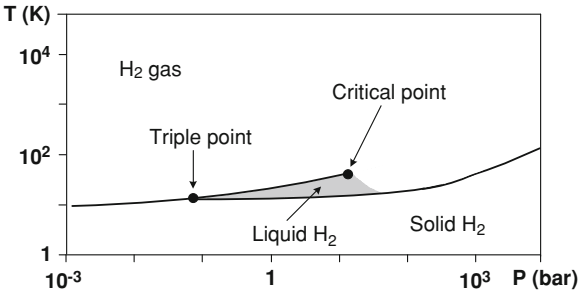

Fig. 2.8 Phase diagram for H_2

Table 2.2 Physical and thermodynamic data for automotive fuels

Property	Gasoline	Diesel	LPG	LNG	Hydrogen		
					Gas 350 bar	Gas 700 bar	Liquid
HHV (kJ/g)	47.5	44.8	50.3	55.5	141.9	141.9	141.9
LHV (kJ/g)	44.5	42.5	45.6	50.0	120.0	120.0	120.0
Gravimetric density (kg/m^3)	737	820–950	510	410–500	23.5	39.5	70.8
Energy density (MJ/L)	34.2	37.3	25.3	25.9	2.9	5.6	10.1

densities. The volumetric energy densities for hydrogen are calculated for liquid and gas form at pressure values varying from 350 to 700 bars.

The analysis of Fig. 2.8 evidences that hydrogen has very low boiling point. Liquid hydrogen exists only in a limited pressure–temperature region starting from the triple point and ending at the critical point. A narrow temperature range between 14 and 33 K is able to maintain the H_2 molecule in the liquid state in dependence of the pressure value (varying from 0.07 to 13 bar). The saturated liquid specific volume at atmospheric pressure is 0.014 m^3/kg, while for H_2 gas in standard conditions (273 K and 1 atm) it results 11.1 m^3/kg.

Table 2.2 evidences that hydrogen has very low gravimetric and volumetric energy densities. Hydrogen has the highest energy to weight ratio values (HHV and LHV), in particular it has nearly three times the energy content of gasoline and diesel fuels, but it contains less energy for a given volume when compared to the other fuels. Liquid hydrogen does not reach a density close to that of typical conventional liquid fuels, while hydrogen in gaseous form reaches a value of volumetric energy density lower than hydrogen in liquid form also at a pressure of 700 bar.

In the last years, the scientific community has investigated another interesting option regarding H_2 storage, based on the adsorption method [107–109]. The idea is that a strong reduction of volumes should be obtained by interaction of hydrogen with solid materials, in particular applying knowledge in gas–solid heterogeneous process and exploiting recent advances of the material science applied to physical and chemical adsorption.

The US Department of Energy (DOE) has established a series of targets which should be met by hydrogen storage tanks, including those related to overall system performance [110]. Both volumetric and gravimetric storage system performances are considered basically crucial; the relative target for the year 2010 is fixed in 1.5 kWh/l and 2 kWh/kg as regarding system volumetric and gravimetric capacity, respectively. These targets imply for the hydrogen storing material volumetric density values of at least 45 g/l and gravimetric density not lower than 6 wt%. The following sections contain an overview on hydrogen storage in molecular form (compressed gas and liquid) and some details about the main technological improvements related to the storage by absorption or adsorption processes.

2.3.1 Hydrogen Storage in High Compressed Gas Form

The compression in cylinders with a maximum pressure of 200 bar is a reliable well-established technology, today widely used for hydrogen and natural gas storage. Higher pressures permit the volumetric capability to be improved but not negligible power consumption has to be taken into account when high compression ratios are reached.

The ideal compression (in isothermal conditions) work can be calculated according to the following equation:

$$L = \Delta G = RTZ \ln \frac{p}{p^0} \tag{2.28}$$

where ΔG is the Gibbs free energy variation (corresponding to the ideal useful work L), R is the gas constant, T the Kelvin temperature, Z the compressibility factor and p/p^0 the ratio between the final and initial pressure value. Z factor is approximately 1 in the range 1–100 bar, when the hydrogen behaviour can be approximately assumed as ideal, while at high pressures the density of H_2 affects its compressibility and Z significantly increases in dependence of critical parameters of temperature and pressure.

It can be derived that for $p/p^0 = 700$ an energy loss due to ideal compression results about 2.2 kWh/kg, but in a real compression stage the energy losses are significantly higher because of the irreversibilities that also determine non-isothermal operation. Pressure increments could affect in a not negligible way the impact of the hydrogen compression step on the well-to-wheel efficiency evaluation for hydrogen fuel cell vehicles [111], the energy consumption at 700 bar is about 10% of the H_2 LHV [112]. Additionally, the heat produced during the compression stage gradually reduces the gas density, limiting the positive impact of compression on energy density of the tank.

Dynamic compressors, commercially used for natural gas compression, could be used in case of moderately high compression (p/p^0 up to 200–300), while alternative volumetric devices are necessary for higher pressure ratios. With respect to

methane the hydrogen compression introduces some specific difficulties, related to the different volumetric energy densities and to the choice of dedicated fixings [107]. On the other hand, at higher pressures the gravimetric density of the tank progressively decreases because of the increasing thickness of cylinder walls.

Austenitic stainless steel or aluminium alloys are widely used for 200 bar cylinders but recent advances in lightweight composite cylinders have permitted hydrogen storage systems reliable up to 700 bar to be developed. Composite materials are constituted by high-strength fibres, mainly carbon-based that are wrapped around the cylinders in layers. Several types of advanced high-pressure cylinders could be designed to improve volumetric and gravimetric density in dependence of the weight ratio between metal and composite: from a whole metal to a plastic liner or a fully wound composite overwrap, passing by different percentages of metal liner and composite overwrap.

In order to match the safety issues, future pressure vessels include three layers: an inner polymer liner, overwrapped with a high-strength and high-elasticity carbon fiber composite, and an outer layer of an aramid-material capable of withstanding mechanical and corrosion damage [107].

Recent approaches aimed at improving the unsatisfactory gravimetric and volumetric capacities are based on compressed cryogenic technique [110]. In particular by cooling a tank to nitrogen liquefaction temperature (77 K) the volumetric capacity results three times higher with respect to conventional high pressure tank.

2.3.2 Hydrogen Storage in Liquid Cryogenic Form

The liquid cryogenic technology might represent a valid alternative to high-pressure gas storage approach [113]. It can be used to increase significantly (see Table 2.2) the unsatisfactory volumetric density values of hydrogen stored as gaseous compound. At a very high pressure (700 bar), the gravimetric density of hydrogen in gaseous form does not reach 40 kg/m^3, while as liquid it reaches about 70 kg/m^3. However, some technical aspects need to be considered for an overall analysis of this technology.

The Linde cycle is a simple cryogenic process based on Joule–Thompson effect. It is composed of different steps: the gas is first compressed, then preliminarily cooled in a heat exchanger using liquid nitrogen, finally it passes through a lamination throttle valve to exploit the benefits of Joule–Thomson expansion. Some liquid is produced, and the vapour is separated from the liquid phase and returns back to the compressor through the heat exchanger. A simplified scheme of the overall process is reported in Fig. 2.9.

The process is rather expensive because of high electricity costs for compression and the low Joule–Thomson inversion temperature of hydrogen (203 K), that involves high energy consumption necessary to maintain the hydrogen continuously cooled (about 30% of its LHV) [114].

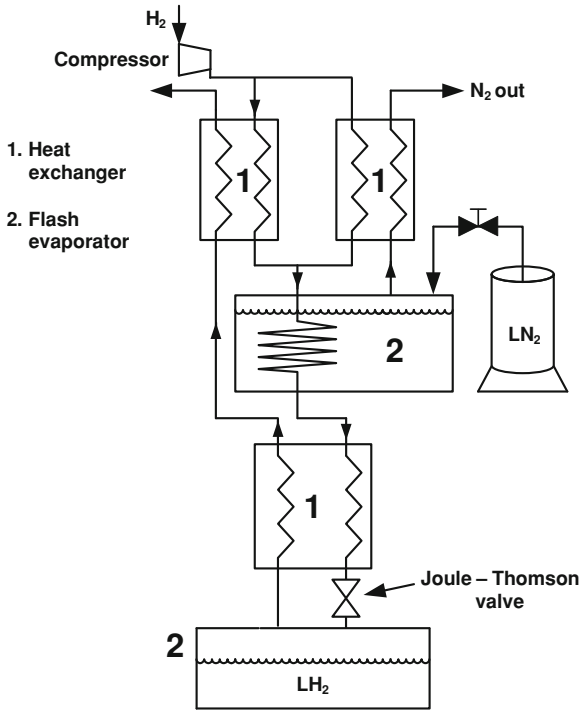

Fig. 2.9 H_2 liquefier block diagram (Linde cycle)

Furthermore, the boil-off effects must be considered because of the liquefaction temperatures (21 K). A very low external thermal exchange fluctuation could produce appreciable vaporization. The font of these variations could be originated by the exothermic transformation of electronic configuration of hydrogen molecule from *ortho* to *para* [107], by the thermal irreversibility of fluid compression, or by the different heat exchange mechanisms with outside. This problem is emphasized for tanks of small size (100 l, typical value for cars), because heat leaks are proportional to the surface to volume ratio, and the high initial density could significantly decrease during the time.

The materials used in the different size vessels are based on stainless steel or aluminium alloys, but also on polymeric materials, such as Teflon. The sphere form is ideal for the minimization of vapour release, due to its minimum surface to volume ratio with respect to all other possible geometries, and for the limitation of stress and uniformity of strain distribution. On the other hand, the manufacturing costs for spheres are too high, in compared with cylindrical shape which is the most economical solution.

Recently, a new liquefaction approach based on the magnetocaloric effect has been proposed [115]. The method is based on the characteristics of some magnetic materials that heat up when placed in a magnetic field and cool down when removed from it. The magnetic refrigeration can develop its potentialities in terms of overall efficiency for liquefaction process, as it is theoretically able to exploit

almost completely (up to 90%) the efficiency of the Carnot cycle, which represents the reference cycle for the cooling process. However, the practical feasibility of an integrated plant based on this method is far to be experimentally verified.

2.3.3 Hydrogen Storage in Solid Materials

Hydrogen storage devices based on high pressure gas and cryogenic liquid technologies do not reach the storage performance of conventional transportation liquid fuels. On the other hand, they suffer also of important safety issues related to the utilization of severe operative conditions necessary to improve, even if only partially, the very low gravimetric and volumetric energy densities typical of hydrogen molecules. An interesting alternative is the storage of hydrogen based on the principle of forming hydrogen containing carriers from which the fuel can be extracted when necessary. Then the idea is to develop materials able to soak up and release hydrogen, thank to absorption and/or adsorption processes [116].

Metal hydrides are 'hydrogen atom'-carriers usable as storage system [107, 110, 116, 117]. The method is based on specific properties of some metals that readily absorb gaseous hydrogen, thanks to their capability to accept hydrogen atoms, derived by its molecule splitting, inside their interstitial sites in reasonable operative conditions.

The *absorption* process is a reaction of hydrogen gas with a metal, and results moderately exothermic. Then during the charging phase, which occurs typically at 30–60 bar, some heat needs to be removed, while during discharging phase slight changes in operative conditions (temperature and pressure) permit the quantitative amounts of gaseous hydrogen molecules previously charged to be released, according to:

$$M + x/2H_2 \leftrightarrows MH_x \tag{2.29}$$

where M indicates the metal used for hydrogen storage.

A schematic hydrogen absorption mechanism consists in the following three steps:

1. mass transport of gas molecules to the solid surface
2. physical adsorption with successive molecule dissociation
3. transition of hydrogen atoms to the metal bulk with formation of new solid phases.

During the third step, at a specified temperature value, the metals bind hydrogen (previously dissociated as atoms in the adsorption step) producing an intermediate solid solution [107, 118]. Increasing the pressure the interaction between hydrogen atoms and metal framework sites becomes stronger, nucleation and growth steps start bringing to the formation of a hydride solution. The concentration limits relative to the formation of the two above solutions (intermediate and hydride)

change with temperature, typically the concentration difference decreases when temperature increases, and becomes zero when the critical point is reached. Until the two solid phases coexist the temperature remains practically constant, and the hydrogen concentration increases inside the intra-metallic mixture, evidencing that the hydrogen amount is reversibly stored at the fixed temperature with slight pressure variations. Finally, the intermediate solution disappears and all hydrogen atoms are entangled in the hydride solid solution. Further hydrogen absorption could occur when the hydrogen concentration increases up to the maximum value compatible with the atom insertion inside the voids of the metal framework.

The strong interest towards metal hydrides is strictly related to the potential of significantly increasing the volumetric density of hydrogen packing (up to 0.2 kg/m^3) that largely exceeds the density of liquid hydrogen (about 0.07 kg/m^3). The operative temperature and pressure of the absorption process depend on the type of hydride, and are the key parameters affecting the efficiency of a hydrogen storage device for automotive application.

The different metal hydrides can be classified in two main categories:

1. Low desorption temperature.
2. High desorption temperature.

The first class is characterized by those metals and metal alloys (iron, titanium and nickel) which require only a small amount of heat to release hydrogen. This heat might be easily withdrawn by the process fluids of a fuel cell powertrain. On the other hand, some hydrogen can be released also at room temperature, but this problem could be overcome by preliminary tank pressurizing, followed by a gradual pressure diminution when hydrogen content within the hydride decreases.

Beside the basic advantages of high volumetric density and low energy inputs, this class of hydrogen storage materials is attractive also for the operational safety. Unfortunately the gravimetric energy density does not reach the targets useful for road vehicle application, essentially because of the high molar mass of metal framework.

The second class includes other hydrides based on light elements, such as alkali and alkaline-earth metals, first of all the metal alloys of magnesium [107, 117–121]. These materials are very interesting because of their acceptable gravimetric hydrogen storage capability, but their poor kinetic properties at moderate temperature strongly limit the practical application. In particular MgH could contain theoretically hydrogen up to about 8% in MgH form, but absorption and desorption processes occur only at elevated temperatures (>200°C), and then require large amount of heat to release hydrogen. The catalytic role of different additional materials such as metal oxides or transition metals has been extensively investigated in magnesium alloys to reduce release temperature and improve kinetics [122, 123], but the results do not evidence significant improvements of their performance.

Recently, metal-doped aluminium hydrides have been proposed as further potential hydrogen storage materials [107, 123]. Among lightweight metal hydrides the lithium and sodium alanates ($NaAlH_4$, $LiAlH_4$) have been widely

studied for their characteristics of high hydrogen content and low release temperatures [124–126]. Reversibility and kinetic of the hydrogen absorption/desorption cycle are critical issues also for this class of compounds. $NaAlH_4$ hydride can provide 5.5 wt% of hydrogen under reasonable conditions, by a decomposition reaction made reversible thank to the usage of a catalyst [127], while lithium alanate utilization appears not possible because of the irreversibility of the first decomposition step.

Other solid materials are able to storage H_2 storage thanks to the *adsorption* method. The process may be physical or chemical, in dependence of the energetics of the adsorption mechanism. Physisorbed hydrogen is weakly bound to the solid surface because of the 'attraction' between the adsorbate (hydrogen) and the adsorbent (solid material); this is due to the induced dipole moment of a non-polar adsorbate interacting with its own image charge in the polarizable solid. On the other hand, chemisorbed hydrogen is strongly 'attached' to the material active sites as result of a chemical bond formation between the adsorbent and the adsorbate in a monolayer on the surface. Both the processes can occur especially on porous materials as they require high surface area to maximize the available sites for hydrogen uptake, while molecular affinity is a key parameter which determines the selectivity of the material towards a particular molecule, especially for chemical adsorption.

In the last decade high storage capacities have been claimed for carbon nanostructures, theoretically able to match the automotive targets by means of adsorption [107, 109]. Activated carbon has been first proposed and has shown promising storage capability of about half of liquid, at 50 bar, but exclusively at 77 K [128]. Other types of carbon materials based on nanostructured frameworks have been then selected and proposed. In particular, the narrow pore size distribution of single-walled carbon nanotubes (SWNTs) makes them attractive candidates as adsorbents for hydrogen molecules [129, 130], but the early promising experimental results have been the object of controversy [131, 132].

On the other hand, also carbon nanofibers based on stacked graphite layers seem show appreciable gravimetric storage capacity at room temperature and at moderate pressure (about 120 bar) [133], but other experimental results obtained on similar nano-materials appear contradictory [134], and the hydrogen storage mechanism is still far to be understood.

Zeolites, which are a well-known class of molecular sieves and have been proposed in the past for several industrial applications (ion exchange, adsorption, heterogeneous catalysis), are also investigated, but their storage capacity remains not satisfactory also at 77 K [135].

A recent scientific interest has been addressed towards a new class of structured nanoporous materials, constituted by metal organic frameworks (MOFs), whose potentialities are related to their low bulk density and very high specific area, ranging from 1000 to 6000 m^2/g [136]. They are synthesized by linking inorganic clusters with various organic linkers [137], through strong bonds. The interest towards MOF compounds is related to the theoretical possibility to optimize the hydrogen storage exploiting both selective binding energy and high specific area

effects. Several MOF have shown promising results at 77 K with adsorption capacities up to 7.3%, while at room temperature hydrogen uptakes is still not higher than 1% [138, 139].

Recent strategies for improving carbon nanostructures performance based on the spillover mechanism have been investigated. Hydrogen spillover uses a supported metallic catalyst able to dissociate the hydrogen molecule. During the successive phase of the process hydrogen atoms migrate to the substrate and finally permeate through the substrate surfaces and/or into the bulk materials [140]. Thanks to this technique, an appreciable higher storage capability at room temperature (up to about 2.4%) has been obtained by some authors for different types of materials [141].

Chemical hydrogen storage could represent another interesting alternative approach. It consists of on-board hydrogen generation through a chemical reaction which starts from a hydrogen-containing material, characterized by high gravimetric energy density, followed by final off-board regeneration. The storage material needs to be produced, and usually involves hydrolysis reaction. Specific chemical hydrides are used, such as sodium borohydride ($NaBH_4$) [142]. The following chemical equation describes the process occurring in aqueous solution:

$$NaBH_4 + 2H_2O \rightarrow NaBO_2 + 4H_2 \tag{2.30}$$

Equation 2.30 is irreversible, moderately exothermic, and can be controlled in the presence of a suitable catalyst. When used on-board of vehicle the residual compounds must be removed and regenerated off-board. This technique could represent an applicative approach especially if liquids are used to store hydrogen, but results too expensive and limited by very high regeneration energy requirements [143]. Recently, the Los Alamos laboratories have proposed a new process able to improve the efficiency of the regeneration phase by addition of appropriate digesting and reducing agents to the spent fuel [144].

References

1. Mcdowall W, Eames M (2006) Forecast, scenarios, visions, backcasts and roadmaps to the hydrogen economy: a review of the hydrogen future literature. Energy Policy 34:1236–1250
2. Hetland J, Mulder G (2007) In search of a sustainable hydrogen economy: how a large-scale transition to hydrogen may affect the primary energy demand and greenhouse gas emissions. Int J Hydrogen Energ 32:736–747
3. Ball M, Wietschel M (2009) The future of hydrogen—opportunities and challenges. Int J Hydrogen Energ 34:615–627
4. Holladay JD, Hu J, King DL, Wang Y (2009) An overview of hydrogen production technologies. Catal Today 139(4):244–260
5. Chorkendorff I, Niemantsverdriet JW (2003) Heterogeneous catalysis in practice: hydrogen. In: Concepts of modern catalysis and kinetics. Wiley-VCH Verlag GmbH & Co, Weinheim
6. Rostrup-Nielsen T (2005) Manufacture of hydrogen. Catal Today 106:293–296
7. Armor JN (1999) The multiple role for catalysis in the production of H_2. Appl Catal A 176:159–176

8. Farrauto RJ (2005) Introduction to solid polymer membrane fuel cells and reforming natural gas for production of hydrogen. Appl Catal B 56:3–7
9. Trimm DL (1991) Thermal stability of catalyst supports. In: Bartholomew CH, Butt JB (eds) Catalyst deactivation. Elsevier, Amsterdam, p 29
10. Gitzen WH (1970) Alumina as a ceramic material. American Ceramic Society, Columbus
11. Rostrup-Nielsen DJR (1974) Coking on Ni catalysts for steam reforming of hydrocarbons. J Catal 33:184–201
12. Trimm DL (1999) Catalysts for the control of coking during steam reforming. Catal Today 49:3–10
13. Rostrup-Nielsen J, Dybkjaer I, Christiansen LJ (1993) Steam reforming opportunities and limits of the technology. In: de Lasa HI, Dogu G, Ravella A (eds) Chemical reactor technology for environmentally safe reactors and products. Kluwer, Dordrecht, p 249
14. Kikuchi E (2000) Membrane reactor application to hydrogen production. Catal Today 56:97–101
15. Barelli L, Bidini G, Gallorini F, Servilli S (2008) Hydrogen production through sorption-enhanced steam methane reforming and membrane technology: a review. Energy J 33:554–570
16. Brejc H, Supp E (1993) Partial oxidation of hydrocarbons. In: Elvers B, Hawkins S, Ravenscroft M, Rounsaville JF, Schulz G (eds) Ullmann's encyclopedia of industrial chemistry, vol A12. VCH, New York, pp 207–243
17. Silberova B, Venvik HJ, Walmsley JC, Holmen A (2005) Small-scale hydrogen production from propane. Catal Today 100(3–4):457–462
18. Tsang SC, Claridge JB, Green MLH (1995) Recent advances in the conversion of methane to synthesis gas. Catal Today 23(1):3–15
19. Wang HY, Ruckenstein (1999) Catalytic partial oxidation of methane to synthesis gas over g-Al_2O_3-supported rhodium catalysts. Catal Lett 59:121–127
20. Koh ACW, Chen L, Leong WK, Johnson BFG, Khimyak T, Lin J (2007) Hydrogen or synthesis gas production via the partial oxidation of methane over supported nickel-cobalt catalysts. Int J Hydrogen Energ 32(6):725–730
21. Lanza R, Jaras SG, Canu P (2007) Partial oxidation of methane over supported ruthenium catalysts. Appl Catal A-Gen 325(1):57–67
22. Pavlova SN, Sazonova NN, Ivanova JA, Sadykov VA, Snegurenko OI, Rogov VA, Zolotarskii IA, Moroz EM (2004) Partial oxidation of methane to synthesis gas over supported catalysts based on Pt-promoted mixed oxides. Catal Today 91–92:299–303
23. De Groote AM, Froment GF (1997) The role of coke formation in catalytic partial oxidation for synthesis gas production. Catal Today 37:309–329
24. Enger BC, Lodeng R, Holmen A (2008) A review of catalytic partial oxidation of methane to synthesis gas with emphasis on reaction mechanism over transition metal catalysts. Appl Catal A 346:1–27
25. Zhang J, Wang Y, Ma R, Wu D (2003) Characterization of alumina-supported Ni and Ni-Pd catalysts for partial oxidation and steam reforming of hydrocarbons. Appl Catal A-Gen 243(2):251–259
26. Kikuchi R, Iwasa Y, Takeguchi T, Eguchi K (2005) Partial oxidation of CH_4 and C_3H_8 over hexaaluminate-type oxides. Appl Catal A-Gen 281(1–2):61–67
27. Corbo P, Migliardini F (2007) Hydrogen production by catalytic partial oxidation of methane and propane on Ni and Pt catalysts. Int J Hydrogen Energ 32:55–66
28. Schulze K, Makoswski W, Chyzy R, Dziembaj R, Geismar G (2001) Nickel doped hydrotalcites as catalyst precursors for the partial oxidation of light paraffins. Appl Clay Sci 18:59–69
29. Liu S, Xu L, Xie S, Wang Q, Xiong G (2001) Partial oxidation of propane to syngas over nickel supported catalysts modified by alkali metal oxides and rare-earth metal oxides. Appl Catal A-Gen 211:145–152
30. Beretta A, Forzatti P (2004) Partial oxidation of light paraffins to synthesis gas in short contact-time reactors. Chem Eng J 99:219–226

31. Caglayan BS, Onsan ZI, Aksoylu AE (2005) Production of hydrogen over bimetallic Pt–Ni/δ-Al_2O_3: II. Indirect partial oxidation of LPG. Catal Lett 102(1-2):63–67
32. Otsuka K, Sunada YWE, Yamanaka I (1998) Direct partial oxidation of methane to synthesis gas by cerium oxide. J Catal 175:152–160
33. Passos FB, de Oliveira ER, Mattos LV, Noronha FB (2005) Partial oxidation of methane to synthesis gas on Pt/$Ce_xZr_{1-x}O_2$ catalysts: the effect of the support reducibility and of the metal dispersion on the stability of the catalysts. Catal Today 101:23–30
34. Muradov N (2001) Hydrogen via methane decomposition: an application for decarbonization of fossil fuels. Int J Hydrogen Energ 26:1165–1175
35. Ahmed S, Aitani A, Rahman F, Ali Al-Dawood, Al-Muhaish F (2009) Decomposition of hydrocarbons to hydrogen and carbon. Appl Catal A-Gen 359:1–24
36. Aiello R, Fiscus JE, Loye HC, Amiridis MD (2000) Hydrogen production via the direct cracking of methane over Ni/SiO_2: catalyst deactivation and regeneration. Appl Catal A-Gen 192:227–234
37. Choundary TV, Sivadinarayana C, Chusuei CC, Klinghoffer A, Goodman DW (2001) Hydrogen production via catalytic decomposition of methane. J Catal 199:9–18
38. Suelves I, Lazaro MJ, Moliner R, Corbella BM, Palacios JM (2005) Hydrogen production by thermo catalytic decomposition of methane on Ni-based catalysts: influence of operating conditions on catalyst deactivation and carbon characteristics. Int J Hydrogen Energ 30:1555–1567
39. Konieczny A, Mondal K, Wiltowski T, Dydo P (2008) Catalyst development for thermocatalytic decomposition of methane to hydrogen. Int J Hydrogen Energ 33:264–272
40. Li J, Smith KJ (2008) Methane decomposition and catalyst regeneration in a cyclic mode over supported Co and Ni catalysts. Appl Catal A-Gen 349:116–124
41. Muradov N (2001) Catalysis of methane decomposition over elemental carbon. Catal Commun 2:89–94
42. Pinilla JL, Suelves I, Lazaro MJ, Moliner R (2008) Kinetic study of the thermal decomposition of methane decomposition of methane using carbonaceous catalysts. Chem Eng J 138:301–306
43. Serrano DP, Botas JA, Guil-Lopez R (2009) H_2 production from methane pyrolysis over commercial carbon catalysts: kinetic and deactivation study. Int J Hydrogen Energ 34:4488–4494
44. Lee KK, Han GY, Yoon KJ, Lee BK (2004) Thermocatalytic hydrogen production from the methane in a fluidized bed with activated carbon catalyst. Catal Today 93–95:81–86
45. Pinilla JL, Moliner R, Suelves I, Lázaro MJ, Echegoyen Y, Palacios JM (2007) Production of hydrogen and carbon nanofibers by thermal decomposition of methane using metal catalysts in a fluidized bed reactor. Int J Hydrogen Energ 32:4821–4829
46. Weizhong Q, Tang L, Zhanwen W, Fei W, Zhifei L, Guohua L, Yongdan L (2004) Production of hydrogen and carbon nanotubes from methane decomposition in a two-stage fluidized bed reactor. Appl Catal A-Gen 260:223–228
47. Muradov N, Smith F, Huang C, Raissi AT (2006) Autothermal catalytic pyrolysis of methane as a new route to hydrogen production with reduced CO_2 emissions. Catal Today 116:281–288
48. Fulcheri L, Schwob Y (1995) From methane to hydrogen, carbon black and water. Int J Hydrogen Energ 20:197–202
49. Fridman A (2008) Plasma chemistry. Cambridge University Press, Cambridge
50. Tsai CH, Chen KT (2009) Production of hydrogen and nano carbon powders from direct plasmolysis of methane. Int J Hydrogen Energ 34:833–838
51. Muradov N, Smith F, Bockerman G, Scammon K (2009) Thermocatalytic decomposition of natural gas over plasma-generated carbon aerosols for sustainable production of hydrogen and carbon. Appl Catal A-Gen 365:292–300
52. Figueiredo JL, Moulijn JA (1985) Carbon and coal gasification science and technology. In: Proceedings of the NATO advanced study institute on carbon and coal gasification. Science and Technology Series: NATO Science Series E, vol 105, p 672

53. Rostrup-Nielsen JR (2000) New aspects of syngas production and use. Catal Today 63:159–164
54. Stiegel GJ, Ramezan M (2006) Hydrogen from coal gasification: an economical pathway to a sustainable energy future. Int J Coal Geol 65:173–190
55. Joshi MM, Lee S (1996) Integrated gasification combined cycle—a review of IGCC technology. Energy Source 18:537–568
56. Damen K, van Troost M, Faaij A, Turkenburg W (2006) A comparison of electricity and hydrogen production systems with CO_2 capture and storage. Part A: review and selection of promising conversion and capture technologies. Prog Energy Combust 32:215–246
57. Cormos CC, Starr F, Tzimas E, Peteves S (2008) Innovative concepts for hydrogen production processes based on coal gasification with CO2 capture. Int J Hydrogen Energ 33:1286–1294
58. Bohm MC, Herzog HJ, Parsons JE, Sekar RC (2007) Capture-ready coal plants—options, technologies and economics. Int J Greenh Gas Control 1:113–120
59. Galvita V, Messerla VE, Urtimenko AB (2007) Hydrogen production by coal plasma gasification for fuel cell technology. Int J Hydrogen Energ 32:3899–3906
60. Saxena RC, Seal D, Kumar S, Goyal HB (2008) Thermo-chemical routes for hydrogen rich gas from biomass: a review. Renew Sust Energy Rev 12:1909–1927
61. Orecchini F, Bucci E (2007) Biomass to hydrogen for the realization of closed cycles of energy resources. Energy J 32:1006–1011
62. Florin N, Harris A (2007) Hydrogen production from biomass. Environmentalist 27:207–215
63. Koroneos C, Dompros A, Roumbas G (2008) Hydrogen production via biomass gasification—a life cycle assessment approach. Chem Eng Process 47:1261–1268
64. Devi L, Ptasinski KJ, Janssen FJJG (2003) A review of the primary measures for tar elimination in biomass gasification processes. Biomass Bioenerg 24:125–140
65. Bangala DN, Abatzoglou N, Martin JP, Chornet E (1997) Catalytic gas conditioning: application to biomass and waste gasification. Ind Eng Chem Res 36:4184–4192
66. Koros W, Mahajan R (2000) Pushing the limits on possibilities for large scale gas separation: which strategies? J Membr Sci 175:181–196
67. Abanades S, Charvin P, Flamant G, Neveu P (2006) Screening of water-splitting thermochemical cycles potentially attractive for hydrogen production by concentrated solar energy. Energy J 31:2805–2822
68. Lattin WC, Utgikar VP (2009) Global warming potential of the sulfur-iodine process using life cycle assessment methodology. Int J Hydrogen Energ 34:737–744
69. Orhan MF, Dincer I, Rosen MA (2008) Energy and exergy assessments of the hydrogen production step of a copper–chlorine thermochemical water splitting cycle driven by nuclear-based heat. Int J Hydrogen Energ 33:6456–6466
70. Engelhardt V (1904) The electrolysis of water; processes and applications. Chemical Publishing Company, Easton
71. Pletcher D, Walsh FC (1990) Industrial electrochemistry, 2nd edn. Kluwer, Dordrecht, London, p 256
72. Rosen MA, Scott D (1998) Comparative efficiency assessments for a range of hydrogen production processes. Int J Hydrogen Energ 23:653–659
73. Hall DE (1981) Electrodes for alkaline water electrolysis. J Electrochem Soc 128:740
74. Dyer CK (1985) Improved nickel anodes for industrial water electrolyzers. J Electrochem Soc 132:64
75. Rami A, Lasia A (1992) Kinetics of hydrogen evolution on Ni-Al alloy electrodes. J Appl Electrochem 22:376–382
76. Barbir F (2005) PEM electrolysis for production of hydrogen from renewable energy sources. Sol Energy 78:661–669
77. Sherif SA, Barbir F, Veziroglu TN (2005) Wind energy and the hydrogen economy—review of the technology. Sol Energy 78:647–660
78. Schiller G, Ansar A, Lang M, Patz O (2009) High temperature water electrolysis using metal supported solid oxide electrolyser cells (SOEC). J Appl Electrochem 39:293–301

79. Millet P, Andolfatto F, Durand R (1996) Design and performance of a solid polymer electrolyte water electrolyzer. Int J Hydrogen Energ 21:87–93
80. Marshall A, Borresen B, Hagen G, Tsypkin M, Tunold R (2007) Hydrogen production by advanced proton exchange membrane (PEM) water electrolysers—reduced energy consumption by improved electrocatalysis. Energy J 32:431–436
81. Grigoriev SA, Porembsky VI, Fateev VN (2006) Pure hydrogen production by PEM electrolysis for hydrogen energy. Int J Hydrogen Energ 31:171–175
82. Onda K, Kyakuno T, Hattori K, Ito K (2004) Prediction of production power for high-pressure water electrolysis. J Power Sources 132:64–70
83. Marangio F, Santarelli M, Calì M (2009) Theoretical model and experimental analysis of a high pressure PEM water electrolyser for hydrogen production. Int J Hydrogen Energ 34:1143–1158
84. Grigoriev SA, Millet P, Fateev VN (2008) Evaluation of carbon-supported Pt and Pd nanoparticles for the hydrogen evolution reaction in PEM water electrolysers. J Power Sources 177:281–285
85. Granovskii M, Dincer I, Rosen MA (2006) Life cycle assessment of hydrogen fuel cell and gasoline vehicles. Int J Hydrogen Energ 31:337–352
86. Jorgensen C, Ropenus S (2008) Production price of hydrogen from grid connected electrolysis in a power market with high wind penetration. Int J Hydrogen Energ 33:5335–5344
87. Mingyi L, Bo Y, Jingming X, Jing C (2008) Thermodynamic analysis of the efficiency of high-temperature steam electrolysis system for hydrogen production. J Power Sources 177:493–499
88. Ni M, Leung MKH, Leung DYC (2008) Technological development of hydrogen production by solid oxide electrolyser cell (SOEC). Int J Hydrogen Energ 33:2337–2354
89. Fujiwara S, Kasai S, Yamauchi H, Yamada K, Makino S, Matsunaga K, Yoshino M, Kameda T, Ogawa T, Momma S, Hoashi E (2008) Hydrogen production by high temperature electrolysis with nuclear reactor. Prog Nucl Energy 50:422–426
90. Coughlin RW, Farooque M (1980) Consideration of electrodes and electrolytes for electrochemical gasification of coal by anodic oxidation. J Appl Electrochem 10:729–740
91. Sathe N, Botte GG (2006) Assessment of coal and graphite electrolysis on carbon fiber electrodes. J Power Sources 161:513–523
92. Jin X, Botte GG (2007) Feasibility of hydrogen production from coal electrolysis at intermediate temperatures. J Power Sources 171:826–834
93. Fujishima A, Honda K (1972) Electrochemical photolysis of water at a semiconductor electrode. Nature 238:37–38
94. Penner SS (2006) Steps toward the hydrogen economy. Energy J 31:33–43
95. Bak T, Nowotny J, Rekas M, Sorrell CC (2002) Photo-electrochemical hydrogen generation from water using solar energy. Materials-related aspects. Int J Hydrogen Energ 27:991–1022
96. Ni M, Leung MKH, Leung DHC, Sumathy K (2007) A review and recent developments in photocatalytic water-splitting using TiO2 for hydrogen production. Renew Sust Energy Rev 11:401–425
97. Kelly NA, Gibson TL (2008) Solar energy concentrating reactors for hydrogen production by photoelectrochemical water splitting. Int J Hydrogen Energ 33:6420–6431
98. Burgess G, Velasco JGF (2007) Materials, operational energy inputs, and net energy ratio for photobiological hydrogen production. Int J Hydrogen Energ 32:1225–1234
99. Kapdan IK, Kargi F (2006) Bio-hydrogen production from waste materials. Enzyme Microb Technol 38:569–582
100. Moore RB, Raman V (1998) Hydrogen infrastructure for fuel cell transportation. Int J Hydrogen Energ 23:617–620
101. Haeseldonckx D, D'haeseleer W (2007) The use of the natural-gas pipeline infrastructure for hydrogen transport in a changing market structure. Int J Hydrogen Energ 32:1381–1386
102. Padro C, Putsche V (1999) Survey of the economics of hydrogen technologies. DOE National Renewable Energy Laboratory Report no. NREL/TP-570-27079, September

103. Siddiqui RA, Abdullah HA (2005) Hydrogen embrittlement in 0.31% carbon steel used for petrochemical applications. J Mater Process Technol 170:430–435
104. Markert F, Nielsen SK, Paulsen JL, Andersen V (2007) Safety aspects of future infrastructure scenarios with hydrogen refuelling stations. Int J Hydrogen Energ 32:2227–2234
105. Hugo A, Rutter P, Pistikopoulos S, Amorelli A, Zoia G (2005) Hydrogen infrastructure strategic planning using multi-objective optimization. Int J Hydrogen Energ 30:1523–1534
106. Leung WB, March NH, Motz H (1976) Primitive phase diagram for hydrogen. Phys Lett A 56:425–426
107. Zuttel A (2008) Hydrogen storage. In: Zuttel A, Borgschulte A, Schlapbach L (eds) Hydrogen as a future energy carrier. Wiley-VCH Verlag GmbH & Co, Weinheim
108. Zhou L (2005) Progress and problems in hydrogen storage methods. Renew Sust Energy Rev 9:395–408
109. David E (2005) An overview of advanced materials for hydrogen storage. J Mater Process Technol 162–163:169–177
110. Satypal S, Petrovic J, Read C, Thomas G, Ordaz G (2007) The U.S. Department of Energy's National Hydrogen Storage Project: progress towards meeting hydrogen-powered vehicle requirements. Catal Today 120:246–256
111. de Wit MP, Faaij PC (2007) Impact of hydrogen onboard storage technologies on the performance of hydrogen fuelled vehicles: a techno-economic well to wheel assessment. Int J Hydrogen Energ 32:4859–4870
112. Aceves SM, Berry GD, Martinez-Frias J, Espinoza-Loza F (2006) Vehicular storage of hydrogen in insulated pressure vessels. Int J Hydrogen Energ 31:2274–2283
113. Peschka W (1992) Liquid hydrogen, fuel of the future. Springer, Wien
114. Berstad DO, Stang JH, Neksa P (2009) Comparison criteria for large-scale hydrogen liquefaction processes. Int J Hydrogen Energ 34:1560–1568
115. Sherif SA, Barbir F, Veziroglu TN (2005) Towards a hydrogen economy. Electr J 18:62–76
116. Ross DK (2006) Hydrogen storage: the major technological barrier to the development of hydrogen fuel cell cars. Vacuum 80:1084–1089
117. Sandrock G (1999) A panoramic overview of hydrogen storage alloys from a gas reaction point of view. J Alloy Compd 293–295:877–888
118. Suda S (2008) Hydrogen–metal systems: technological and engineering aspects. Encyclopedia of Materials: Sci Tech 4:3970–3976
119. Yvon K, Bertheville B (2006) Magnesium based ternary metal hydrides containing alkali and alkaline-earth elements. J Alloy Compd 425:101–108
120. Ouyang LZ, Qin FX, Zhu M (2006) The hydrogen storage behavior of Mg_3La and $Mg_3LaNi_{0.1}$. Scripta Mater 55:1075–1078
121. Andreasen A (2008) Hydrogenation properties of Mg-Al alloys. Int J Hydrogen Energ 33:7489–7497
122. Jung KS, Lee EY, Lee KS (2006) Catalytic effects of metal oxide on hydrogen absorption of magnesium metal hydride. J Alloy Compd 421:179–184
123. Sakintuna B, Lamari–Darkrim F, Hirscher M (2007) Metal hydride materials for solid hydrogen storage: a review. Int J Hydrogen Energ 32:1121–1140
124. Hauback BC (2008) Metal hydrides: properties and applications of alanates. Encyclopedia of Materials: Sci Tech 1–5
125. Bogdanovic B, Brand RA, Marjanovic A, Schwikardi M (2000) Metal-doped sodium aluminium hydrides as potential new hydrogen storage materials. JAlloy Compd 302:36–58
126. Corbo P, Migliardini F, Veneri O (2009) Hydrogen release properties of lithium alanate for application to fuel cell propulsion systems. J Power Sources 193:285–291
127. Onkawa M, Zhang S, Takeshita HT, Kuriyama N, Kiyobayashi T (2008) Dehydrogenation kinetics of Ti-doped NaAlH4—influence of Ti precursors and preparation methods. Int J Hydrogen Energ 33:718–721
128. Dillon AC, Heben MJ (2001) Hydrogen storage using carbon adsorbents: past, present and future. Appl Phys A 72:133–142

129. Dillon AC, Jones KM, Bekkedahl TA, Kang CH, Bethune DS, Heben MJ (1997) Storage of hydrogen in single-walled carbon nanotubes. Nature 386:377–379
130. Bethune DS (2002) Carbon and metals: a path to single-wall carbon nanotubes. Phys B- Phys Condens Matter 323:90–96
131. Bénard P, Chahine R (2007) Storage of hydrogen by physisorption on carbon and nanostructured materials. Scripta Mater 56:803–808
132. Züttel AA, Sudan P, Mauron PH, Kiyobayashi T, Emmenegger CH, Schlapbach L (2002) Hydrogen storage in carbon nanostructures. Int J Hydrogen Energ 27:203–212
133. Chambers A, Park C, Terry R, Baker K, Rodriguez NM (1998) Hydrogen storage in graphite nanofibers. J Phys Chem B 102:4253–4256
134. Orimo S, Zuttel A, Schalapbach L, Majer G, Fukunaga T, Fujii H (2003) Hydrogen interaction with carbon nanostructures: current situation and future prospects. J Alloy Compd 356–357:716–719
135. Dong J, Wang X, Xu H, Zhao Q, Li J (2007) Hydrogen storage in several microporous zeolites. Int J Hydrogen Energ 32:4998–5004
136. Hirscher M, Panella B (2007) Hydrogen storage in metal-organic frameworks. Scripta Mater 56:809–812
137. Yaghi OM, Li G, Li H (1995) Selective binding and removal of guests in a microporous metal-organic framework. Nature 378:703
138. Mulder FM, Dingemans TJ, Schimmel HG, Ramirez-Cuesta AJ, Kearley GJ (2008) Hydrogen adsorption strength and sites in the metal organic framework MOF5: comparing experiment and model calculations. Chem Phys 351:72–76
139. Latroche M, Surblé S, Serre C, Mellot-Draznieks C, Llewellyn PL, Lee JH, Chang JS, Jhung SH, Férey G (2006) hydrogen storage in the giant-pore metal-organic frameworks MIL-100 and MIL-101. Angew Chem Int Ed 45:8227–8231
140. Cheng H, Chen L, Cooper AC, Sha X, Pez GP (2008) Hydrogen spillover in the contest of hydrogen storage using solid-state materials. Energy Environ Sci 1:338–354
141. Yang RT, Li Y, Lachawiec AJ (2006) Hydrogen storage in graphite nanofibers and the spillover mechanism. DOE hydrogen program. Annual Progress Report. http://www.hydrogen.energy.gov/annual_progress06_storage.html#c. Accessed 12 February 2010
142. Kojima Y, Suzuki K, Fukumoto K, Sasaki M, Yamamoto T, Kawai Y, Hayashi H (2002) Hydrogen generation using sodium borohydride solution and metal catalyst coated on metal oxide. Int J Hydrogen Energ 27:1029–1034
143. Cakanyildirim C, Guru M (2008) Hydrogen cycle with sodium borohydride. Int J Hydrogen Energ 33:4634–4639
144. Davis BL, Dixon DA, Garner EB, Gordon JC, Matus MH, Scott B, Stephens FH (2009) Efficient regeneration of partially spent ammonia borane fuel. Angew Chem Int Ed 48(37):6812–6816

Chapter 3
Fuel Cells for Automotive Applications

According to the general definition of *galvanic cell*, any type of fuel cell can be regarded as a device able to produce DC electricity *directly* from chemicals. The same definition could also be applied to batteries during its discharging phase, but two substantial differences exist between batteries and fuel cells: (i) in a battery the chemicals providing the electron flow are contained into the same body of the device, putting a limit to its capacity (*specific energy* of the battery) while in a fuel cell they are continuously supplied from external sources, (ii) a battery is able to give back the DC electricity previously stored in it (during its operation as *electrolytic cell*, in the recharging phase), and produced elsewhere, while a fuel cell generates DC electricity by fuel electrochemical oxidation. When a rechargeable battery receives DC electricity, a chemical reaction is forced to occur, composed by two semi-reactions on each of the two electrodes, which are involved in the chemical transformation (*electrolysis*, see Sect. 2.1.2). The electricity stored as chemical energy into the new materials formed on electrodes is ready to be spontaneously released when an electric circuit is closed between the two terminals, with reinstatement of the original electrode materials. Differently, in a fuel cell the electrochemical oxidation of an external fuel takes place on electrodes which do not undergo chemical changes, in particular the fuel is oxidized at the anode, while the oxygen is reduced at the cathode, producing DC electricity, heat, and other chemical compounds, whose nature depends on the type of fuel oxidized at the anode. For applications in the transportation sector, electricity is considered the main product, while the chemicals produced and heat are byproducts (for stationary applications, such as co-generation plants, also heat has to be considered as prime product).

A more detailed description of different types of batteries and other electric energy storage systems for electric vehicles can be found in Sect. 5.3, while a description of the main characteristics and properties of fuel cells for automotive application is given here, starting from some basic concepts of electrochemistry and thermodynamic, and focusing the attention on the operative parameters to be regulated to obtain the best performance in the specific application.

P. Corbo et al., *Hydrogen Fuel Cells for Road Vehicles*,
Green Energy and Technology, DOI: 10.1007/978-0-85729-136-3_3,

3.1 Basic Concepts of Electrochemistry

The fundamental process by which a galvanic cell produces DC electricity starting from chemicals is an oxidation–reduction reaction (*redox reaction*), defined as a reaction in which the atoms of the species involved have their *oxidation state* changed. The oxidation state is described by the *oxidation number* of the atom in the given compound, and expresses the amount and the sign of the charge *ideally* assumed by the atom in the specie in question, after attribution of the pairs of electrons in each bond to the most electronegative atom in the molecule (some practical rules, compatible with this general principle, are used to calculate the oxidation number of a specific atom in a compound [1]). In a redox reaction an atom is oxidized when its oxidation number increases, whereas it is reduced when that number decreases. Regarding the reaction mechanism, the variation of the oxidation state can be realized by a transfer of either electrons or atoms, but in many cases both of them are observed. If a transfer of electrons is present, an oxidation corresponds to a loss of electrons, while a reduction implies a gain of electrons, and the overall redox reaction can be utilized in an electrochemical system, which can be regarded as an energy converter in which chemical energy is transformed into electric energy (galvanic cell) or vice versa (electrolytic cell).

In an electrochemical converter an overall redox reaction is divided into two semi-reactions which take place on physically separate electrodes, anode, and cathode, for oxidation and reduction semi-reactions, respectively. For a generic redox reaction, involving the species A and B in equilibrium, the overall reaction and two semi-reactions can be schematized as follows:

$$\text{Overall Redox} : A_{\text{red}} + B_{\text{ox}} \leftrightarrows A_{\text{ox}} + B_{\text{red}} \tag{3.1}$$

$$\text{Oxidation (anode)} : A_{\text{red}} \leftrightarrows A_{\text{ox}} + ne^{-} \tag{3.2}$$

$$\text{Reduction (cathode)} : B_{\text{ox}} + ne^{-} \leftrightarrows B_{\text{red}} \tag{3.3}$$

where n is the number of electrons involved in semi-reactions.

The electrons transferred during the redox reaction move through an external circuit, exiting from the anode after oxidation, and entering into the cathode for reduction. The two semi-reactions can occur because the two separate spaces are inter-connected by a conductive liquid or solid phase (*electrolyte*) able to transfer ionic species, thus permitting the closing of the electric circuit. Then the electrolyte has to be ionically conductive, whereas the electrodes have to be electrically conductive and, in the case of gaseous reactants, sufficiently porous to allow the transfer of reactants and products to and from the reaction sites (see Sect. 3.2).

It is possible to build a scale of potentials for different electrochemical pairs in standard conditions (298 K, 1 atm for gases or unit concentration for solutions) assuming the pair hydrogen/ion-hydrogen as an arbitrary reference semi-reaction, and assigning to it a potential of zero volt:

$$2\text{H}^{+} + 2\text{e}^{-} \leftrightarrows \text{H}_2 \quad \text{E}^{\circ} = 0\text{V} \tag{3.4}$$

The potential in standard conditions ($E°$) of other electrochemical pairs can be obtained with respect to Eq. 3.4, permitting the compilation of a list of semi-reaction potentials (*electrochemical series*). In this list, all the semi-reactions are written in such a way to evaluate the tendency of the oxidized forms to accept electrons and become reduced forms (positive potentials correspond to spontaneous reductions) [2]. These potentials can be correlated to thermodynamic quantities if the electrochemical system behaves in a reversible way from a thermodynamic point of view, i.e., when the electrochemical system is connected against an external cell with the same potential, no chemical reaction occurs, while any infinitesimal variation of the external potential either to produce or to absorb current is exactly inverted when the opposite variation is applied (*reversible* or *equilibrium potentials*, E_{eq}). When the equilibrium of the semi-reaction considered is established rapidly, its potential against the reference can be experimentally determined.

Any redox reaction is accompanied by a change of free energy (ΔG) at a given temperature and pressure. However, when the reaction is carried out in an electrochemical way, the transport of electric charges due to a total potential difference is associated with an *electric work*, which is given by:

$$W_{el} = qE \tag{3.5}$$

where E is the difference between cathode and anode potentials ($E_c - E_a$), and q is the total charge transported, which can be expressed as a product of number of moles of electrons transferred in the simplest balanced equation for the reaction in question (n) by the Faraday constant (F, amount of charges on 1 mol of electrons):

$$q = nF \tag{3.6}$$

On the other hand, a fundamental thermodynamic equation defines the change of free energy of a reaction as:

$$-\Delta G = W_{rev} - P\Delta V \tag{3.7}$$

where $-\Delta G$ represents the *total* reversible work obtainable from the reaction (W_{rev}), diminished by the work associated with any possible volume change in the reaction system ($P\Delta V$, work of expansion). Since in an electrochemical reaction neither work of expansion nor any other form of work are involved, from Eqs. 3.5 to 3.7:

$$-\Delta G = W_{el,rev} \tag{3.8}$$

Hence, if the electrochemical system is reversible (or has no losses, all the free energy can be converted into electric energy):

$$\Delta G = -nFE_{eq} \tag{3.9}$$

from which

$$E_{eq} = -\frac{\Delta G}{nF} \tag{3.10}$$

This equation permits the calculation of the equilibrium cell potential E_{eq} from the change of free energy associated with a redox reaction for a given temperature.

If the pair oxygen–water in acidic solution is considered against the reference pair, the following semi-reactions can be written:oxidation of hydrogen at the anode:

$$H_2 \leftrightarrows 2H^+ + 2e^- \quad E_a^\circ = 0 \text{ V} \tag{3.11}$$

reduction of oxygen at the cathode:

$$\frac{1}{2}O_2 + 2H^+ + 2e^- \leftrightarrows H_2O \quad E_c^\circ = 1.23 \text{ V} \tag{3.12}$$

therefore the over all redox reaction is:

$$H_2 + \frac{1}{2}O_2 \leftrightarrows H_2O \quad E^\circ = 1.23 \text{ V} \tag{3.13}$$

which is the spontaneous reaction occurring in fuel cells using hydrogen as fuel. The value of $E^\circ = 1.23$ V for the cell of the reaction (3.13) can be calculated from Eq. 3.10, with the change in free energy at 25°C and 1 atm $\Delta G^\circ = -237.2$ kJ/mol, $n = 2$, $F = 96.485$ Coulombs/electron-mol. It represents the *theoretical* potential for the electrochemical cell based on reaction (3.13), or also the *reversible* open-circuit voltage of the cell, at 25°C and atmospheric pressure.

Equation 3.8 gives the maximum amount of useful work (electricity) obtainable at the outlet of the electrochemical converter, whereas the amount of energy entering the converter is given by the chemical energy contained in chemical substances providing the electron flow. For hydrogen fuel cells this energy corresponds to the enthalpy variation of the reaction (3.13) (ΔH), also called the hydrogen's *heating value*, defined as the difference between the heats of formation of products and reactants. At 25°C and atmospheric pressure, water is in liquid form, and in these conditions its heat of formation is −286 kJ/mol, whereas for vapor water is 242 kJ/mol, the difference being the heat of evaporation of water at 25°C (44 kJ/mol). As heat of formation of elements is by definition equal to zero, the enthalpy of reaction (3.13) results to be −286 kJ/mol if the produced water is considered in the liquid state (*higher heating value* of hydrogen, ΔH_{HHV}), and −242 kJ/mol if vapor water is obtained as product at 25°C (*lower heating value* of hydrogen, ΔH_{LHV}). The negative sign for ΔH means, by convention, that heat is released by the reaction (exothermic reaction).

While hydrogen heating value can be used as a measure of energy input in a fuel cell, the creation of entropy, which accompanies every spontaneous chemical reaction, is regarded as a measure of irreversible losses which limit the amount of useful work obtainable from the fuel cell, according to the second principle of Thermodynamics. The fraction of hydrogen enthalpy which can be transformed into electric work in a fuel cell is then given by the following equation:

$$\Delta G = \Delta H - T\Delta S \tag{3.14}$$

Table 3.1 Free energy, enthalpy (higher heating value), and entropy for the reaction (3.13) at different temperatures in the range 298–373 K [4]

T (K)	ΔG (kJ/mol)	ΔH_{HHV} (kJ/mol)	ΔS (kJ/mol/K)
298	−237.3	−286.0	−0.163
333	−231.6	−284.8	−0.160
353	−228.4	−284.2	−0.158
373	−225.2	−283.5	−0.156

where ΔS is the difference between entropies of products and reactants in reaction (3.13), and the product $T\Delta S$ represents the fraction of inlet chemical energy converted into thermal energy instead of electricity.

If the same reaction (3.13) is realized in an internal combustion engine, i.e., as combustion reaction, the entropy change remains unaltered (because it depends only on the same overall chemical reaction involved in both processes), but not 100% of ΔG can be converted in useful work, but only a fraction of it, according to Carnot theorem [3].

The substitution of (3.14) into (3.10) gives the dependence of the theoretical potential on temperature (potential value decreases when cell temperature increases); however, the values of thermodynamic quantities involved in Eq. 3.14 do not change in significant way up to 100°C (as shown in Table 3.1), which is the temperature range typical of polymeric electrolyte fuel cells, suitable for automotive applications (as discussed later). Then the effect of temperature on the theoretical potential can be neglected for these types of cells, while its effect on practical potentials of operating fuel cells is positive and not completely negligible, and it is examined in Sect. 3.3.2.

For a fuel cell based on reaction (3.13) a basic thermodynamic analysis can also evidence the positive effect of reactant pressures on cell potential, which is expressed by the Nernst equation written for gaseous reactants and products [5]:

$$E = E^{\circ} + \frac{RT}{nF} \ln \frac{p_{H_2} p_{O_2}^{0.5}}{p_{H_2O}} \tag{3.15}$$

where $p_{H_2O} = 1$ if liquid water is produced by the fuel cell.

Equation 3.15 shows that the cell potential E increases at higher reactant pressures, and of course it is lower when a diluted oxidant is used, i.e., air instead of pure oxygen. The practical effects of reactant pressures in real fuel cells will be discussed in Sect. 3.2.

The above recalls of basic thermodynamics are also useful to define the concept of theoretical fuel cell efficiency. If ΔG represents the useful electrical work obtainable at the outlet of a fuel cell, and ΔH the inlet chemical energy, the theoretical efficiency η_{th} can be calculated by the following equation:

$$\eta_{th} = \frac{\Delta G}{\Delta H} \tag{3.16}$$

which becomes for the cell based on reaction (3.13), considering the higher heating value for hydrogen and ΔG at 25°C:

$$\eta_{th} = \frac{237.3}{286.0} = 0.83 \tag{3.17}$$

As the efficiencies for internal combustion engines are generally calculated with respect to the lower heating value of the fuel, also for fuel cells the theoretical efficiency can be evaluated using the hydrogen's lower heating value as ΔH value, in this case Eq. 3.16 becomes:

$$\eta_{th} = \frac{228.7}{242.0} = 0.94 \tag{3.18}$$

This last calculation is justified by the fact that both internal combustion engines and fuel cells produce water in vapor form; however, since some devices for recovery of heat of evaporation could be adopted in designing of fuel cell systems, and taking into account that the hydrogen's higher heating value represents *all* the energy available at the inlet of the electrochemical converter, the use of ΔH_{HHV} can be considered more appropriate for the calculation of the maximum theoretical efficiency of a fuel cell. By applying Eq. 3.10 to hydrogen's higher heating value, it is possible to calculate the cell potential corresponding to all the energy entering the converter based on the reaction (3.13) (which results to be 1.48 V), then Eq. 3.16 applied to hydrogen fuel cells can be written also as:

$$\eta_{th} = \frac{\Delta G/nF}{\Delta H/nF} = \frac{1.23}{1.48} = 0.83 \tag{3.19}$$

Of course, since ΔG and ΔH are used in the definition (3.16), the theoretical efficiency of a fuel cell depends on the redox reaction on which it is built. In any case the theoretical efficiency, calculated from thermodynamic quantities, corresponds to an operative condition of infinitesimal electronic flow (by definition of reversible process), which practically means no current drawn from the converter. As it is shown in the following sections, also at open-circuit (no current through the *external* circuit) the voltage of real fuel cells is slightly lower than $E°$, and the main problem of the electrochemical energy conversion is to obtain potentials in practical conditions (when current is drawn) as near as possible the open-circuit voltage, in order to maximize the real efficiency of the device.

3.2 Proton Exchange Membrane Fuel Cells

Any type of fuel cell is based on a redox reaction in which a fuel is oxidized at anode side by an oxidant which is reduced at the cathode side. The result is the production of an electronic flow through an external circuit, together with chemicals and heat, while the presence of the electrolyte permits the electric circuit to be closed inside the cell. Several types of fuel cells can be today used for many applications, and they differ in dependence of the nature of the electrolyte, which determines the operative range of the cell, and then the type of used fuel. In particular, the most used fuel is hydrogen; thanks to its high reactivity also at

Table 3.2 Classification of fuel cells and their main characteristics

Fuel cell	Electrolyte (ions exchanged)	Catalyst	Fuel	Oxidant	Temperature (°C)
PEM	Polymeric membrane (H^+)	Pt	H_2	O_2 air	40–90[a]
AFC	KOH (OH^-)	Pt/Pd Ni	H_2	O_2 air	60–220
PAFC	Phosphoric acid (H^+)	Pt	H_2	O_2 air	160–200
MCFC	Li and K carbonates (CO_3^{2-})	Ni	H_2 Light HC[b]	O_2 air	600–700
SOFC	Zr oxides (O^{2-})	–	H_2 Light HC[b]	O_2 air	600–1000
DMFC	Polymeric membrane (H^+)	Pt Pt–Ru	CH_3OH	O_2 air	90–130

[a]Operative temperature range of current PEM fuel cells, not taking into account for the new materials for high-temperature membrane (>100°C) under study
[b]Light hydrocarbons, mainly methane or products deriving from methane reforming reactions (see Sect. 2.1)

relatively low temperatures, but in fuel cells operating at higher temperatures (>500°C) also hydrocarbons can be oxidized. The most used oxidant in all fuel cells is oxygen, contained in sufficient concentration in atmospheric air. All fuel cells today known can be classified on the base of the electrolyte, to which their acronyms are usually referred:

- Polymer electrolyte membrane or proton exchange membrane (PEM) fuel cells
- Alkaline fuel cells (AFC)
- Phosphoric acid fuel cells (PAFC)
- Molten carbonate fuel cells (MCFC)
- Solid oxide fuel cells (SOFC)
- Direct methanol fuel cells (DMFC)

Table 3.2 reports the classification of the different types of fuel cells with some technical characteristics [6]. In this table the different electrolytes are specified together with the type of ions exchanged through them, while the catalysts indicated are those used on both anode and cathode to accelerate the semi-reactions (not necessary for SOFC; thanks to their high operative temperature).

The field of employment of a particular fuel cell is determined by its working characteristics, in particular by its operating temperature and fuel utilized.

High-temperature fuel cells are very promising for electric energy generation in large stationary plants, offering higher electric efficiencies with respect to conventional electric power generators, with minor environmental impact. In this field PAFC, MCFC, and SOFC are in demonstration stage, from few hundred kilo Watts up to mega Watts units.

Low-temperature fuel cells (PEM and DMFC) present the major possibility of diffusion in transportation means and portable devices, because high temperature could be a problem for both these types of application. However, regarding DMFCs, the high toxicity of the fuel (CH_3OH) discourages their utilization on vehicles, where large fuel tanks are necessary, and restricts their diffusion to the field of consumer electronic portable equipments. On the other hand, the current stage of development of DMFCs requires further improvements of these devices before their wide practical utilization, especially regarding low efficiency and fast

decay issues [7]. AFCs could operate at room temperature, but their major limit is the CO_2 sensitivity of the electroclyte (KOH); therefore, the use of this kind of cell is restricted to special applications.

PEM fuel cells, based on the redox reaction (3.13), are the most suitable for transportation applications for a number of reasons. Beside their low operative temperature, they are also characterized by quick start-up, high efficiency, good transient response, and absence of corrosive liquid electrolytes, all features strongly appreciated for automotive utilizations.

The PEM fuel cell operating principle is schematized in Fig. 3.1, where pure hydrogen is indicated as fuel. Hydrogen ions produced by the semi-reaction (3.11) flow from anode to cathode passing through the electrolyte, whereas electrons are forced to take the external electric circuit in order to provide useful work. Hydrogen ions are driven through the electrolyte by the potential difference across it, deriving from the anode fuel oxidation.

At cathode side the electrons coming from the external circuit combine with hydrogen ions coming from the anode side and with oxygen from air feeding to produce water. This is removed from cathode side by the air stream, and exit together with nitrogen and excess of oxygen not consumed in the overall electrochemical reaction. As the reaction (3.13) is exothermic (see Table 3.1), another

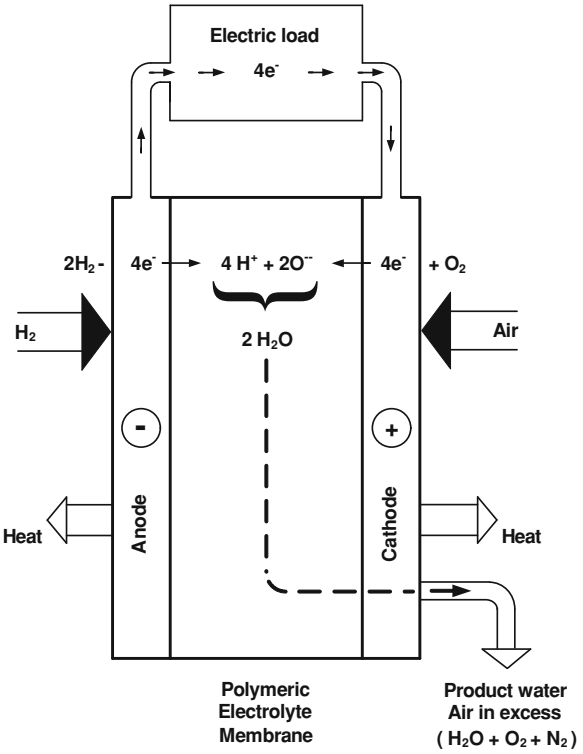

Fig. 3.1 Basic principle of a PEM fuel cell (relative dimensions are not to scale)

product obtained at the cell outlet is heat, which needs to be controlled by a cooling system (see Sect. 4.4).

Regarding its structure, a PEM fuel cell is constituted by three types of components: a membrane–electrode assembly (MEA), two separators or bipolar plates, and seals between MEA and plates. The MEA consists of a thin sheet of an ion-conducting polymeric membrane, two dispersed catalyst layers, and two gas diffusion layers (GDL). A number of cells can be connected in series, obtaining a *stack* of fuel cells, able to reach the total power required by a specific application. In this case the stack voltage is simply the sum of single cell voltages, the stack current is the product of current density (A/cm^2) by the cell active area (cm^2), and the output power is of course the product of stack voltage and current. For each practical realization both active area and number of cells have to be determined on the base of design inputs, i.e., desired power output and voltage, other than weight, volume, and cost restrictions.

3.2.1 The MEA: Membrane

The key characteristic of a PEM fuel cell resides in the nature of the electrolyte, a polymeric membrane whose optimal working temperature is currently restricted in the range 40–90°C. This implies that fuels less reactive of hydrogen cannot be used, and also with this fuel the addition of a catalyst on both electrodes is necessary. Moreover, the low operative temperature implies also the necessity to use a very pure hydrogen, in order to avoid the contamination of catalysts by impurities. In particular, the processes providing the hydrogen to be used in PEM fuel cells must involve a phase of post-purification of hydrogen-rich stream to reduce at ppm level the concentration of carbon monoxide (deriving from the not complete oxidation of the feedstock, see Sect. 2.1), because CO can be easily adsorbed on Pt catalysts at the operative temperature of PEM fuel cells, hindering the dissociative adsorption of hydrogen, thus dramatically lowering the cell potential [8].

The function of the polymeric membrane electrolyte is to permit the transfer of protons produced in anodic semi-reaction (3.11) from anode to cathode, where they react with reduced oxygen to give water. This process is of course essential for fuel cell operation, as it allows the electric circuit to be closed inside the cell. On the other hand, the membrane must also hinder the mixing between fuel and oxidant, and exhibit chemical and mechanical properties compatible with operative conditions of the fuel cell (temperature, pressures, and humidity).

The most diffused material for membranes is based on co-polymers of tetrafluoroethylene (TFE) with perfluorosulfonate monomers. The resulting co-polymer is constituted by polytetrafluoroethylene polymeric chain (PTFE, commercially known as Teflon) in which some fluorine atoms are substituted by sulfonated side chains. The monomer perfluoro-sulfonyfluoride ethyl-propyl-vinyl ether is used in membranes commercialized by Dupont with the registered trademark Nafion™ (Fig. 3.2), which is the most well-known material used as electrolyte in PEM fuel cells.

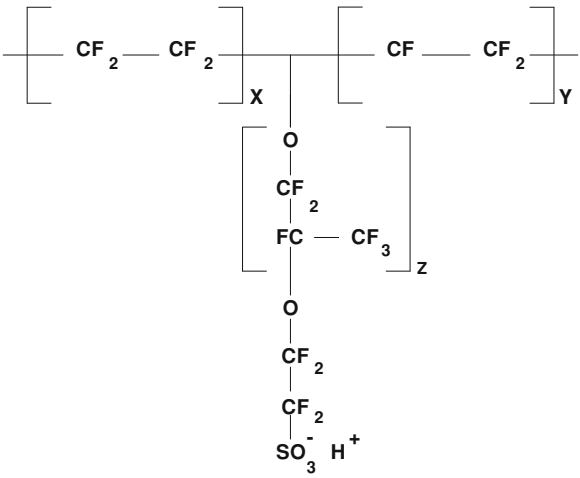

Fig. 3.2 Molecular structure of Nafion membranes. The values of *x*, *y*, and *z* coefficients vary with the manufacturer

In this type of membrane, as well as in similar products made by other manufacturers, the Teflon-like backbone is responsible of very high chemical resistance (due to the strong bond between carbon and fluorine), high hydrophobic characteristics, and good mechanical properties. The hydrophobic feature is useful to favor the expulsion of product water out of the cell, in order to prevent flooding phenomena, while the mechanical strength permit the production of very thin films (down to 50 μm).

On the other hand, the ionic bond between oxygen and hydrogen in sulfonic groups favors a mechanism of clustering of side chains within the overall structure of the co-polymer, due to the mutual attraction between protons and sulfonate anions from different molecules. As sulfonic groups are highly hydrophilic, their clustering inside a material substantially hydrophobic generates nano-domains of strong affinity toward water molecules, which can significantly be absorbed by the co-polymer up to 50% of its dry weight. An abundant collection of water molecules around the hydrophilic regions creates large water reservoirs, where protons result weakly bonded to sulfonate anions (dissociation of proton from sulfonic acid is of course promoted by water) and able to move and transfer among neighboring nano-domains, and then through the supporting long polymeric chain. This mechanism of proton conduction is a mixture of a diffusion through water solvent and proton skipping between the sulfonic acid groups. It is the most accepted mechanism to explain the proton transport in Nafion membranes [9]. In order to have a satisfying proton conductivity (at least 0.01 S/cm) the ratio of the number of hydrophobic monomers to hydrophilic monomers has to be approximately comprised in the range 3–7. The proton conductivity achieved in well-humidified Nafion-like membranes can be as high as 0.2 S/cm at PEM fuel cell operative conditions.

The necessity of adequate membrane hydration, with the associated risk of drying out, limits the operative temperature of PEM fuel cells under 100°C.

As water in a PEM fuel cell is initially produced in the vapor phase, the membrane hydration from this phase is more relevant with respect to water uptake from liquid phase. In particular, when water is collected by vapor phase, two distinct mechanisms can be individuated: at lower vapor concentration ion solvation occurs inside the membrane, while in conditions of pre-saturated vapor phase polymer swelling is observed with accommodation of a larger amount of water. At this regard an experimental polynomial equation has been proposed to correlate water content of membrane with water partial pressure [10]:

$$\lambda = 0.043 + 17.18\frac{p}{p_{\text{sat}}} - 39.85\left(\frac{p}{p_{\text{sat}}}\right)^2 + 36\left(\frac{p}{p_{\text{sat}}}\right)^3 \tag{3.20}$$

where λ is the number of water molecules per sulfonic group present in the co-polymer, p is water partial pressure, and p_{sat} is the saturation pressure.

The maximum amount of water that can be taken by the polymeric membrane depends also on the state of water, in particular a Nafion membrane in liquid water can take approximately 50% of water more than from vapor phase. However, an excess of liquid water in contact with the membrane of a PEM fuel cell can determine flooding phenomena which strongly decrease its proton conductivity. On the other hand, an increase of temperature up to 90°C favors a strong improvement in proton conductivity with respect to room temperature, while low humidity conditions have been found to cause fast degradation of Nafion-like membranes [11]. As a consequence, the necessity of an accurate humidification of the polymeric membrane is one of the key aspects affecting both performance and reliability of PEM fuel cells (see Sect. 4.5). If the currently used polymeric membranes exhibit their interesting properties (high conductivity, chemical stability, and mechanical flexibility) in highly hydrated conditions, then the maintenance of high humidity at temperatures higher than 90°C would require heavy pressurization, that could imply energy costs not compatible with high efficiency expected from these systems. For this reason many studies are currently being carried out about the possibility to realize proton exchange membranes characterized by more water-independent proton conductivity, or by higher water retention capability, then able to operate in PEM fuel cells at temperature higher than 100°C (in the range 120–150°C) and low pressures. Such membranes could also provide an improved CO tolerance, being well known from thermodynamic analyses that adsorption capacity of platinum toward carbon monoxide decreases at higher temperatures. In particular it has been found that while CO tolerance is 10–20 ppm at 80°C, it becomes 1000 ppm at 130°C and rises up to 30,000 ppm at 200°C [12, 13]. Recent results confirm that a typical reformate gas with CO percentage comprised in the range 2–5% can be fed to PEM fuel cells working at temperature above 180°C directly from the fuel processor [14]. In this way the need for CO cleanup by catalytic selective oxidation of the fuel reforming stream could be eliminated, significantly improving the overall system efficiency. In addition, as the rate of heat removal is proportional to the temperature difference between the system and the environment, the increase in PEM fuel cell working temperature above 120°C

would simplify the fuel cell cooling device, making possible the use of radiators currently adopted in internal combustion engine vehicles, with a gain in weight energy density and then in overall efficiency [15]. On the other hand, the heat recovered by a high-temperature PEM fuel cell would be higher, making more attractive the applications in the co-generation field. Lastly, also the water management would be greatly simplified, because in a PEM fuel cell operating above 100°C water on the membrane would exist only in vapor state, while the absence of liquid water would increase the exposed area of electrocatalysts, thus improving the diffusion of reactants into the reaction layer [16].

High-temperature operation in PEM fuel cells using Nafion-like membranes is presently impeded by polymer degradation above 120°C and increase of membrane resistance as a consequence of loss of hydration (alteration of proton transport mechanism due to reduction of water nano-domains). In particular, conductivity losses correlated to low humidity conditions on Nafion-like membranes can reach some orders of magnitude [17], strongly increasing the Ohmic losses (see Sect. 3.3.1) with lowering of voltage, power, and efficiency. This has determined the direction of studies aimed at finding new materials able to overcome the above limitations [18]. These materials can be subdivided into four classes: (1) modified perfluorosulfonic acids, (2) non-fluorinated hydrocarbon polymers, (3) inorganic–organic composites, and (4) acid–base polymers (polybenzimidazoles, PBI). The first class of materials is based on the incorporation of hydrophilic inorganic additives into the perfluorinated membrane to increase the polymer swelling and the binding energy of water. Several hygroscopic additives have been proposed for incorporation in Nafion membranes ($Zr(HPO_4)_2$, SiO_2, TiO_2) with different methods of preparation, obtaining composite materials characterized by variable water retention and electrochemical performance [19, 20]. The second approach is based on the utilization of aromatic polymers as membrane backbone, which are cheaper than perfluorinated ionomers, and can contain polar groups characterized by high water absorption in a wide temperature range [21]. Thermal and chemical stability of these materials are the main limitations hindering their practical application. The third solution is based on the rationale of using an inert organic polymer as binding medium for a large quantity of an inorganic proton conductor of high performance [22]. As high proton conductivity materials are often crystalline, they are suspended in inert organic polymers, such as polyvinylidene fluoride (PVDF), nevertheless the difficulty of obtaining satisfactory film-forming properties is the main limitation of this option. Acid–base polymers represent the state of the art in the field of high-temperature polymeric electrolytes, and are essentially constituted by a basic polymer doped with a non-volatile inorganic acid or blended with a polymeric acid [23].

PBI is today considered the most interesting basic polymer for preparation of acid–base membranes, especially if doped with phosphoric acid [24]. In Fig. 3.3 the scheme of the commercial PBI known as Celazole® is shown.

The aromatic nuclei of PBI are responsible of its good characteristics of chemical stability, whereas the basic functional groups act as proton acceptors like a normal acid–base reaction. Amphoteric acids, such as phosphoric or phosphonic

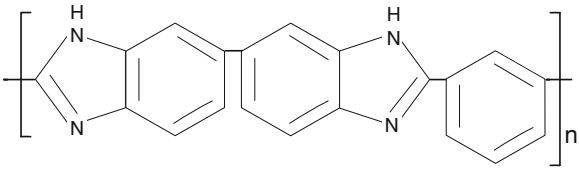

Fig. 3.3 Molecular structure of Celazole® (poly-2,2′-m-(phenylene)-5,5′-bibenzimidazole)

acids, are preferred due to their capability to act as both proton donor and acceptor, they permit proton transfer by a dynamic process of breaking and forming of hydrogen bonds [25]. These membranes present interesting features in terms of proton conductivity, mechanical flexibility, and thermal stability; however, durability, start up time, and dynamic response are still critical issues, especially if automotive applications are considered [26].

Apart from water uptake and proton conductivity, another important physicochemical property of a polymeric membrane for PEM fuel cells is its gas permeation, which can be considered a measure of membrane impermeability toward reactant species. Permeability is defined as the product of diffusivity and solubility:

$$P = DS \tag{3.21}$$

if D is expressed in cm^2/s and S in $mol/cm^3/Pa$, the permeability can be expressed in mol cm/s/cm^2/Pa, where cm represents the membrane thickness, the surface area of the given material is expressed in cm^2, mol/s is the gas flow rate passing through the membrane at the pressure of 1 Pa. The most used unit for gas permeability is Barrer, being:

$$1\ \text{Barrer} = 10^{-10} \text{cm}^2/\text{s/cmHg} \tag{3.22}$$

An ideal membrane for PEM fuel cells should hinder the passage of other species other than solvated protons, but due to material porosity and solubility of hydrogen and oxygen in water, some reactant can actually permeate through the membrane. For a dry Nafion membrane hydrogen permeability is comprised between 20 and 70 Barrer in the temperature range 25–100°C and 1 bar, whereas oxygen permeability is about one order of magnitude higher, and both are higher for a wet membrane [27]. Regarding the permeation rate, this is of course proportional to permeability, pressure, and exposed surface of the membrane, and inversely proportional to its thickness.

3.2.2 The MEA: Electrocatalysts

The electrodes in a PEM fuel cell have the fundamental function to provide a support where the electrochemical reactions take place. As both the electrochemical semi-reactions have to be catalyzed, to occur at temperatures under 90°C, the

electrodes must offer an adequate support for highly dispersed catalyst particles. These are the reaction sites which have to be reached not only by gaseous reactants, but also by electrons and protons. Therefore, the catalyst layer must be in intimate contact with a porous and electrically conductive structure for gas and electrons transfer (GDL, see Sect. 3.2.3) and with the electrolytic membrane.

The most diffused catalyst for both semi-reactions is platinum, which is supported on carbon powders (typically 40 nm) in order to optimize the dispersion of metal particles and the active surface area, then to increase the reaction rate. The carbonaceous material of the support assures the conduction of the electrons produced at the anode and received by the cathode. The ratio Pt/C has to be optimized, in fact while a thin layer of carbon support (high Pt/C) could give advantages on the rate of proton transfer and gas permeation into the catalyst layer, a lower Pt/C ratio (smaller Pt particles) permits a larger surface area to be obtained. Moreover, the impregnation of catalyst particles with a calibrated amount of proton conductor (the same ionomer used for membrane) allows all catalyst particles to be reached by protons and extends the three-phase boundary contact between gas, electrolyte, and catalyst, with great benefit in terms of reduction of platinum concentration. Optimal values of Pt/C ratios for current realizations have been found to be comprised between 10 and 40 wt%, with a platinum loading of 0.4 mg/cm^2 [28], whereas the optimized content of ionomer in the catalyst layer results to be in the range 20–50 wt%, in dependence of fabrication method and platinum loading [29]. At this regard novel carbon supports are currently under development to improve PEM fuel cell performance, in particular materials able to assure more efficient proton conduction from the catalytic sites to the membrane are considered. Recently, the grafting of polymers onto carbon black surfaces has been proposed, and promising results have been obtained with polystyrene sulfonic-grafted carbon black as support of platinum–ruthenium-based catalysts, in terms of reduced ohmic drop and increased proton transfer with respect to commercial carbonaceous supports [30]. As carbon supports can undergo electrochemical oxidation within the PEM cell in some severe operative conditions, such as fast dynamic phases and repeated start up/shut down actions, the platinum surface area can be reduced with worsening of cell performance [31, 32]. About this issue some studies have proposed the use of carbon nanocages as catalyst support, evidencing the possibility to significantly reduce the electrochemical carbon corrosion; thanks to both the strong hydrophobic nature and graphitic structure of these materials [33].

3.2.3 The MEA: GDL

Two GDL, whose main task is to allow uniform access of gaseous reactants to the catalyst layer, are located on both anode and cathode side, and can be considered as an integrant part of the MEA. They are interposed between the catalyst layer and bipolar plates, and are constituted by a porous carbonaceous material, such as

paper or cloth, able to conduct the electrons exiting from the anode and entering the cathode. The GDL does not participate in the electrochemical reaction, but carries on many important functions, in particular: electron transfer between catalyst layer and bipolar plates, diffusion of gaseous reactants from bipolar plates to catalyst layers, water transfer between catalyst layers and bipolar plates, heat transfer from reaction sites to bipolar plates, mechanical separation between membrane and bipolar plates. Typical values of thickness in commercial GDL are comprised between 100 and 400 μm, with densities ranging from 0.2 to 0.7 g/cm^3 and porosity between 70 and 80% [34].

While both through-plane and in-plane electronic conductivities play a key role in controlling the capability of the GDL to transfer electrons from reaction sites to bipolar plates, the porous nature of the GDL material guarantees an effective diffusion of all reactant molecules from the high concentration region outside of the GDL to the inner side at lower concentration, next to the catalyst layer, where the molecules are consumed by the electrochemical reaction. An effect of spread out of the gases thorough the porous structure ensures the uniform contact of gas molecules with the entire surface of the membrane. As the mean free path of gas molecules is many orders of magnitude lower than pore diameters of a GDL, the diffusion of reactants is not regulated by a Knudsen mechanism, but mainly by the convective flow resistance [34]. The GDL porosity is also fundamental for water management inside the cell, as it offers a pathway for the transfer outside the MEA of liquid water produced by the cathodic reaction, preventing flooding phenomena at 100% RH (relative humidity), but also permits water coming from external humidification systems to reach the membrane and avoid electrolyte drying out at higher operative temperature and low RH (see Sect. 4.5).

The importance of this aspect has determined the tendency to treat the surface of the GDL with different substances. While the hydrophilicity of GDL could help the membrane correct humidification at low RH, they are in general treated with hydrophobic polymeric microporous sheets (mostly PTFE, or fluorinated ethylene propylene), privileging flooding issues [35, 36]. The effect of hydrophobic polymer content on liquid water and oxygen gas transport has been investigated, with results showing how the trade-off between hydrophobicity and permeability can be solved by an optimal PTFE loading in the GDL (20%) that reduces the mass transport limitations and increases the oxygen diffusion kinetics [37]. On the other hand other studies have been recently presented about the possibility to use additional coatings, different from hydrophobic polymers, with the aim of finding an optimal balance between hydrophilic and hydrophobic properties and of extracting the maximum power from the stack. In particular, thin films of nano-scaled inorganic oxides (Al_2O_3, TiO_2) have been deposited on hydrophobic commercial GDL with formation of three-dimensional surface structures able to improve both transport of gases and water retention in low-humidity conditions [38]. Chemical vapor deposition techniques have been used to deposit microporous carbon nanotubes structures on commercial macroporous carbon papers, without addition of hydrophobic coatings. This type of GDL has shown significant advantages in terms of mechanical robustness; thanks to the reinforcing presence of multi-walled carbon

nanotubes (MWCNT) in the microporous layer on carbon paper fibers, and valuable polarization characteristics of the cell at 80°C and RH in the range 70–100%, attributed to hydrophobic properties of MWCNTs and absence of PTFE [39].

3.2.4 The Bipolar Plates

In a single cell the electrons produced at the anode side are directly transferred to the cathode through the external circuit, whereas in a multicell configuration adjacent electrodes have to be electrically connected each other (the terminal electrodes permit the transfer of electrons to the electric load). In principle this can be realized by the direct connection of adjacent electrodes; however, the low electric conductivity of electrodes and the thinness of their structure could cause a not negligible loss of voltage, suggesting the utilization of specific components to transport electrons from the anode of a cell to the cathode of the adjacent cell. This fundamental task is carried out by bipolar plates, which are built with the aim to accomplish several important functions associated with the stack assembly. In particular, a part from the electric contact between adjacent cells, they have to favor the heat transfer between cells and cooling separators, and to house the gas "flow field," i.e., a channel system machined into the plate that permits the movement of reactants from the gas inlet to the cell outlet, assuring in this way the uniform feeding of the MEA and the management of water adduction and/or removal. A single bipolar plate inside the stack is machined on both sides in order to carry hydrogen gas on one side and air on the other, while the end plates have a channel system only on one side and are electrically connected via the external circuit. On the other hand, cooling units can be inserted inside the bipolar plate, separating the two flow fields, and operate as inactive cells through which a cooling fluid (generally deionized water) can flow and remove the heat produced by the electrochemical reaction.

Different concepts have been studied and used for the configuration of the channel system, from simple parallel channels to more complex arrangements [40], while several materials have been proposed to meet the requirements of chemical compatibility, corrosion resistance, electric and thermal conductivity, gas impermeability, robustness, lightness, and cost [41]. In particular, gas impermeability is a very important requisite, because it is necessary to avoid the direct oxidation of the fuel that would imply consequent loss of useful electrons and local heating dangerous for the MEA.

An example of a stainless steel serpentine-based gas flow field is reported in Fig. 3.4 for a simple small size PEM stack (64 cm^2 as active area).

The most suitable materials result to be non-porous graphite, metals (aluminum, stainless steel, titanium, and nickel), and composite solids. Graphite made non-porous by impregnation with impermeable substance was early used for bipolar plates, but its applicability is limited by difficulties in machining and consequent costs. The metal plates present the obvious advantages of high robustness and low

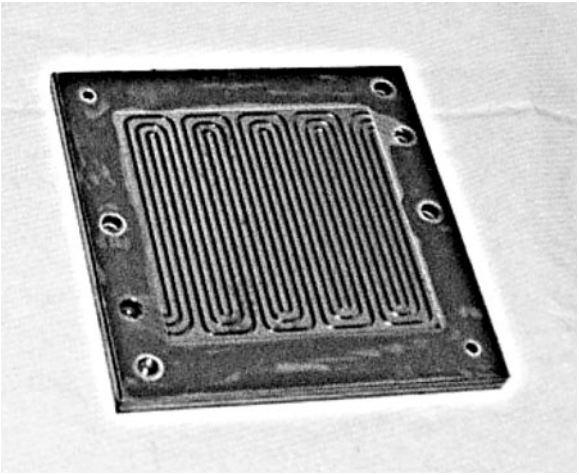

Fig. 3.4 Serpentine gas flow field in a bipolar plate of a simple PEM stack

cost, but their high specific weight affects negatively the power density of the stack, whereas the severe operating environment inside the fuel cell (pH 2-3 and temperatures of 60–80°C) could cause their rapid corrosion, with metal dissolution and diffusion of metal ions inside the membrane (blocking of sulfonic acid sites) and consequent reduction of proton conductivity and cell durability. Moreover, a layer of corroded metal on the plate surface increases its electric resistance and reduces the output power of the cell. For these reasons the surface of metal plates is treated with not corrosive and electrically conductive coating layers, such as conductive polymers, graphite, noble metals, metal carbides, or nitrides.

The lightness and robustness of titanium plate has suggested recent studies about the possibility to improve its surface properties with the aim of preventing the formation of passive films (high resistivity oxides), which while would act as corrosion protectors, could also work as electric insulator increasing the interfacial contact resistance between the bipolar plate and the GDL, with consequent augment of the ohmic losses [42]. On the other hand, due to the high cost of the pure metal, as well as of proposed surface modifications (platinum and iridium), titanium could not meet the low-cost requirements typical of the automotive field. In this view inexpensive metals, such as stainless steel and aluminum, have been object of major applications. In particular, aluminum has been modified by electroplated nickel alloys, providing materials characterized by the typical robustness and machining facility of metals, high electric conductivity, and corrosion resistance in the acidic medium of the fuel cell environment [43]. Recent researches have also analyzed the possibility to improve the surface properties of stainless steel plates, to find a compromise between corrosion resistance and electric conductivity, i.e., between graphite and metal properties, by coating with conductive amorphous carbon layer [44].

A large diffusion may be found also for composite materials, carbon, or metal based. In the first case different types of polymeric resins (thermoplastics, such as polypropylene, polyethylene, and PVDF, or thermosettings, such as epoxies and phenolics) are filled with carbonaceous powders (graphite or carbon blacks), to provide a material characterized by very high chemical stability in the fuel cell environment and satisfactory properties of electrical conductivity, but which cannot offer sufficient robustness at thickness lower than 2 mm. The metal composite plates are essentially based on combinations (sandwiches of different layers) of stainless steel, porous graphite, and polycarbonates, with the aim to exploit the characteristics of different materials. Their fabrication can be more complex but this is compensated by the possibility to incorporate other functional components, such as manifolds, seals, and cooling layers.

3.3 Sensitivity of PEM Stacks to Operating Conditions

As anticipated in Sect. 3.1, when a current is drawn from a fuel cell, the actual potential is always lower than its equilibrium value $E°$. Then the variation of the actual potential with the current, when an electric load is applied to the cell, is the main factor affecting its actual efficiency. The relationship between cell potential and current is described by the so-called *polarization curve*.

3.3.1 The Polarization Curve

In Fig. 3.5, the experimental polarization curve for a PEM stack of 500 W is reported together with the output power supplied by the stack in the experimental conditions indicated in the caption. This stack is constituted by 32 individual fuel

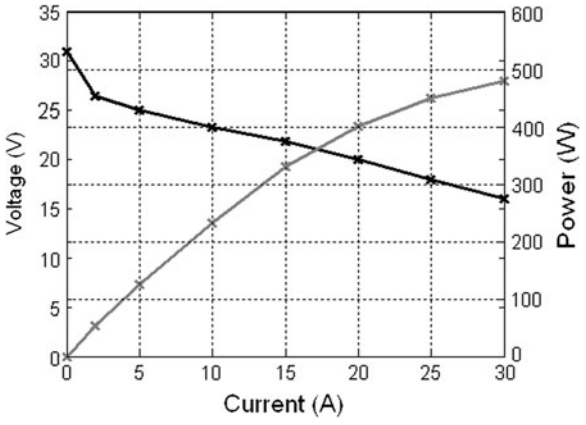

Fig. 3.5 Optimized polarization curves for a 500 W PEM stack in terms of voltage and power versus current. $T_{stack} = 333$ K, $p_{air} = 40$–60 kPa, $p_{H_2} = 20$ kPa, stoichiometric ratio $R = 2$–5

cells connected in series, with an active area of about 64 cm^2 each (one example of its bipolar plate is shown in Fig. 3.4) [45]. On the abscissa of Fig. 3.5 the current delivered by the stack is reported, while the current density could be used to compare stacks based on cells of different sizes, making the ratio between the current delivered and the cell active area.

The parameter R reported in the legend of Fig. 3.5 (stoichiometric ratio) is defined as $R = R_{eff}/R_{stoich}$, where R_{eff} is the ratio between the air and hydrogen mass flow rates, while R_{stoich} is the same ratio as required by the stoichiometric equation of H_2 oxidation (see Sects. 4.3 and 6.2).

It can be noticed that also in the absence of electric load, when gaseous reactants are fed to the stack but the electric circuit is open (zero current) the total stack voltage is lower than the theoretical or thermodynamic value (OCV = 1.23 V × 32 cells = 39.4 V at 25°C and ambient pressure), and it corresponds to a voltage at zero current of about 0.96 V per cell (31 V/32 cells), which cannot be explained by the slight shifting from standard conditions of temperature and pressure (see Sect. 3.3.2). The terms polarization or *overpotential* are used to describe the difference between the actual electrode potential and the equilibrium potential, and represent the driving force for the electrochemical reaction, i.e., the potential difference necessary to produce current. On the other hand, the existence of overpotential in real systems evidences that also without circulation of current in the external circuit some energy losses are present, which of course are expected to increase when an electric load is applied. In fact, the characteristic curve of Fig. 3.5 shows also that, for the real system considered, after a voltage drop of about 5 V at lower current (up about 2 A), a slower and linear voltage diminution occurs up to the maximum power (480 W at 30 A). Starting from the energy supplied by a specific electrochemical reaction, all voltage losses can be generally associated with the fraction of that energy which is used by the cell to accomplish the electrode reactions at the desired speed, then they are somehow correlated to the electrode kinetics, while the rest of the reaction energy remains available for external use, such as production of useful work.

3.3.1.1 Losses Due to Activation Overpotential

The theoretical interpretation of the first voltage drop at low current is based on the Butler–Volmer equation, which is derived by an analysis of electrode kinetics and provides a general description of the relationship between current density and surface overpotential for an electrochemical converter [46]:

$$i = i_0 \left\{ \exp\left[\frac{-\alpha_{Rd} F(E - E^\circ)}{RT}\right] - \exp\left[\frac{\alpha_{Ox} F(E - E^\circ)}{RT}\right] \right\} \tag{3.23}$$

where i is the current density delivered by the cell and i_0 is the *exchange current density*, which represents the continuous flow of electrons occurring at the electrodes when reactants and products are in equilibrium conditions, i.e., when no

net current is observed through the external circuit and the rates of forward and backward reactions are equal. It can be considered as the rate of electrochemical forward and backward reactions at equilibrium, and can be regarded as analogous to the rate constant of chemical reactions. Moreover in equation 3.23:$E - E^{\circ} =$ over potential

α_{Rd} is the *charge transfer coefficient* for the reduction reaction, which represents the fraction of overpotential necessary to move from the equilibrium condition. It is comprised in the range 0 to 1.0 and depends on the reaction involved and electrode material

α_{Ox} = charge transfer coefficient for the oxidation reaction

F = Faraday, R = universal gas constant, T = absolute temperature.

Equation 3.23 evidences that some difference between equilibrium and actual potential ($E - E^{\circ} \neq 0$) is necessary to realize an electrochemical reaction and to observe a current density through the external circuit. The overpotential in this equation is called *activation polarization*, it is present at both anode and cathode of a fuel cell and is correlated with electrode kinetics. The activation polarization is associated with the energy required to break and reform the chemical bonds involved in the transformation of reactants into products. The consequent reduction of energy available to produce useful power is related to the reaction rate, in particular higher electrode kinetics imply lower activation losses. A measure of the electrode activity in the specified electrochemical reaction is given by the exchange current density i_0 (higher i_0 means higher electrode activity). In hydrogen/oxygen fuel cells the reduction reaction at cathode is much slower than the anodic oxidation, in particular the cathode exchange current density is several order of magnitude lower with respect to the anodic exchange current density. This means that the overpotential on the cathode is much larger than that on the anode, then the Butler–Volmer equation, which is valid for both anode and cathode of a fuel cell, can be written solely for the cathode reaction:

$$i_c = i_{0,c}\left\{\exp\left[\frac{-\alpha_{Rd,c}F\left(E_c - E_c^{\circ}\right)}{RT}\right] - \exp\left[\frac{\alpha_{Ox,c}F\left(E_c - E_c^{\circ}\right)}{RT}\right]\right\} \tag{3.24}$$

and assuming valid the "high polarization" approximation (E_c much lower than E_c°, cathode overpotential is negative), the second term of Eq. 3.24 can be neglected [47], obtaining:

$$i_c = i_{0,c}\exp\left[\frac{-\alpha_{Rd,c}F\left(E_c - E_c^{\circ}\right)}{RT}\right] \tag{3.25}$$

From Eq. 3.25 the cathode activation overpotential can be derived:

$$E_c^{\circ} - E_c = \frac{RT}{\alpha_{Rd,c}F}\ln\frac{i_c}{i_{0,c}} \tag{3.26}$$

Equation 3.26, derived by electrode kinetics, has the same form of an empirical equation proposed by Tafel [48, 49], which gives the relationship between

activation overpotential (V_{act}) and current density. Setting $RT/\alpha_{Rd,c}\,F$ equal to a constant A, Eq. 3.26 becomes:

$$V_{act,c} = A \ln \frac{i_c}{i_{0,c}} \tag{3.27}$$

where the constant A (called Tafel constant) is higher when the electrochemical reaction is slower, whereas $i_{0,c}$ is higher for a faster reaction.

Equation 3.27 can be written also in the form:

$$V_{act,c} = a + b \log(i) \tag{3.28}$$

where

$$a = -2.3\left(\frac{RT}{\alpha_{Rd,c}F}\right)\log(i_0) \quad \text{and } b = 2.3\frac{RT}{\alpha_{Rd,c}F}$$

The plot of overpotential versus current density in log scale gives the parameters a, b, and i_0 (b is called the Tafel slope). Equation 3.28, which is only valid for $i > i_0$, suggests that the exchange current density i_0 can be also regarded as the current density value at which the overpotential begins to exert its function to make possible the electrochemical reaction, becoming different from zero.

The Tafel equation can be used to model the activation losses in polarization curve, in fact assuming that these are the only losses in a fuel cell, the cell voltage is given by:

$$E = E_c - E_a = E^\circ - V_{act,c} - V_{act,a} \tag{3.29}$$

As seen before, in a hydrogen/oxygen fuel cell the anode polarization can be neglected, then Eq. 3.29 for this type of fuel cell can be written:

$$E = E^\circ - V_{act} = E^\circ - \frac{RT}{\alpha F}\ln\left(\frac{i}{i_0}\right) \tag{3.30}$$

For PEM fuel cells with platinum-based electrocatalysts α is about 0.5 for hydrogen electrode, and comprised in the range 0.1–0.5 for oxygen electrode, while typical values for the constant i_0 at 25°C and ambient pressure are about 0.1 mA/cm^2 at the cathode and about 200 mA/cm^2 at the anode [50].

From the above consideration it is clear that the exchange current density is the main factor affecting the activation overpotential, then the optimization of a PEM fuel cell performance requires the maximization of i_0. This can be obviously accomplished by increasing the catalyst activity, that means to raise the surface area, cell temperature, and reactant pressure (this last effect should also favor gas adsorption on catalyst sites).

Equation 3.30 with the proper values of the parameters α and i_0 can be used to fit the polarization curve in the region of low current, in particular the logarithmic dependence of current on polarization can model the fast decrease of voltage observed under 2 A (Fig. 3.5). However, it cannot explain the shift from the OCV value, for which a further interpretation is necessary.

3.3.1.2 Losses Due to Fuel Crossover and Internal Current

Even if the polymeric membrane in a PEM fuel cell is designed to permit only the passage of hydrated hydrogen ion, some electric conductivity and gas permeation cannot be avoided. Then at open-circuit, when no current can be observed through the external circuit, two phenomena can occur at the anode side of a PEM fuel cells, called *fuel crossover* and *internal current*. They can be described as follows:

fuel crossover: some not oxidized hydrogen can pass through the electrolyte membrane to reach the cathode, where it can be directly oxidized by oxygen, wasting two electrons for each hydrogen molecule. The hydrogen crossover depends on membrane permeability and thickness, and on difference between hydrogen partial pressure on the two side of the membrane.

internal current: some hydrogen is oxidized at the anode side with production of two electrons per molecule. These do not flow through the external circuit (which is open) but pass through the electrolyte membrane directly to the cathode.

Both the above phenomena produce the same effect to transfer electrons directly from anode to cathode and to consume a small quantity of hydrogen at open-circuit, in spite of no useful current is generated. Then this hydrogen consumption correspond to a current density associated with electron flow through the electrolyte membrane, which is a current density subtracted from that necessary for useful work production. This loss could be considered negligible in energy terms, but for conditions close to open-circuit the consequent reduction of potential is significant. The occurring of internal current allows the application of Eq. 3.30 also at open-circuit, using the internal current density in the ratio i/i_0 at the place of the external one. For the entire range of current densities Eq. 3.30 becomes:

$$E = E^{\circ} - V_{\text{act,in}} = E^{\circ} - \frac{RT}{\alpha F} \ln\left(\frac{i + i_{\text{in}}}{i_0}\right) \tag{3.31}$$

where the total cell current density is sum of the current density circulating through the external circuit far from the equilibrium conditions (i) and of the current density lost through the membrane at open-circuit (i_{in}). Setting $i = 0$ in Eq. 3.31, it is possible to calculate the open-circuit voltage of a PEM fuel cell, which generally results significantly lower with respect to the theoretical value. At practical current density values, that is when an appreciable electron flow is present in the external circuit, the difference between hydrogen concentrations on the two sides of the membrane decreases, then the driving force for hydrogen permeation is strongly reduced, and the crossover losses become negligible (a typical value for i_{in} is 2 mA/cm^2 [50]).

3.3.1.3 Losses Due to Electric Resistance

The sharp slope change of the polarization curve in Fig. 3.5 suggests that after the first steep voltage diminution up to 2 A, attributed to activation and internal current polarization, another type of losses become predominant.

The linear and slower decrease of stack potential with current shown in Fig. 3.5 can be simply explained with the Ohm's law, then the voltage losses due to this effect are described by the following equation:

$$V_{\text{ohm}} = (i + i_{\text{in}})R_{\text{in}} \tag{3.32}$$

where i is the current density and R_{in} is the total cell internal resistance, mainly constituted by electric resistance of cell components and resistance to ionic flow through the electrolyte membrane. Typical values of R_{in} are comprised in the range 0.1–0.2 Ω cm^2 [34].

High conductivity of electrodes, GDL and bipolar plates, and membrane thinness are the obvious ways to reduce the effect of resistive losses.

3.3.1.4 Losses Due to Mass Transport Resistance

The polarization curve in Fig. 3.5 stops when the stack power is close to its maximum nominal value (480 W at 30 A), because other sources of voltage losses would become predominant for higher values of current, whose effect could seriously damage the stack. These losses derive from resistance to the mass transport of gaseous reactants toward the catalytic sites, and of products water out of the cell. The mass transport resistance becomes predominant at high current density, when the rate of reactant consumption is higher than its supply flow rate, and water accumulation inside the cell is faster than its removal. The consequence of this phenomenon is that for a particular current density value (called *limiting current*, i_{L}), the concentration of reactants on electrode surface, and then the stack voltage, would rapidly decrease down to zero. The voltage drop associated with the effect of mass transport resistance can be described by applying the Nernst equation (3.15) to the hydrogen partial pressure gradient density between gas bulk and electrode surface at high current:

$$V_{\text{tr}} = \frac{RT}{2F}\ln\left(\frac{p_{\text{b}}}{p_{\text{s}}}\right) \tag{3.33}$$

where V_{tr} is the voltage change due to mass transport resistance, and p_{b} and p_{s} are the hydrogen partial pressure in the bulk and at the electrode surface, respectively. Assuming a linear diminution of hydrogen partial pressure when the current density increases from i to i_{L}, the variation of p_{s} with current density results:

$$p_{\text{s}} = p_{\text{b}} - p_{\text{b}}\frac{i}{i_{\text{L}}} \tag{3.34}$$

Equation 3.34 evidences that the hydrogen partial pressure on the electrode surface is the same as in the bulk at zero current density, and becomes zero when the current density reaches the limiting value i_{L}. By combining Eqs. 3.33 and 3.34

the relationship for voltage losses associated with mass transport polarization is obtained:

$$V_{\mathrm{tr}} = \frac{RT}{2F} \ln\left(\frac{i_{\mathrm{L}}}{i_{\mathrm{L}} - i}\right) \tag{3.35}$$

which takes into account for the fast voltage drop associated with mass transport losses when the current density approaches its limiting value. This rapid voltage decrease is not represented in Fig. 3.5 as it would occur at current values dangerous for the stack. In these conditions the sudden lack of uniformity of individual cell voltages, accompanied by the straight down potential diminution, could cause the reversal of the electrochemical reaction in some cells, which would operate as electrolysis cells, with direct mixing of hydrogen and oxygen, strong rise of local temperature, and possible damages to the MEA.

All polarization phenomena described above can occur at both anode and cathode of a PEM fuel cell, but due to the higher reaction rate of the hydrogen anodic oxidation with respect to the oxygen cathodic reduction, the anodic polarization can be considered much smaller.

If the contribution of ohmic losses (Eq. 3.32) is substituted in Eq. 3.31, the following general relationship between cell potential and current density can be obtained:

$$E = E^{\circ} - V_{\mathrm{act,in}} - V_{\mathrm{ohm,in}} = E^{\circ} - \frac{RT}{\alpha F} \ln\left(\frac{i + i_{\mathrm{in}}}{i_0}\right) - (i + i_{\mathrm{in}}) R_{\mathrm{in}} \tag{3.36}$$

Equation 3.36 is valid for current densities lower than the limiting value i_{L}, then it does not consider the mass transport resistance, but with the proper values of the parameters α, i_{in}, and i_0 it can be used to fit the polarization curve of Fig. 3.5, taking into account for the cell active area and number of cells.

3.3.2 *Effect of Operative Parameters on the Polarization Curve*

The operative parameters which can be regulated to optimize the stack performance are MEA humidification, reactant pressure, stack temperature, and stoichiometric ratio. While the role of membrane humidification, already partially discussed in Sect. 3.2, is closely considered in Sect. 4.5 and in case studies (Chaps. 6 and 7), the influence of the other parameters is examined here with reference to the stack of Fig. 3.5. These effects have already been described from a thermodynamic point of view (see Sect. 3.1), while kinetic implications are considered in this section for their importance in determining the stack efficiency.

As an example, Fig. 3.6 shows the effect of the relative air pressure on the stack voltage for two different current values, 12 and 25 A [45].

During the above experiment the pressure difference between anode and cathode is maintained under 40 kPa, according to instructions of the stack

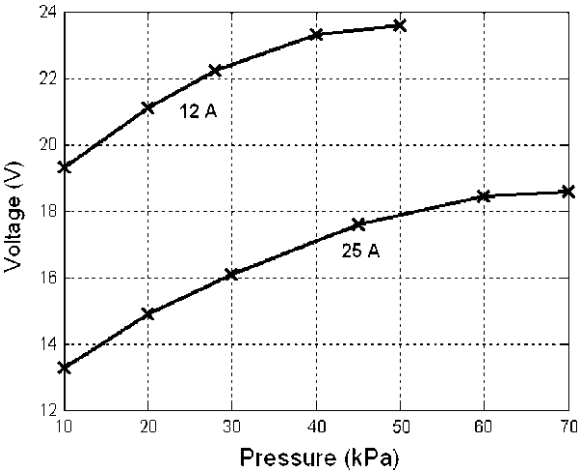

Fig. 3.6 Effect of air pressure on stack voltage for a 500 W PEM stack at two values of stack current. $T = 333$ K, $R = 2$, $p_{H_2} = 10$ kPa

manufacturer, while the other experimental conditions are indicated in the figure legend.

The positive effect of pressure is evident at both the current values considered, in particular if the air pressure is increased at 12 A from 10 to 50 kPa, a stack voltage gain of about 4 V is obtained, while raising the air pressure up to 70 kPa at 25 A, a stack voltage of 18.5 V is observed, with an increase of about 5 V with respect to the value at 10 kPa. An analogue behavior can be observed when the hydrogen pressure is increased, with a stack voltage gain of about 2 V for a pressure raise from 10 to 20 kPa (data not shown in Fig. 3.6).

A higher polarization curve when cell operating pressure is increased can be expected on the base of the Nernst equation (3.15), but the concomitant increase of i_0, due to the higher concentration of reactant gases on electrodes, with the consequent improvement of the hydrogen/oxygen reaction rate, has to be also considered [34].

The effect of stack temperature on the polarization curve is shown in Fig. 3.7, for the temperature range 303–333 K.

Figure 3.7 shows that varying the stack temperature from 303 to 333 K, a voltage increase of about 10% is obtained at all current values after 2 A. This effect cannot be significantly enhanced because of the narrow temperature range which is usually adopted in real stacks (comprised between 300 and 350 K).

Since the electrochemical reaction (3.13) is exothermic (Table 3.1), a potential loss should be expected by thermodynamics; however, the results reported in Fig. 3.7 evidence that kinetic implications are prevalent in determining the global effect of temperature on stack efficiency, in particular the increase in the exchange current density and the improvement of mass transport properties can be invoked to explain the behavior represented.

The effect of the stoichiometric ratio on the stack performance is shown in Fig. 3.8 in terms of total stack voltage versus R for different values of current.

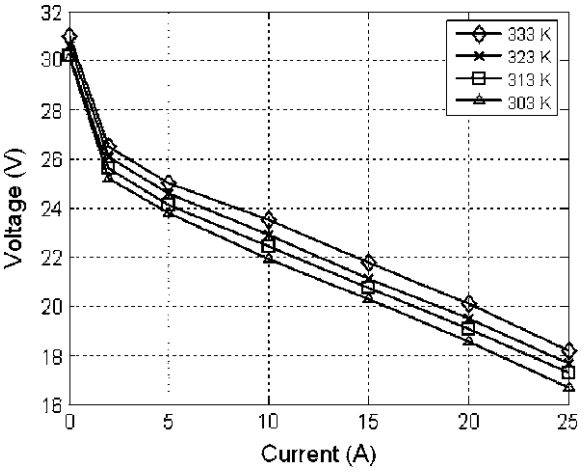

Fig. 3.7 Effect of temperature on the polarization curve of a 500 W PEM stack. $R = 2$–5, $p_{air} = 60$ kPa, $p_{H_2} = 20$ kPa

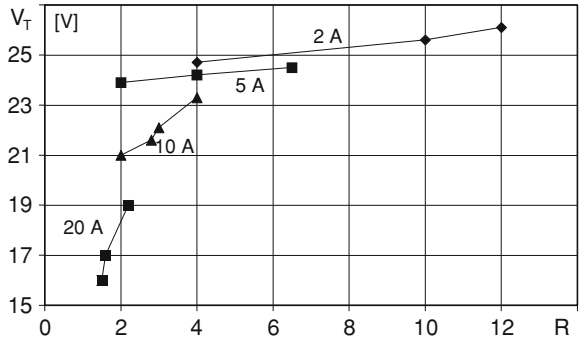

Fig. 3.8 Effect of the stoichiometric ratio R on total stack voltage V_T for a 500 W PEM stack at different values of current. $T = 303$–313 K, $p_{air} = 10$–50 kPa, $p_{H_2} = 10$ kPa

The oxidant is easily supplied to a PEM stack as air fed by compressor. In order to obtain satisfactory and uniform performance for all cells in the stack it is necessary to feed an excess of air with respect to the stoichiometric reaction of hydrogen oxidation ($R > 1$), to overcome the limitations on mass transport on the cathode side.

The experimental data of Fig. 3.8 show that the effect of R on stack performance is limited at low current (2–5 A), and becomes more evident increasing the load (5–20 A); however, for all current values it is advantageous to run the stack at $R > 2$. The upper limit of R which is convenient to use in different conditions depends on the load that is on the hydrogen flow rate consumed at the anode side. In fact to assure an excess of air at high current implies a not negligible power consumption of the compressor used to supply the oxidant to the cathode side.

Also this aspect is closely examined in Chap. 4 and in case studies of Chaps. 6 and 7, but it is anticipated here by the analysis of data reported in Fig. 3.9, where the ratio between the power absorbed by the air compressor used for the tests of Fig. 3.8 and the power supplied by the stack is plotted versus the power supplied by the fuel cell system (FCS power). The results show that an acceptable

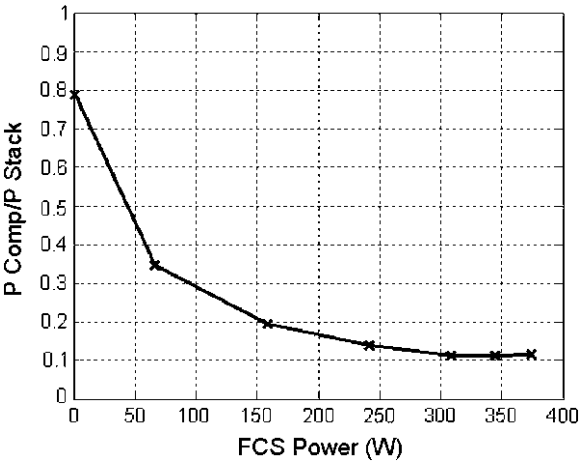

Fig. 3.9 Effect of air compressor consumption for a 500 W PEM stack

compressor consumption (about 10% of stack power) is obtained for high output power (from 200 W up to maximum load) maintaining the stoichiometric ratio not higher than 2, while at low loads the necessity to maintain a minimum air flow rate implies that the energy losses due to the compressor represent a large fraction of the power supplied by the stack.

3.4 Durability of PEM Fuel Cells

Durability is a fundamental and necessary feature for PEM fuel cells to see a wide diffusion as a practical power source in any application field. The requirements for fuel cell lifetime vary with the specific application, in particular a duration of at least 5000 h is mandatory for use on cars, while even longer periods are needed for bus and stationary employments (for most applications an acceptable degradation rate is considered to be comprised in the range 2–10 μV/h [51]). However, the wide variability of operative conditions usually encountered in automotive applications, such as dynamic driving cycles, startup/shutdown phases, and freeze/thaw, makes also the target for car very difficult to be met with the current technologies.

Since the concept of durability decay is strictly connected to that of aging, in the sense of a progressive and not reversible loss of performance, a general examination of this feature for PEM fuel cells has to include some considerations about the main processes that can cause the degradation of materials used for components of these systems (electrocatalysts, membranes, GDL, and bipolar plates), which is mainly related to working conditions of high humidity and temperature, oxidizing or reducing environment, and dynamic operation.

As discussed before the amount of platinum catalyst used in electrocatalysts of a PEM fuel cell is supported on carbon in the form of nanoparticles, in order to

achieve high metal dispersion at relatively low precious metal loading. Then the main problem of aging of electrocatalysts to be avoided or controlled is the increase in catalyst particle size, which causes diminution of active surface area and then of catalytic activity. The coarsening of Pt nanoparticles during PEM fuel cell operation has been extensively studied, and different mechanisms have been proposed [52], among which the so-called *Ostwald ripening* is supported by experimental evidences [53]. This mechanism is based on dissolution and diffusion of Pt particles in the ionomer phase, with successive redeposition on other particles, leading to their size growth. The same mechanism of dissolution and diffusion of Pt particles into the membrane produces also the effect of a degradation of proton conductivity properties of the ionomer, caused by platinum reduction (the presence of hydrogen can determine an effective reducing ambient) and its precipitation inside the membrane bulk [54]. Other possible routes for catalyst agglomeration have found experimental supports, and they are based on coalescence of Pt nanoparticles caused by nanocrystallite migration on the carbonaceous support surface [55].

Also corrosion problems of the carbon support have been considered as a cause of electrocatalyst durability loss [32], in particular carbon oxidation can occur through electrochemical oxidation at the cathode, with formation of CO_2 ($C + 2H_2O = CO_2 + 4H^+ + 4e^-$), or through water gas shift reaction, with the production of CO ($C + H_2O = CO + H_2$). Both these routes are catalyzed by Pt [56, 57] and subtract carbon useful for platinum loading, with consequent metal sintering and decrease of the electrochemical surface area [58].

Since Pt dissolution is favored by high electrode potential, relative humidity, and temperature, the possibility to limit the risk of electrocatalyst aging is based on the use of Pt–alloy catalyst instead of pure platinum, at least for the cathode, which is characterized by higher potential with respect to anode, and by adoption of operative conditions not too severe in terms of humidity and temperature. While this last point requires interventions on the membrane structure, the study of catalyst materials has evidenced that a minor tendency to sintering can be obtained by the addition of non-noble metals, such as Ni, Cr, or Co, to the Pt cathode catalyst [59, 60], suggesting a possible pathway for future work. On the other hand also the potential application of non-platinum catalysts is under study, in particular transition metal complexes with structures based on porphyrines and related derivatives have been proposed to substitute noble metals [61], but their activity performance is still far from those of Pt-based catalysts.

The carbon corrosion issues are faced by the study of different carbonaceous supports, such as carbon black or carbon nanostructures. Recent results evidence the superiority of graphitized carbon with respect to amorphous carbon black in terms of corrosion resistance, and the promising characteristics of carbon nanocages when Pt sintering effects are considered [62].

Another critical issue regarding durability of PEM fuel cells is the reliability of the electrolytic membrane, which can undergo mechanical, thermal, and chemical/electrochemical degradations [63]. The mechanical degradation consists in different types of failure (cracks, pinholes, perforations) which are favored by

varying operative conditions of fuel cells, especially when used for transportation applications. In particular the possibility of degradation is mainly related to different RH conditions, whose effect can range from membrane shrinkage in the absence of external humidification to swelling and in-plane compression at high RH levels. Any type of mechanical failure is very dangerous for stack life, especially pinholes and perforation, because they can allow the crossover of reactant gases with direct hydrogen combustion on the catalyst surface, consequent strong heat release, and local hot spot generation. This initiates a cyclic process of increasing crossover and perforations which can lead to the fast stack degradation.

The thermal degradation of the membrane is connected not only to diminution of proton conductivities properties at high temperatures and low RH levels, but also to decomposition of Nafion in proximity of local hot spots. Moreover, the frequent temperature changes typical of automotive applications can produce severe limitations to proton conductivity, gas impermeability, and mechanical resistance of Nafion membranes, due to phase transformations associated with the wide range of temperatures encountered (from freezing to about 80°C). The mitigation strategies for this degradation cause consist essentially in removal of residual water by gas purging.

The chemical/electrochemical degradation is related to the attack on the membrane and catalysts by peroxide and hydroperoxide radicals, produced by anode and cathode reactions. The formation of these species and the consequent membrane aging is accelerated in OCV and low-RH conditions. The overcoming of this problem requires the developing of new materials able to resist against peroxy radicals, either by addition of free-radical inhibitors (or peroxide decomposition catalysts [64]) during the membrane fabrication or by modifications of its structure [65].

The degradation of the GDL is not clearly assessed because of the difficulties in separating the effects from contiguous elements, such as catalysts and bipolar plates. While some decrease of GDL conductivity and hydrophobicity has been associated with loss of PTFE and carbon, due to temperature and electrochemical surface oxidation during fuel cell operation [66], a recent study suggests that hydrophobicity changes of GDL can be considered negligible in 10000 h tests under high humidification [67].

References

1. Mahan BM (1968) University chemistry. Addison-Wesley Publishing Company, Reading
2. Lange NA (1967) Handbook of chemistry. McGraw Hill, New York
3. Zemansky MW, Abbott MM, Van Hess HC (1975) Basic engineering thermodynamics. McGraw Hill, New York
4. Lide DR, Frederikse HPR (eds) (1996) CRC handbook of chemistry and physics. CRC Press, Boca Raton
5. Atkins P, de Paula J (2002) Physical chemistry. Oxford University Press, Oxford
6. Weaver G (ed) (2002) World fuel cells—an industry profile with market prospect to 2010. Elsevier Advanced Technology, Kidlington, Oxford

7. Kamarudin SK, Achmad F, Daud WRW (2009) Overview on the application of direct methanol fuel cell (DMFC) for portable electronic devices. Int J Hydrogen Energ 34: 6902–6916
8. Gottesfeld S, Pafford J (1988) A new approach to the problem of carbon monoxide poisoning in fuel cells operating at low temperatures. J Electrochem Soc 135(10):2651–2652
9. Kreuer KD (2001) On the development of proton conducting polymer membranes for hydrogen and methanol fuel cells. J Membrane Sci 185:29–39
10. Zawodzinski TA Jr, Spronger TE, Davey J, Jestel R, Lopez C, Valerio J, Gottesfeld S (1993) A comparative study of water uptake by and transport through ionomeric fuel cell membranes. J Electrochem Soc 140(7):1981–1985
11. Chen C, Fuller TF (2009) The effect of humidity on the degradation of Nafion® membrane. Polym Degrad Stabil 94:1436–1447
12. Jiang R, Kunz HR, Fenton JM (2005) Electrochemical oxidation of H_2 and H_2/CO mixtures in higher temperature ($T_{cell} > 100°C$) proton exchange membrane fuel cells: electrochemical impedance spectroscopy. J Electrochem Soc 152(7):A1329–A1340
13. Li Q, He RH, Gao JA, Jensen JO, Bjerrum NJ (2003) The CO poisoning effect in PEMFCs operational at temperatures up to 200°C. J Electrochem Soc 150(12):A1599–A1605
14. Das SK, Reis A, Berry KJ (2009) Experimental evaluation of CO poisoning on the performance of a high temperature proton exchange membrane fuel cells. J Power Sources 193:691–698
15. Mathias MF, Makharia R, Gasteiger HA, Conley JJ, Fuller TJ, Gittleman CJ, Kocha SS, Miller DP, Mittelsteadt CK, Xie T, Yan SG, Yu PT (2005) Two fuel cell cars in every garage? Electrochem Soc Interface 14(3):24–35
16. Hogarth WHJ, da Costa JCD, Lu GQ (2005) Solid acid membranes for high temperature (>140°C) proton exchange membrane fuel cells. J Power Sources 142(1–2):223–237
17. Sone Y, Ekdunge P, Simonsson D (1996) Proton conductivity of Nafion 117 as measured by a four-electrode AC impedance method. J Electrochem Soc 143(4):1254–1259
18. Peinemann KV, Nunes SP (eds) (2008) Membranes for energy conversion. Wiley-VCH Verlag Gmbh & Co. KGaA, Weinheim
19. Yang C, Costamagna P, Srinivasan S, Benziger J, Bocarsly AB (2001) Approaches and technical challenges to high temperature operation of proton exchange membranes fuel cells. J Power Sources 103:1–9
20. Santiago EI, Isidoro RA, Dresch MA, Matos BR, Linardi M, Fonseca FC (2009) Nafion-TiO_2 hybrid electrolytes for stable operation of PEM fuel cell at high temperature. Electrochim Acta 54:4111–4117
21. Harrison WL, Hickner MA, Kim YS, MaGrath JE (2005) Poly(arylene ether sulphone) copolymers and related systems from disulphonated monomer building blocks: synthesis, characterization and performance—a topical review. Fuel Cells 5:201–212
22. Herring AM (2006) Inorganic polymer composite membranes for proton exchange membrane fuel cells. J Macromol Sci C 46:245–296
23. Quinfeng L, Jensen JO, Savinell RF, Bjerrum NJ (2009) High temperature proton exchange membranes based on polybenzimidazoles for fuel cells. Prog Polym Sci 34:339–477
24. Wainright JS, Wang JT, Weng D, Savinell RF, Litt M (1995) Acid-doped polybenzimidazoles—a new polymer electrolyte. J Electrochem Soc 142:L121–L123
25. Schuster M, Rager T, Noda A, Kreuer KD, Majer J (2005) About the choice of the protogenic group in PEM separator materials for intermediate temperature, low humidity operation: a critical comparison of sulphonic acid, phosphonic acid and imidazole functionalized model compounds. Fuel Cells 5:355–365
26. Peng J, Shin JY, Song TW (2008) Transient response of high temperature PEM fuel cell. J Power Sources 179:220–231
27. Sakai T, Takeraka H, Torikai E (1986) Gas diffusion in the dried and hydrated Nafions. J Electrochem Soc 133(1):88–92
28. Paganin VA, Ticianelli EA, Gonzales ER (1996) Development and electrochemical studies of gas diffusion electrodes for polymer electrolyte fuel cells. J Appl Electrochem 26:297–304

29. Sasikumar G, Ihm JW, Ryu H (2004) Dependance of optimum Nafion content in catalyst layer on platinum loading. J Power Sources 132(1–2):11–17
30. Carmo M, Roepke T, Roth C, dos Santos AM, Poco JGR, Linardi M (2009) A novel electrocatalyst support with proton conductive properties for polymer electrolyte membrane fuel cell applications. J Power Sources 191:330–337
31. Wang J, Yin G, Shao Y, Zhang S, Wang Z, Gao Y (2007) Effect of carbon black support corrosion on the durability of Pt/C catalyst. J Power Sources 171:331–339
32. Maass S, Finsterwalder F, Frank G, Hartmann R, Merten C (2008) Carbon support oxidation in PEM fuel cell cathodes. J Power Sources 176:444–451
33. Lim KH, Oh HS, Kim H (2009) Electrochem Commun 11:1131–1134
34. Barbir F (2005) PEM fuel cells. Theory and Practice. Elsevier Academic Press, Burlington
35. Bevers D, Rogers R, Bradke M (1996) Examination of the influence of PTFE coating on the properties of carbon paper in polymer electrolyte fuel cells. J Power Sources 63:193–201
36. Lim C, Wang CY (2004) Effects of hydrophobic polymer content in GDL on power performance of a PEM fuel cell. Electrochim Acta 49:4149–4156
37. Park S, Popov BN (2009) Effect of cathode GDL characteristics on mass transport in PEM fuel cells. Fuel 88:2068–2073
38. Cindrella L, Kannan AM, Ahmad R, Thommes M (2009) Surface modification of gas diffusion layers by inorganic nanomaterials for performance enhancement of proton exchange membrane fuel cells at low RH conditions. Int J Hydrogen Energ 34:6377–6383
39. Kannan AM, Kanagala P, Veedu V (2009) Development of carbon nanotubes based gas diffusion layers by in situ chemical vapour deposition process for proton exchange membrane fuel cells. J Power Sources 192:297–303
40. Li X, Sabir I (2005) Review of bipolar plates in PEM fuel cells: flow-field designs. Int J Hydrogen Energ 30:359–371
41. Mehta V, Cooper JS (2003) Review and analysis of PEM fuel cell design and manufacturing. J Power Sources 114:32–53
42. Wang SH, Peng J, Lui WB (2006) Surface modification and development of titanium bipolar plates for PEM fuel cells. J Power Sources 160:485–489
43. Abo El, Enin SA, Abdel-Salam OE, El-Abd H, Amin AM (2008) New electroplated aluminum bipolar plate for PEM fuel cells. J Power Sources 177:131–136
44. Feng K, Shen Y, Sun H, Liu D, An Q, Cai X, Chu PK (2009) Conductive amorphous carbon-coated 316L stainless steel as bipolar plates in polymer electrolyte membrane fuel cells. Int J Hydrogen Energ 34:6771–6777
45. Corbo P, Corcione FE, Migliardini F, Veneri O (2006) Energy management in fuel cell power trains. Energy Convers Manage 47:3255–3271
46. Crow DR (1998) Principles and applications of electrochemistry. Stanley Thornes (Publisher) Ltd., Cheltenham
47. Mann RF, Amphlett JC, Peppley BA, Thurgood CP (2006) Application of Butler-Volmer equations in the modelling of activation polarization for PEM fuel cells. J Power Sources 161:775–781
48. Petrii OA, Nazmutdinov RR, Bronshtein MD, Tsirlina GA (2007) Life of the Tafel equation: current understanding and prospects for the second century. Electrochim Acta 52:3493–3504
49. Gutman EM (2005) Can the Tafel equation be derived from first principles? Corros Sci 47:3086–3096
50. Larminie J, Dicks A (2003) Fuel cell systems explained. Wiley, Chichester
51. Knights SD, Colbow KM, St. Pierre J, Wilkinson DP (2004) Aging mechanisms and lifetime of PEFC and DMFC. J Power Sources 127:127–134
52. Shao Y, Yin G, Gao Y (2007) Understanding and approaches for the durability issues of Pt-based catalysts for PEM fuel cells. J Power Sources 171:558–566
53. Watanabe M, Tsurumi K, Mizukami T, Nakamura T, Stonehart P (1994) Activity and stability of ordered and disordered Co-Pt alloys for phosphoric acid fuel cells. J Electrochem Soc 141:2659–2668

54. Akita T, Taniguchi A, Maekawa J, Siroma Z, Tanaka K, Kohyama M, Yasuda K (2006) Analytical TEM study of Pt particle deposition in the proton-exchange membrane of a membrane-electrode-assembly. J Power Sources 159:461–467
55. Zhai Y, Zhang H, Xing D, Shao Z (2007) The stability of Pt/C catalyst in H3PO4/PBI PEMFC during high temperature life test. J Power Sources 164:126–133
56. Li W, Lane AM (2009) Investigation of Pt catalytic effects on carbon support corrosion of the cathode catalyst in PEM fuel cells using DEMS spectra. Electrochem Commun 11:1187–1190
57. Stevens DA, Hicks MT, Haugen GM, Dahn JR (2005) Ex situ and in situ stability studies of PEMFC catalysts. J Electrochem Soc 152:A2309–A2315
58. Shao YY, Yin GP, Gao YZ, Shi PF (2006) Durability study of Pt/C and Pt/CNTs catalysts under simulated PEM fuel cell conditions. J Electrochem Soc 153:A1093–A1097
59. Colon-Mercado HR, Popov BN (2006) Stability of platinum based alloy cathode catalysts in PEM fuel cells. J Power Sources 155:253–263
60. Zhang S, yuan XZ, Cheng Hin JN, Wang H (2009) A review of platinum-based catalysts layer degradation in proton exchange membrane fuel cells. J Power Sources 194:588–600
61. Charreteur F, Jaouen F, Dodelet JP (2009) Iron porphyrin-based cathode catalysts for PEM fuel cells: Influence of pyrolysis gas on activity and stability. Electrochim Acta 54:6622–6630
62. Oh HS, Lim KH, Roh B, Hwang I, Kim H (2009) Corrosion resistance and sintering effect of carbon support in polymer electrolyte membrane fuel cells. Electrochim Acta 54:6515–6521
63. Collier A, Wang H, Yuan X, Zhang J, Wilkinson DP (2006) Degradation of polymer electrolyte membranes. Int J Hydrogen Energ 31:1838–1854
64. Ramani V, Kunz HR, Fenton JM (2005) Stabilized composite membranes and membrane electrode assemblies for elevated temperature/low relative humidity PEFC operation. J Power Sources 152:182–188
65. Curtin DE, Lousenberg RD, Henry TJ, Tangeman PC, Tisack ME (2004) Advanced materials for improved PEMFC performance and life. J Power Sources 131:41–48
66. Kangasniemi KH, Condit DA, Jarvi TD (2004) Characterization of Vulcan electrochemically oxidized under simulated PEM fuel cell conditions. J Electrochem Soc 151:E125–E132
67. Hiramitsu Y, Sato H, Hosomi H, Aoki Y, Harada T, Sakiyama Y, Nakagawa Y, Kobayashi K, Hori M (2009) Influence of humidification on deterioration of gas diffusivity in catalyst layer on polymer electrolyte fuel cell. J Power Sources 195:435–444

Chapter 4
Design of Hydrogen Fuel Cell Systems for Road Vehicles

A fuel cell stack does not work by itself, but its operation requires the utilization of several auxiliary sub-systems to permit an efficient and reliable electric power production. In this chapter all these components are described, evidencing their role in determining the fuel cell stack operation. In particular, this discussion is aimed at verifying if and how a fuel cell system (FCS) could really match all vehicular requirements, evidencing the parasitic losses of auxiliary components and dynamic performance in terms of response to start-up, frequent stop and go phases, fast load changes, variable power levels. The interaction between FCS performance and management strategies necessary to guarantee an optimal stack operation in automotive applications is discussed, with a brief overview of FCS costs.

Several models of FC vehicles fuelled by H_2 have been produced by many car's industries in the past two decades, characterized by interesting performance and promising reliability (i.e., Mercedes-Benz presented at the end of 2009 the new model B class F-Cell equipped with new generations of fuel cells, Li-ion batteries, and advanced fuel storage tanks). Other solutions with the stack fed with liquid fuels (methanol, gasoline, and diesel) have been also proposed, but they require an on-board fuel processor to transform the liquid mixture into hydrogen. In this case the impact of the fuel processor on the choice of the hybridization level for the whole propulsion system (see Sect. 5.5) and on stack durability needs to be carefully considered. Dynamic response of FCS with processor unit would be too slow mainly because of its thermal inertia, implying that the stack has to operate almost in steady state conditions, while the unavoidable presence of some compounds in reformer outlet stream, such as CO or NH_3, also in very low concentrations, are dangerous contaminants for the activity of stack electrodes. Recently it has been estimated that start-up time would be less than 4 min to lower the CO level present in the stream at acceptable values [1], but long-term durability of stacks fed by reformate stream is far to be demonstrated.

P. Corbo et al., *Hydrogen Fuel Cells for Road Vehicles*,
Green Energy and Technology, DOI: 10.1007/978-0-85729-136-3_4,

On the other hand, the use of a fuel processor on-board of a vehicle makes it too complex for a practical commercialization in the automotive field, independently on carbon emissions associated to utilization of not renewable fuels.

Moreover, PEMFC systems fed by pure hydrogen show the highest relative performance in terms of system dynamics, costs of fuel cells (the precious metal loading of anode is minimum), and in terms of stack and system power densities, which result 1.3 and 0.6 kW/l, respectively [2, 3].

In this chapter the discussion is limited to the so-called *direct hydrogen fuel cell system* (H_2FCS) excluding from the analysis alternative configurations utilizing hydrogen containing carriers (hydrocarbon mixtures, methanol) instead of pure hydrogen as feed.

4.1 Hydrogen Fuel Cell Systems: Preliminary Remarks

The main operative characteristics of PEMFC stacks can be summarized in the following points:

1. Different fuels can be used but hydrogen is the best reducing agent for an efficient and reliable operation of PEMFC.
2. Oxygen is the ideal reactant to feed cathode side of the stack, however also air feed is suitable, but in this case an excess of oxidant is required.
3. Water is the product of the electrochemical reaction.
4. Pressure and temperature increase the individual cell performance.
5. The electrolytic membrane needs to be maintained properly hydrated in all operative conditions of pressure and temperature.
6. Heat is a by-product of fuel cell reaction and progressively boosts the stack temperature.
7. The stack temperature cannot exceed 90°C.

Thus, the optimization of PEMFC performance in terms of efficiency and reliability requires a proper design and management of reactant feeding sections, as well as of cooling and humidification sub-systems [4].

The selection and sizing of auxiliary devices, also called ‘balance of plant’ (BOP) components, depends on their interactions with the stack and on all other possible inter-connections inside the overall system.

In Fig. 4.1 a scheme of a direct hydrogen FCS is reported. The scheme points out all input and outputs of the plant: the oxidant is ambient air, while the fuel enters into the FCS coming from the selected H_2 storage device (see Sect. 2.3). The electrochemical hydrogen oxidation produces electric energy, water and heat, the last two can be partially recovered for stack management. The same Fig. 4.1 indicates the main FCS subsystems necessary to manage reactant feeding, control stack temperature, and assure adequate membrane humidity level during stack operation. The interconnections between all sub-systems, shown in Fig. 4.1, underline the necessity of a complex integration among BOP components and

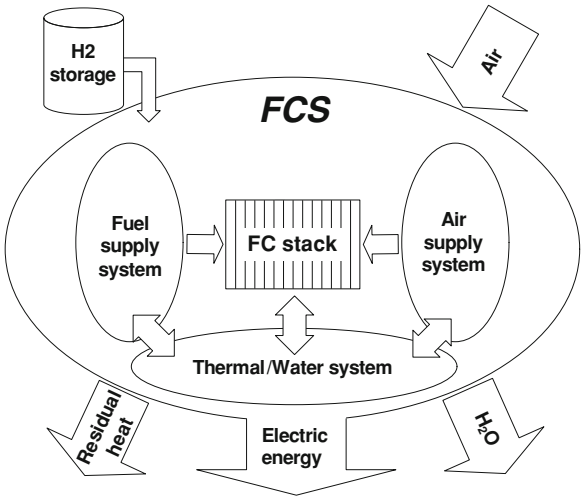

Fig. 4.1 General scheme of a direct H_2 PEMFC system (H_2FCS) for vehicles

stack, to optimize the FCS efficiency and reliability and to fully exploit the dynamic performance of PEMFC.

The design of the fuel feeding section has to be focused on the optimal feeding of hydrogen to the anode compartment of the stack. Details about the behavior of the main components involved in hydrogen feeding management are given in Sect. 4.2.

Different typologies of air supply systems are examined in Sect. 4.3, in particular their performance are analyzed in terms of pressure working and power consumption.

Thermal management system is necessary because the reaction heat gradually elevates the MEA temperatures. This aspect, related also to humidification issues, requires the development of a sub-system able to control both stack temperature and heat flux inside the overall system. The related discussion is presented in Sect. 4.4.

FCS water management is the key factor for an efficient and reliable operation of a PEMFC stack. Membrane hydration control and water balance for a durable operation of FCS are the main objectives of this sub-system, whose design and control issues, strictly connected to thermal management but also to reactant sub-system components, are discussed in Sect. 4.5. The possibility of interactions between the wet and warm cathode outlet stream and the components of thermal and water management sub-systems is also discussed.

The analysis of the above sub-systems refers to BOP components suitable for fuel cell vehicle applications, and underlines the main aspects related to the framework of interactions inside a whole FCS.

A discussion about a basic configuration for a H_2FCS is carried out in the Sect. 4.6, where an integrated plant is studied analyzing the main issues to be faced for optimizing overall efficiency and reliability. The effect of the main operative parameters on the system working is discussed, analyzing the dynamic behavior issues related to fast load changes and warm-up phases. A brief overview on costs expected for stack and BOP components closes this chapter.

4.2 Hydrogen Feeding System

The layout of the fuel feeding sub-system and its management strategy depends on the typology of fuel tank installed on-board. For any type of hydrogen storage system (see Sect. 2.3), the main parameters to be controlled in hydrogen feeding sub-systems are: working pressure, relative humidity, fuel purity grade, and fluid-dynamic conditions.

Hydrogen can be supplied either in dead-end or in a flow-through mode. The choice of feeding pure hydrogen as fuel, rather than hydrocarbon derived hydrogen mixtures, permits the choice of the so-called "dead-end" configuration as option of fuel feeding. In this case hydrogen is loaded to the stack as pressurized gas, thanks to a valve normally closed placed at the outlet. It means that the current supplied by the stack determines the occurrence of a fuel flow rate through the anode channels, exclusively related to the power required. On the other hand, the hydrogen flux stops in the absence of load. This solution needs generally a purge valve to drain out the possible excess of nitrogen and water accumulated in the anode side during stack operation. This valve is generally an electronic controlled solenoid valve. An alternative operative mode, suitable also if fuel cell vehicle is equipped with a fuel reformer, is represented by the so-called "flow-through" configuration. This option requires additional components such as hydrogen recycle pump or ejectors. The choice between the two configurations affects the design of the specific sub-system and could influence its integration with the other FCS components.

A scheme of a fuel feeding sub-section in a direct hydrogen FCS for automotive application is shown in Fig. 4.2. Pressure regulation sub-system design has the objective to regulate inlet pressure to assure the hydrogen flow rate necessary to the chemical reaction. The inlet pressure and fuel purge represent the main parameters to be controlled in both operative modes, however, the role of the purge valve is different for the two possible configurations. In a dead-end configuration and when air is used as oxidant, nitrogen tends to crossover from the

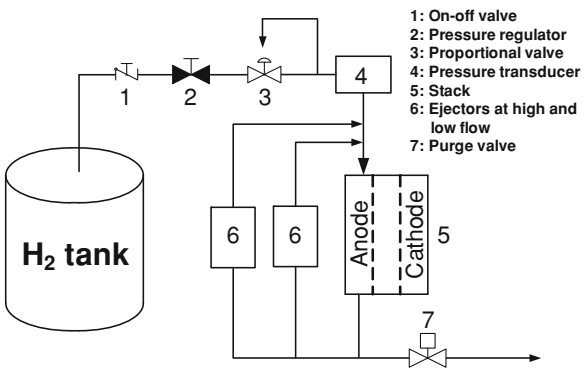

Fig. 4.2 A scheme of a generic pure hydrogen feeding sub-system in flow-through mode. Without ejectors the same scheme refers to dead-end mode

cathode flow field through the electrolyte to the anode side. As fuel is consumed in the fuel cell, the concentration of nitrogen in the anode compartment increases, thus accumulating therein and negatively impacting the performance of the fuel cell [5]. Moreover, the humidification control (see Sect. 4.5) could create operative phases characterized by a dangerous stagnation of liquid droplets on surface of electrodes in cathode and anode sides, favoring flooding of the compartments and fuel starvation, and then interfering with the access of the hydrogen fuel during stack power requirement. Then the purge action, draining out the possible excess of nitrogen and water accumulated in anode compartment, can eliminate most of liquid molecules from the catalyst surface and refresh the feed. As a consequence the overall strategy for maintaining the well-hydrated cell membranes, assuring a reliable and efficient stack operation with minimization of nitrogen crossover and simultaneously avoiding the flooding phenomena, should involve the periodic acting of the purge valve. This is normally closed but, when necessary, the control strategy expects to open it by managing the opening frequency for a specified opening time, sufficient to drain the contaminants but not too long for undesired leaking of useful fuel. In order to evaluate the effect of purge operation on FCS efficiency, it is possible to define a coefficient expressing the ratio of fuel converted to fuel supplied (η_{util} in Sect. 6.2), which can reach values higher than 90% in optimized realizations [6, 7].

On the other hand, in flow-through mode a system layout based on fuel recirculation by means of a pump or ejector-diffusers can be adopted in the anode circuit [8]. In this case a portion of the exhausted fuel is recirculated from the outlet to the inlet section through a loop and mixes with fresh fuel from the fuel supply. An important advantage of this solution is that the mixed fuel entering the fuel cell stack is at least partially humidified, and this aspect can bring strong benefits to an overall humidification management strategy, avoiding or minimizing external humidification of anode stream (see Sect. 4.5). However, nitrogen could cross-over from the cathode side through the conductor membrane to the anode side and then could affect the fuel purity in the recirculation loop. This behavior reduces the performance of the fuel cells and the efficiency of the recirculating device. In addition, contaminants from the fuel source can also be accumulated in the anode flow fields (and/or in anode recirculation loop) as fuel is consumed. Thus, this approach does not exclude the use of a purge valve; indeed it is highly recommended that a remainder portion of anode stream is purged periodically, in order to limit fuel purity decrement during FCS operation. However, the proper management of this layout of fuel feeding section could improve the control of anode humidity and purity, minimizing hydrogen escape. In ejector systems, based on Bernoulli's principle, the supply flow passes down through a nozzle and Venturi tube. They are passive devices that need no parasitic power, however, their actual performance, in terms of optimal regulation of anode humidity with recirculating flow, should be improved to match all automotive FCS requirements [9]. Instead of ejectors a blower could be inserted in the anode loop to increase the pressure and recirculate hydrogen. This solution permits sizing and controlling the sub-system adding an independent parameter for FCS management, but it is not

immune from problems. In particular a proper cooling of the warm gaseous mixture containing hydrogen, nitrogen and steam, is required to maintain a satisfactory durability of the hydrogen recirculation blower. Furthermore, the addition of other components determines an increase of parasitic power consumption of the overall FCS [8].

Finally the possibility to utilize electrolysers to elevate hydrogen pressure and recirculate it inside anode flow fields in H_2FCS power sources has been recently considered [10]. This electro-chemical approach for hydrogen pumping could be effected with an external additional smaller PEMFC component, connected to the stack devoted to electric power generation, or alternatively using in electrolysis mode a group of cells of the main PEMFC stack.

In flow-through operation a slight voltage decrease of individual cells is observed with respect to the simple dead-end configuration, but also a more stable fuel cell performance, i.e., due to a minimum intervention of parasitic purge. The role of purge in an integrated humidification strategy is further discussed in Sect. 4.5.

4.3 Air Feeding Systems

The sub-system described in this section has the function to feed the oxidant to the cathodic compartment. Air is the oxidant commonly used in PEMFC, while the use of pure oxygen in high pressure cylinders, in spite of higher stack performance, is generally not preferred for a practical application on fuel cell vehicles since the addition of oxygen tanks in fuel cell propulsion systems would limit the space available for the hydrogen fuel storage devices, which is one of the most critical issues for a practical application of hydrogen fuel cell vehicles. Moreover, oxygen must be produced, concurring to a well-to-wheel efficiency decrease.

The key parameters to be controlled in this sub-system are air mass flow rate and pressure. Therefore, this section is focused on the characteristics of devices capable to realize useful pressure and flow rate of the oxidant feed (blowers and compressors), postponing the discussion about the integration of air supply system with the other FCS sub-systems to the successive three sections, which are dedicated to thermal and water management strategies and to overall system performance optimization.

Free convection mode is not sufficient to assure a satisfactory oxygen concentration at the cathode surface and then an acceptable fuel cell power [11]. Thus, the most adopted solution for the design of oxidant feeding section is represented by the utilization of a compact air compressor device [1]. The overall air supply system is based on the air compressor, but could also include an expander in high pressure plants (pressure higher than 2 bar), to recover a part of pressure energy.

An important aspect related to air supply sub-system for the attainment of optimal FCS operation is the selection of a compressor highly efficient in all operative conditions suitable for automotive application.

The theoretical energy consumption of a compressor (as well as any machine transforming mechanical energy) in reversible adiabatic conditions can be calculated by the following equation:

$$L_{\text{mecc}}^{\text{id}} = h_2 - h_1 = \int_{p_1}^{p_2} v\mathrm{d}p \tag{4.1}$$

where $L_{\text{mecc}}^{\text{id}}$ is the reversible ideal mechanical work necessary to actuate the compressor, h_1 and h_2 are the enthalpy of the fluid before and after the compression stage, v is the specific volume of the fluid, and p is the working pressure, that changes from the entering value p_1 to the exit value p_2.

The operative conditions suitable for air feeding section in H_2FCS suggest that the air stream can be considered as ideal gas mixture. The relationship of polytropic compression for an ideal gas is:

$$T_2 = T_1 \times \left(\frac{p_2}{p_1}\right)^k \tag{4.2}$$

and in adiabatic conditions:

$$k = (\gamma - 1)/\gamma \quad \gamma = c_p/c_v$$

where T_1 is the entering temperature value, T_2 represents the exit value after compression stage, c_p and c_v are the specific heat at constant pressure and volume, respectively. The parameter k assumes the value of 0.285 for air.

The ideal power consumption (P_{id}) related to isoentropic (adiabatic) compression can be calculated according to:

$$P_{\text{id}} = m_\text{a} \cdot c_\text{p} \cdot T_1 \cdot \left[\left(\frac{p_2}{p_1}\right)^k - 1\right] \tag{4.3}$$

where m_a is the air mass flow rate. The equation (4.3) evidences that the theoretical energy losses necessary to run a compressor depend almost exclusively on mass flow rate and on compression ratio (p_2/p_1).

Furthermore, a real machine designed for adiabatic compression does not reach the ideal point of reversible iso-entropic process, because of unavoidable irreversible transformations. The reversible work associated to the pressure increase inside a fluid can be always calculated as $\int_{p_1}^{p_2} v\mathrm{d}p$, while the net enthalpy variation is directly related to mechanical energy consumption, which increases with irreversibilities.

Then the efficiency (η_c) of a compressor is defined as:

$$\eta_\text{c} = \frac{\int_{p_1}^{p_2} v\mathrm{d}p}{L_{\text{mecc}}} \tag{4.4}$$

where L_{mecc} is the total mechanical energy required to reach the final desired pressure value. Furthermore, the efficiency parameter η_c includes also the additional contribution related to friction of moving parts (mechanical losses). Finally the real power consumption of a compressor device can be calculated as:

$$P_{real} = \frac{P_{id}}{\eta_c} \tag{4.5}$$

On the other hand, a fraction of power consumption related to compressor can be recovered from the electric work obtainable from exhaust gas by using a turbine. This electric power can be calculated according to the following equation:

$$P_{real} = m_{ex} \cdot c_{pex} \cdot T_{ex} \cdot \left[1 - \left(\frac{p_{atm}}{p_{ex}}\right)^{\frac{k-1}{k}}\right] \times \eta_{exp} \tag{4.6}$$

where η_{exp} represents the turbine efficiency while the other parameters are strictly related to FCS management. In particular, m_{ex} is the exhaust flow rate, T_{ex} and p_{ex} correspond to stack temperature and pressure, while c_{pex} is the specific heat of the exhaust mixture. The choice of a proper high efficiency compressor is an important criterion also when Compressor Expander Module (CEM) groups are selected in high pressure plants [4].

In Fig. 4.3 two schemes of the air supply sub-system are reported, related to both low and high pressure fuel cell plants. As the air supply sub-system implies the highest power consumption among all BOP components, and could heavily affect the overall system efficiency (see Sect. 4.6), the utilization of blowers (Fig. 4.3a) would permit to limit power losses, even if their impact on the overall efficiency would not be negligible. In fact, blowers not only require a not negligible electric power consumption especially at minimum load, but they can provide low air pressure values, then limiting cell voltages and thus stack efficiency (see Sect. 3.3). In any case the low cost and simplicity make this solution more appropriate for small size power trains (1–10 kW).

On the other hand, high pressure determines a higher energy consumption associated to the compressor, then a CEM can be used to recover some energy from the pressurised cathode exhaust stream (Fig. 4.3b). This solution adds complexity to the on-board power plant and can be usefully applied in medium large-size fuel cell power trains (10–100 kW).

The air feeding strategy must minimize the disadvantages related to an excessive parasitic power consumption and meanwhile to oxygen starvation. The last problem exists when air is fed to cathode side instead of pure oxygen, and depends on variable partial pressure of oxygen during stack dynamic operation. The control strategy capable to overcome the O_2 starvation is based on a careful regulation of inlet pressure to realise values of air flow rate higher with respect to stoichiometric requirements. Oxygen concentration in the air intrinsically decreases crossing through the reaction cells. The inert nitrogen moles contained in the air remain unchanged during stack operation, and oxygen concentration drops at the catalyst

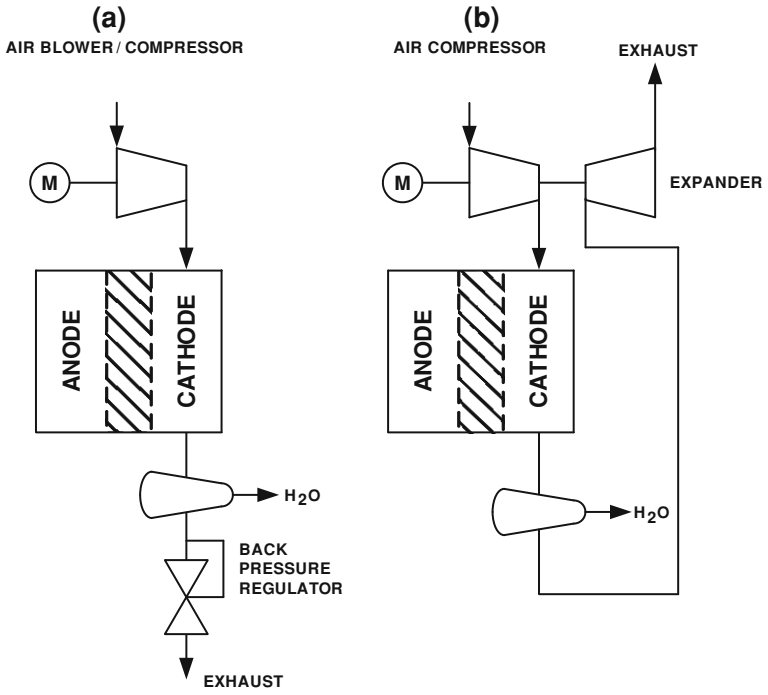

Fig. 4.3 Scheme of air feeding sub-system in low (**a**) and high (**b**) pressure plants. *M* compressor motor

surface, requiring then an excess of air variable as function of load. In particular the stoichiometric ratio *R* (defined in Sect. 3.3) needs to be about 2 in a wide range of operative conditions (details about air management strategy and related *R* values are reported in case studies, Chaps. 6 and 7). On the other hand, if the risk of starvation is reduced, the energy consumption related to compression stage of higher mass flow rates could increase dramatically, strongly limiting the overall FCS efficiency (see also Sect. 4.6).

A further requirement to be satisfied by the oxidant supply device is represented by dynamic performance in a wide range of air flow rates. This aspect is crucial in some hybrid power train operative modes characterized by high stack dynamics (*full power* or *soft hybrid* configurations, see Sect. 5.5).

A compressor should also match the other typical requirements of a road vehicle, in particular noise, cost reduction, and compactness. A further consideration derives from the quality of oxidant required by the stack. The air must be very clean since the presence of few small oil droplets or traces of chemical contaminants could damage dramatically the fuel cells, reducing their efficiency and durability. Therefore, PEMFC systems require oil-free compressors or air filtration for removing particulate and contaminants (sulfurs, salts, CO, and hydrocarbons).

Several typologies of blowers or compressors are potentially suitable for fuel cell application. In Fig. 4.4 a flow diagram of all compressor types is reported, distinguishing two main classes (dynamic and positive displacement) and different typologies for each (reciprocating and rotary as positive displacement devices, and centrifugal and axial as dynamic machines).

Among dynamic machines a centrifugal compressor results more efficient and cheaper than axial compressors in the power range useful for vehicular applications. Motor-driven compressor/blowers for air feeding in small medium-size FCSs are based on centrifugal type impellers [4]. In a side channel blower (Fig. 4.5) the energy coming from the motor is transferred to the air which is accelerated radially and circumferentially. The fluid is forced into the side channels, determining a pressure and kinetic energy increase. Thus, the air is again accelerated and transported along a spiral path through the impeller and the side channels until it is discharged. The balanced rotating impeller represents the unique moving part of the compressor. A further advantage of this device is that there is no contact between the impeller and the housing, eliminating abrasion phenomena and generally material consumption, thus improving its reliability and durability. Finally the side channel blower is completely oil-free and produces low noise levels.

The blowers operate in a limited pressure range, but they are able to satisfy the overall pressure drop through stacks operating at low pressure (lower than 0.5 relative bar) [12, 13].

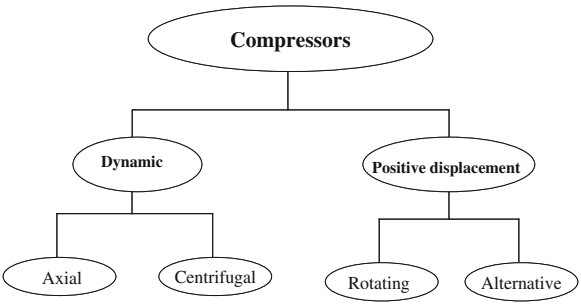

Fig. 4.4 A basic scheme of compressor classification

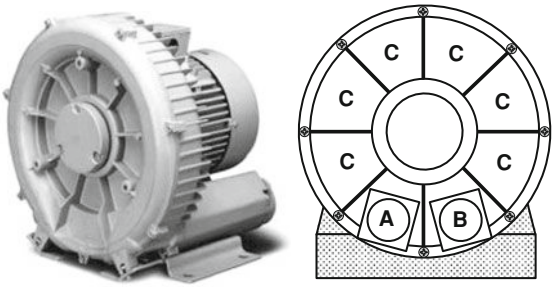

Fig. 4.5 Side channel blower for fuel cell applications. *A*/*B* air inlet/outlet, *C* side channels

The centrifugal air compressor at high speed seems the actual best choice for FCS sized up to 100 kW [14]. The operation principle is the same of the centrifugal blower, depending on transfer of energy from a rotating impeller to the air. The pressure is created by converting the angular momentum determined by the rotating impeller. Higher speeds permit high efficiency values to be reached. The centrifugal air compressor is an oil-free compressor by design. The oil lubricated running gear is separated from the air by shaft seals and atmospheric vents. A high pressure air management system based on dynamic machines has been successfully developed and applied to an 80 kWe FCS. It consists of a CEM group, constituted by axial-radial liquid-cooled compressor coupled to a variable nozzle radial turbine [15].

Positive displacement compressors offer more flexible compression ratio at low fuel cell loads, moreover rotating devices offer the additional advantage of a not fluctuating or flow rate with respect to alternative machines.

Within the class of rotating positive displacement particular interest has been recently addressed toward scroll and screw compressors.

A scroll compressor uses two interleaved spiral-like vanes to compress air stream. Generally one of the scrolls is fixed, while the other scroll is mobile and orbits without friction in eccentrical way. Several air bladders are formed and moved towards the center of the two spirals reducing their volume. The pressure increases and then the air can be discharged. The operation of this kind of machine results less noise and more smooth than alternative devices and reliable in the low volume range [16]. Water in a scroll compressor could be used as both lubricant and coolant, permitting nearly isothermal compression to be obtained [17]. The advantages of scroll compressors have been then exploited in the development of prototypes of compressor/expander modules to be used for designing air supply in pressurized FCS [18].

Rotary screw compressors represent a different type of rotating positive displacement and have been largely used in the last decades for industrial applications and in particular for air conditioning and refrigeration systems. Their performance is attractive in terms of efficiency, compactness, simplicity, and reliability. A screw machine consists essentially of a pair of meshing helical lobed rotors which rotate within a fixed casing that totally encloses them. As the mechanism rotates, the meshing and rotation of the two helical rotors produces the internal air compression by means of a series of volume-reducing cavities which capture the inlet stream. Outlet stream is then discharged after volume reduction in the cavities. Capacity control for these compressors is accomplished by variable speed and variable compressor displacement.

Screw compressors can be either single or multistage machines, in dependence of the final desired pressure level. In multistage option the air is compressed by several sets of screws and can achieve pressure values higher than 0.5 relative bars.

Recently twin screw devices equipped with water injection have been intensively studied in order to optimize their performance in view of a possible application as BOP component suitable to feed cathode stream in FCS. The utilization of water as cooling and sealing medium permits controlling both operating

temperatures and air leakage, limiting power consumption and thus optimising the compressor efficiency [19]. On the other hand, the additional power consumption due to water injection slightly reduces the overall consumption.

4.4 Thermal Management System

The design of the temperature control system has a strong effect on both performance and dynamics PEMFC [20–22]. The electrochemical conversion of hydrogen occurring in polymeric electrolyte fuel cells produces heat as by-product, due to the unavoidable irreversibilities of the process. This heat elevates the temperature of local reaction sites inside the MEA, and progressively of the entire stack by conductive transmission through bipolar plats and by convective flow within the reactant feeding channels. As the cell voltage during stack operation drops well below the reversible value (about 1.2 V), ranging from 0.9 V to about 0.5 V in the entire current density range, according to the Ohm's law (see Sect. 3.3), the following equation can be used to calculate the thermal power produced inside the stack:

$$\dot{Q} = \Delta V = (V_{\mathrm{id}} - V) \times I \tag{4.7}$$

where $\dot{Q}$ is the produced heat rate, I is the electric current flowing through the cells, while V_{id} and V are the reversible and actual cell voltage values, respectively.

The dynamics of temperature change associated with the produced power is derived by the following differential equation:

$$\partial T/\partial t = \frac{\dot{Q}}{m \times c_{\mathrm{p}}} \tag{4.8}$$

where $\partial T/\partial t$ (time derivative) is the rate of temperature change, m is the whole mass stack, c_{p} represents the stack average specific heat. Equation 4.8 is further discussed in Sect. 4.6, where the dynamic behavior of the overall FCS and the optimization of integrated management strategies are clarified.

The design issues of thermal management sub-system depend on the total produced heat and of consequence on the sizing of the stack. The mass flow rate of coolant (usually deionised water) can be derived by the definition of thermal capacity described by the following equation:

$$\dot{m}_{\mathrm{H_2O}} = \frac{\dot{Q}}{c_{\mathrm{p}} \times (T_{\mathrm{f}} - T_{\mathrm{i}})}$$

where Q is the produced heat rate, c_{p} is the specific heat of water, while $T_{\mathrm{f}} - T_{\mathrm{i}}$ is the temperature difference of the coolant between stack output (T_{f}) and input (T_{i}). A value of $T_{\mathrm{f}} - T_{\mathrm{i}}$ not higher than 5 K is advisable [11].

In Fig. 4.6 a scheme of cooling circuit related to FCS for automotive application is shown. The main components are the pump for liquid circulation, the water reservoir and the heat exchanger with fan. For small size stacks (from 100 to 500 W) it is possible to use only air forced by fan to cool directly the stack, while for higher powers, more suitable for automotive requirements (1–100 kW), it is reasonable to use an internal coolant circuit fed by a liquid, such as de-ionised water or ethylene glycol–water mixtures, to improve the heat removing capacity of an order of magnitude with respect to the gas.

The stack cooling is not the unique aspect to be examined in the context of FCS thermal management, but also the possibility of heat recovery has to be also considered. At this regard, additional devices have to be used, such as air-to-air heat exchangers, humidifiers, or condensers that partially exploit the enthalpy content of cathode outlet and coolant streams [23]. In particular enthalpy wheels, which are rotary air-to-air heat exchanger, can be used to preheat the inlet exploiting the enthalpy content of the wet and warm cathode outlet stream, which is a gaseous mixture at the approximately the same temperature of the stack in saturated conditions. They transfer mainly heat but allow also moisture to be exchanged. The device is quite compact and can achieve high energy transfer effectiveness. It is constituted by a cylinder filled with a permeable material with high surface area (polymer, aluminum, or synthetic fiber), necessary for the sensible heat transfer. The driving force for realizing the exchange is the thermal gradient between the opposing air streams.

The enthalpy exchange is accomplished through the use of typical adsorbent materials such as silica gel, zeolites or other molecular sieves which transfer water molecules by the difference in the partial pressure of vapor within the opposing air streams. The operation of a FCS that includes this component requires specific

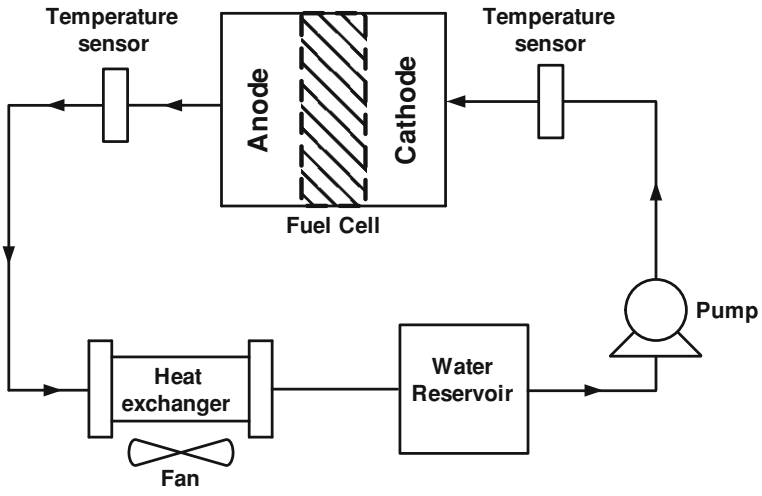

Fig. 4.6 Water cooling sub-system for H_2FCS

methods able to dynamically control the rotational speed of the wheel according to the process variables.

4.5 Water/Humidification Management System

Polymeric proton exchange membrane needs to be maintained properly humidified to guarantee a satisfactory ion conductivity during stack operation (see Sect. 3.2). In fact it exists a strong relationship between proton conductivity and water content of Nafion material used as membrane in PEMFC [24, 25]. Unfortunately the water produced at cathode side and the air moisture could be not sufficient to maintain properly wet the membranes in all working conditions, because of complex phenomena involving water within MEA [26] (Fig. 4.7).

The Fig. 4.7 refers to water fluxes occurring inside a MEA fed by pure hydrogen in dead-end configuration (see Sect. 4.2) and by not saturated air stream. The following four events are evidenced:

1. The water is produced on cathode electrode surface ($O_2 + 2H^+ + 2e^- \rightarrow H_2O$).
2. A back diffusion occurs from cathode side to anode through the electrolyte because of concentration gradient.
3. H_2O molecules are dragged by protons during stack power requirement (electro-osmotic drag).

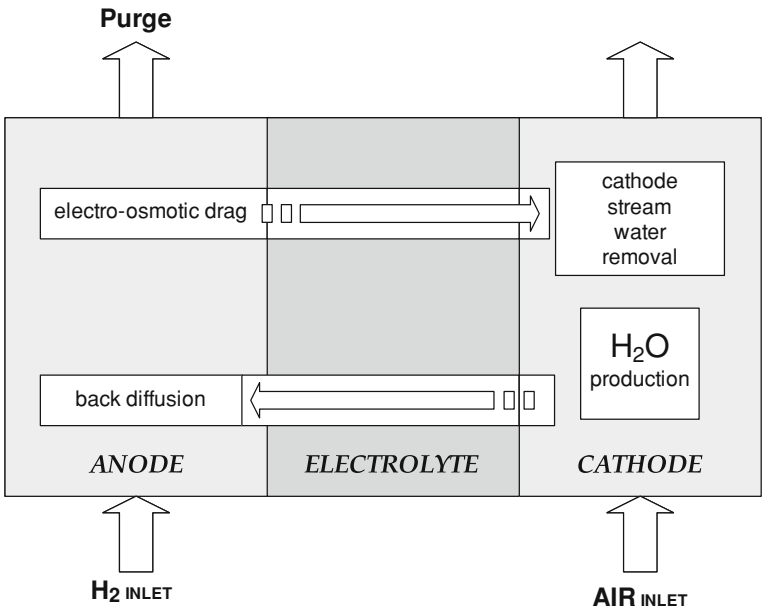

Fig. 4.7 Water behavior inside MEA of PEMFC

4. H_2O molecules in cathode compartment are removed by continuous flow of not saturated air stream; a similar event, but of minor magnitude, occurs also in the anode compartment in recycling hydrogen configuration or during purge in dead end configuration.

The electro-osmotic drag could limit the effect of back diffusion mechanism by transfer of water from the anode to cathode side, thanks to the drag of hydrated protons, with a linear relationship with current density [27].

Finally water removal capacity of reactant streams, especially air stream, withdraws definitively a part of the water from the cell module. These quantities could become very significant at high temperature, exceeding the water produced by electrochemical reaction. This happens because evaporation rate and saturated vapor pressure of water increase with temperature in a non-linear relationship [1].

In Table 4.1 saturation pressure of water vapor and related maximum humidity ratio are reported as function of temperature in the range of interest for PEMFC utilization and atmospheric pressure. The humidity parameter is defined as ratio between the mass of water vapor present in saturated air to the mass of the dry air.

At high temperatures air streams could contain large water amounts as vapor phase, maintaining a continuous strong potential of drawing water molecules by electrode surface, as relative humidity value (RH, defined as ratio between gravimetric density of actual vapor to gravimetric density of saturated vapor at the same temperature) remains always well below 100% along the entire cathode feeding channel. The temperature of wet air stream typically remains lower than local surface temperature of electrode, thus evaporation rate is fast concurring to drying out of membrane that represents one of the main problems to be faced for an optimal operation of FCS [1], especially at low pressure. The above criticality is well evidenced if we consider that the electro-osmotic drag causes a movement of water molecules from anode to cathode side, only partially balanced by the counterflow related to diffusion by concentration gradient. On the other hand, the working pressure could strongly affect the maximum humidity amount of air stream, as pressures higher than atmospheric value reduce the water requirement necessary to reach the saturation.

Table 4.1 Effect of temperature on saturated air parameters, $P = 1$ atm

Temperature (°C)	Saturated pressure of water vapor (kPa)	Maximum humidity ratio ($g_{H_2O}kg_{dry\ air}$)
0	0.6	3.8
10	1.2	7.5
20	2.3	15
30	4.2	27
40	7.4	49
50	12	78
60	20	120
70	31	190
80	47	270

The above considerations about the effect of several operative conditions (current density, temperature, and pressure) on membrane hydration evidence that the primary target of water management strategy is to avoid possible drying out phenomena, making necessary the development of proper strategies to maintain an adequate humidity grade inside the membrane during all FCS operative conditions suitable for automotive application. Water addition to reactant streams could be an useful approach, as the control of the humidity content of hydrogen and air streams entering into the stack certainly limits the above described drying phenomena.

But another important complication is related to a not uniform distribution of humidity inside the electrolyte and on the catalyzed electrodes, and to the eventuality of incipient flooding phenomena, due to an excess of water bulked inside the fuel cell module that could dangerously limit the reactant entrance to active sites of catalyzed electrodes. This phenomenon could be present also without external water addition, because dry air streams entering into the cell module gradually moisturize creating the possibility of local flooding at the end of their path [28].

Flooding phenomena should be avoided by careful management of the entire FCS, but if the complication occurs, it is necessary to act rapidly on hydrogen feeding management procedure or on air flow rate control, in order to drain the excess of water overheaped in both anode and cathode compartments. The purge valve in fuel feeding circuit (see also Sect. 4.2) should be open with different frequency or delay, as well as air flow rate should be varied modifying transitorily the stoichiometric ratio (see also Sect. 4.3). As better discussed in Sect. 4.6 humidification management procedures can surely affect overall FCS efficiency, furthermore the careful control of both drying and flooding phenomena could condition not only the design of the stack (MEA and flow field channels) but also the layout of the integrated FCS, by inclusion of additional ancillary components, that can cooperate to a limitation of overall efficiency.

The different humidification approaches could be classified as internal or external methods. Internal humidification means that humidification procedure concerns exclusively the inner spaces of fuel cell stack, while external humidification involves modifications in feeding stream humidity ratio outside of the stack [1, 29].

The simplest method is the "self-humidification", based on the principle that a fraction of water content of the membrane remains inside the polymeric material and water produced by reaction during stack operation is sufficiently absorbed by the electrolyte [30]. No external humidification is required and the membrane humidification is controlled acting on internal operative parameters, with a management that exploits exclusively the transport mechanisms through the electrolyte. Self-humidification is limited by the membrane diffusion properties. At high MEA temperature (>90°C) the back diffusion rate of water becomes the limiting factor, because water uptake by reactant gases increases with temperature and water transport due to electro-osmotic drag increases with current density. Since the membrane limits the back diffusion rate, the electro-osmotic drag becomes

the dominant mechanism and water is transported away from the anode and hence the anode will dry out while cathode will become flooded. Then temperature and stack power are the key parameters to maintain wet the membranes in self-humidification conditions.

The membrane hydration is related also to air flow management. Air stream passes through cathodic compartment becoming progressively warm and wet, and favors a drying effect, that is strongly non linear in its relationship with temperature. At temperature higher than 60°C the relative humidity of outlet air can result easily lower than saturation (100%). By controlling the *R* parameter it is possible to manage RH close 100% of exit cathode streams and then to control hydration of membranes. Small size FCS (<3 kW) could operate in reliable self-humidification condition if a proper working temperature (<60°C) was adopted in FCS management, correlated to adequate stack powers during the execution of pre-defined driving cycles [6]. The maximum power drops of about 40% but the efficiency remains high.

A further "internal" technique, known as "internal membrane humidification" uses liquid water injection directly inside the stack, specifically designed to receipt "water droplet spray". A portion of the membrane is set aside to humidify the inlet gas and liquid water is injected directly into this inactive portion of the stack, permitting then the possibility for a more flexible water management thanks to an additional governable parameter [31, 32]. Internal humidification strategies generally reduce the complexity of the FCS design, and present a further important advantage: the gases are conditioned inside the stack, and their temperature is very close to membrane temperature itself, avoiding fast evaporation and then dehydration. However, a portion of membrane is not used for reaction and the power density decreases.

On the other hand, the use of external humidification is essential at high temperatures, because the concentration gradient of H_2O in the membrane of individual cells would be more uniform if both air and hydrogen streams were humidified externally. The external water supply helps to balance the combined effects of electro-osmotic drag and back diffusion permitting to maintain the performance of the membrane. External humidification is practically useful also below 60°C, at least for medium large-size FCS.

A possibility is to saturate at different temperatures the reactants before they enter into the stack [33]. This approach can be accomplished by several procedures based on external dewpoint, external evaporation, steam injection with downstream condensers, or flash evaporation. High temperature values allow to absorb significant water amount in gas streams and then transport it inside the stack compensating the water losses due to internal fast evaporation. However, the main problem with external humidification is that the gas cools after the humidifier device, the excess of water could condense and enter the fuel cell in droplet form, which floods the electrodes near the inlet, thereby preventing the flow of reactants. On the other hand, "internal liquid injection" method appears preferable for example with respect to the steam injection approach because of the need of large energy requirement to generate the steam.

Most common humidifier devices are used mainly for air hydration, but sometimes also for hydrogen humidification, and are based on bubblers, water evaporators, enthalpy wheels, membranes, or on a pump for liquid water injection inside a mixer or directly inside the first part of the cathode side collector. Membrane humidifiers or injection pumps have been prevalently proposed for hydrogen humidification.

In bubblers the gas directly passes through the liquid in an external wash bottle, but the control of relative humidity is hard to be accomplished in all operative conditions. Furthermore, the wet stream cooled before entering the stack can form small droplets very dangerous for cell performance maintenance.

The humidification of the reactant gases could be successfully realized by using membrane humidifiers [34, 35]. The water content of a wet stream can be transferred across a semi-permeable membrane to a dry stream (Fig. 4.8). The membrane separates the dry stream compartment from the other compartment crossed by with liquid water or wet stream. Theoretically the dry stream could increase its water vapor content along the entire interface area of the membranes from the inlet up to close the saturation value at the exit of the device. The design includes a tubular form for the humidifier and a counterflow to optimize the exchange. This device could be more suitable for FCS management with respect not only to bubbler humidifier but also to water vapor injection method, as the last systems need additional equipments, make the whole system complex and increase

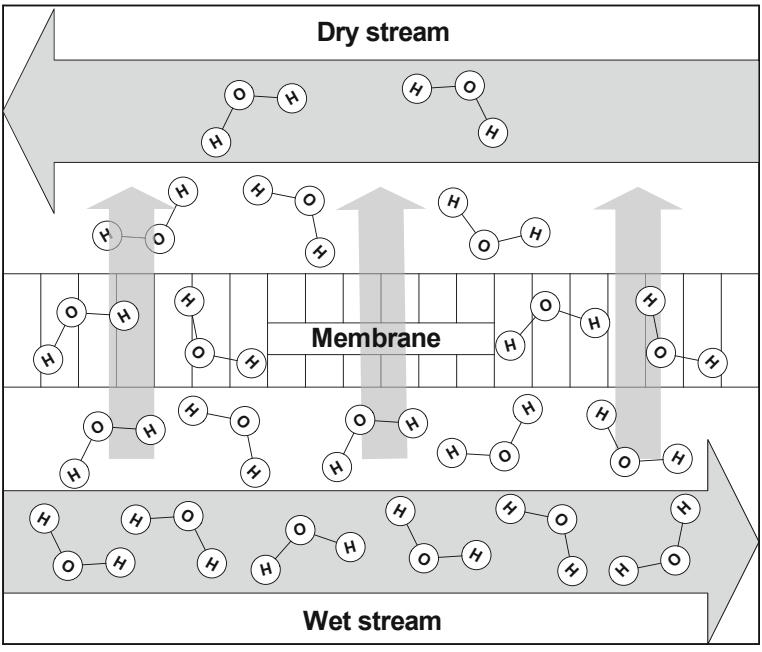

Fig. 4.8 Principle of membrane-based humidification

parasitic energy consumption. The basic material used in membrane technology of PEMFC (Nafion) has been also proposed for membrane fabrication in humidifier devices [35] (see Sect. 3.2).

In the last decade some companies have patented new solutions that combine humidification and cooling [36]. Plug Power Inc. has designed an innovative cooler-humidifier [37], constituted by a plate with a flow of liquid water to remove heat on one side, and wicks that moisten the reactant gases on the other side. Evaporation of water at the humidification side provides additional cooling.

There have also been attempts to control the water in the cell by using porous graphite plates or by external wicking connected to the membrane to either drain or supply water by capillary action. More reliable forms of H_2O management are based on continuous flow field design and appropriate operating conditions [38]. A temperature rise can be used between the inlet and outlet of the flow field to increase the water vapor carrying capacity of the gas streams. Recent studies have been addressed towards the development of advanced materials for improving membrane performance. A new method involves multilayer composite polymer electrolytes [39] where the humidifying layer contains platinum catalyst particles.

Another widely used method involves evaporation of liquid water injected into the gas stream [36]. An atomizing nozzle could be used to inject water into the gas flow streams of hydrogen and air. The latent heat required for H_2O evaporation causes gas temperature decrease, thus a heater around the injection chamber is necessary. In addition, a long pipe equipped with heaters is useful to fully water evaporation, avoiding condensation. In this case humidity control could be difficult as well as the transient response would result very low, limiting the practical application of this solution.

The water balance inside FCS requires at least a water condenser located at the outlet of the stack. This device has the dual role to condense a significant part of the water content of the warm and wet cathodic outlet stream (a mixture of nitrogen, oxygen, and water vapor with the probable presence of small water liquid droplets) for re-cycling in humidification devices, and to transfer/recover a part of significant thermal energy content of the cathode stream. The condenser could also collect, but in minor quantities, the excess water content of the anode compartment. The condenser is then aimed at maintaining the vehicle endurance and to cooperate to efficiency maximization.

4.6 Integrated Fuel Cell System: Efficiency, Dynamics, Costs

Life cycle assessment studies demonstrate the potentialities of vehicles powered by fuel cells in terms of both total emission and energy consumption reduction [40–42].

In particular, while the global environmental benefits of hydrogen are essentially depending on the selected production technology (see Sect. 2.1), and the

electrochemical approach for hydrogen oxidation assures intrinsically zero local emissions, the potentialities of the fuel cell power generator play the crucial role in determining the efficiency of a fuel cell propulsion system. On the other hand, the expected fuel consumption of a vehicle depends not only on energy conversion efficiency of the FCS but also on lightness and compactness of all propulsion system components.

The FC power system could be practically applied in transportation field if it demonstrated to own some essential qualifications, not limited to energy efficiency, but extended to operation durability, also in terms of water neutrality, and to FCS dynamic response during start-up and variable driving requirement phases.

Beside the characteristics of the main components involved in stack management, already previously underlined, in this section the system integration concerns involving dynamic behavior of individual sub-systems are analyzed, detailing their impact on efficiency evaluation and stack response in automotive conditions. The inter-connections between the stack and some crucial ancillary components are specifically discussed to itemize the basic design issues of an integrated FCS and to support the analysis of management strategies for vehicle consumption optimization in several automotive conditions.

For a low pressure configuration the air supply system includes the compressor preceded by a filter, while for a high pressure option a CEM group could be adopted, adding an expander to the compressor and recovering the high energy content of the outlet stream. In low pressure plant the hydrogen section is based on dead-end configuration with a purge valve electronically controlled, while in high pressure configuration the purged hydrogen should be used optionally in a burner to enhance operation of the expander/turbine [43]. Higher hydrogen exhaust flow rate increases the electric power recovered from turbine reducing parasitic losses but the net efficiency results lower because of a minor utilization of the fuel [43].

A representative scheme of a low pressure FCS plant for automotive application is shown in Fig. 4.9. The reactant supply sub-systems could directly interact with thermal and water management sub-systems, by means of a simultaneous transfer of heat and mass into the humidifier devices, which should be inserted at the entrance of the stack for both reactants. Thermal sub-system includes an internal coolant circuit that is essentially constituted by a liquid pump, a radiator necessary to reject the stack waste heat, and a liquid reservoir. Other minor but equally important components are the de-ionizer filters, thermostat, and valves.

However, the cooling sub-system should expect interactions with the humidification devices inserted in air and hydrogen feeding pipelines. In particular the warm cooling liquid outgoing from the stack can transfer a fraction of its enthalpy content to feeding streams for their humidification, before passing through the air cooled radiator. Humidification/water sub-system is constituted by all humidifiers inserted in the overall layout, and by a water recovery loop, which concur to realize an overall process water circuit.

This sub-system includes in particular condensers and demisters at the outlet of cathode and anode compartments to recover a significant part of the high water

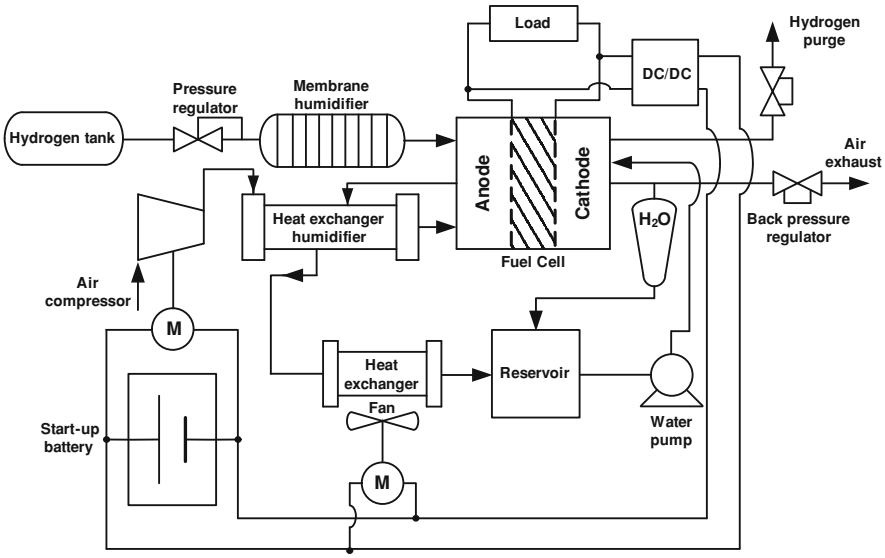

Fig. 4.9 Example of a low pressure H_2FCS integrated plant

content of the exhaust cathodic stream, and in minor quantities of the anode outlet stream. The recovered water could be used as feed of humidifiers installed in the entrances of the stack for oxidant or for both reducing and oxidant streams, concurring to the operation of stack in water neutral conditions, improving reliability of the power generator.

4.6.1 FCS Efficiency

The behavior of fuel cells in terms of individual and overall voltage as function of current density represents the basic performance from which an overall efficiency evaluation has to start. The impact of the parasitic consumption of auxiliary components involved in the system management strategies on the net power produced by the fuel cell stack represents the second important step to be carefully evaluated.

The main ancillary components that concur to reduce the gross stack power are reported in Fig. 4.10. The auxiliaries are actuated electrically, and the total DC power produced by stack is partially consumed by the motors that move the compressors and pumps, and by the electricity necessary to supply the radiator fan and the controller.

The power consumption of ancillary components results particularly significant in the low power ranges [44], and among them the air compressor provides the

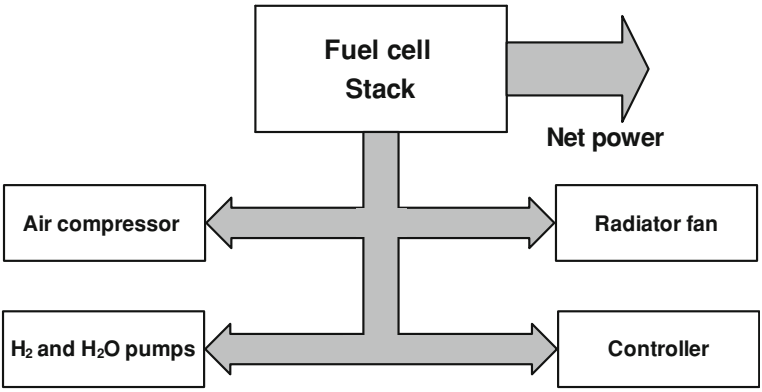

Fig. 4.10 Main energy losses related to ancillary components of a H_2FCS

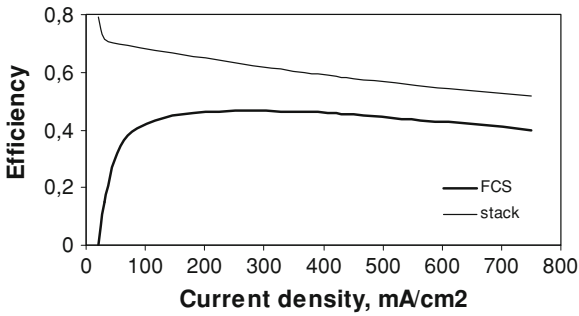

Fig. 4.11 Stack and fuel cell system efficiency as function of current density [46]

major contribution, in particular an air compressor alone in low pressure plants, or Compressor Expander Modules in high pressure plants, would spend about 7–10% of the net produced power by the stack. All the auxiliary components determine an average consumption of about 25% of the net stack power [12, 45].

The role of auxiliaries can be also clarified by curves of Fig. 4.11, where stack and system efficiency are shown as function of current density for a PEMFC stack of 2.5 kW [46]. The FCS curve shows unsatisfactory efficiency values at very low current density (lower than 100 mA/cm^2), in particular evidence that electrical ancillary devices strongly affect the net stack power in the power range corresponding to the non-linear variation region of cell voltage. When net stack power increases a profile tending almost to a plateau in a wide range of load is obtained [12, 13, 45, 47], corresponding to the linear profile of polarization curve.

Stack needs to operate in this last range in most part of driving conditions in order to guarantee high conversion efficiency. Efficiency loss due to fuel cells is then limited to the resistance to proton flow through the polymeric membrane. The system efficiency profile at low current density can be explained taking into account that fuel cells are more efficient at part load (see stack efficiency curve), and the impact of parasitic component consumption on net produced power

gradually reduces with the load (see the area comprised between the two curves of Fig. 4.11).

The performance of the air compressor affects both stack and system efficiency by means of the impact of flow rate level and working pressure on both cell voltage and compressor consumption [48, 49]. Low pressures and low stoichiometric ratios minimize the compressor consumption but stack efficiency results negatively affected (see also Sect. 3.3).

On the other hand, the choice of working at high pressure assures improvements in individual cell performance, beside the disadvantage related to the not acceptable energy consumption of the compressor, but it determines other advantages, essentially related to the possibility of reducing the severe requirements for thermal and water/humidification devices. In particular the water necessary for stream humidification is reduced as well as the higher temperature differences minimize the costs and the sizes of heat exchangers [1, 45]. The size of power plant could address the choice of working pressure (see Sect. 4.3).

4.6.2 FCS Dynamics

Another important automotive qualification for a fuel cell engine is its dynamic response to driving requirements. Vehicle drivability should require very fast accelerations and rapid decelerations. It is desirable that the power generator is able to deliver maximum power (almost up to 90%) with very short time delay. Conventional engines are able to support the dynamic drivability requirements, but the fuel consumption on overall driving cycles results strongly affected by the contribution of these phases characterized by several not optimized working conditions. Hybrid solutions have been recently proposed to improve pollutant emission levels and fuel economy, exploiting the best efficiency conditions of internal combustion engines. Hybridization approach, that involves a significant contribution of energy storage systems (traction batteries, supercapacitors), should be used also in fuel cell vehicles with the aim of minimizing hydrogen consumption and maximizing the performance of the overall propulsion system. Electric energy storage systems can assist the FCS or the internal combustion engines in supporting high power dynamic requirements of the vehicle and permit energy recovery during braking phases. Then the hybridization approach would permit the steady state operation of the power generator. This possibility results really interesting for IC engines, because emissions and fuel consumption could be strongly reduced, while these advantages need to be carefully verified in fuel cell vehicles. Hybridization does not change significantly the concern of evaluating the dynamic characteristics of the FCS [45], as fuel cells present high efficiency at part load and system efficiency is high in a wide range of loads. Load variations could then intercept many working points at high efficiency. Thus, the analysis of their dynamic performance in a wide range of operative conditions appears desirable.

First of all it is important to analyze the response rate to transient or dynamic requirements of all individual sub-systems, included the stack [50]. The electrochemical phenomena that occur inside the fuel cell stack are very fast, while water and thermal management systems show an enormous inertia with respect to typical vehicle requirements. In particular working temperature is a crucial parameter for designing BOP components such as heat exchangers, condensers and humidifiers devices to match dynamic requirements. Equation 4.8 could be used to demonstrate that the thermal capacity of the whole stack limits the dynamic in temperature change.

On the other hand, fuel supply system response (when hydrogen is stored in high pressure tanks) results intrinsically faster than air supply system. The dynamics of this last sub-system appear particularly significant for the evaluation of dynamic performance of an overall FCS [48], as air compressor response is the limiting step for an adequate response of stack to load requirement changes. In particular the variations in air flow rates have to guarantee instantaneous stoichiometric ratios always not much lower than 2 during fast accelerations [49].

A dynamic corresponding to a variation rate from 10 to 90% of maximum power in about 5 s appears the best actual performance of a well-balanced FCS for automotive application [6]. However, the reliability of the stack undergone to several dynamic cycles based on the above power variation rate need to be verified. The question is firstly to instantaneously avoid flooding at low temperature or de-hydration at high temperatures. FCS management strategies have to consider the low response rate to changes in working conditions of water/thermal sub-system. A variation of operating temperature may occur only slowly, while dynamic operation of FCS requires rapid shifting in electric power production.

Two crucial phases have to be considered:

1. Taking into account that an optimal strategy should expect a maximum temperature level (about 75°C), during minimum power working points at high temperature the water produced inside the stack results very low, in spite of a fast evaporation from the membrane. Humidifier operation is then essential to assure saturated streams inside the stack. Fortunately the operative conditions are beneficial (low air flow rate and high temperature) for exploiting the performance of thermal/humidification devices.
2. During start up, when the stack temperature and then performance (voltage) are low the passive BOP devices devoted to stream and stack humidification (enthalpy wheels membrane humidifiers) do not work as they are essentially based on the difference of temperature and then are practically excluded by the FCS management; on the other hand, at low temperature the requirements for stack humidification are strongly reduced and membrane could self-hydrate if a sufficient water production (proportional to power requirement) occurs.

The presence of water in the system makes FCS susceptible to freezing, and specific procedures are necessary to purge almost completely the stack when it stops during winter seasons in cold countries [43]. A portion of catalyst surface (especially at cathode side) could be covered with ice becoming not capable to carry

out the electrochemical reaction. At present, rapid unassisted cold start of PEMFC stacks is still hardly feasible, especially when room temperatures reach values lower than −20°C [51]. The warm-up of the stack starting from subfreezing temperatures implies that stack temperature must be raised above 0°C before the ice completely covers the cathode surface, blocking the reaction progress. Managing buildup of ice is the key to realize an effective start-up, and recent modeling studies suggest that it is useful to operate the stack near short-circuit conditions [51], as "ohmic heat" (Eq. 4.7) is the largest heating source at low cell voltages [52].

4.6.3 FCS Costs

A discussion on manufactured costs of fuel cell vehicles, with particular emphasis to PEMFC stacks and BOP components, is useful to assess the present limits for the commercialization with high production volumes. Recent evaluations evidenced that the estimated costs related to PEMFC and integrated FCSs results too high, at least four to five times higher than conventional engines [15, 53, 54]. At this regard PEMFC stack materials and the relative complexity of FCS play an important role in determining the overall expected cost. A drastic reduction of the costs is then crucial for a realistic application in automotive field.

Projected costs for an high pressure plant of about 80 kWe realized by Argonne Laboratories in 2005 have been fully estimated [15], considering the existent technology but also including some conceptual future possibilities for improved materials and related FCS management strategies. In the Table 4.2 a breakdown of the most significant costs for FCS components, expressed as percentage ratio between the individual component and actual reference FCS cost, is summarized. It can be noted that the stack is largely the most expensive device in H_2FCS (63%), but future developments could strongly reduce its impact on overall cost (about 30%).

The electrodes represent, in stack manufacture, the main outlay (77%), while membranes (6%), gas diffusion layers (5%), and bipolar plats (5%) follow spaced out. Electrode costs are strictly related to the very expensive Pt content. Thus,

Table 4.2 Projected costs for stack and BOP components

FCS component	Projected actual cost (%)	Projected future cost (%)
Stack	63	30
Air management system	13	12
Water management system (humidifiers)	7	3
Fuel supply system (blowers and ejectors)	4	4
Coolant pumps and fans	4	3
Miscellaneous and assembly	9	9
Total		
Overall FCS cost	100	61

Adapted from ref. [15]

many efforts are aimed at significantly reducing Pt loading in electrocatalysts [55, 56]. Recent results evidence that the activity of Pt catalysts in cathode reaction can be maintained or even enhanced by partially replacing the noble metal with the cheaper nickel [57], while a new deposition method could offer promising potentialities in terms of interfacial durability [58]. On the other hand, the degradation mechanisms of the different components of MEA and in particular related to Pt particle sintering [59] need to be continuously verified for future innovative cheaper materials.

The most important cost abatement of BOP components will probably derive by further developments in fuel cell membrane technology, especially in terms of higher resistance to humidity level changes during power system operation [15]. In particular these advances would permit to reduce dramatically the requirements for the water management sub-system by eliminating some expensive devices. The necessity to operate at high pressure should be suppressed as option, making the turbine not necessary, but especially the plant could exclude membrane humidifiers (impact on costs reduces from 7 to 3%) and hydrogen purge valves. These actions have obvious positive effects not only on the overall cost, but also on the reliability and simplicity of the FCS. On the other hand, the high costs of MEA, bipolar plates of the stacks as well as of dedicated BOP components could benefit from the potential of cost reduction trend related to larger volume of production.

References

1. Bowers BJ, Zhao JL, Ruffo M, Khan R, Dattatraya D, Dushmann N, Beziat JC, Boudjemaa F (2007) Onboard fuel processor for PEM fuel cell vehicles. Int J Hydrogen Energ 32:1437–1442
2. Mench MM (2008) Fuel cell engines. Wiley, Hoboken, NJ
3. Von Helmolt R, Eberle U (2007) Fuel cell vehicle: status 2007. J Power Sources 165: 833–843
4. Larminie J, Dicks A (2000) Fuel cell systems explained. Wiley, Chichester
5. Ahluwalia RK, Wang X (2007) Buildup of nitrogen in direct hydrogen polymer-electrolyte fuel cell stacks. J Power Sources 171:63–71
6. Corbo P, Migliardini F, Veneri O (2007) Performance investigation of 2.4 kW PEM fuel cell stack in vehicles. Int J Hydrogen Energ 32:4340–4349
7. Sasaki H, Soga T, Yatake T, Kano A (2002) Development of 30 kW class PEFC system with pure hydrogen fuel. FCDIC Fuel Cell Symp Proc 9:117–121
8. Rodatz P, Buchi F, Onder C, Guzzella L (2004) Operational aspects of a large PEFC stack under practical conditions. J Power Sources 128:208–217
9. Kima M, Sohna YJ, Choa CW, Lee WY, Kim CS (2008) Customized design for the ejector to recirculate a humidified hydrogen fuel in a submarine PEMFC. J Power Sources 176(2): 529–533
10. Barbir F, Gorgun H (2007) Electrochemical hydrogen pump for recirculation of hydrogen in a fuel cell stack. J Appl Electrochem 37:359–365
11. Li PW, Zhang T, Wang QM, Schafer L, Chyu MK (2003) The performance of PEM fuel cells fed with oxygen through the free-convention mode. J Power Sources 114:63–69

12. Corbo P, Migliardini F, Veneri O (2007) Experimental analysis and management issues of a hydrogen fuel cell system for stationary and mobile application. Energ Convers Manage 48:2365–2374
13. Corbo P, Corcione FE, Migliardini F, Veneri O (2006) Experimental assessment of energy-management strategies in fuel-cell propulsion systems. J Power Sources 157:799–808
14. Tirnovan R, Giurgea S, Miraoui A, Cirrincione M (2008) Surrogate modelling of compressor characteristics for fuel-cell applications. Appl Energ 85:394–403
15. Ahluwalia RK, Wang X (2008) Fuel cell systems for transportation: status and trends. J Power Sources 177:167–176
16. Yuanyang Z, Liansheng L, Jiang S, Wei Z, Pengcheng S (2003) Research on oil-free air scroll compressor with high speed in 30 kW fuel cell. Appl Therm Eng 23:593–603
17. Zhao Y, Li L, Wu H, Shu P (2005) Theoretical and experimental studies of water injection scroll compressor in automotive fuel cell systems. Energ Convers Manage 46:1379–1392
18. Mc Taggart P (2004) Development of a hybrid compressor/expander module for automotive fuel cell applications. Final Technical Report for DOE Contract DE-FC36-01AL67603
19. Jianfeng L, Huagen W, Bingming W, Ziwen X, Pengcheng S (2009) Research on the performance of water-injection twin screw compressor. Appl Therm Eng 29:3401–3408
20. Hussain MM, Baschuk JJ, Li X, Dincer I (2005) Thermodynamic analysis of a PEM fuel cell power system. Int J Therm Sci 44:903–911
21. Kandlikar SG, Lu Z (2009) Thermal management issues in a PEMFC stack–A brief review of current status. Appl Thermal Eng 29:1276–1280
22. Ahn JW, Choe SY (2008) Coolant controls of a PEM fuel cell system. J Power Sources 179:252–264
23. Bao C, Ouyang M, Yi B (2006) Analysis of the water and thermal management in proton exchange membrane fuel cell systems. Int J Hydrogen Energ 31:1040–1057
24. Ciureanu M (2004) Effects of Nafion dehydration in PEM fuel cells. J Appl Electrochem 34:705–714
25. Weng FB, Jou BS, Li CW, Su A, Chan SH (2008) The effect of low humidity on the uniformity and stability of segmented PEM fuel cells. J Power Sources 181:251–258
26. Park YH, Caton JA (2008) Development of a PEM stack and performance analysis including the effects of water content in the membrane and cooling method. J Power Sources 179:584–591
27. Andreaus B, Scherer GG (2004) Proton-conducting polymer membranes in fuel cells—humidification aspects. Solid State Ionics 168:311–320
28. Karimi G, Jafarpour F, Li X (2009) Characterization of flooding and two-phase flow in polymer electrolyte membrane fuel cell stacks. J Power Sources 187:156–164
29. Huizing R, Fowler M, Mérida W, dean J (2008) Design methodology for membrane based plate-and-frame fuel cell humidifiers. J Power Sources 180:265–275
30. Büchi FN, Srinivasan S (1997) Operating PEMFC fuel cells without external humidification of the reactant gases—fundamental aspects. J Electrochem Soc 144:2767–2772
31. Jung SH, Kim SL, Kim MS, Park Y, Lim TW (2007) Experimental study of gas humidification with injectors for automotive PEM fuel cell systems. J Power Sources 170: 324–333
32. Wood D, Yi JS, Nguyen TV (1998) Effect of direct liquid water injection and interdigitated flow field on the performance of proton exchange membrane fuel cells. Electrochim Acta 43:3795–3809
33. Sun H, Zhang G, Guo LJ, Dehua S, Liu H (2007) Effects of humidification temperatures on local current characteristics in a PEM fuel cell. J Power Sources 168:400–407
34. Park SK, Cho EA, Oh IH (2005) Characteristics of membrane humidifiers for polymer electrolyte membrane fuel cells. Korean J Chem Eng 22:877–881
35. Chen D, Li W, Peng H (2008) An experimental study and model validation of a membrane humidifier for PEM fuel cell humidification control. J Power Sources 180:461–467
36. Hoogers G (2003) Fuel cell technology handbook. CRC Press, Boca Raton, FL
37. Vitale NG, Jones DO (2000) U.S. patent US6,066,408,2000

38. Hogarth WHJ, benzinger JB (2006) Operation of polymer electrolyte membrane fuel cells with dry feeds: design and operating strategies. J Power Sources 159:968–978
39. Liu F, Yi B, Xing D, Yu J, Hou Z, Fu Y (2003) Development of novel self-humidifying composite membranes for fuel cells. J Power Sources 124:81–89
40. Hussain MM, Dincer I, Li X (2007) A preliminary life cycle assessment of PEM fuel cell powered automobiles. Appl Therm Eng 27:2294–2299
41. Granovskii M, Dincer I, Rosen MA (2006) Life cycle assessment of hydrogen fuel cell and gasoline vehicles. Int J Hydrogen Energ 31:337–352
42. Wagner U, Eckl R, Tzscheutschler P (2006) Energetic life cycle assessment of fuel cell powertrain systems and alternative fuels in Germany. Energ J 31:3062–3075
43. Barbir F (2005) Fuel cells theory and practice. Elsevier, Burlington, MA
44. Pei P, Ouyang M, Lu Q, Huang H, Li X (2004) Testing of an automotive fuel cell system. Int J Hydrogen Energ 29:1001–1007
45. Ahluwalia RK, Wang X (2005) Direct hydrogen fuel cell systems for hybrid vehicles. J Power Sources 139:152–164
46. Corbo P, Migliardini F, Veneri O (2009) PEFC stacks as power sources for hybrid propulsion systems. Int J Hydrogen Energ 34:4635–4644
47. Wishart J, Dong Z, Secanell M (2006) Optimization of a PEM fuel cell system based on empirical data and a generalized electrochemical semi-empirical model. J Power Sources 161:1041–1055
48. Philipps F, Simons G, Schiefer K (2006) Dynamic investigation of PEFC stacks in interaction with the air supply system. J Power Sources 154:412–419
49. Corbo P, Migliardini F, Veneri O (2008) Experimental analysis of a 20 kWe PEM fuel cell system in dynamic conditions representative of automotive applications. Energ Convers Manage 49:2688–2697
50. Zhao H, Burke AF (2009) Optimization of fuel cell system operating conditions for fuel cell vehicles. J Power Sources 186:408–416
51. Ahluwalia RK, Wang X (2006) Rapid self-start of polymer electrolyte fuel cell stacks from subfreezing temperatures. J Power Sources 162:502–512
52. Jiao K, Li X (2009) Three-dimensional multiphase modeling of cold start processes in polymer electrolyte membrane fuel cells. Electrochim Acta 54:6876–6891
53. Bar-On I, Kirchain R, Roth R (2002) Technical cost analysis for PEM fuel cells. J Power Sources 109:71–75
54. Mert SO, Dincer I, Ozcelik Z (2007) Exergoeconomic analysis of a vehicular PEM fuel cell system. J Power Sources 165:244–252
55. Qi Z, Kaufman A (2003) Low Pt loading high performance cathodes for PEM fuel cells. J Power Sources 113:37–43
56. Zeis R, Mathur A, Fritz G, Lee J, Erlebacher J (2007) Platinum-plated nanoporous gold: an efficient, low Pt loading electrocatalyst for PEM fuel cells. J Power Sources 165:65–72
57. Wu H, Wexler D, Wang G (2009) Pt_xNi alloy nanoparticles as cathode catalyst for PEM fuel cells with enhanced catalytic activity. J Alloy Compd 488:195–198
58. Ramaswamy N, Arruda TM, Wen W, Hakim N, Saha M, Gullà A, Mukerjee S (2009) Enhanced activity and interfacial durability study of ultra low Pt based electrocatalysts prepared by ion beam assisted deposition (IBAD) method. Electrochim Acta 54:6756–6766
59. Wu J, Yuan XZ, Martin JJ, Wang H, Zhang J, Shen J, Wu S, Merida W (2008) A review of PEM fuel cell durability: degradation mechanisms and mitigation strategies. J Power Sources 184:104–119

Chapter 5
Electric Vehicles in Hybrid Configuration

While hybrid thermal electric vehicles (HTEV) are emerging as a viable option to improve efficiency and environmental impact of private cars, the alternative of pure electric vehicles have been always considered with the aim of decoupling the use of oil from transportation sector assuring zero local emissions [1]. However, the limitations of electric vehicles equipped with traditional energy storage systems, essentially vehicle range and battery recharging time, justify the strong research interest towards new solutions based on the hybridization of basic electric vehicles by adding other energy storage devices and electric power generators on board. In this context, fuel cells are the prime candidates, thanks to their high efficiency and capability to use hydrogen as fuel without generating pollutant emissions [2].

The utilization of fuel cells in propulsion systems for road transport applications raises the question of the optimal hybridization level between on board generation and storage of electric energy (batteries, supercapacitors).

The main issues of hybrid propulsion systems are discussed in this chapter, drawing attention to basic characteristics of power train components and aspects of energy management within each hybrid configuration. The main characteristics of electric drives are described in Sect. 5.2, different types of electric energy storage systems are analyzed in Sect. 5.3 and Sect. 5.4, while different configurations of hybrid electric vehicles are discussed in Sect. 5.5, with particular reference to fuel cell propulsion systems (Sect. 5.5.4).

5.1 Electric Vehicles: Preliminary Remarks

After the invention of the first electric carriage by R. Anderson between 1832 and 1839, practical and more successful electric road vehicles were realized by both T. Davenport and R. Davidson around 1842, using non-rechargeable

P. Corbo et al., *Hydrogen Fuel Cells for Road Vehicles*,
Green Energy and Technology, DOI: 10.1007/978-0-85729-136-3_5,

electric batteries. Improved-capacity storage batteries were developed by G. Plante in 1881, paving a promising way for electric vehicles. Then, mass production of rechargeable batteries made possible a fairly wide use of electric vehicles, which began to be commercialized by the end of the nineteenth century. The first car to exceed 100 km/h was an electric vehicle, well know as 'La Jamais Contente', driven by the Belgium racing driver Camille Jenatzy. Later in 1916, Woods proposed a hybrid car with both an internal combustion engine and an electric motor. At that time electric vehicles had many advantages over the other vehicles, such as gasoline or steam cars, especially in terms of reliability, vibration, smell, and noise. On the other hand, the other type of vehicles, such as steam engine and internal combustion engine vehicles, needed start up devices and their thermal efficiency were low. Nevertheless, at the beginning of the twentieth century, the decline of electric vehicles occurred, and was caused by several factors: the long time required to recharge the batteries, the increasing necessity of longer-range vehicles, discovery of new oil wells, the invention of the electric starter by Charles Kettering, the mass production of internal combustion engine vehicles. Among the above problems, the limited range of battery electric vehicles (BEVs) still remains the most critical one, together with the higher cost with respect to internal combustion vehicles of similar size [3, 4].

The use of electric vehicles on a large scale implies that batteries need to be recharged, and this can be accomplished by three different ways.

The first solution to recharge an electric vehicle is the domestic charger installation, used for overnight charging. The second form of charging is represented by public charging stations, which provide the recharge of batteries while cars are parked at supermarket, railway stations, work places or even residential roads. Finally, the third form of recharging is represented by roadside recharging stations with similar service as petrol station offer for conventional vehicles nowadays.

The wide use of electric vehicles should imply the widespread of battery charging facilities, which represent an essential and substantial investment for the development of the electric vehicle technology. The consequence would be the further development of both battery chargers and power supply infrastructures, together with the innovation of the components strictly related to electric vehicles.

In any case, the recharge of an electric vehicle would take much longer time than the few minutes required for refueling the tank of both liquid and gaseous fuels. The possibility to overcome the problem of refueling rate by the adoption of hybrid electric technologies represents one of the reasons that justify the increasing interest towards these vehicle configurations [3].

The main components of BEVs are a rechargeable battery pack, an electric machine with its power drive, a cabling system, a cooling system and a vehicle structure [5]. The electric and mechanical connections between the main components of a BEV are shown in Fig. 5.1. The battery pack is generally recharged from the electric distribution network via a plug. The battery charger can either be on board or part of the charging point.

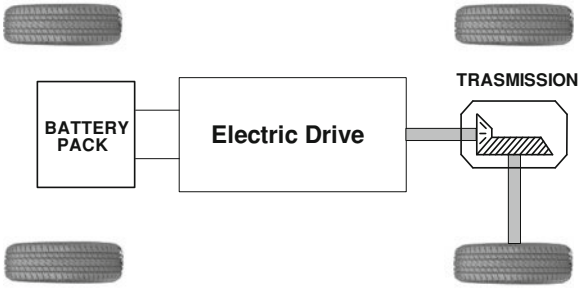

Fig. 5.1 Electric and mechanical connections between the main components of a BEV

Nowadays the worldwide market offers a range of electric vehicles which fundamentally use the configuration described in Fig. 5.1. For example, from the smallest to the biggest ones it is possible to mention: electric bicycles, electric wheel chairs, tricycles, small commuter vehicles, delivery vehicles, electric golf buggies, electric cars, delivery trucks and buses. The fact of the matter is that private electric cars do not play an important role in the field of BEVs, but each of the above types of vehicles fills a different niche in its specific market.

The scheme of Fig. 5.1 represents the base of all other types of electric vehicles, both those using an additional traction engine on board (HTEV) and those adopting alternative storage/generation electric energy systems to power the electric drive (hydrogen fuel cell electric vehicles, HFCEV, solar vehicles and vehicles using flywheels and supercapacitors).

5.2 Electric Drives for Road Vehicles

The main characteristics of electrical drives are reported in this section from the point of view of the application of these components to road electric vehicles.

Electrical drives are composed of rotating electric machines (which transform electric energy into mechanical energy or viceversa), power electronic converters and controllers connected together in order to operate the whole electrical drive in steady state or variable speed working operations.

Rotating electric machines fundamentally can be subdivided in two main types: *direct current* (*DC*) *machines* and *alternating-current* (*AC*) *machines*. All types of rotating electric machines have a stationary part, called *stator*, and a rotating part, called *rotor*. Generally the rotor is connected to a shaft which the mechanical torque acts on.

In rotating electrical machines, several conductors are distributed along the inner and outer sides of the air gap between rotor and stator, which are electrically excited. These conductors carry currents in the rotor and stator conductors creating resultant magnetic fields, which vary in space and time. The interaction between the two magnetic fields causes a resultant electromagnetic torque, which have a very important effect on the steady-state and transient behavior of the machine.

The main technologies of electric machines used for electric road vehicles are: DC motors, induction motors, permanent-magnet brushless, DC-switched reluctance motors [2]. These different types of electric machines are analyzed in the following sections of this chapter.

5.2.1 DC Electric Machines

The DC motor, whose basic principle is shown in Fig. 5.2, represents the simplest typology of electric machine, widely used for many domestic and industrial applications.

The most common DC machine, also called brushed DC motor, is characterized by the presence of a collector, which is essentially a set of electric contacts electrically insulated among them. The rotor windings are equally distributed along the rotor surface and their terminals depart from and arrive to each contact of the collector. The application of a DC voltage to the rotor windings, by means of carbon brushes in contact with the collector, generates a magnetic field with a polarity spatially changed by the position of brushes with respect to the collector. At the same time a stationary magnetic field is generated in the stator part, by means of permanent magnets or winding collocated on a magnetic structure. The interaction of these two magnetic fields generates a rotation of the rotor with respect to the stator.

Classic brushed DC motors present limitations due to the need for brushes to press against the collector, with the consequence of friction resistance. At higher

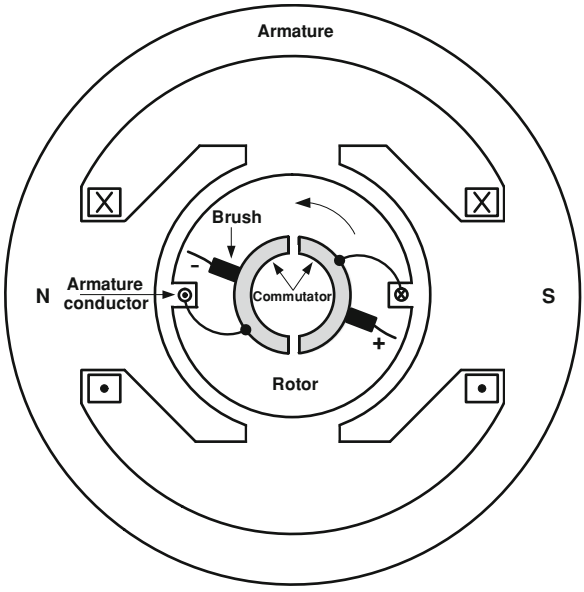

Fig. 5.2 Principle of operation of a DC machine

speeds, brushes increase difficulty in maintaining contact, creating sparks, because of some irregularity in the collector surface. This sparking limits the maximum speed of the machine, as too-rapid sparking will overheat, erode, or even melt the collector. The current density per unit area of the brushes, in combination with the resistivity of the material, limits the performance of the motor also causing electrical noise. Brushes eventually wear out and require replacement, and the collector itself is subject to wear and maintenance or replacement.

Other types of DC motors are classified according to their specific stator excitation, based on four standard methods of supplying current to the excitation windings for brushed DC motor: *parallel DC machines*, *series DC machines*, *compound DC machines and separately excited DC machines* (Fig. 5.3a–d) [6–8]. The parallel DC motor has the ability to self-regulate its speed, but it is particularly difficult to control, because in some circumstance, a reduction in supply voltage have very little effect on the speed. The main advantage of the series DC motor is that the torque is very high at low speed and falls off while the speed is increasing. This characteristic is useful in some applications, for example, the starter device of internal combustion engines, but it is not what a road vehicle generally requires. The compound DC motor is designed to combine the advantaged of the motors from which is derived.

In *separately excited DC machines* (Fig. 5.3d) the excitation is obtained by means of field windings which have a supply separated from the rotor windings, and this gives a separated control of speed and torque, according to what is required in an electric vehicle. Separately excited brushed DC motors were widely

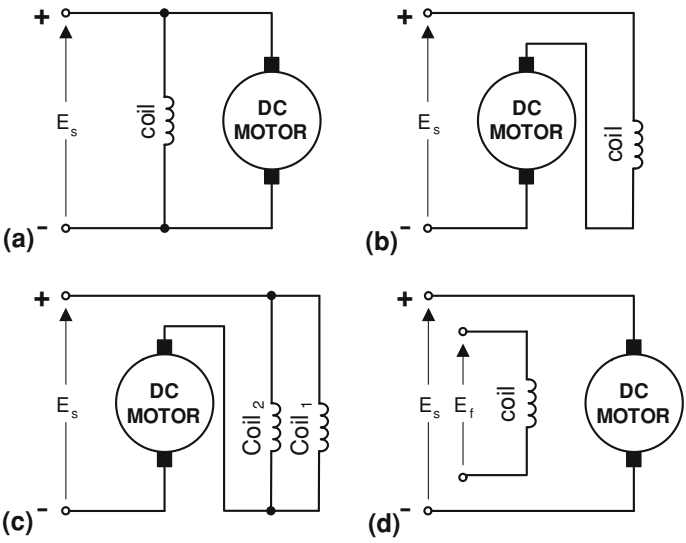

Fig. 5.3 Different methods of supplying current to the excitation windings for brushed DC motor. **a** parallel DC machines, **b** series DC machines, **c** compound DC machines, **d** separately excited DC machines

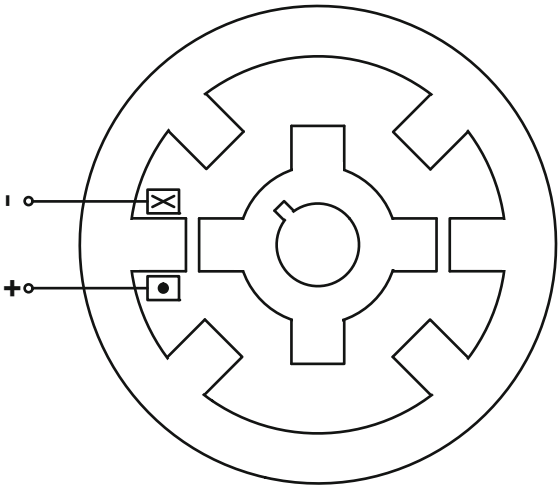

Fig. 5.4 Scheme of a switched reluctance motor

used in the past as traction motors for electric vehicle, especially for their easy regulation. They were then substituted by induction motors for their robustness, reliability and low cost, as described in the following paragraphs.

In *permanent-magnet DC machines*, the excitation static magnetic field is generated on the stator by using permanent magnets. *DC-switched reluctance motors* have 'notches' or 'teeth' on both stator and rotor, which are called salient poles. Each couple of opposite poles on the stator carries a couple of excitation coils electrically connected in series to form a couple of magnetic poles, whereas the rotor has no windings. When a DC voltage supplies a phase of the stator windings, the rotor rotates to minimize the reluctance of the magnetic circuit through rotor and stator. In Fig. 5.4, an example of switched reluctance motor is shown [1, 3].

The DC motor is still used for some specific traction applications, but has been almost completely substituted by other types of motors, which are becoming more common for the electric vehicles.

5.2.2 AC Electric Machines

AC machines have one or more sets of three-phase windings distributed on the stator. The number of these set of windings is called number of poles of the electric machine. These three-phase windings are distributed along the stator in a symmetrical way in the space. For that reason, when a three-phase AC voltage is applied to the stator winding a rotating and sinusoidal magnetic field is generated along the air gap. The orientation of that magnetic field changes according to the sign of the three-phase AC currents flowing in the windings. The rotating magnetic field rotates at the so-called synchronous speed, which is equal to the pulsation of the three-phase voltage ($\omega = 1/f$) divided by the number of poles [9].

Fig. 5.5 Example of squirrel gage

Asyncronous AC machines, also called *induction machines*, have rotor windings realized with conductors soldered together with two end rings, realizing what is known as *squirrel gage* (see Fig. 5.5). The interaction of the rotor conductors with the rotating magnetic field generated by the stator windings induces electromotive forces and thus currents in the rotor windings, which interact with the cause that generates the same currents (*Lenz's law*) [10]. The consequence of that magnetic mutual interaction is that also a rotor magnetic field is generated, rotating at the same synchronous speed and with alternative poles. The attraction and repulsion between the stator magnetic field with the rotor magnetic field generates an electromagnetic torque, which is different from zero only when there is synchronization between the two magnetic fields of rotor and stator, or in other words when the two magnetic fields rotate at the same speed with respect to the stator or the rotor and the rotor speed is different from the synchronous speed.

The working principle of the induction machines is based on the fact that rotor currents are induced by the stator currents, and this is the main cause of losses in the rotor windings, which makes these types of machines less efficient than other brushless machines [11]. However, asynchronous machines are widely used and their mass production makes them reliable and well developed, for that reason their cost is quite low.

Synchronous AC machines have a stator similar to the asynchronous machines, which has usually a three-phase stator winding. Whereas there are two types of rotor structures: *round cylindrical rotor* and *salient pole rotor* as illustrated schematically in Fig. 5.6. The rotor field is generated by permanent magnets or a DC current winding, as reported in the same figure. In the first case they are called *permanent-magnet synchronous AC machines*.

The DC rotor winding is supplied with an external DC voltage by means of a brush–ring system, similar to the brush-collector system for the DC electric machine. The excitation of the rotor winding can also be obtained with a DC generator, known as exciter, located on the rotating shaft, or other excitation systems using AC exciter and solid state rectifiers.

In synchronous AC machines the synchronization between the stator and rotor magnetic fields is achieved since the rotor magnetic field is fixed with respect to a rotor observer and thus it operates at the same speed as the rotor, which is the same speed of the stator magnetic field.

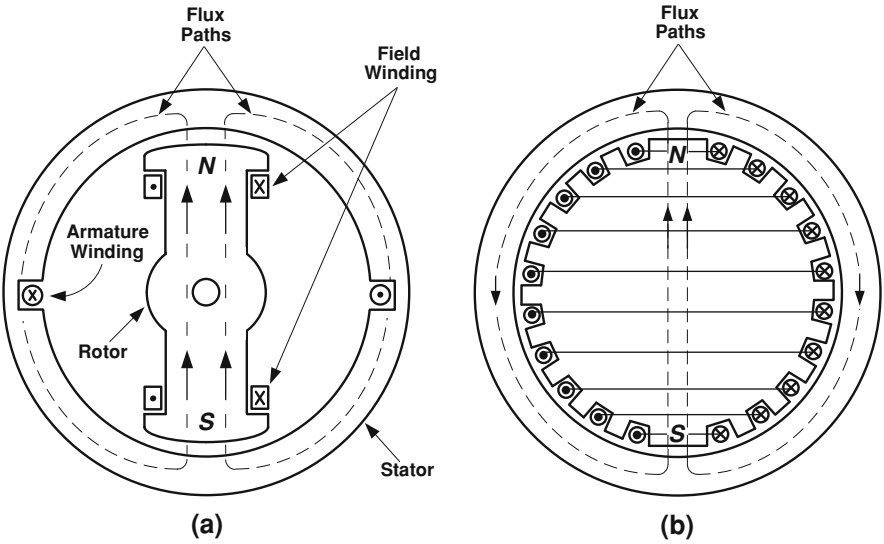

Fig. 5.6 Schematic illustration of synchronous machines of **a** round or cylindrical rotor and **b** salient rotor structures

Variable reluctance synchronous AC machines represent other types of synchronous machines which do not require any excitation system on the rotor [3].

5.2.3 Control and Power Electronics

DC machines are simpler and cheaper, because their speed regulation is based on scalar controls. For that reason they need simple electronic boards to control the DC electric drive operations. Moreover, they have the advantage that they can be fed by the DC supply already on board. On the other hand, the principal disadvantage is represented by the maintenance required, since for instance brushes need to be periodically checked and changed. Another point to take in consideration is that fuel cell electric vehicles equipped with brushed electric machines would require specific safety devices to avoid that sparks of the collector during the commutation might interact with the hydrogen used as fuel on board.

Asynchronous machines have the great advantage to be mechanically robust, because of their simple rotor windings. Nevertheless, AC electric drives require sophisticate control algorithms, based on vector relationships between the regulation parameters and the cost of their implementation is quite high. Although, nowadays electronic components and especially microcontrollers are becoming cheaper than in the past and for this reason AC drives are now more competitive than DC drives also in terms of cost.

Variable speed drives are generally based on a set of an electric machine driven by power electronic converters and controls, which are implemented in electronic cards. The whole system makes possible the speed regulation of the electric machine.

In Fig. 5.7, the scheme of a generic DC electric drive supplied by a battery pack is shown, and it also represents the traction drive for a BEV.

The DC–DC converter changes the electric characteristics of voltage and current supplied by the electric source in order to feed the electric machine and satisfy the load mechanic requirements.

AC electric drives require more sophisticated converters when they are supplied with DC sources, because electric machines requires periodic voltage and current waves with a variable frequency depending on the load requirements. In Fig. 5.8, the scheme of an example of three-phase induction motor driven by a pulse-width-modulated inverter is reported. In this scheme a three-phase bridge connection with six power modules is shown to form the so-called inverter. Each power module can be composed by a number of power switches connected in parallel to carry higher currents. Across each power switch (IGBT) a parallel diode is connected to provide a return path for the phase current when the power module is switched off.

For the design of an electric vehicle, it is important taking into account that the use of high battery pack voltage affects the design of the power electronics. In fact, high values of voltage mean low current and then reduced losses due to voltage drops in the power electronics. However, the values of voltage are limited by safety considerations.

The voltage waveform which feeds the motor is controlled by *pulse-width modulation* (PWM) of each of the six power modules, by means of control signals optimizing the motor phase currents. The PWM is controlled evaluating the motor

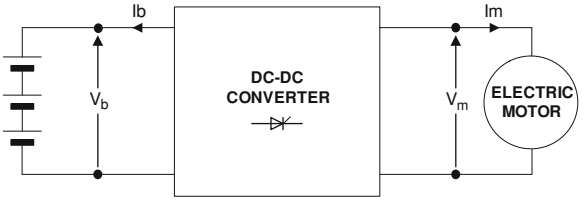

Fig. 5.7 DC electric drive of a BEV

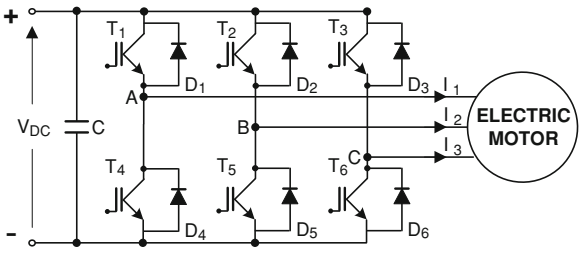

Fig. 5.8 Scheme of a three-phase induction motor driven by inverter

Table 5.1 Characteristics of power switching components

Transistor type	Maximum blocking voltage (V)	Maximum steady current (A)	Maximum operating frequency (kHz)	Easy of paralleling	Cost
Thyristor	6000	4000	1	Not required	Low
GTO	6000	6000	1	Not required	High
Mosfet	1000	100	1000	Easy	High
IGBT	1200	400	100	Easy	High

Adapted from Ref. [12]

torque by measuring stator currents and deducing the air gap flux from the motor phase voltages and then controlling the whole electric drive in order to produce the maximum load torque for the minimum value of current. Snubber circuits can be connected across each power module to control the shape of the switching waveform, they generally consist of a resistance-capacitor in parallel with the power module and an inductance in series with the power module. A capacitor bank is generally connected between the positive and negative input terminals of the inverter to filter the DC input voltage and to reduce the ripple of the high frequency currents generated during the PWM switching.

Before 1990s, thyristors and transistors were used as power modules for AC drive systems. Since then other semiconductor switching power modules have been used, such as GTO, MOSFETs, IGBTs, and combination of them. Nowadays IGBT and MCT-based inverters are used by electric drives manufacturers for the electric car market. The key characteristics of the different types of technology used for power electronic component are reported in Table 5.1. However, other power switching modules are currently under development [12].

The power dissipated by the semiconductor components is considerable for an electric road application and for that reason heat-sinks are essential. This means that the voltage drops across the semiconductor component and this value of voltage drop is an important characteristic to be considered in the selection of the component for the specific application. Moreover, it should be taken into account that in AC drives each current passes through two power components in series rather than through a single component required in DC converters.

Since the same voltage drops across each electronic switch when it is conducting, it means that the losses in AC inverters are significantly higher than those in DC converters. Another consideration to be taken into account for the design of an inverter for electric cars is the necessity of a cooling system. Natural air, forced air or liquid cooling systems could be used, the dimensions of the heat-sink being designed by the efficiency of each cooling method.

5.3 Storage Electrochemical Batteries

The term *storages batteries* or *accumulators* is used for devices able to supply electric energy stored in active materials by means of electrochemical

oxidation–reduction reactions, which convert chemical energy to electrical energy (see Sect. 3.1). They consist of one or more cells joined together and generally connected in series, depending on the voltage or capacity required by the designer [13]. After their discharge, batteries are recharged electrically to their original state by passing a controlled current through them in the reverse direction to that of discharge. The term *battery pack* is often used by electric vehicle designers to refer to the overall storage system composed by more batteries connected in series or parallel, with the function of supplying the electric drive.

Next sub-sections report the definition of the main operative parameters that characterize the battery working and some details about the electrochemistry of different types of batteries.

5.3.1 Main Operative Parameters of Batteries

5.3.1.1 Battery Voltage

The battery voltage is the voltage value measured at the battery terminals when the battery is delivering energy. The nominal voltage for a battery is a voltage reference value which the battery is referred to and it gives approximately the voltage when the battery works properly in the working range defined by the manufacturer. Traction batteries are usually referred as 6 or 12 V nominal voltage batteries, and these units are connected in series to produce the required voltage. In practice, this voltage changes as a function of the battery current: the voltage falls when the current is given out and rises when the battery is being charged. For example, Figs. 5.9 and 5.10 show the lead–acid cell voltage as a function of time for a constant current charge and discharge.

The voltage drop observed in 5.10, typically 0.02–0.03 V, at the beginning of discharge, is related to the delay of the anodic discharge reaction (see Sect. 5.3.2), due to the electrolyte saturation with lead ions.

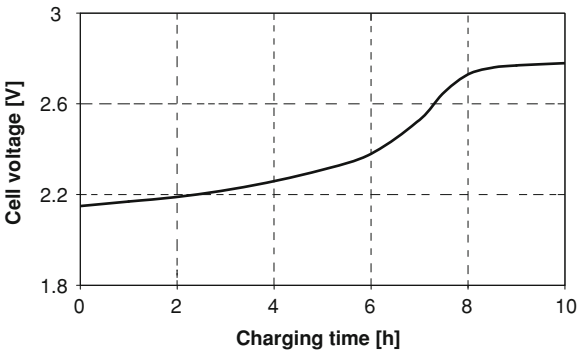

Fig. 5.9 Lead–acid cell voltage charge for a constant charge as a function of time

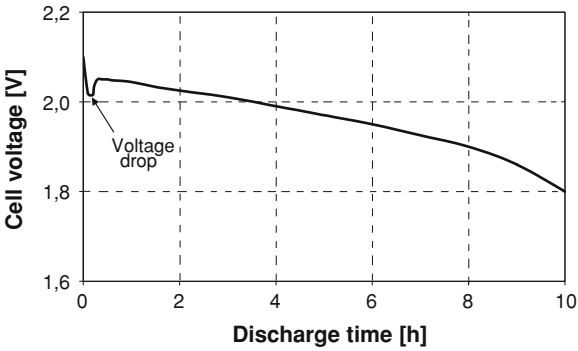

Fig. 5.10 Lead–acid cell voltage discharge for a constant current discharge as a function of time

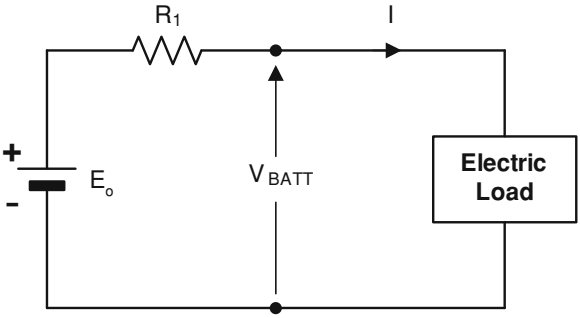

Fig. 5.11 Discharging equivalent circuit for a battery

The operative working condition of a battery can be represented by simple equivalent circuits, which are only valid for charging or discharging operations without considering the current transient phenomena. The discharging equivalent circuit of a battery is shown in Fig. 5.11.

In this case, the battery is represented by a fixed voltage E_o connected in series with a resistance R_1. The voltage V_{batt} at the terminals of the battery is different from the open circuit voltage E_0, because of the drop in voltage caused by the internal resistance R_1. Thus, if I is the current flowing out of the battery, as shown in Fig. 5.11, the terminal voltage of the battery is expressed by the following equation:

$$V_{batt} = E_o - R_1 I. \tag{5.1}$$

If $I = 0$, obviously the terminal voltage equals the open circuit voltage:

$$V_{batt} = E_0. \tag{5.2}$$

The internal resistance R_1 for electric vehicle batteries should be evidently as low as possible. The charging equivalent circuit of a battery is shown in Fig. 5.12.

The difference with the discharging equivalent circuit is the resistance R_2 and the switch S. The resistance R_2 takes in account the charging losses, which start to

be effective when the switch is closed and that happens for values of V higher than a specific value depending on constructive characteristics of the battery.

5.3.1.2 Battery Capacity

The battery capacity represents the electric charge that a battery can supply. Instead of using the Coulomb, which is the SI unit for the electric capacity but is an inconveniently small unit, the Amphour (Ah) is commonly used to refer to the capacity of electric vehicle batteries. Batteries are characterized by a nominal value of capacity, determined with predefined procedures. However, the real capacity of a battery depends on the current values drawn out from it. This changing in the expected capacity is caused by uncompleted or unwanted reactions inside the cell. This effect occurs in all the types of batteries, but it is particularly accentuated for lead–acid batteries. Figure 5.13 shows typical discharge curves for different discharge rates (I_1, I_2,…, I_6), where the black line shows the available capacity as a function of the discharge time.

The capacity of batteries used to supply electric vehicles is generally referred to a 5 h discharge, and in that case, the capacity is represented with the symbol C_5. Moreover, the value of battery capacity is often used to represent a current value,

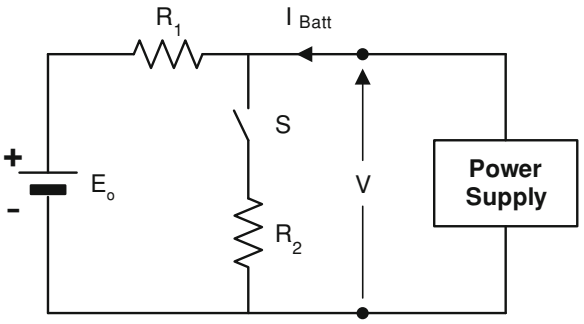

Fig. 5.12 Charging equivalent circuit for a battery

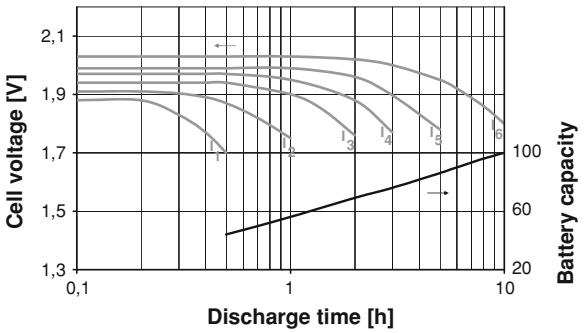

Fig. 5.13 Typical lead–acid battery discharge voltage as a function of time

for example a battery with a capacity $C = 52$ Ah, can be discharged at a current of $2C$ or $0.4C$, to mean that the discharging current is 104 or 20.8 A, respectively.

5.3.1.3 Battery Energy and Power

The SI unit for energy is the Joule, but for batteries the Watthour (Wh) is preferred to Joule, which is a very small unit. 1 Wh is equal to 3600 J. The energy stored in a battery (E_{batt}) depends directly on the charge (C) and voltage at its terminals (V_{batt}), as expressed by the following relation:

$$E_{\text{batt}}\ (Wh) = V_{\text{batt}}\ (\text{V}) \cdot C\ (\text{Ah}). \tag{5.3}$$

However, as both battery voltage and capacity depend on the battery charge and discharge rate, the evaluation of the energy stored in a battery could reduce sensibly if the electric energy is released or charged quickly, with high discharge or charge current.

Specific energy is the electric energy stored for one kilogram of battery mass and its unit is Wh/kg. Since the energy stored in a battery depends on many factors such as temperature and discharge rate, the specific energy can be only approximately evaluated for the battery mass.

Specific power is the electric power obtainable per kilogram of battery and its unit is W/Kg. The evaluation of this variable has to take in consideration that the real power given out by a battery is highly dependent on the load connected to its terminal. Moreover, it is convenient to operate the battery at its maximum power only for a short time of few seconds, otherwise the battery life might be seriously compromised and the battery would operate in a very inefficiently way.

Generally batteries with high specific energy have a low specific power. In other words many types of batteries can store a large amount of energy, but they can only give it out at low rate. That means to drive the vehicle over a long distance at a low speed.

To compare different types of batteries, in terms of specific power and specific energy, it is helpful using the *Ragone plot*, which is a graph of specific power versus specific energy. Figure 5.14 shown a Ragone plot for the main typologies of battery currently under development. Ragone plots are also used to make a comparison between batteries and other technologies of energy storage, such as the super capacitors and flywheels [1, 3, 5].

5.3.1.4 Amperhour and Energy Efficiency

The amperhour efficiency is defined as the ratio of the amperhours supplied by a battery to the amperhours required to give it back to the state before discharge. The amperhour efficiency is generally less than 100% and the real value depends on the type of battery, temperature, rate of charge and state of charge. In particular,

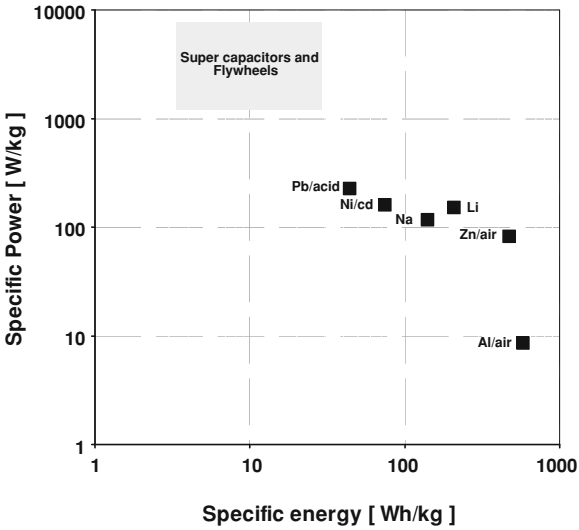

Fig. 5.14 Ragone plot for different types of electric energy storage systems

the amperhour efficiency could be very close to 100% for a state of charge ranging from about 20 to 80%, but the efficiency might fall down greatly for values of the charge under 20%, depending on the type of battery.

Energy efficiency is defined as the ratio of electrical energy supplied by a battery to the electrical energy required to give it back to the state before discharge. The energy efficiency is strongly dependent on how the battery is used, in particular the energy efficiency can decrease considerably when the battery is charged or discharged very rapidly.

5.3.1.5 Battery Lifetime

The number of cycles of a battery is a parameter representative of the battery lifetime of the battery and it affects the vehicle maintenance costs. The number of cycles of a battery represents the number times the battery can be completely charged and then discharged, without compromising its properties to store energy. Hundreds of cycles are guaranteed by many battery companies, although this number depends on the battery type.

Many types of batteries loss a certain amount of the initial charge when they are unused, and this phenomenon is called *self-discharge*. For that reason, some batteries need to be periodically recharged, if they are left unused for long periods of time. Self-discharge is related to kinetics of chemical reactions occurring inside each type of battery, and then it is strongly dependent on temperature.

Several types of storage batteries have been studied and tested for many years to be used on electric vehicles and other of them are presently under development. The key characteristics of the most used batteries to supply electric cars and the more promising ones are presented and analyzed below.

5.3.2 Main Characteristics of Different Types of Batteries

5.3.2.1 Lead–acid Batteries

The lead batteries had their industrial beginning with the first experiments of Plantè on storage batteries in 1859 [14]. Since then many other type of storage batteries have been studied and tested, but lead–acid batteries have been the most largely developed and represent the type of battery most widely used in the past century.

A lead–acid battery is constituted by a spongy lead anode, a porous lead dioxide cathode and an electrolyte based on a aqueous solution of H_2SO_4 (about 2.3 M). During the discharge phase, when current is drawn, both electrodes react with the electrolyte to form surface lead sulfate, according to the following semi-reactions [15]:

at Pb anode (negative terminal)

$$Pb + SO_4^{2-} \rightarrow PbSO_4 + 2e^- \tag{5.4}$$

where the generation of electrons due to lead oxidation allows the occurring of an electric current through an external circuit

at PbO_2 cathode (positive terminal)

(i) $$PbO_2 + 4H^+ \rightarrow Pb^{4+} + 2H_2O \tag{5.5}$$

(ii) $$Pb^{4+} + 2e^- \rightarrow Pb^{2+} \tag{5.6}$$

(iii) $$Pb^{2+} + SO_4^{2-} \rightarrow PbSO_4 \tag{5.7}$$

where the hydrogen from sulfuric acid reacts with oxygen of lead dioxide to form water, while the lead is reduced by the electrons coming from the external circuit to a form suitable to react with the sulfate ion.

Then the overall electrochemical process involved in the voltage production by a lead–acid battery is:

$$Pb + PbO_2 + 2H_2SO_4 \rightarrow 2PbSO_4 + 2H_2O \tag{5.8}$$

to which an open circuit voltage is 2.1 V at room temperature is associated. The reversed reaction is of course involved in the charge process, when the lead sulfate is broken down, lead oxide is deposited on the positive electrode and lead is deposited on the negative electrode.

Different types of lead–acid batteries have been developed as energy sources for many power applications, like traction and backup or standby power systems. The flooded lead–acid batteries have an excess or flooded electrolyte and they were the largest used at the beginning of the last century for many applications. Valve-regulated lead–acid (VRLA) batteries were developed as an alternative to the flooded lead–acid batteries, in order to maintain levels of distilled water and prevent drying of cells, which means safe operation for battery packs in electric

vehicles applications. They are characterized by an specific energy of 35–50 Wh/kg and specific power higher than 150 W/kg, and are called "no maintenance" battery, because they require minimal attention or low maintenance by the user. Two types of VRLA batteries are available commercially: the first is based on absorbed glass mat (AGM) and the second on the gel technology. AGM batteries have the best performance, because they have the lowest internal resistance, whereas their specific gravity is about 1.2 times the flooded Pb-acid and about 1.3 the VRLA gel batteries, but several critical factors such as ventilation, space requirements, acid containment, safety, environmental impact, material recyclability have to be carefully taken in consideration by the designer.

5.3.2.2 Nickel–Zinc Batteries

Nickel oxide electrodes constitute the positive plates of several storage systems (among which nickel–zinc, nickel cadmium, nickel metal–hydride, sodium–nickel chloride) [16]. In recent years, the high-specific energy and specific power of Ni–Zn systems has increased the interest in their use for electric vehicles with respect to the past years, when their application was essentially limited by a short cycle life.

In these systems, the discharge semi-reaction occurring at the nickel electrode is:

$$2\mathrm{NiOOH} + 2\mathrm{H_2O} + 2e^- \rightarrow 2\mathrm{Ni(OH)_2} + 2\mathrm{OH^-} \tag{5.9}$$

while the zinc electrode is involved in the following dissolution-precipitation semi-reactions:

(i) $$\mathrm{Zn} + 4\mathrm{OH^-} \rightarrow \mathrm{Zn(OH)_4^{2-}} + 2\mathrm{e^-} \tag{5.10}$$

(ii) $$\mathrm{Zn(OH)_4^{2-}} \rightarrow \mathrm{ZnO} + 2\mathrm{OH^-} + \mathrm{H_2O} \tag{5.11}$$

The electrolyte is a solution of aqueous KOH (usually 20–35 wt%) with 1 wt% of LiOH (which is saturated with ZnO), whose function is to enhance the charge acceptance of NiOOH electrode. The overall discharge reaction is the following:

$$\mathrm{Zn} + 2\mathrm{NiOOH} + \mathrm{H_2O} \rightarrow \mathrm{ZnO} + 2\mathrm{Ni(OH)_2} \tag{5.12}$$

with a cell voltage of 1.75 V at room temperature. During the charge phase ZnO and $Ni(OH)_2$ are dissolved with re-deposition onto the electrodes of zinc and nickel oxide.

This type of batteries is characterized by a specific energy of about 70 Wh/kg and a specific power of about 150 W/kg, great temperature tolerance, from −39 to 81°C, and a quire flat discharge characteristic. Nevertheless, the key problem for these batteries was the maximum number of deep discharge cycles, principally caused by the high solubility of the zinc oxide. After years of development, the Ni–Zn batteries have today reached the commercial viability, and present performance comparable to those of Ni–Cd and Ni–MH systems.

5.3.2.3 Nickel–Cadmium Batteries

Nickel–cadmium batteries use a hydrate nickel oxide as positive electrode, a metallic cadmium as negative electrode and an aqueous solution of potassium hydroxide as electrolyte [17]. The production of electrons at the negative plate during discharge occurs via the following semi-reaction:

$$\mathrm{Cd} + 2\mathrm{OH}^- \rightarrow \mathrm{Cd(OH)}_2 + 2e^- \tag{5.13}$$

while at the nickel positive plate the discharge reaction involves a mechanism of proton transfer between nickelic and nickelous hydroxide within the homogeneous solid phase:

$$\mathrm{NiOOH} + \mathrm{H}^+ + e^- \rightarrow \mathrm{Ni(OH)}_2 \tag{5.14}$$

As a consequence the overall discharge reaction is the following:

$$2\mathrm{NiOOH} + \mathrm{Cd} + \mathrm{H_2O} \rightarrow 2\mathrm{Ni(OH)}_2 + \mathrm{Cd(OH)}_2 \tag{5.15}$$

with a cell voltage of 1.30 V at room temperature. During charge cadmium hydroxide at the negative electrode is re-converted to metallic cadmium, while at the positive electrode a proton is lost by nickelous hydroxide to re-form nickelic hydroxide.

Nickel–cadmium batteries represent a good compromise between specific energy, specific power and reliability, but they suffer from the memory effect, due to the growth of cadmium crystalline particle size. In particular, they have a specific energy of 50 Wh/kg, a specific power of 200 W/kg and can accept high charge and discharge current rate, and this last characteristic makes them interesting for electric vehicle manufacturers. Moreover nickel–cadmium batteries can store slightly more energy per unit in weight than lead–acid batteries, and have a fairly high rate of self-discharge at high temperature. Nevertheless a very important issue to take into consideration is the toxicity of cadmium and the danger of an environment contamination, because the recycling of nickel–cadmium batteries is complex. Those reasons have arrested the use of these systems and made more attractive other types of batteries.

5.3.2.4 Nickel–Metal Hydride Batteries

The Ni–MH batteries use the same positive electrode and electrolyte as the Ni–Cd systems, while hydrogen storage alloys are adopted as the negative electrode in substitution of toxic cadmium. The metal alloys in which hydrogen is stored can be based on mixtures of nickel with rare earth, or blends of nickel with titanium, vanadium and zirconium. During discharge the cathodic semi-reactions are the same as the Ni–Cd batteries, while at the anode the electron production is given by the following semi-reaction:

$$MH + OH^- \rightarrow M + H_2O + e^- \tag{5.16}$$

during charge reduction of water determines hydrogen adsorption into the lattice of the inter-metallic alloy to form the metal hydride.

The overall discharge cell reaction can be written as:

$$NiOOH + MH \rightarrow Ni(OH)_2 + M \tag{5.17}$$

to which a cell voltage of 1.32 V at room temperature is associated. Unlike other nickel based batteries the charge–discharge mechanism in a Ni–MH system is not based on anodic dissolution–precipitation, but employs the proton transfer in homogeneous solid phase between nickel hydroxide and hydrogen storage alloy.

The Ni–MH batteries started their existence since the beginning of the last century and their performance, especially in terms of capacity, have been improving dramatically. Today nickel–metal hydride batteries are considered a better solution for electric vehicle applications than nickel–cadmium batteries, because of their better performance without the toxicity issues of cadmium [18]. They have a specific energy greater than 50 Wh/kg and a specific power of 200 W/kg. Moreover, these batteries tolerate over 600 full charge/discharge cycles to 80% depth of discharge and they can be recharged in a quite fast way to 80% of the full capacity. Their cells tolerate both overcharge and over-discharge, because of the reactions of gas recombination inside the cells. The disadvantages of Nickel–metal hydride batteries are low power, fast self-discharge, and sensibility to temperature. More recent versions of this type of batteries present cooling by air or liquid systems to reduce their size and obtain a faster recharge. Moreover, they are rather more expensive than lead batteries in automobile applications.

5.3.2.5 Sodium–Nickel Chloride (Zebra) Batteries

The last type of nickel based battery here considered is the so-called sodium-nickel chloride or Zebra battery, firstly developed in 80s in Pretoria, South Africa (Zebra stands for ZEolite Battery Research Africa). The anode is made of liquid sodium, the electrolyte is based on sodium ion conducting β-alumina and the cathode is constituted by nickel chloride. This is flooded with liquid $NaAlCl_4$ which acts as a secondary electrolyte, i.e., its function is to enhance the transport of sodium ions from the solid nickel chloride to and from the alumina electrolyte [19]. They work at high temperature (157°C is the temperature necessary to have sodium in its molten state, but the better performance is obtained in the range 250–350°C) and operate with the following discharge semi- reactions:at the anode:

$$Na \rightarrow Na^+ + e^- \tag{5.18}$$

at the cathode:

$$NiCl_2 + 2Na^+ + 2e^- \rightarrow Ni + 2NaCl \tag{5.19}$$

to have the following overall cell reaction:

$$2Na + NiCl_2 \rightarrow 2NaCl + Ni \tag{5.20}$$

with a cell potential of 2.58 V at the working temperature. During discharge the sodium ions produced at the anode are transported through the electrolyte to the cathode, where react with $NiCl_2$ to form $NaCl$. During charge sodium metal and nickel chloride are re-generated. The specific energy is about 100 Wh/kg with a specific power of 150 W/kg.

Generally, the heat insulation is guaranteed by a double skinned stainless steel box with 2-3 cm insulation layer between the skins. Moreover the insulation is completely empty of all gas and it works in vacuum condition.

In order to keep the *Zebra* batteries at the high temperature required for their operation, they need to be kept connected to the electric network when they are not in use. This represents a limitation of their application, and makes them more suitable specifically for public transportation means, rather than small private vehicles.

Limitations in the production and commercial development of these batteries are essentially due to the fact that they will never be used for laptop and mobile phones.

5.3.2.6 Lithium Batteries

Lithium batteries are showing a great potential to provide electric vehicles with sufficient performance in terms of acceleration and driving range [5]. Lithium metal is attractive as battery anode material mainly due to its lightness and high voltage. The use of a lithium based anode in these systems implies some concerns of safety hazard, due to the high reactivity of the metal. For this reason, in the so-called lithium-ion batteries, both positive and negative electrodes employ lithium "host" compounds, where an intercalation process occurs, i.e., lithium ions are reversibly removed or inserted without a significant structural change to the host.

The negative material is based on graphitic carbon, while the positive one is realized by using a metal oxide as lithium source compound, of the $LiMO_2$ or $LiMO_4$ type (M = Co, Ni, or Mn). In these systems the lithium ion conducting electrolyte is based on a solution of a lithium salt in organic solvents [20]. The resulting electrochemical reaction is the following:

$$xC + LiMO_2 \underset{\text{discharge}\leftarrow}{\overset{\rightarrow \text{charge}}{\Leftrightarrow}} Li_xC + Li_{1-x}MO_2 \tag{5.21}$$

which involves a cyclic transfer of lithium ions from the cathode (the lithium source) to the graphite anode, with no metallic lithium present in the system. The cell voltage is 3.8 V at room temperature.

This type of Li battery has already widely diffused in the electronic consumer market, however for automotive applications the presence of a liquid electrolyte is not considered the best solution in terms of safety, then for this type of utilization the so-called lithium polymer batteries appear more convenient. They are based on a polymeric electrolyte which permits the transfer of lithium ions between the electrodes [21]. The anode can be composed either of a lithium metal foil (in this case the device is known as lithium metal polymer battery) or of lithium supported on carbon (lithium ion polymer battery), while the cathode is constituted by an oxide of lithium and other metals, of the same type used in lithium-ion batteries, in which the lithium reversible intercalation can occur. For lithium metal polymer batteries the overall cycling process involves the lithium stripping-deposition at the anode, and the deintercalation–intercalation at the anode, according to the following electrochemical reaction, written for a Mn-based cathode:

$$xLi + LiMn_2O_4 \underset{\leftarrow discharge}{\overset{\rightarrow charge}{\leftrightarrows}} Li_{1+x}Mn_2O_4 \tag{5.22}$$

The absence of liquid phases facilitates the construction of leak-proof and light-weight containers, which represents an additional advantage for automotive applications. In particular it is possible to realize sandwich of foils at low cost, with the great advantage on the packaging flexibility and insensitivity to shock and vibration damage, as required by users.

Recent developments in the field of lithium batteries have been focused on the possibility to reach very high energy and power densities by using new types of anode and cathode. Metals and semiconductors, such as Al, Si, Sn, Bi, have been considered for their capacity to form alloys with lithium, which are characterized by a theoretical charge capacity very higher than traditional carbon materials (in particular, a Si–Li alloy presents a theoretical specific capacity of 4200 mAh/g, to be compared with 371 mAh/g of graphite [22, 23]). However, the large volume change associated with the formation of the alloys (by lithium intercalation/de-intercalation) rapidly leads to electrode pulverization, strongly limiting the cycling capability of the battery [23]. To overcome this type of limitation different solutions are under study, from reduction of metal particle size down to nanoscale [24, 25] to utilization of composite materials (in which an inactive component added to the active metal acts as a buffer for volume variations [26, 27]) or metal hydrides as anode [28]. The researches about the cathode of lithium ion batteries are intensively oriented on high voltage spinels and high capacity layered lithium metal oxides [29–32].

Even with the current technology the lithium polymer batteries represent the state of the art in the field of electric energy storage systems, since they are characterized by very interesting values of the basic electrochemical parameters, as already reported in Table 1.8 in comparison with other batteries today available.

The main advantage of lithium–ion batteries consists in the fact that they can be charged and discharged faster than other batteries, such as Pb-acid and NiMh batteries, because of the quick reversibility of the lithium ions. Moreover, the specific energy of lithium–ion batteries is about 150 Wh/kg, this means for electric vehicles a large increase of driving range with respect to the previous types of batteries (Fig. 5.14; Table 1.8).

As with Pb-acid and NiMH batteries, lithium–ion batteries must be controlled during their operation to prevent that overcharging conditions might occur damaging the battery. For this reason the development of battery management systems to guarantee the correct behavior in each working condition is a key issue for this type of batteries.

The Li batteries have recently received much attention from automobile industries thanks to their characteristics of light weight and good specific power; however, the lower costs of Ni–MH batteries, together with their demonstrated durability and reliability performance, could retard the application of Li ion systems [33].

5.3.2.7 Zinc–Air Batteries

These are non-rechargeable batteries (so-called primary batteries, while rechargeable ones are known as secondary batteries) which utilize a metallic zinc anode, an aqueous solution of KOH as electrolyte and a porous carbon-based air diffusion cathode. The discharge semi-reactions are the following:at the anode:

$$\mathrm{Zn} + 4\mathrm{OH}^- \rightarrow \mathrm{Zn(OH)}_4^{2-} + 2e^- \tag{5.23}$$

where oxidation of zinc produces electrons that flow through the external circuit, while at the cathode water and oxygen from air react to form hydroxyls, which migrating through the electrolyte reach the zinc anode:

$$\mathrm{O_2} + 2\mathrm{H_2O} + 4e^- \rightarrow 4\mathrm{OH}^- \tag{5.24}$$

The overall cell reaction is:

$$2\mathrm{Zn} + \mathrm{O_2} + \mathrm{H_2O} + 4\mathrm{OH}^- \rightleftarrows 2\mathrm{Zn(OH)}_4^{2-} \tag{5.25}$$

to which a cell voltage of 1.65 V at room temperature is associated.

The main problem of this type of battery is the scarce recharge ability of the negative electrode due to the formation on zinc of deposits which degrade the anode behavior [34]. As a consequence, these batteries are usually recharged by

mechanical replacement of the spent anode, for remote recharging. Because of this type of recharging the zinc–air batteries can be also regarded as zinc–air fuel cells, where the zinc is the replaceable fuel and the air flow, supplied from outside of the battery system to the cathode side, controls the reaction rate. Because of their specific operation zinc-air batteries require a proper air-management system to ensure the right amount of air into the battery for the required power. These batteries require particular attention during their operation, because quick charge rates and deep discharges below the minimum voltage could permanently damage the battery. High value of energy (200 Wh/kg) can be stored in zinc–air batteries with a low specific power (80 W/kg) (Fig. 5.14; Table 1.8), for that reason zinc-air batteries could be conveniently connected to high power energy storage systems (supercapacitors, Sect. 5.4.2).

5.3.2.8 Aluminum–Air Batteries

The study of aluminum anodes for high specific power Al–air batteries is gaining in recent years an increasing attention [35] due to the very promising theoretical performance of this type of batteries (theoretical specific energy higher than 8000 Wh/kg, Table 1.8). These systems generally use alkaline electrolytes and are based on the following discharge semi-reactions:at the anode:

$$\mathrm{Al} + 3\mathrm{OH}^- \rightarrow \mathrm{Al(OH)_3} + 3e^- \tag{5.26}$$

at the cathode:

$$\mathrm{O_2} + 2\mathrm{H_2O} + 4e^- \rightarrow 4\mathrm{OH}^- \tag{5.27}$$

Then the overall energy productive cell reaction is:

$$4\mathrm{Al} + 3\mathrm{O_2} + 6\mathrm{H_2O} \rightarrow 4\mathrm{Al(OH)_3} \tag{5.28}$$

The main practical problem of this type of battery is the tendency of the anode to corrosion, according the following parasitic reaction:

$$\mathrm{Al} + 3\mathrm{H_2O} \rightarrow \mathrm{Al(OH)_3} + 3/2\mathrm{H_2} \tag{5.29}$$

This phenomenon degrades the Coulombic efficiency of the anode, then it has to be minimized for practical applications where high capacity is required. This could be overcome by particular aluminum alloys more resistant to corrosion, but the competing requirement of fast anodic dissolution makes very difficult the research of the suitable material [36, 37]. Another possibility to improve the anode performance is to modify the electrolyte composition by adding corrosion inhibitors [38]. The difficulties met up today in this field leave the possibility to use the aluminum-air batteries only as mechanically rechargeable systems, with practical performance (300–500 Wh/kg) very far from the theoretical values (Table 1.8; Fig. 5.14).

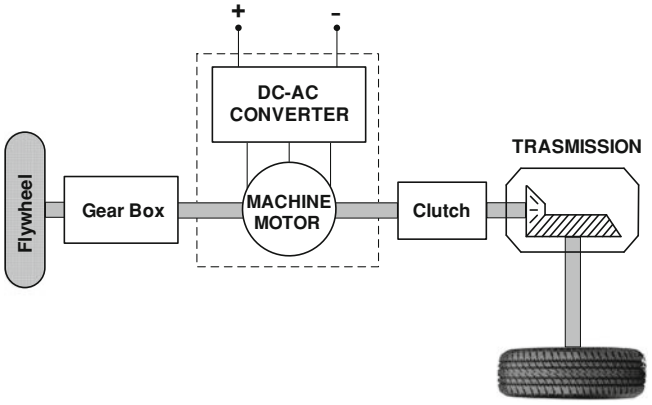

Fig. 5.15 Principle of operation of a vehicle using a flywheel as auxiliary energy storage

5.4 Alternative Energy Storage Systems

In this section, the main characteristics of alternative electrical energy storage systems, such flywheels and super capacitors, are described, as these devices might play an important role in the development of vehicles powered by electric propulsion systems.

5.4.1 Flywheels

An energy storage system using flywheels is essentially composed by a plane disk rotating around its axis of symmetry. The kinetic energy of the spinning disk is released when the rotating velocity slows down. This can be obtained connecting an electric machine working as a generator to the disk by means of a gearbox, as shown in Fig. 5.15. Power electronics is required to match the electric generator output to the electric drive to power the vehicle. The flywheel is reaccelerated mainly during the regenerative braking, when the kinetic energy of the vehicle can be transformed in kinetic energy of the spinning disk. In particular, the electric energy coming from the main power drive of the vehicle during breaking supplies the electric machine, which works as a motor in this case. Alternatively, the flywheel is connected to the wheels of the vehicle by means of a clutch. The intervention of the clutch depends on both the speed of the vehicle and the power chosen by the designer for the electric machine and the control technique of the DC–AC converter [3, 4].

The energy E stored by a flywheel is given by:

$$E = \frac{1}{2} I_{\mathrm{m}} \omega^2 \tag{5.30}$$

where I_m is the moment of inertia and ω is the rotational speed of the disk in radians per second. Taking into account the above formula, it is clear that the energy storage capability for a flywheel depends on its size and rotating speed, and also on the resistance of the material of which the flywheel is made. For this reason, many efforts have been made to increase the intrinsic low specific energy of flywheels by using ultra-strong materials, magnetic bearings and running the flywheel in inert gas or vacuum to reduce friction losses.

However, the use of flywheels needs to take into consideration also their safety due to the consequence of a breaking of the flywheel, which can be made more likely by the gyroscopic effect of the rotating disk [39], or of a crush of the vehicle currying a rotating flywheel on board. In this case, without the proper precautions, the flywheel energy would be released almost instantly with dangerous consequences.

5.4.2 Super Capacitors

Capacitors are devices composed by two conducting plates which are separated by an insulating material. A schematization of a capacitor is shown in Fig. 5.16, where a DC voltage is applied to the capacitor, obtaining as a consequence one plate positively charged and the other one negatively, with the result that the device can store a charge and hence energy, since opposite charges attract each other.

The charge Q_c stored by a capacitor of capacitance, C (F), at the voltage of V volt is expressed by the equation:

$$Q_c = C \cdot V \tag{5.31}$$

Generally capacitors are used in small size as components in electronic circuits, but they can provide large energy storage in the same way as flywheels. The capacitors with large plate areas have large energy storage capability and they are called super capacitors. The energy in Joules that a capacitor can store is expressed by the following equation:

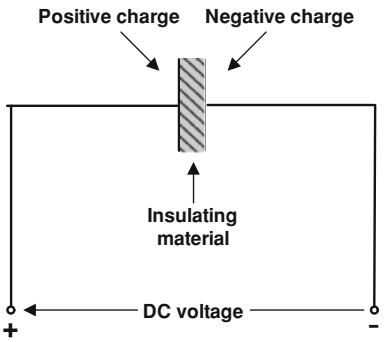

Fig. 5.16 Schematization of a capacitor

$$E_c = \frac{1}{2} C \cdot V^2 \tag{5.32}$$

whereas the capacitance C (F) of the capacitor is given by the equation:

$$C = \varepsilon \frac{A}{d} \tag{5.33}$$

where ε (Farad per meter) is the permittivity of the material between the plates. A is the plate area and d is the distance of separation between the plates. Modern super capacitors have distance of separations between the plates very small and this make them really interesting as energy storage systems. The capacitance results from the formation on the electrode surface of a layer of electrolytic ions. They can have high surface areas, e.g., 10^6 m^2/kg, and this make possible to fit capacitors of thousand of Faradays in small containers [3, 39].

However, the voltages at the terminals of each capacitor can only be between 1 and 3 V, and this represents the main problem of this technology, because it limits the amount of energy that can be stored. For this reason, more capacitors have to be connected in series in order to store energy at a reasonable voltage, since from Eq. 5.32, it derives that the energy stored increases as the voltage squared. However, being the total capacitance C of n capacitors C_1, C_2, C_n connected in series given by the formula:

$$\frac{1}{C} = \frac{1}{C_1} + \frac{1}{C_2} + \cdots + \frac{1}{C_n} \tag{5.34}$$

this type of connection implies a reduction of the total capacitance, in addition to an increase of costs.

Another problem of capacitors connected in series is given by the charge equalization between each capacitor forming the stream, since the same current flows through the series circuit. The difference in charge of each capacitor is generally caused by self-discharge phenomena due to small difference in the insulation between the plates of each capacitor, or by a small difference in capacitance among the capacitors of the same series. The consequence may be an overcharging of some capacitors, which means a voltage value higher than 3 V, with irreversible damages of the device.

The solution for this problem is the use of an *equalisation circuit*, which is essential in systems composed by at least six capacitors in series. This equipment monitors each capacitor testing the voltage across each pair of its terminals, and eventually moves charge from one capacitor to another to guarantee the same value of voltage across the series.

Equalisation circuits increase the cost of capacitor energy storage systems. They also require energy to work. However, these circuits are very efficient and have a very low current consumption [40].

Super capacitors have relatively high specific power and low specific energy, like flywheels. For this reason both these devices can be used as energy storage

systems for regenerative breaking. They could be also used alone in a vehicle, but the best use of these components is in hybrid configurations for giving out energy during accelerations and receiving it during braking in a rapid way. Moreover, super capacitors are safer than flywheels, as they do not present problems of mechanical breakdown and gyroscopic effects; however, other devices such as power electronics converters are generally required to step up and down the voltage.

Several research studies have been carried out with super capacitors playing a significant role in the management of energy on board [41–45].

5.5 Hybrid Propulsion Systems

A generic hybrid vehicle is powered by at least two different power sources on board. There are many possible variations of hybrid vehicles depending on the type of source and the mechanical and electric connections among them. The battery pack play a key role in any type of hybrid vehicle, and has to be designed taking into account that battery duty cycle and therefore depth and frequency of discharge is dependant on the hybrid configuration chosen for the vehicle. In hybrid configurations for which the battery storage system is used to assist energy sources on board only during acceleration, hill climbing and slow-speed moving, the battery remains in the same state of charge for most of its life, and thus deep discharges do not happen very often. This way of operate for batteries tends to make the battery life longer that those used for pure electric drives or hybrid configurations with a small storage system where the power is mainly supplied by the energy source on board, such as a motor-generator with a thermal engine or a fuel cell system. On the other hand, vehicles with a low energy storage system require a high recharging rate during regenerative braking, which is a characteristic satisfied by storage systems with a high specific power.

These considerations are closely examined in the following sections, where different type of hybrid vehicles are described, starting from those already commercially diffused (HTEV) up to hydrogen fuel cell electric vehicles (HFCEV), passing through less usual solutions, such as vehicles using solar energy or alternative storage systems [3, 4].

5.5.1 Hybrid Thermal Electric Vehicles

Hybrid vehicles equipped with an internal combustion engine, batteries and an electric motor/generator (HTEV) is the most commonly studied and experimented.

The basic configurations for HTEVs are the *series hybrid* and the *parallel hybrid,* which are shown in the Figs. 5.17 and 5.18, respectively [1]. In the series

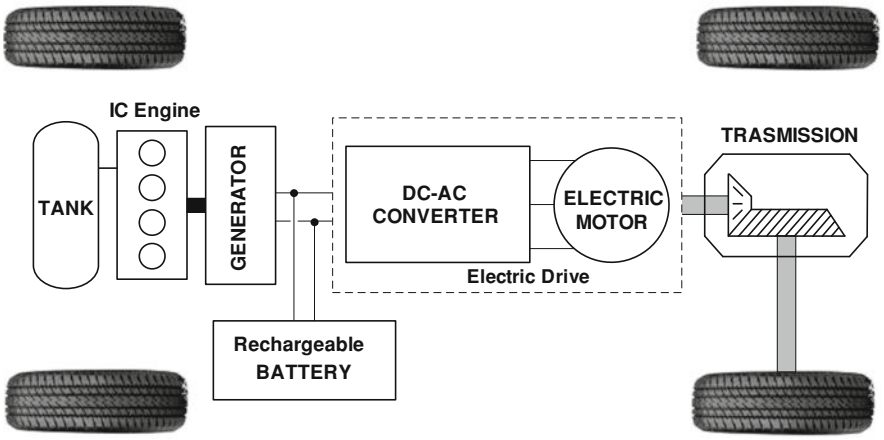

Fig. 5.17 Series hybrid configuration

hybrid, the mechanical force for the traction of the vehicle comes from the electric drive, which is supplied either by a rechargeable battery pack, or by an electric generator driven by an IC engine, or by both of them. Whereas, in the parallel hybrid the mechanical force for the traction of the vehicle can come either from an IC engine, or from the electric drive, or from both of them at once.

The electric connections shown in Figs. 5.17 and 5.18 evidence that in series hybrid configuration the battery can be recharged by both the IC-based generator and the electric drive, while in parallel configuration only by the electric drive. The electric drive for both the configurations can operate also as a generator to recover energy into battery during the regenerative braking operations, when the kinetic energy of the vehicle can be converted in electric energy.

The series hybrids are actually used only for particular applications, and the principal ones are diesel powered railway engines, ships, vehicles with a separated motor for each wheel. The main disadvantage of the series hybrid is that there is only an energy flow from the storage system to wheels, which must pass through all components of the configuration, while the fundamental advantage consists in a considerably low cost of the system.

On the other hand, the parallel hybrid has two main energy fluxes from the storage systems to wheels (from battery or fuel tank), with the advantage that the machines and the other components can be smaller and cheaper, because only part of the total energy that reaches the wheels has to pass through them. Moreover, a parallel hybrid can operate in different ways. For instance, the IC engine can be switched off, in that case the vehicle is powered only electrically with batteries, and this operation could result particularly advantageous in city districts with restrictions on the environmental pollution. Another simple way to operate this configuration is when the batteries are disconnected and only the IC engine give power to the vehicle, an operative way useful when traveling on highways and a low constant power is required. Alternatively, a parallel hybrid vehicle can

usefully operate with a proper balance between the powers coming from both the engines, which are typically regulated to optimize the performance of the IC engine in terms of exhaust emissions and fuel economy. This mixed operation strategy is typically managed to operate the IC engine in steady-state regime, i.e., in a high efficiency working point. In this case, if additional power is required, it can be taken from the electric motor, while a possible surplus of energy produced by the IC engine can be saved into batteries through the electric motor which in this case operates as a generator. The IC engine can be turned off when the battery is fully charged or when the total power required by the road mission is low, because in that case the thermal engine has a very low efficiency.

The 'degree of hybridization' is a useful parameter characterizing parallel hybrid vehicles. The value of this parameter is defined as the total power of the electric motor divided by the sum of the total power of electric motor and IC engine, according to the following equation:

$$\text{DOH} = \frac{\text{total power of electric motor}}{\text{total power of electric motor} + \text{total power of IC engine}}$$

A high value of the degree of hybridization means that the hybrid vehicle has a small IC engine that operates at its maximum efficiency for most of its operation time.

There is a large number of possible variations for the parallel hybrid configuration, besides that shown in Fig. 5.18, proposed by most of the major automobile companies. Some of them, for example, have a small electric machine in line with the crankshaft, where is usually located the flywheel in a IC engine vehicle. Another parallel hybrid configuration has the IC engine and the electric drive connected to different axles, as shown in Fig. 5.19, in particular in this case the IC engine drives the front wheels, the electric system the rear wheels and the road

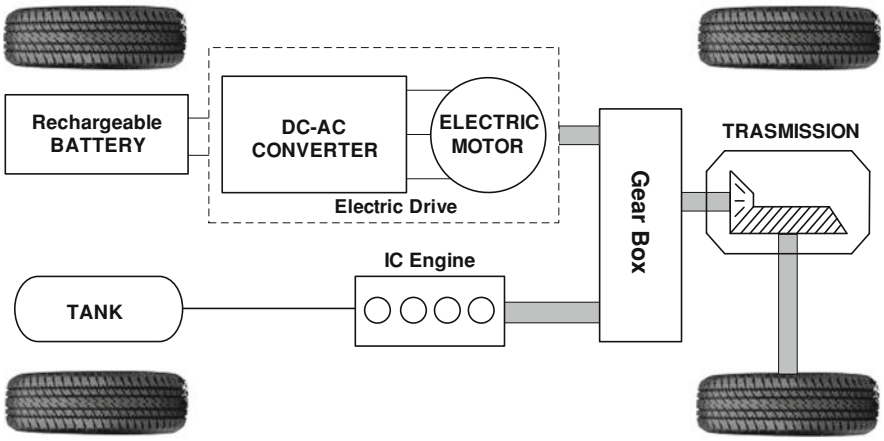

Fig. 5.18 Parallel hybrid configuration

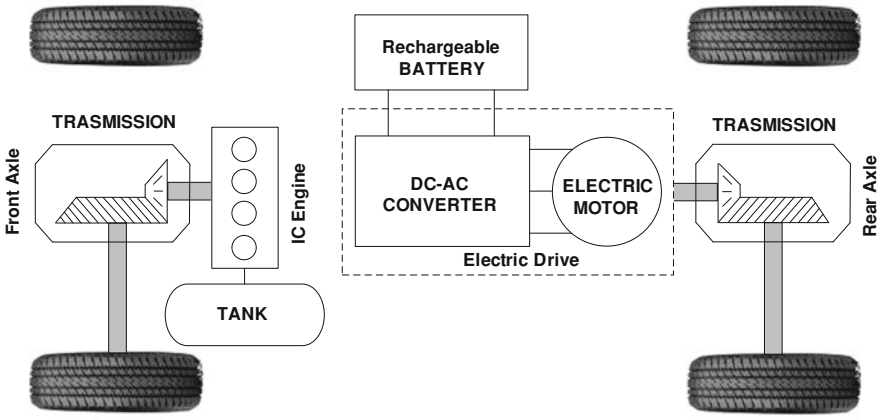

Fig. 5.19 Parallel hybrid configuration with IC engine and electric drive connected to separate axles

connects the electric with the mechanical system. For this configuration, the battery is charged by regenerative braking operations, but the IC engine could power harder to maintain speed and charge the battery by means of the road connection, which transfers energy from the IC engine to electric drive operating as electric generator.

Other variations of the above configurations are possible considering that the energy recharging the battery could comes from the electric network or other power supply units, while the car is parked or, however, not in use [3].

Hybrid thermal vehicles are more expensive than traditional vehicles, because they include more than one energy source on board. However, there are some components of traditional vehicles which are not required for hybrid vehicles and can be made some savings. For instance, in the series configuration there is no need for the gear box because the electric drive regulates the motor speed electronically, transmission is simplified and differential is useless if the motors are directly connected to the wheels. The starter can be eliminated in both series and parallel configuration since electric machines do not need any specific devices to start. Many hybrid vehicles are currently on the market and this sector is growing rapidly worldwide.

5.5.2 Solar Vehicles

Vehicles powered by solar panels located on board are quite expensive because of the high cost of photovoltaic cells, which require high sunshine to work efficiently. Nowadays photovoltaic cells are raising high efficiencies with decreasing cost but it is unlike that cars for everyday use could be exclusively powered by solar panels essentially because of large surfaces for the photovoltaic cells required to power a

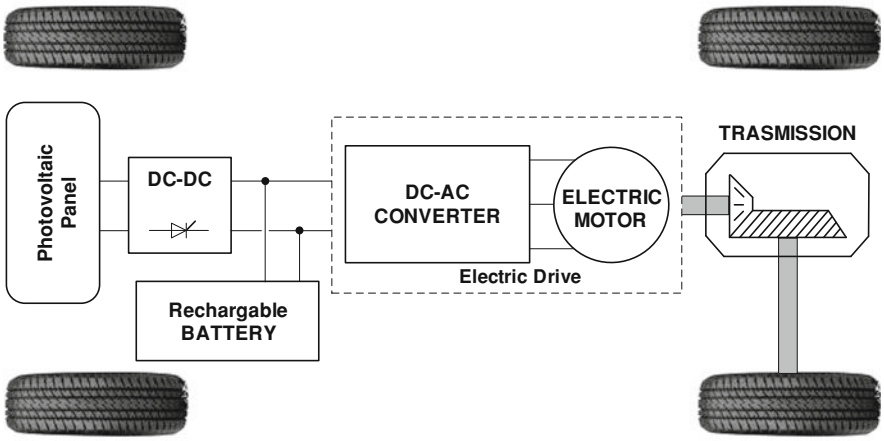

Fig. 5.20 Solar vehicle configuration

road vehicle. However, solar cells could be used to keep the batteries of any type of electric vehicle topped up.

In Fig. 5.20, the scheme for the configuration of a solar vehicle is reported. The DC–DC converter is required to adapt the voltage generated by the solar system to the voltage range proper of battery pack and electric drive. The converter is mono-directional because no energy flux goes from the battery and motor drive toward the solar panel [3, 4].

5.5.3 Vehicles Using Flywheels and Super Capacitors

Due to the small amount of energy that flywheels can store, vehicles using flywheels are generally trams or city busses equipped with one or more flywheels. These devices can be speed up by an electric motor, supplied when the vehicle stops at the bus station to pick up passengers. Moreover, the flywheel is accelerated by the regenerative braking, when the kinetic energy of the vehicle is transferred to the kinetic energy of the flywheel. Flywheels can also be combined with batteries with the advantage of reducing battery weight. In Fig. 5.21, a simplified scheme for a vehicle equipped with battery and flywheel is shown.

Super capacitors can be used in addition to batteries in electric vehicles. In Fig. 5.22, a simplified scheme for a vehicle equipped with battery and super capacitors is shown [4]. The super capacitors allow the kinetic energy of the vehicle to be recovered when the vehicle slows down, increasing the availability of power peaks during rapid accelerations. In this way, an optimal management of batteries can be accomplished.

Super capacitors and flywheels, as high power storage systems, can be used in a wide range of hybrid vehicles, combined with one or more power energy devices,

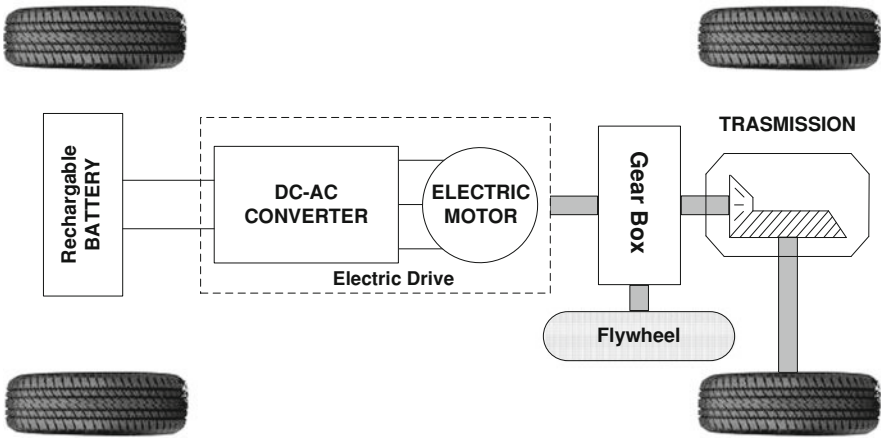

Fig. 5.21 Configuration of electric vehicle equipped with flywheel and batteries

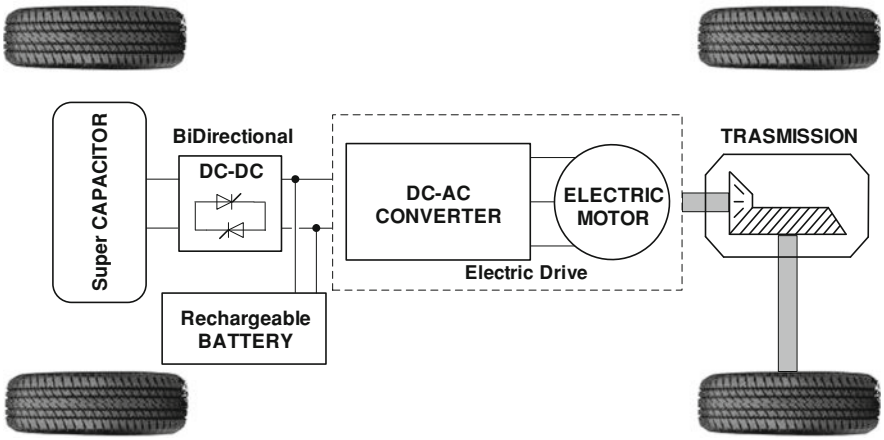

Fig. 5.22 Configuration of electric vehicle equipped with super capacitors and batteries

such as batteries, fuel cells, solar panels, and IC engines. Plenty of combinations are possible and imaginable in that sense [4, 13].

5.5.4 Fuel Cell Electric Vehicles

The integration of a fuel cell system in an electric power train results in a rather complex system constituted by the combination of energy storage systems, energy sources, electric converters and various auxiliary devices.

In principle, a fuel cell power train could operate in so-called *full power* mode, i.e., all the power required by the electric drive could be supplied by the FCS,

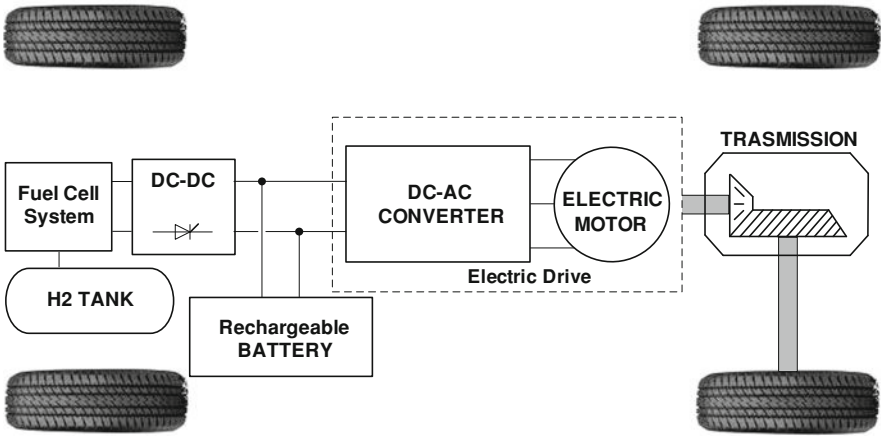

Fig. 5.23 Configuration of fuel cell vehicle equipped with rechargeable batteries

while a small battery would permit the vehicle start up. This option would permit the elimination of a heavy and large battery pack, but requires the FCS follows all the load variations imposed by the road mission. As seen in Chap. 4, such a solution implies the acquisition of a stack of power at least equal to that of the electric drive, with consequent significant impact on costs, and the difficulty of the FCS to follow in a reliable way all fast dynamic demands typical of automotive applications. For this reason, the hybrid configuration is generally preferred in a fuel cell propulsion system, where the electric energy storage system is generally connected in electric parallel with the fuel cell system, and a DC–DC converter is used to match the FCS variable voltage to the voltage required by the electric drive (Fig. 5.23).

The simultaneous utilization of FCS and battery within a fuel cell propulsion system can be accomplished by two basic ways: (i) the battery pack can be minimized (but not eliminated as in *full power*) assigning the role of generating most energy required by the load to the FCS (*soft hybrid* configuration), (ii) the FCS can be sized to provide the base load, i.e. a power value close to the average power of the expectable road mission (*hard hybrid* configuration), while larger battery pack are necessary to satisfy the dynamic requirements.

The main benefit of the *soft hybrid* option is the reduced use of batteries, which could have the minimum capacity necessary to feed the vehicle auxiliaries, giving a limited contribution to peak powers and save energy during the regenerative braking phases. On the other hand, the *hard hybrid* option offers the possibility to limit the cost of the FCS, which would work mainly in steady-state conditions, then in more reliable way.

The *soft hybrid* configuration represents the most flexible solution for the energy management in all the possible driving conditions of an automotive

application. For instance, if the dynamic requirement is not too demanding the FCS can follow the load variation up to its maximum power, while the assistance of batteries becomes essential when very high acceleration performance are required by the driver. On the other hand, the *hard hybrid* option assigns to batteries the task to satisfy also the fastest dynamic requirements, but could not be able to manage the energy of batteries in not expectable driving conditions. However, when the driving cycle is previously known, and is characterized by an average power much lower than the cycle power peaks, the *hard hybrid* configuration is preferred, because a much smaller FCS can be adopted.

The electric energy storage system usually adopted in fuel cell power trains consists of electrochemical batteries and/or super capacitors. The latter represent a promising alternative to batteries, because they have an extremely high specific power and higher charge and discharge efficiency than any types of batteries. For these reasons super capacitors can be used to cover power peaks, especially required during accelerations and during regenerative breaking to save the vehicle kinetic energy.

Other configurations of fuel cell vehicles can be realized combining the advantages of different types of storage systems. As an example, the Fig. 5.24 shows the combination of rechargeable batteries with a super capacitor system. In this case, a three-way converter is required to connect the two storage systems with the fuel cell stack and interface the different voltage versus current characteristics of the devices interconnected [46].

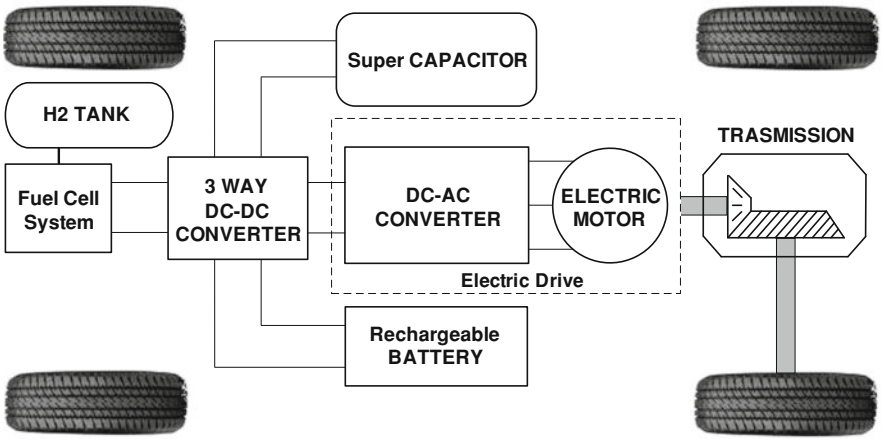

Fig. 5.24 Configuration of fuel cell vehicle equipped with rechargeable batteries and super capacitors

References

1. Guzzella L, Sciarretta A (2005) Vehicle propulsion systems. Springer, Berlin
2. Maggetto G, Van Mierlo J (2001) Electric vehicles, hybrid vehicles and fuel cell electric vehicles: state of the art and perspectives. Ann Chim Shi Mater 26(4):9–26
3. Larminie J, Lowry J (2003) Electric vehicle technology explained. Wiley, Chichester
4. Westbrook MH (2001) The electric and hybrid electric car. Society of Automotive Engineers, Warrendale
5. Dhameja S (2002) Electric vehicle battery systems. Newnes, Boston
6. Fitzgerald AE, Kinsley C (2003) Electric machinery. McGraw-Hill, New York
7. Muller G (1966) Elektrische Maschinen. Verlag-Technik, Berlin
8. Richter (1953) Elektrische Maschinen, vol I, II, III. Verlag-Birkhauser, Basel
9. Vas P (1992) Electrical machines and drives. Claredon Press, Oxford
10. Langsdorf AS (1955) Theory of alternating-current machinery. McGraw-Hill, New York
11. West JGW (1994) DC, induction, reluctance and PM motors for electric vehicles. Power Eng J 8(2):77–88
12. Moan N, Undeland TM, Robbins WP (2003) Power electronics: converters, applications, and design, 3rd edn. Wiley, New York
13. Linden D, Reddy TB (2001) Handbook of batteries, 3rd edn. McGraw-Hill Handbooks, New York
14. Vinal GW (1951) Storage batteries. Wiley, New York
15. Keusch VP, Baran J, Pohl JP (2001) Messungen zum Laden und Entladen eines Modell-Bleiakkumulators. Unterricht Chemie 66:1–5
16. Shukla AK, Venugopalan S, Hariprakash B (2001) Nickel-based rechargeable batteries. J Power Sources 100:125–148
17. Morioka Y, Narukawa S, Itou T (2001) State-of-the-art of alkaline rechargeable batteries. J Power Sources 100:107–116
18. Taniguchi A, Fujioka N, Ikoma M, Ohta A (2001) Development of nickel/metal-hydride batteries for EVs and HEVs. J Power Sources 100:117–124
19. Sudworth JL (2001) The sodium/nickel chloride (ZEBRA) battery. J Power Sources 100:149–163
20. Nishi Y (2001) Lithium ion secondary batteries; past 10 years and the future. J Power Sources 100:101–106
21. Scrosati B, Croce F, Panero S (2001) Progress in lithium polymer battery R&D. J Power Sources 100:93–100
22. Kuribayashi I, Yokoyama M, Yamashita M (1995) Battery characteristics with various carbonaceous materials. J Power Sources 54:1–5
23. Peng B, Chen J (2009) Functional materials with high-efficiency energy storage and conversion for battery and fuel cell. Coordin Chem Rev 253:2805–2813
24. Ma H, Cheng F, Chen JY, Zhao JZ, Li CS, Tao ZL, Liang J (2007) Nest-like silicon nanospheres for high-capacity lithium storage. Adv Mater 19:4067–4070
25. Chan CK, Peng H, Liu G, McIlwrath K, Zhang XF, Huggins RA, Cui Y (2008) High-performance lithium battery anodes using silicon nanowires. Nat Nanotechnol 3:31–35
26. Ng SH, Wang J, Wexler D, Konstantinov K, Guo ZP, Liu HK (2006) Highly reversible lithium storage in spheroidal carbon-coated silicon nanocomposites as anodes for lithium-ion batteries. Angew Chem Int Ed 46:6896–6899
27. Hassoun J, Panero S, Simon P, Taberna PL, Scrosati B (2007) High rate, long life Ni-Sn nanostructured electrodes for lithium ion batteries. Adv Mater 19:1632–1635
28. Oumellal Y, Rougier A, Nazri GA, Tarascon JM, Aymard L (2008) Metal hydrides for lithium-ion batteries. Nat Mater 7:916–921
29. Fergus JW (2010) Recent developments in cathode materials for lithium ion batteries. J Power Sources 195:939–954

30. Patoux S, Daniel L, Bourbon C, Lignier H, Pagano C, Le Cras F, Jouanneau S, Partinet S (2009) J Power Sources 189:344–352
31. Katiyar RK, Singhal R, Asmar K, Valentin R, Katiyar RS (2009) High voltage spinel cathode materials for high energy density and high rate capability Li ion rechargeable batteries. J Power Sources 194:526–530
32. Gao J, Manthiram A (2009) Eliminating the irreversible capacity loss of high capacity layered $Li[Li_{0.2}Mn_{0.54}Ni_{0.13}Co_{0.13}]O_2$ cathode by blending with other lithium insertion hosts. J Power Sources 191:644–647
33. Automotive Engineering on line. NiMh battery has high-volume future. http://www.sae.org/mags/AEI/7552. Accessed 09 February 2010
34. Lee CW, Sathiyanarayanan K, Eom SW, Yun MS (2006) Novel alloys to improve the electrochemical behaviour of zinc anodes for zinc/air battery. J Power Sources 160:1436–1441
35. Yang S, Knickle H (2002) Design and analysis of aluminium/air battery system for electric vehicles. J Power Sources 112:162–173
36. Li Q, Bjerrum NJ (2002) Aluminum as anode for energy storage and conversion: a review. J Power Sources 110:1–10
37. Han B, Liang G (2006) Neutral electrolyte aluminium air battery with open configuration. Rare Met 25:360–363
38. Tang Y, Lu L, Roesky HW, Wang L, Huang B (2004) The effect of zinc on the aluminium anode of the aluminium-air battery. J Power Sources 138:313–318
39. Alonso M, Finn EJ (1980) Fundamental university physics—mechanics and thermodynamics, vol 1, 2nd edn. Addison Wesley Publishing Company Inc., California
40. Conway BE (1999) Electrochemical supercapacitors: scientific fundamentals and technological application. Kluwer Academic/Plenum Publishers, New York
41. Jung DY, Kim YH, Kim SW, Lee SH (2003) Development of ultracapacitor modules for 42-V automotive electrical systems. J Power Sources 114:366–373
42. Yoo H, Sul SK, Park Y, Jeong J (2008) System integration and power-flow management for a series hybrid electric vehicle using supercapacitors and batteries. IEEE T Ind Appl 44:108–114
43. Mishima T, Hiraki E, Yamamoto K, Tanaka T (2006) Bidirectional DC-DC converter for supercapacitor-linked power interface in advanced electric vehicles. IEEJ T Ind Appl 126:529–530
44. Mir L, Etxeberria-Otadui I, De Arenaza IP, Sarasola I, Nieva T (2009) A supercapacitor based light rail vehicle: System design and operations modes. In: Proceedings of the IEEE energy conversion congress and exposition, San Jose CA, pp 1632–1639. ISBN: 978-142442893-9
45. Buchi F, Tsukada A, Rodutz P, Garcia O, Ruge M, Kotz R, Bartschi M, Dietrich P (2002) Fuel cell supercap hybrid electric power train. In: Proceedings of European fuel cell forum conference, Lucerne, pp 218–231
46. Thounthong P, Raël S, Davat B (2006) Control strategy of fuel cell/supercapacitors hybrid power sources for electric vehicle. J Power Sources 158:806–814

Chapter 6
Case Study A: Fuel Cell Power Train for Mopeds

6.1 Description of the 3.5 kW Fuel Cell Power Train

The experimental results discussed in this case study are obtained on a fuel cell power train installed on a laboratory test bench. It is constituted by a 3.5 kW electric drive connected in hybrid configuration to a 2 kW PEM fuel cell system (FCS) and an electrical energy storage system (lead batteries). The main technical specifications of the FCS are reported in Table 6.1, whereas its scheme is shown in Fig. 6.1 [1, 2].

The system is based on a PEM fuel cell stack (2.5 kW maximum power) equipped with all the auxiliary components required for the stack operation, such as air supply unit, fuel supply unit, cooling system, humidification system, and a management unit. Hydrogen is supplied by 200 bar cylinders connected to a laboratory gas decompression unit. A side channel compressor (see Sect. 4.3), operating in the range 25–40 kPa, is used to feed air to the cathode side, the cooling system is realized by a de-ionized water circuit equipped with sensors to measure temperature and flow rate. The diameter of the hydrogen purge valve guarantees a minimum absolute value of pressure at anode inlet, in particular not lower than 130 kPa while in order to control the stoichiometric ratio (R), air flow rate is regulated through the speed regulation of the electric motor directly connected to the air compressor and then measured by a variable-area flow meter.

Two pressure transducers are located upstream of the stack to monitor anode and cathode pressure during the experimental runs. A spiral heat exchanger, using external water at room temperature as second fluid, is used to control the temperature of the cooling water. The FCS humidification strategy is based on the deionized water injection method (see Sect. 4.5), activating the injection when the outlet air temperature is higher than 60°C.

The fuel cell system is equipped with several sensors able to measure the air and water flow rates, the temperatures of cathode outlet stream and of water in cooling circuit, the hydrogen pressure, stack current and voltage, and individual

P. Corbo et al., *Hydrogen Fuel Cells for Road Vehicles*,
Green Energy and Technology, DOI: 10.1007/978-0-85729-136-3_6,

Table 6.1 Technical specifications of the fuel cell system

Fuel cell system	
Stack output electric power	Max. 2.5 kW, dead-end
Electric power after DC–DC	Max. 2.0 kW
Stack output voltage range	22–34 V
Power rate	Max 500 W s^{-1}
Cell number	34 cells
Hydrogen	Purity: 99.999 H_2 FCS inlet gas pressure: 500 kPa FCS inlet gas stream: at least 3 Nm^3 h^{-1}
Nitrogen	Purity: 99.999 N_2 FCS inlet gas pressure: 500 kPa FCS inlet gas stream: at least 1 Nm^3 h^{-1}
Max stack temperature	343 K
Max cooling water	333 K
Air compressor	Side channel, 24VDC, max press. 16 kPa
Hydrogen purge valve	Cut-off valve, normally closed, 24VDC, NPT 1/8”
Cooling water pump	24VDC, 20 kPa, 7 l/min
Humidification water pump	24VDC, 500 kPa, 0.17 l/min

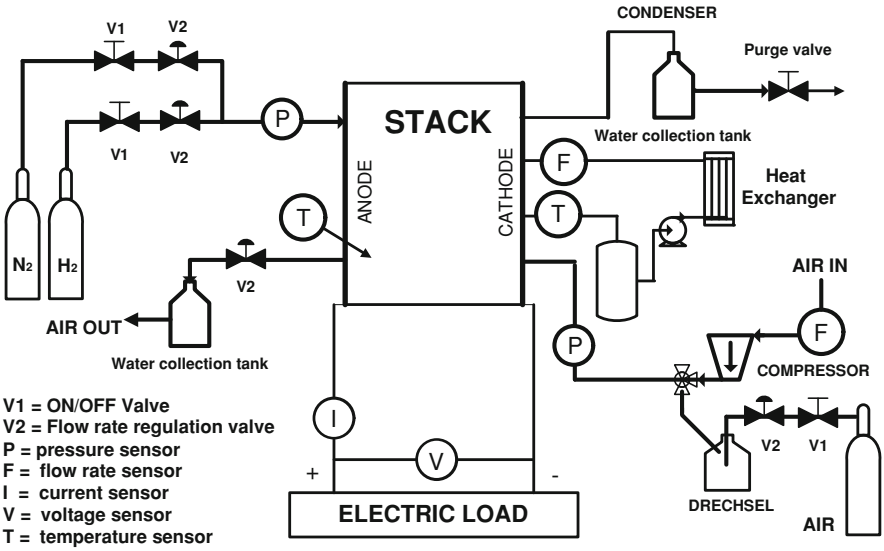

Fig. 6.1 Scheme of the fuel cell system experimental apparatus and location of the sensors

cell voltages. National Instruments FieldPoint units are used to acquire all the voltage signals generated by the sensors and to control the overall system. The system is also provided with a small lead-acid battery of 24 V and 6 Ah for the start-up operation of the system, when the energy supplied by the stack is lower than the electric request by the auxiliaries.

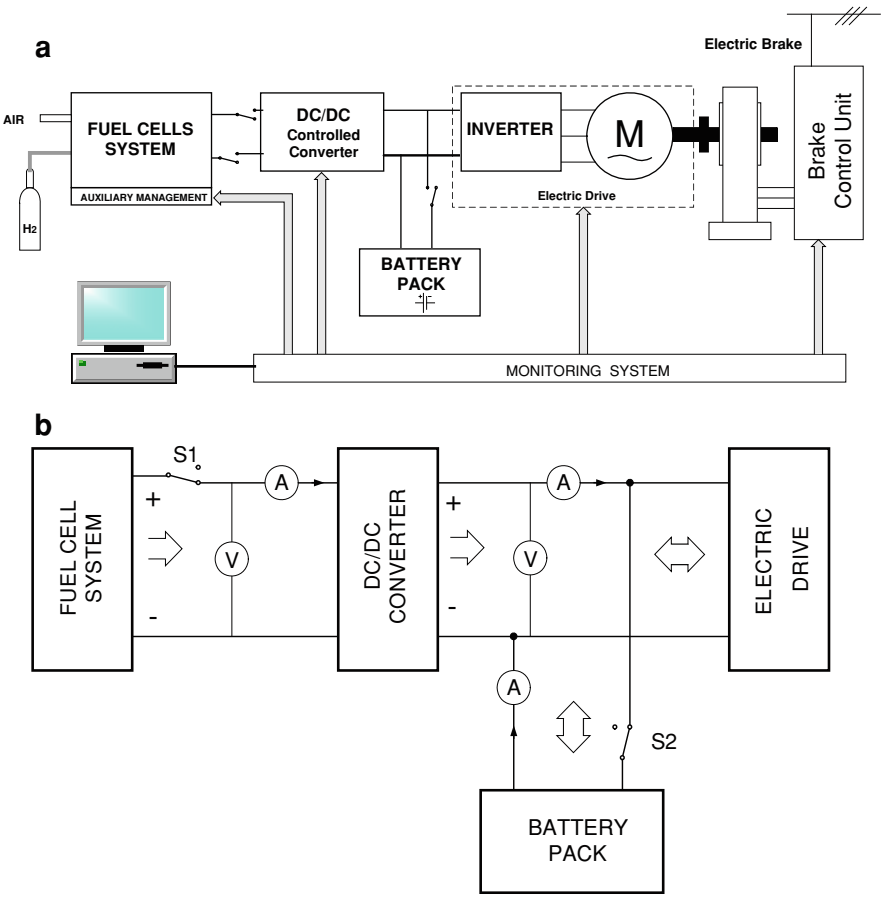

Fig. 6.2 **a** Overall scheme of fuel cell power train on test bench. **b** Electrical connections between stack, batteries, and load with location of sensors

Figure 6.2a shows the scheme of the integrated fuel cell power train as installed on the laboratory test bench, whereas Fig. 6.2b shows the electric connections between the stack, storage system and electric drive. In particular, the stack electric outputs are connected to the DC–DC converter, whose function is to raise the stack output voltage to the value required by the battery pack and electric drive connected in electric parallel. The energy flow is unidirectional from stack toward DC bus, while the battery pack can be recharged by both stack and engine (during regenerative braking) as well as discharged when the energy required from the engine is higher than the energy provided by the fuel cell system. Current and voltage transducers are used for monitoring the main power flows between the components of the system. Furthermore, some security switches are installed in case of unpredictable events which require the instantaneous disconnection of the battery pack and/or stack from the other parts of the system to avoid any damage.

Table 6.2 Technical specifications of the electrical drive

Type of drive	Brushless
Maximum power	3.5 kW
Rated current	32 A
Maximum current	100 A
Link voltage	48 V
Motor voltage	35 V
Rated speed	3000 rpm
Maximum speed	6000 rpm

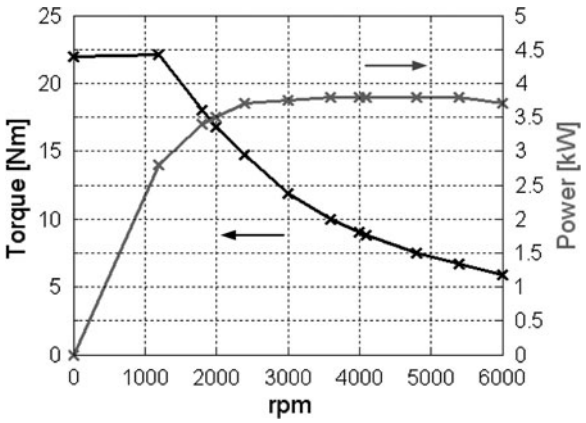

Fig. 6.3 Characteristic curves of the electric engine

The electric drive is selected among those commercially available for applications on electric mopeds. In particular, a brushless electric drive with a rated power of 3.5 kW and maximum speed of 6000 rpm is used. The technical specifications of this electrical drive are reported in Table 6.2, while the Fig. 6.3 shows its characteristic curves in terms of power and torque versus revolution speed.

This engine is supplied by an inverter and is coupled to an eddy current braking machine. The electric drive performs the speed regulation electronically in forward and backward directions, for this reason the ratio between the engine and wheel speed is fixed for this kind of vehicle and therefore no gear is present, but only a speed reducer between the wheel and motor shaft. A flywheel, previously designed taking into account the vehicle inertia, is interposed between the electric motor and the electric brake. The vehicle mass was fixed considering a commercial electric scooter as reference vehicle (178 kg driver included).

The electric brake is an eddy current brake, which can simulate different aerodynamic drags, rolling resistances, and driving cycles using a specific software developed in *Labview*.

The stack output voltage ranges from 34 V at open circuit to 22 V at full load, while the electric motor is supplied at 48 V DC. For this reason, a DC–DC converter (see Sect. 5.2) is used to match the stack output voltage with that required by the engine. In Table 6.3, the technical specifications of the DC–DC converter are shown.

Table 6.3 Technical specifications of the DC–DC converter

Type of converter	DC–DC
Nominal power	2.8 kW
Maximum input voltage	36 V
Minimum input voltage	16 V
Nominal input voltage	24 V
Nominal output voltage	48 V
Output current	1–50 A

Table 6.4 Technical specifications of the lead-acid battery pack

Type of battery	Lead-acid
Nominal voltage of the pack	48 V
Nominal voltage of each battery	12 V
Number of batteries	4
Battery capacity	38 Ah

Downstream of the converter, a DC bus connects this device in electric parallel with the battery pack to supply the electric drive. Voltage and current sensors are installed on batteries and upstream–downstream the DC–DC converter, as shown in Fig. 6.2, to monitor the electric energy flows between the different components of the propulsion system. The DC–DC converter allows the stack output power to be varied according to the selected control strategy. Furthermore, some security switches are adopted, in order to instantaneously disconnect the electric load from battery pack and/or stack. An I/O laboratory board is used for data acquisition and setting of the electrical parameter affecting the DC–DC converter behavior.

A lead-acid battery pack is used as electrical energy storage system, constituted by 4 units, each one of 12 V and 38 Ah. The choice of using lead-acid batteries is essentially motivated by its low cost and good efficiency [2]. The technical specifications of the battery pack are reported in Table 6.4.

A dedicated acquisition system is connected to the single cells of the stack to monitor and save data of cell voltages during the different runs. Moreover, a d-Space board was dedicated to acquire and control all the signals of the fuel cell power train.

The control strategies are programmed in Matlab-Simulink, compiled in C++ and then downloaded into the DSP processor of the d-Space board. The controlled management of the fuel cell system during the dynamic tests operates on hydrogen purge, air flow rate regulation (stoichiometric ratio), external humidification, and stack temperature.

6.2 Efficiency Calculations

In this paragraph, the efficiency calculations to evaluate both the fuel cell system alone and the overall propulsion system are reported starting from the parameters

acquired by sensors located in the experimental plant introduced in the previous sections. These calculations are also valid for the other case study analyzed in the next chapter.

The stack efficiency is calculated by the following equation:

$$\eta_{\text{stack}} = \frac{V}{V_{\text{id}}} \tag{6.1}$$

where V is the measured output stack voltage and V_{id} is the reversible open circuit stack voltage (1.23 V), given by $-\Delta G_{\text{f}}/2F$ (see Sect. 3.1), while the theoretical or thermodynamic stack efficiency is given by the Eqs. 6.3–6.9.

As discussed in Sect. 4.2, during stack operation a partial hydrogen purge is necessary, then it is possible to define a fuel utilization efficiency (η_{util}) as ratio between mass of fuel reacted in the stack and mass of fuel entering the stack. It can be experimentally set by fixing the opening time and the opening frequency of the anode purge valve. The efficiency losses due to all the auxiliary components (air compressor, water pump, cable resistance, other electrical, and minor components) necessary to the stack operation can be taken into account by an experimental coefficient (η_{abs}) expressed as ratio between power at DC–DC converter inlet and stack power. The total efficiency of the fuel cell system is then calculated by the following equation:

$$\eta_{\text{FCS}} = \eta_{\text{th}} \cdot \eta_{\text{util}} \cdot \eta_{\text{stack}} \cdot \eta_{\text{abs}} \tag{6.2}$$

which expresses the ratio between the power at DC–DC converter input and the theoretical power associated with the fuel entering the stack. The experimental determination of DC–DC converter (η_{DC}) and electrical drive (η_{ED}) efficiency is also performed. Both are calculated as ratio between outlet and inlet power of the devices. The electrochemical efficiency of storage batteries is defined as ratio between the integral of the instantaneous current during a discharge and the same integral during a charge, if the status of the battery before and after the calculation is the same:

$$\eta_{\text{batt}} = \frac{\int_0^{t_{\text{d}}} I_{\text{d}} \mathrm{d}t}{\int_0^{t_{\text{c}}} I_{\text{c}} \mathrm{d}t} \tag{6.3}$$

where I_{d} and I_{c} are the battery current during the discharge and charge periods, respectively, while t_{d} and t_{c} are the lengths of these periods. The determination of this efficiency for a specific type and sample of battery, with reference to a particular driving cycle, requires the experimental evaluation of the battery state of charge (SOC), which is based on specific tests which are beyond the scope of this case study. On the other hand, for lead-acid batteries, used in this case study, it has

been experimentally verified that very low energy losses can be detected if charge and discharge operations are very fast, in particular in short cycles of charge and discharge (about 30 min) an energy efficiency higher than 92% has been obtained. Since for the experiments presented in this case study and the following in the next chapter the single periods of charge and discharge of the battery pack last not more than 2 min, and the current involved is higher than 10 A only during the fast acceleration phase of the R47 cycle (see next paragraphs), a value of 100% for the battery energy efficiency is assumed valid in all tests. On this hypothesis, it is possible to define the battery state of charge as:

$$\mathrm{SOC}(t) = \mathrm{SOC}^0 + \int_{t^0}^{t} I_{\mathrm{batt}}(t)\,\mathrm{d}t \tag{6.4}$$

where SOC^0 is the known battery state of charge at the time t^0. This definition is utilized in this paper to instantaneously calculate the battery SOC during the driving cycles, starting from the experimental measurements of battery current and voltage.

Finally, the total efficiency of the power train (η_{PT}) on the driving cycle is defined by the following equation:

$$\eta_{\mathrm{PT}} = \frac{E_{\mathrm{load}}}{E_{\mathrm{H_2}} + E_{\mathrm{batt}}} \tag{6.5}$$

where:

$$E_{batt} = \int_{t_1}^{t_2} V_{\mathrm{batt}} \cdot I_{\mathrm{batt}}\mathrm{d}t \tag{6.6}$$

$$E_{\mathrm{load}} = \int_{t_1}^{t_2} T_{\mathrm{m}} \cdot \omega_{\mathrm{m}}\mathrm{d}t \tag{6.7}$$

$$E_{\mathrm{H_2}} = \frac{1}{\eta_{\mathrm{util}}} \int_{t_1}^{t_2} M_{\mathrm{H_2}} \cdot n_{\mathrm{cells}} \cdot I \cdot \frac{\Delta_{H_{\mathrm{f}}}}{2F}\mathrm{d}t \tag{6.8}$$

where V_{batt} is the battery voltage, I_{batt} the battery current, T_{m} the brake torque, λ_{m} the engine speed, $M_{\mathrm{H_2}}$ the hydrogen molecular weight, n_{cells} the cell number, I the stack current, E_{load} the energy provided by the engine during the overall test procedure, while $E_{\mathrm{H_2}}$ is the energy coming from hydrogen and E_{batt} is the net energy exchanged by the battery pack during the cycle.

6.3 FCS Characterization: Energy Losses in Steady-State Conditions

The Fig. 6.4 shows the characteristic curves of the stack, in terms of voltage and power versus stack current. The stack output voltage decreases from 32 V, at low load, to about 22 V, at the highest load tested (115 A), when the stack power reaches the peak value of 2.5 kW. The polarization curve presents a linear relationship between voltage and current in the working range of 10–90 A, with a voltage decrease from 27 to 24 V.

The experimental conditions to obtain these characteristics are the following: stack temperature of 60°C, hydrogen pressure ranging from 20 to 50 kPa, air pressure ranging from 10 to 16 kPa, and stoichiometric ratio (R) ranging from 2 to 6 (for definition of R see Sect. 3.3). As regarding the purge intervention strategy, the opening frequency of the purge valve adopted for all tests reported in this chapter is proportional to stack power (and then to the water amount produced by the reaction), corresponding to a constant value of η_{util} (0.90).

The Fig. 6.5 shows the relation between R and the stack power, which is used for all the tests reported in this chapter. This figure evidences that the selected air management strategy determines R values decrease from $R = 9$ at open circuit to about $R = 2$ for a stack power between 500 and 2000 kW. These values of R are specifically selected to minimize the air compressor energy losses (see Sect. 4.3).

As regarding the humification strategy, the quantity and frequency of water injected is chosen according to the criterion of regulating both water injection and fuel purge (see Sect. 4.2) according to individual cell voltage uniformity (see Sect. 6.4). Apart from this general criterion, the injection pump is automatically activated when outlet air temperature is higher than 333 K, with water flow rate of 0.17 l/min and injection time of 1 s every 10 s [1], to assure sufficient membrane hydration also in conditions of high temperatures.

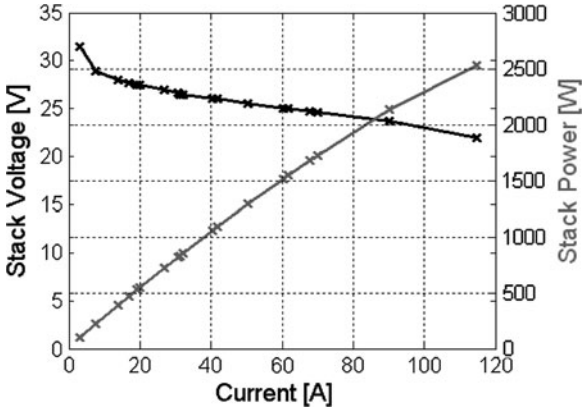

Fig. 6.4 Stack characteristic curves ($R = 2$–6, $T = 333$ K, $P_{H_2} < 50$ kPa, $P_{air} < 20$ kPa)

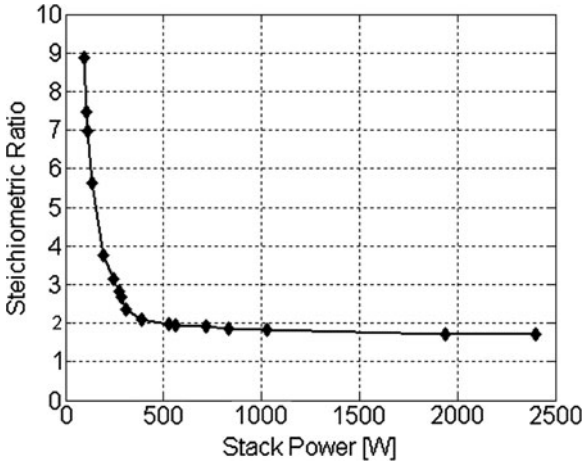

Fig. 6.5 Stoichiometric ratio values utilized in experimental tests as function of stack power

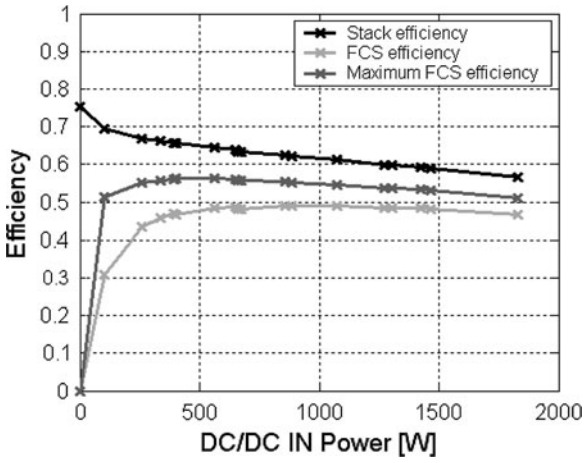

Fig. 6.6 Stack and fuel cell system efficiency versus DC–DC converter inlet electric power under the experimental conditions of Fig. 6.4

The voltage data of Fig. 6.4 are presented also in terms of stack efficiency curve in Fig. 6.6, where η_{stack} is plotted against the electric power produced by the FCS and measured at the DC–DC converter inlet. In the same figure, the actual and "theoretical" curves of FCS efficiency (η_{FCS}) are also reported, they refer to the real consumptions of ancillary components or to the "ideal" losses expected for that same system after optimization of all individual components (maximum FCS efficiency in Fig. 6.6). The stack efficiency varies from 0.7 at 0.1 kW to 0.56 at 1.8 kW of FCS power, while actual FCS efficiency does not result higher than 50%, due to the different sources of energy loss inside the system.

In order to better understand the above values for FCS efficiency, the main parasitic losses are shown in Fig. 6.7, where each curve is representative of the electric power absorbed by each auxiliary component of the FCS, and is reported as a function of the DC–DC converter power. The major consumption is due to the

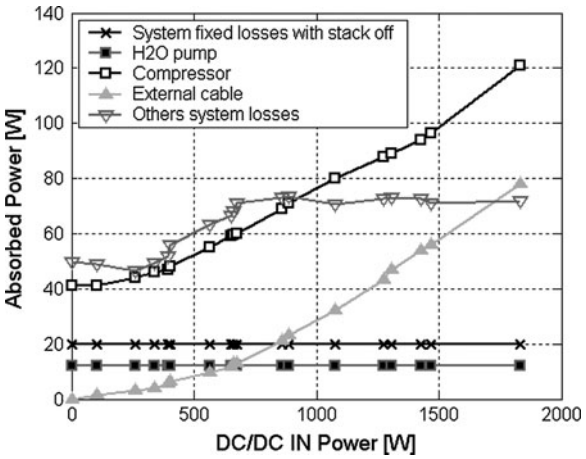

Fig. 6.7 Power losses associated with the main fuel cell system components versus DC–DC converter inlet power under the experimental conditions of Fig. 6.4

air compressor (about 120 W, when the FCS generates a power of 1.8 kW), while minor losses are related to the cooling and humidification of water pump (about 10 W each and constant with respect to the load). Further energy consumptions are due to cables connecting the FCS to DC–DC converter (about 80 W at the highest load) and undetermined system losses, measures as about 20 W when the stack is off and about 70 W when is switched on, and depending on several electric components, necessary in a FCS designed for laboratory tests, such as sensors, electric valves, wires, induction relays, and electronic control boards.

The consumption of these last auxiliary components might be partially reduced with a specific design of the FCS for a real vehicle, but the energy losses due to the air and water management system would be quite difficult to be lowered. In this respect, the maximum FCS efficiency (55% at medium load, see Fig. 6.6) takes in regards to the only loss sources due to the air compressor, hydrogen purge, and water pump.

6.4 Dynamic Performance of the FCS

The dynamic behavior of the FCS is firstly verified starting from the analysis of the energy lost during the start-up phases, evaluating the performance as function of acceleration rates [2]. In particular, warm-up tests are performed starting from two different initial stack temperatures, 15 and 30°C. For each one of these temperatures, two accelerations of 20 and 200 Ws^{-1} are used up to the stack power of 1200 W. At the end of each acceleration phase, a steady-state operation follows until the stack temperature reaches the value of 45°C.

Other dynamic tests are affected varying the stack power and evaluating the stack response to hydrogen purge, external humidification, and air management

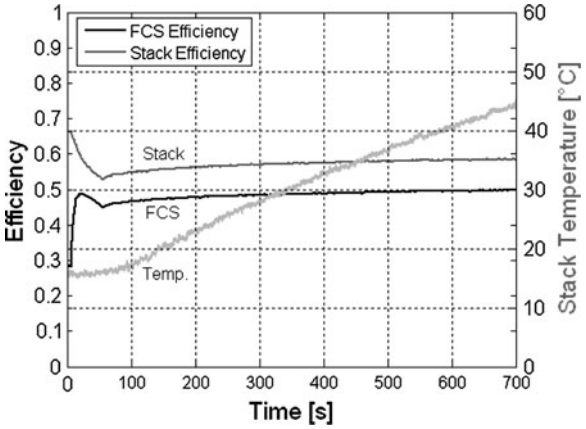

Fig. 6.8 FCS warm up from 15 to 45°C, at 20 W s^{-1} up to 1.2 kW stack power. FCS efficiency, stack efficiency, and temperature versus time

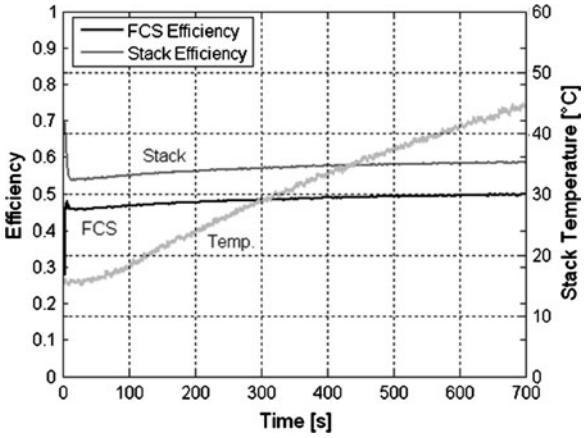

Fig. 6.9 FCS warm up from 15 to 45°C, at 200 W s^{-1} up to 1.2 kW stack power. FCS efficiency, stack efficiency, and temperature versus time

strategies described in the previous sections. These elements can be utilized with the aim to individuate the areas of reliable working to be used in the dynamic tests.

The Figs. 6.8 and 6.9 show stack and FCS efficiencies versus time for the tests starting from the temperature of 15°C. In both these two tests, the selected value of final stack temperature of 45°C is reached in about 10 min, while the stack efficiency achieves a value (0.53) a little bit lower than that maximum (0.59) already at the end of the accelerations ramps (1200 W).

When the stack temperature reaches the value of 45°C, the stack efficiency increases from 0.53 to 0.59, and when power reaches its set maximum value (1200 W) the FCS efficiency increases from 0.45 to 0.50 in both tests. From Figs. 6.8 and 6.9, it is possible to evaluate the energy losses due to the warm-up period of 600 s, they resulted about 5% of the FCS steady-state maximum efficiency. Moreover, the energy losses are not significantly affected by the power acceleration variation from 20 to 200 Ws^{-1}. Start-up operations are also verified at the starting temperature of 30°C and 200 W s^{-1} (Fig. 6.10), the results evidence

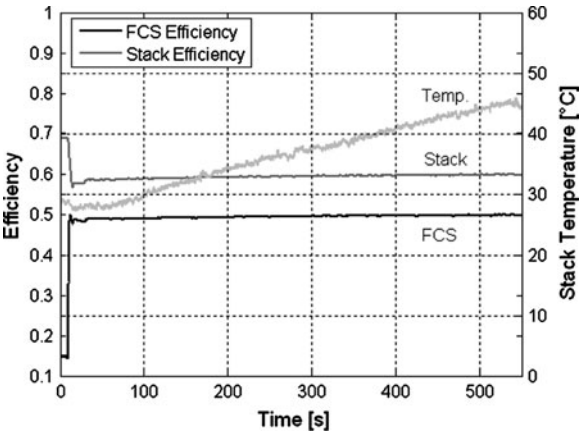

Fig. 6.10 FCS warm up from 30 to 45°C, with 200 W s^{-1} up to 1.2 kW stack power. FCS efficiency, stack efficiency, and temperature versus time

that energy losses associated with the warm-up phase in these conditions decrease to about 2%.

An important point to consider about the stack management, with reference to an electric power train operating in dynamic conditions, as determined by road requirements, is the regulation of the stack temperature together with the other control parameters of water and reactants to avoid mass transfer limitations and membrane drying out or flooding. Moreover, the interaction between stack and auxiliaries has to be balanced taking into account the optimization of fuel cell system efficiency and reliability (see Sect. 4.6).

A statistical indicator can be used for the evaluation of the individual cell uniformity, which is selected as representative of a reliable operation of the stack [3]. This indicator is a coefficient of percentage variation, C_v, that can be calculated by the following equation:

$$C_v = \sqrt{\frac{\sum_1^n \left(\frac{V_i - \bar{V}}{\bar{V}}\right)^2}{n}} \cdot 100, \tag{6.9}$$

where V_i is the voltage of individual cells, $\bar{V}$ is the average cell voltage and n is the number of cells. A value of C_v of 2% is considered acceptable for a regular working of the stack in tests described in the following [3].

The results reported in Figs. 6.11, 6.12, 6.13, 6.14, 6.15, 6.16, and 6.17 [3] refer to experiments performed using a series of power steps up and down, each of them characterized by a rate of about 150 W/s. The Fig. 6.11 shows stack power, stoichiometric ratio, and temperature acquired as a function of time, whereas the coefficient of variation C_v related to individual cells is reported in Fig. 6.12.

Two time acquisition windows (in the range of 0–1040 s and 1820–2120 s) are specifically analyzed in Figs. 6.13 and 6.14. In the first window, the stack power increases up to 1.8 kW, while no temperature control is adopted until 335 K.

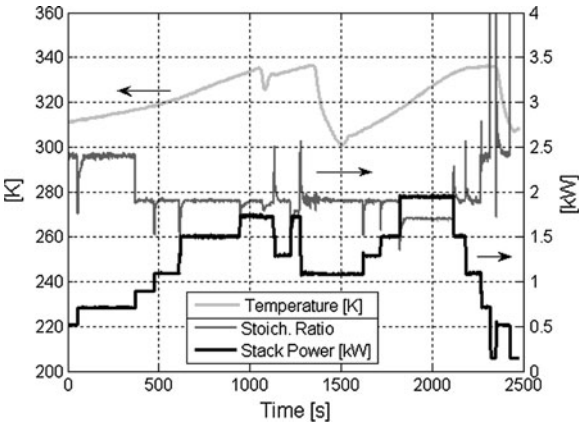

Fig. 6.11 Acquisition of temperature, stoichiometric ratio, and power versus time for the fuel cell system during different steps of stack power variations

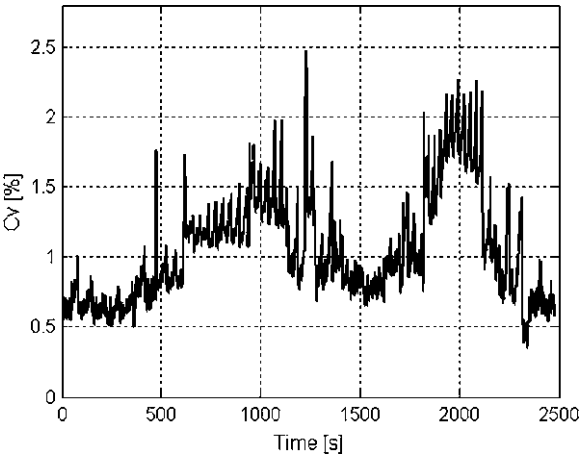

Fig. 6.12 Coefficient of percentage variation (C_v) versus time of individual cell voltage for the experiment of Fig. 6.9

This implies a spontaneous stack heating characterized by an initial temperature increase rate of 1.5 K/min, which becomes 2.5 K/min for a stack power higher than 1 kW. The stoichiometric ratio, following the relation reported in Fig. 6.5, reduces rapidly from 2.4 to 1.7 during the acceleration phases. The coefficient of variation C_v results much less than 2% in the range of time considered, indicating an acceptable regularity of stack working (Fig. 6.12). The function of the hydrogen purge is highlighted in Fig 6.13 showing the individual cell voltages with the relative pressure of hydrogen measured at anode inlet for the total acquisition time.

Moreover, it is possible to observe that the drops of hydrogen pressure, due to the purge action, are followed by a voltage recovery for those cells more affected by flooding phenomena. This behavior is more evident at the highest loads and temperatures, as confirmed during the second phase of the experiment (Figs. 6.11, 6.12). In fact, after cooling from 335 K (1356 s) to 300 K (1510 s), obtained switching on the external water circuit of the heat exchanger, a steady-state condition at 2 kW with stoichiometric ratio of 1.7 is reached in a time window of 300 s

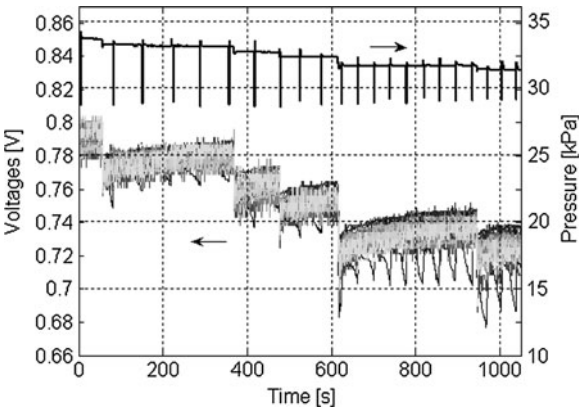

Fig. 6.13 Acquisition versus time of individual cell voltages and hydrogen relative pressure at anode inlet for a particular time window (0–1040 s) of the experiment of Fig. 6.11

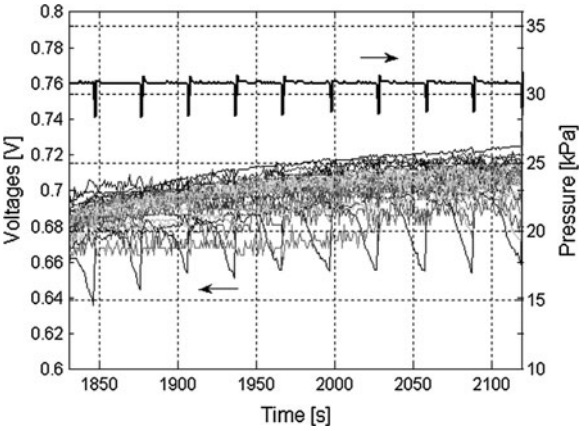

Fig. 6.14 Acquisition versus time of individual cell voltage and hydrogen relative pressure at anode inlet for a particular time window (1820–2120 s) of the experiment of Fig. 6.9

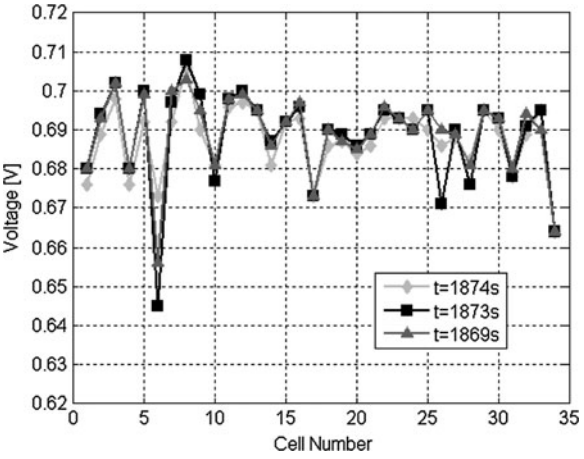

Fig. 6.15 Individual cell voltage acquisition during one single purge operation for the experiment of Fig. 6.11

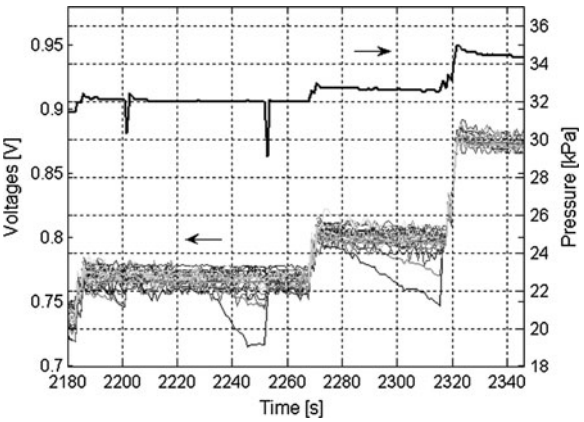

Fig. 6.16 Acquisition versus time of individual cell voltage and hydrogen relative pressure at anode inlet for a particular time window (2180–2400 s) of the experiment of Fig. 6.11

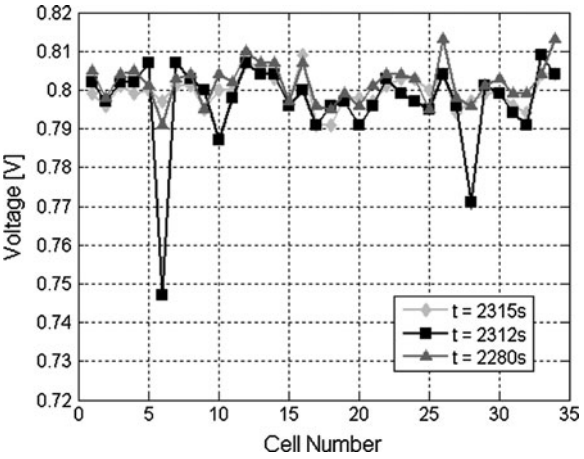

Fig. 6.17 Individual cell voltage during humidification intervention for the experiment of Fig. 6.16

(1820–2120 s in Fig. 6.11). No temperature control is adopted during this period of test, obtaining a temperature increase from 315 to 333 K at about 3 K/min. The result in terms of individual cell voltage and inlet hydrogen pressure as function of time is reported in Fig. 6.14, that shows as the effect of the purge determines a stronger positive effect on cell voltage recovery with respect to the lowest load conditions. In fact, several peaks of C_v reach values slightly higher than 2%, indicating faster but still tolerable flooding phenomena in some individual cells (Fig. 6.12).

A detail of individual cell voltage acquisition during one single purge operation is reported in Fig. 6.15, which refers to the purge peak at about 1870 s corresponding to the stack power of 2 kW (Fig. 6.14).

The three curves correspond to three acquisition instants, two of them before the purge, and the third one just after it. This last figure evidences that some cells,

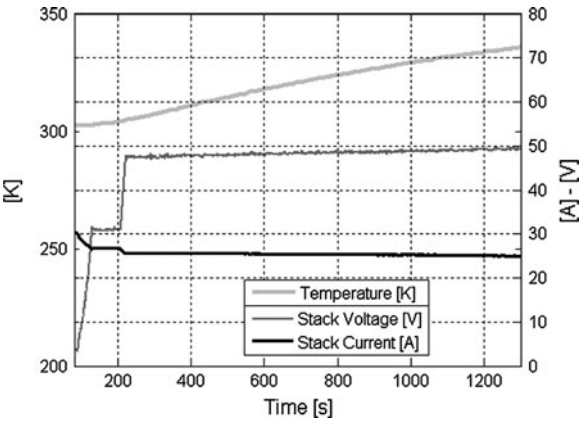

Fig. 6.18 Acquisition versus time of stack voltage, current, and temperature during a steady-state test at 1.2 kW ($R = 1.9$)

in particular those closer to the end plates, are more sensitive to flooding since purge intervention permits a clear voltage recovery.

The effect of the humidification strategy can be deducted by analyzing a third acquisition window (2180–2400 s) for the experiment of Fig. 6.11, shown in Fig. 6.16, where the individual cell voltage and hydrogen pressure measured at anode inlet are reported versus time.

The Fig. 6.11 evidences that during this time window three different steady-state conditions are reached at 338 K, when the stack load decreases from 1.5 to 0.15 kW. In detail, the stack current is hold at 40 A (1.1 kW) for about 60 s, at 23 A (0.7 kW) for 40 s, and finally at 5 A (0.15 kW) for 30 s. During the entire test phase both purge and humidification management appear to be suitable for the optimal stack operation. This is evidenced by maximum C_v peaks of 1.5% in correspondence with purge intervention (at 2250 s, Fig. 6.12) and 1.4% at 2315 s due to external humidification, whose effect becomes more evident at lower stack power (from 0.7 kW), when the purge is not utilized and the minor water production enhances the membrane dehydration. The voltage recovery of individual cells due to external humidification is detailed in Fig. 6.17, where the voltage is reported for three instants, just before the second cell voltage reduction (2280 s in Fig. 6.16), then for the instant corresponding to the maximum of this peak (2312 s), and for the final value after the stabilization of the voltage (2315 s). In spite of the particular sensitivity of some cells (N.6 and N.28) to water management, the C_v values result acceptable also for the last phase of the experiment of Fig. 6.11.

In order to clarify the effectiveness of the external humidification strategy in stack managing, a further experiment is shown in Figs. 6.18 and 6.19. This test is effected in a steady-state condition corresponding to the maximum efficiency of the FCS at 1.2 kW and $R = 1.9$. Stack current, voltage, and temperature are reported as function of time in Fig. 6.18, while C_v and hydrogen pressure are shown in Fig. 6.19.

During this test, the stack temperature is left rising from 303 to 338 K, with a variable increase rate from 2.5 to 1.5 K/min. The regular stack operation is

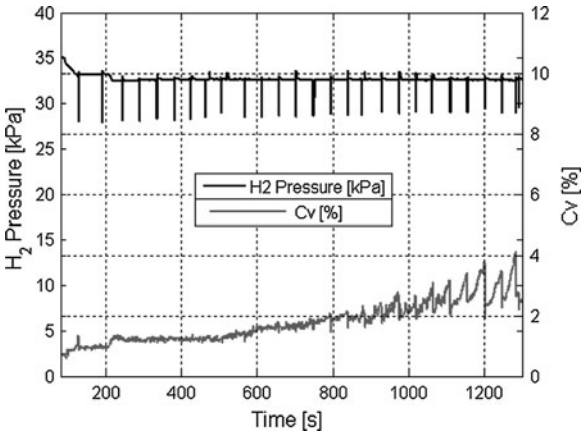

Fig. 6.19 Acquisition versus time of C_v and hydrogen relative pressure at anode inlet for the experiment of Fig. 6.18

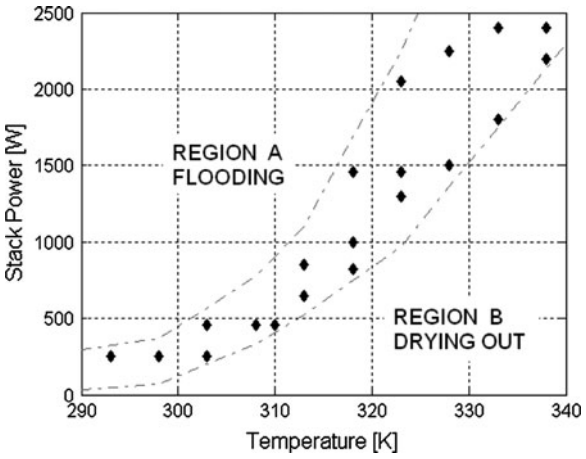

Fig. 6.20 Correlation diagram between stack power and temperature after 1 h steady-state tests

maintained with the purge strategy described above (see Sect. 6.3), at least for temperatures up to 325 K (800 s), while for higher temperatures a slow and progressive increase of the coefficient of variation is observed from 2 to 4%. Over 800 s, the progressive increase of membrane electric resistance, due to its dehydration, evidenced the necessity for the stack of external humidification already from 325 K in steady-state conditions at 1.2 kW. After this temperature, the humidification technique previously described is adopted, but this does not result in C_v diminution (Fig. 6.19) while the more evident effect of purge confirmed the lasting phenomenon of membrane dehydration.

The results of Figs. 6.11, 6.12, 6.13, 6.14, 6.15, 6.16, 6.17, 6.18, and 6.19 evidence that water management in a PEM fuel cell system has to be accurately optimized with strategies depending on stack power and temperature, for predefined values of stoichiometric ratio. The results of Fig. 6.20 and Table 6.5, which refer to 20 different steady-state experiments of about 1 h, can be used to analyze

Table 6.5 Stack and FCS efficiency, and C_v for the experimental points reported in Fig. 6.18

Experiment No.	Stack temperature (K)	Stack power (W)	Stack efficiency	FCS efficiency	Coefficient of variation C_v (%)
1	293	245	0.655	0.171	0.32
2	298	252	0.661	0.173	0.36
3	303	255	0.667	0.175	0.35
4	303	460	0.633	0.398	0.41
5	308	465	0.635	0.400	0.42
6	310	465	0.649	0.408	0.44
7	313	650	0.638	0.452	0.43
8	313	855	0.614	0.472	0.51
9	318	820	0.619	0.472	0.55
10	318	1010	0.608	0.472	0.59
11	318	1460	0.579	0.461	0.94
12	323	1290	0.617	0.480	0.96
13	323	1460	0.588	0.466	1.04
14	323	2050	0.554	0.446	1.72
15	328	1502	0.588	0.470	1.44
16	328	2240	0.556	0.448	1.88
17	333	1815	0.578	0.464	1.96
18	333	2395	0.553	0.449	1.92
19	338	2220	0.563	0.456	1.98
20	338	2405	0.541	0.439	1.97

this important issue. In Fig. 6.20, the relation between stack power and temperature is reported for those experimental points corresponding to the reliable fuel cell system operation ($C_v \leq 2\%$). As previously discussed, the purge strategy is based on the criterion to increase the purge frequency in proportional way with the stack power, maintaining constant the fuel utilization coefficient (about 0.90), while the external humidification is used only when temperature is above 333 K. The region upward of the upper dotted line corresponds to operative conditions characterized by flooding phenomena (region A), while that downward of the lower line comprises working points characterized by the tendency to dehydration of cell membranes (region B).

This diagram gives useful indications about the control strategy to be adopted during dynamic operations, in particular regarding humidification, purge, and cooling procedures. For instance, if during a particular transient operation the stack working point falls inside the region A, the control system has to react by increasing purge frequency and stopping the heat removal from cooling circuit, taking into account the slow stack heating dynamics with respect to automotive demands. On the other hand, if the working point falls inside the region B, it is necessary to reduce the stack temperature and increase the quantity of external water injected.

In Table 6.5 the C_v values for all experimental points of Fig. 6.20 are reported. These data, calculated as average on the entire length of acquisition runs, increased

with the stack power from 0.32 to about 2%, while the instantaneous values, not reported in Table 6.2, were not higher than 4%. In the same Table 6.5, the stack and FCS efficiencies are also reported, the values obtained indicate that in the range of temperatures investigated in Fig. 6.28 the FCS efficiency is comprised between 0.40 and 0.48, except for the conditions of low load, when auxiliary components consume most of the produced electric energy [3].

6.5 Characterization of the Overall Power Train on Driving Cycles

The aim of the experimental tests performed on the overall power train is the evaluation of efficiency and the individuation of the basic energy management strategies necessary to assure proper vehicle operation. The experimental investigation is performed in dynamic conditions on two different urban driving cycles, the R47 and R40, considered by the European regulations on vehicle emission control. In Fig. 6.21a and b, the two cycles are reported in terms of motor speed versus time.

In particular, the R47 cycle (Fig. 6.21a) is imposed by European legislation for exhaust emission measurements of mopeds powered by internal combustion engine, and here is used in absence of specific legislation regarding electrical mopeds. The R47 cycle requires the maximum power in the initial phase up to the maximum speed (6000 rpm), then a period of constant speed of 50 s at maximum speed, a fast deceleration up to 2400 rpm, a second period of constant speed, a final deceleration up to zero speed. The R40 cycle (Fig. 6.21b) comprises three phases, the first two characterized by acceleration, constant speed (1500 and 3200 rpm) and deceleration steps, while the last one presents two steps at constant speed (5000 and 3500 rpm), before returning to zero speed.

The R40 cycle is required by the European legislation to evaluate the exhaust emissions of motorcycles and, after addition of a fourth phase at higher speed, also for passenger cars. It is used in this chapter to evaluate the performance of the fuel cell power train on a typical urban route, not strictly associated with the driving way assumed for a moped. The acceleration phases of the two cycles correspond to stack power increase rates of 100 W/s for R40 and 500 W/s for R47.

6.5.1 Analysis of the FCS Dynamic Behavior on Driving Cycles

In Fig. 6.22a, b, the acquisition versus time of stack current, voltage, and temperature is reported for one R40 and four consecutive R47 driving cycles, respectively [1]. The purge, humidification, and stoichiometric ratio control strategies described in the previous sections are used also during these tests.

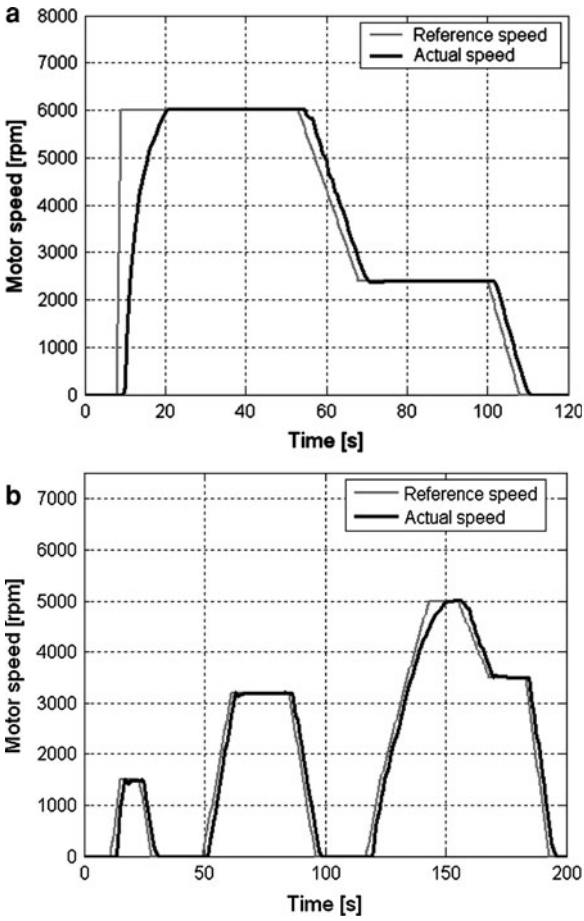

Fig. 6.21 **a** European driving cycle R47. Motor speed versus time. **b** European driving cycle R40. Motor speed versus time

The experiments are described without taking into account the start-up issues, already analyzed in Sect. 6.4.

Since the power train operates in soft hybrid configuration (with a power limit only for the R47 cycle), the stack power is imposed by the engine requirements, and only the stack temperature can be regulated. However, as all water management interventions produce their effects on times longer than typical dynamics of driving cycles (an order of magnitude of 100 s with respect to 1 s) and are correlated to slow stack temperature dynamics, an optimal temperature profile cannot be imposed on the basis of instantaneous power requirements, but the choice of operative temperature ranges is necessary. This choice is taken considering the mean stack power of the two cycles (400 W for R40, 760 W for R47), according to results of Fig. 6.20 (about 310 K for R40, 320 K for R47). As a consequence, any shifting from the reliable performance could be attributed only to working peculiarities of dynamic phases.

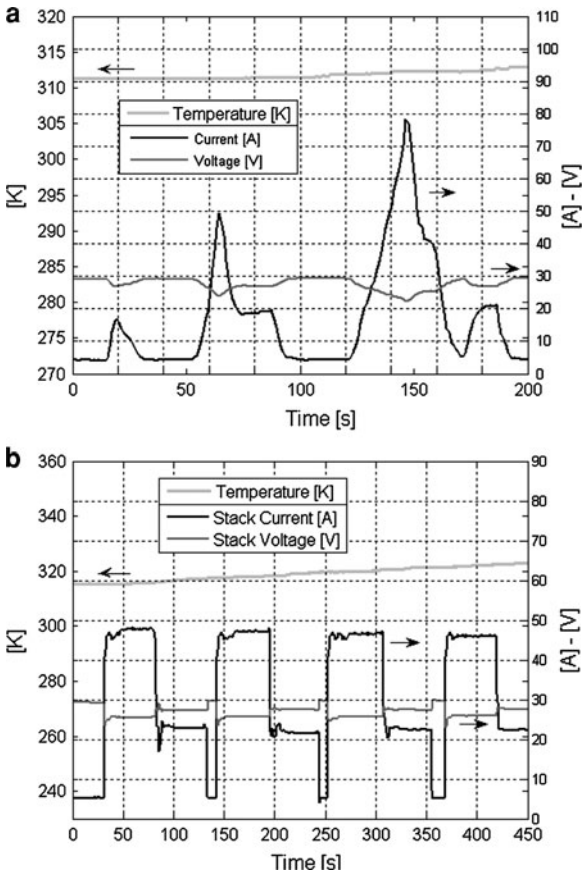

Fig. 6.22 Stack voltage, current, and temperature profiles versus time during **a** R40 cycle and **b** R47 cycle

Figure 6.22a shows that during the R40 cycle the stack current profile versus time reproduces the cycle peaks reported in Fig. 6.21b, with accelerations always $\leq$100 W/s, while voltage varies accordingly and temperature does not appreciably increase (about 0.25 K/min). Instead, during R47 cycle (Fig. 6.22b) the maximum power value reached by the FCS is limited to about 1 kW (about 48 A in Fig. 6.22b), while the temperature increases at 0.5 K/min from 315 to 323 K (a value reached after the fourth cycle), because of the higher power involved and longer test duration with respect to the experiment of Fig. 6.22a.

In Fig. 6.23a, b, the coefficient of variation is reported as function of time for R40 and R47 driving cycles, respectively. Fast and transient excursions outside the optimal region of Fig. 6.20 occur at fuel cell system minimum power of both cycles and for the highest power peak of R40 (170 s in Fig. 6.22a). However, for R40 cycle these excursions do not involve significant losses of cell voltage uniformity, as evidenced by values of coefficient of variation always below 2% (Fig. 6.23a), indicating that the short durations of shifts from the optimal region of

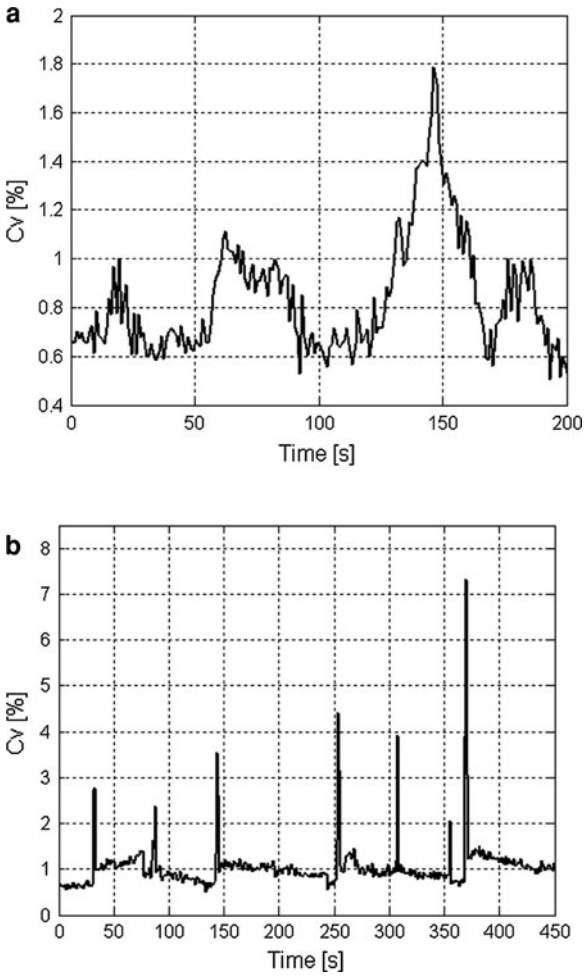

Fig. 6.23 C_v profiles versus time during **a** R40 cycle and **b** R47 cycle

Fig. 6.28 do not affect the cell uniformity neither during minimum power nor during transient phases. On the other hand, during R47 the excursions outside the optimal working region have comparable duration with respect to R40, but the higher accelerations involved in the cycle determine some peaks of C_v overcoming 4% in correspondence with the transient phases (Fig. 6.23b).

A detail of individual cell voltages for the peak at 410 s is shown in Fig. 6.24, where three instants are reported, the one just before the acceleration, the time corresponding to the maximum acceleration, and just after voltage stabilization. It is possible to observe that several cells are responsible of the C_v value higher than 4% and that all cells show a lower voltage during acceleration with respect to the stabilized values.

This behavior seems related to the different dynamic response of stack and air compressor, as evidenced in Fig. 6.25a and b, where air flow rate and stack power

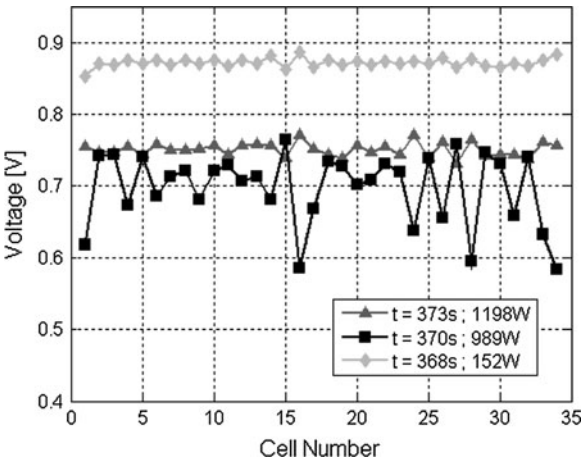

Fig. 6.24 Individual cell voltage during maximum acceleration in the experiment of Fig. 6.22b (R47 cycle)

are reported for the phases of maximum load variations in R40 and R47 cycles, respectively. While for R40 cycle air flow rate and power increase with comparable ramps during the acceleration (Fig. 6.25a), for R47 the air flow rate is not able to follow the power profile (Fig. 6.25b), because of the dynamic limits of the air compressor. R acquisitions for R47 test are reported in Fig. 6.26. This figure shows that R values <1 are reached in points of maximum acceleration, in contrast with the necessity of using an excess of air.

However, these transient excursions do not affect significantly the reliable operation of the stack, which results capable for this reason to tolerate not only fast shifting from power–temperature correlation, but also instantaneous not optimal values of R.

6.5.2 *Analysis of the Overall Propulsion System on Driving Cycles*

The behavior of the overall power train on driving cycles is analyzed considering both the soft and hard hybrid configurations (see Sect. 5.5). For each procedure, the stack power is regulated by acting on the DC–DC converter output voltage and current. In particular, a constant value of the voltage reference is adopted, always higher than any possible battery voltage, in order to continuously direct the energy flow from stack toward load and/or batteries. Regarding the DC–DC converter output current, this is controlled as function of the hybrid configuration adopted.

The main results of the experimental tests regarding the *hard hybrid* configuration on the R47 cycle are reported in Fig. 6.27a–c. The Fig. 6.27a shows the distribution of the power between FCS, electric drive, battery pack versus the cycle length. The output power of the fuel cell system is fixed at two constant values by

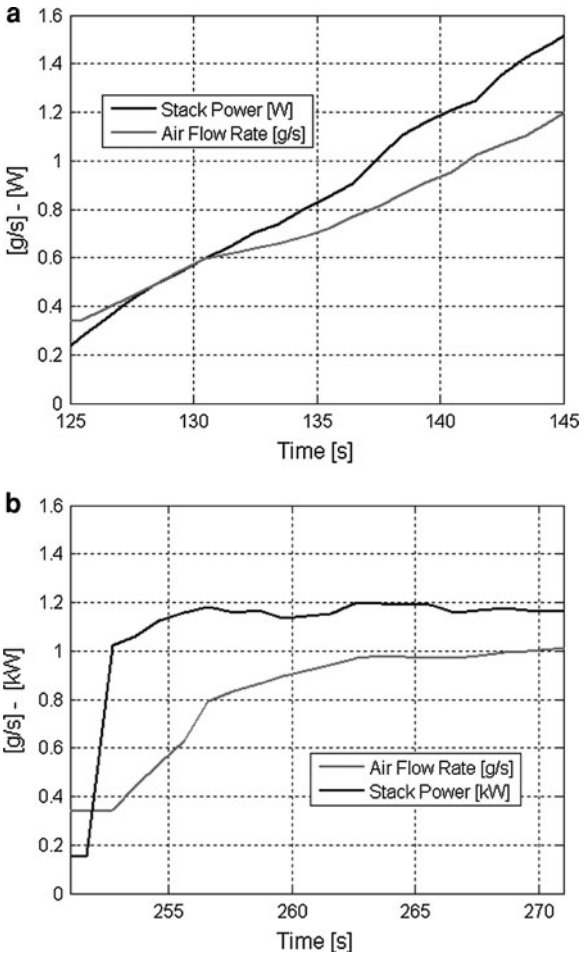

Fig. 6.25 Stack power and air flow rate profiles versus time during **a** R40 cycle and **b** R47 cycle

limiting the DC–DC converter output current. The two values of power are chosen equal to 900 and 450 W, corresponding to the two phases of the cycle at constant engine speed. The motor power (Fig. 6.27a) reaches its highest value (3500 W) during the first acceleration phase, then decreases up to 1200 W corresponding to the first step at constant motor speed, finally decreases up to negative power values during the deceleration phase, when the electric machine operates as generator. At the end of this deceleration, the motor power reaches the second phase at constant speed (220 W), followed by the last deceleration phase up to zero speed.

The battery power curve shows that the storage system plays the role of compensating the difference between the motor power requirements and power supplied by the fuel cell system (Fig. 6.27a). In particular, the electric energy flowing from the battery pack permits the motor power peak to be satisfied, whereas during the regenerative braking, when the electric machine is operating as

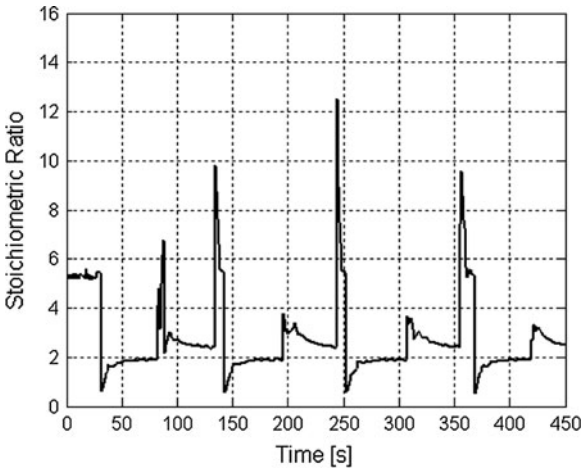

Fig. 6.26 Acquisition of stoichiometric ratio versus time during the experiment of Fig. 6.22b (R47 cycle)

generator, the battery power drops to negative values indicating a partial recovery of energy. During the driving cycle, the battery pack changes its state of charge (Fig. 6.27c). The fastest discharge is observed during the first acceleration, whereas the fastest recharging happens during the first deceleration phase, when the batteries are recharged by both the electric machine working as generator and stack.

During the first step at constant speed, a slower SOC decrease is observed, whereas the last two phases of the cycle (second constant speed step and last deceleration) define the further battery recharging. The power associated with the amount of hydrogen entering the stack and power measured at inlet and output of the DC–DC converter during the cycle are specifically reported in Fig. 6.27b. The last two curves evidence the energy loss caused by the DC–DC converter, whereas the comparison with the hydrogen power plot visualizes the energy loss associated with the fuel cell system.

The main results obtained by the tests performed in *soft hybrid* configuration with the R40 cycle are shown in Fig. 6.28a–c. During these tests, the contribution of the batteries to the energy requirement, which comes from the electric drive, is minimized by controlling the DC–DC output power. In Fig. 6.28a, electric drive, battery, and DC–DC converter powers versus cycle length are reported. The DC–DC converter dynamic behavior is shown in Fig. 6.28b, where the DC–DC converter input and output powers are monitored during the cycle together with the hydrogen power, in this way indication of the energy losses before the electric drive is given.

The Fig. 6.28c reports the behavior of batteries during this test by the profile of battery state of charge versus the cycle length. The dynamic behavior of the fuel cell system permits the energy requirements from the electric drive to be instantaneously satisfied by the stack, with only a small contribution of the batteries. Therefore, in this test the batteries play the main role of recovering electric energy during the regenerative braking phases, as evidenced by negative values reached

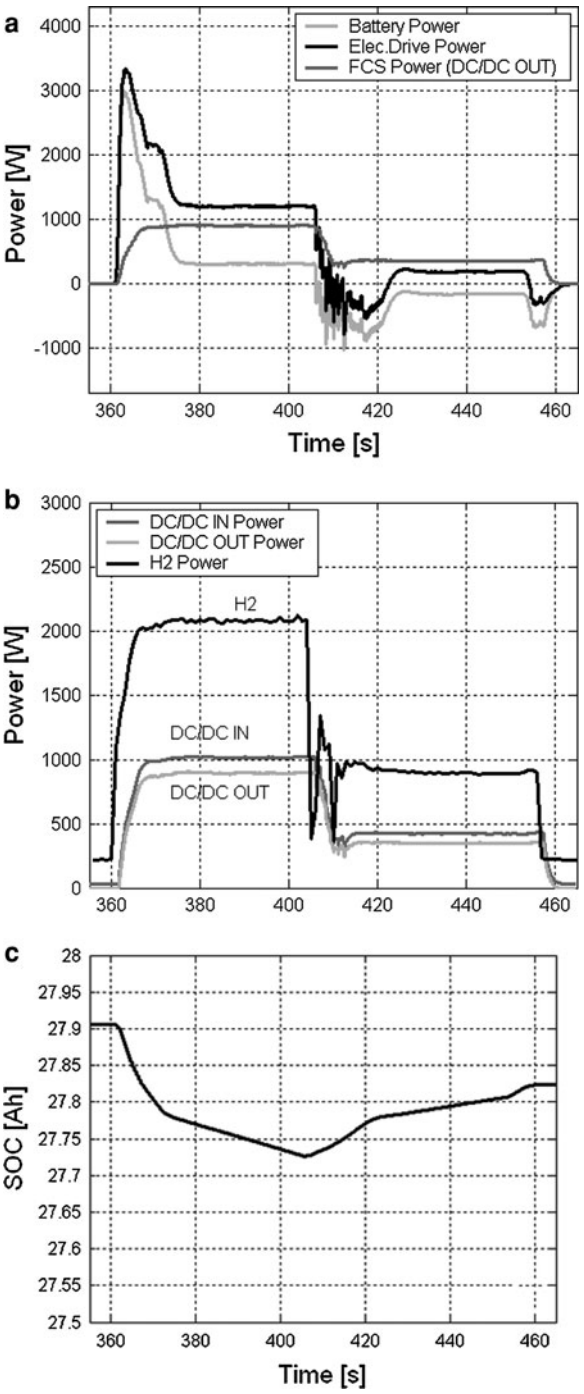

Fig. 6.27 Experimental results obtained on the fuel cell power train in hard hybrid configuration for the R47 driving cycle: **a** battery, input electric drive, and output DC–DC converter powers versus cycle length, **b** hydrogen, input and output DC–DC converter powers versus cycle length, **c** battery state of charge versus cycle length

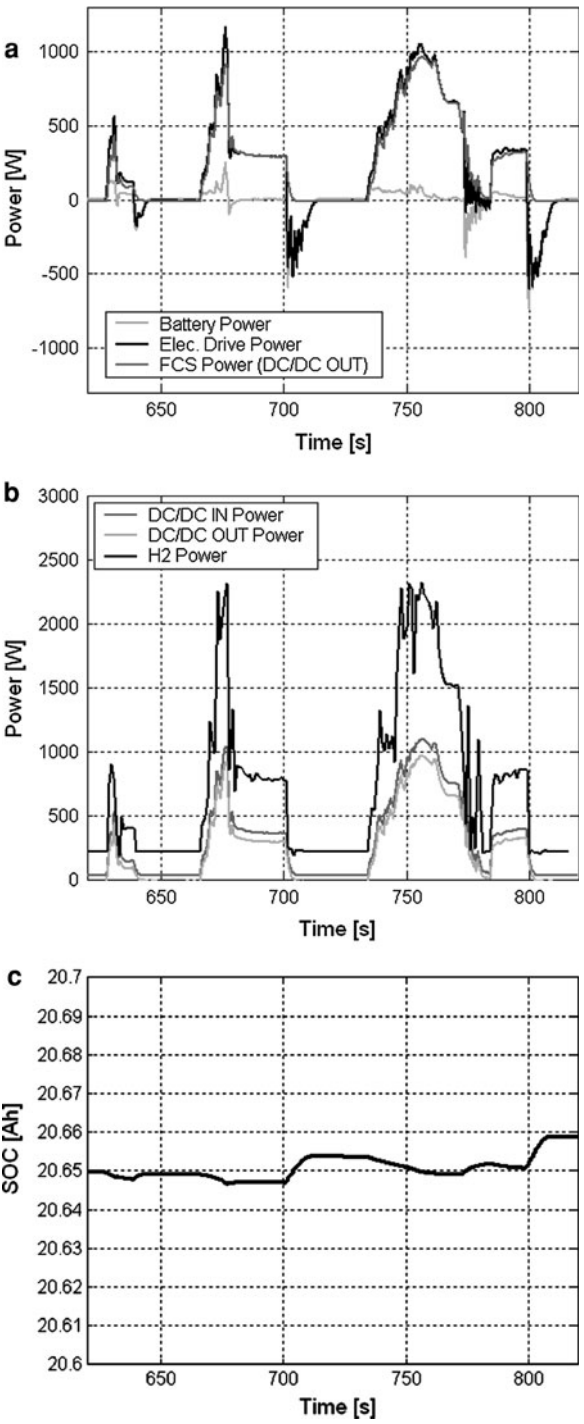

Fig. 6.28 Experimental results obtained on the fuel cell power train in load following configuration on the R40 driving cycle: **a** battery, input electric drive, and output DC–DC converter powers versus cycle length, **b** hydrogen, input and output DC–DC converter powers versus cycle length, **c** battery state of charge versus cycle length

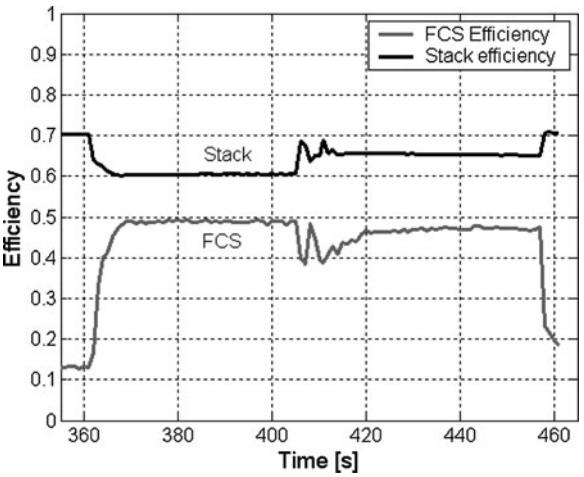

Fig. 6.29 Stack and fuel cell system efficiency versus cycle length in hard hybrid configuration on the R47 driving cycle

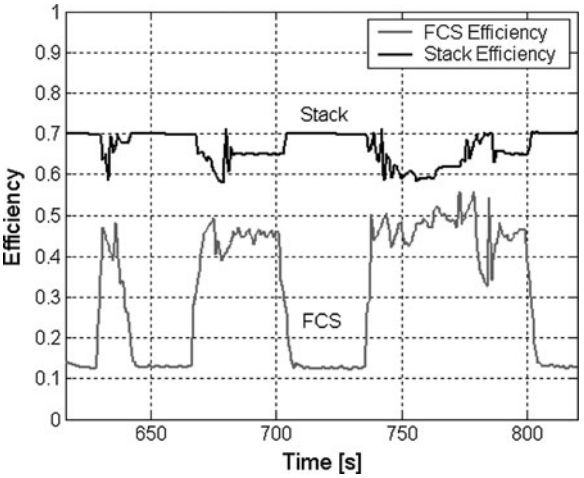

Fig. 6.30 Stack and fuel cell system efficiency versus cycle length in soft hybrid configuration on the R40 driving cycle

by the battery and electric drive power curves. It can be observed from Fig. 6.28c that two recharging steps are obtained when the electric drive operates as generator during the second and fourth deceleration phase of the cycle.

The electric energy recovered during the regenerative braking phases can be evaluated for both cycles, as percentage of the energy entering the electrical drive, it results about 8 and 16% for R47 (Fig. 6.27) and R40 (Fig 6.28), respectively.

The instantaneous efficiency of the stack and FCS are shown in Fig. 6.29 for R47 cycle in hard hybrid configuration and in Fig. 6.30 for R40 cycle in soft hybrid configuration. According to the results obtained in steady-state operation, during the low load phases the stack efficiency reaches the value of about 0.7, whereas during the power variations required by the electric drive the efficiency decreases down to the lowest value of about 0.6, in correspondence with the most

Table 6.6 Efficiency of the power train and its subsystems during R40 cycle [2]

	Fuel cell system	DC–DC converter	Electric engine	Power train
Soft hybrid	0.48	0.80	0.75	0.29
Hard hybrid	0.51	0.87	0.75	0.33

demanding phase of the driving cycles, and to about 0.65 at medium load conditions. With regard to the FCS efficiency in soft hybrid approach, it varies between 0.13 and 0.48 (Fig. 6.30) and follows the load curve of the cycle reproducing the same efficiency values obtained for each power in the corresponding steady-state operation (see Sect. 6.3). In the soft hybrid, the stack operates for several minutes at the minimum load, for this reason the system energy losses determine a strong decrease of the instantaneous system efficiency. This fact negatively affects the average efficiency calculated on the entire cycle (see Table 6.6). In the hard hybrid configuration, the instantaneous efficiency of the system is almost equal to the highest steady-state value for most of the time lasting the cycle (Fig. 6.29), providing this way a better average efficiency.

The comparison between *soft* and *hybrid* approach can be further accomplished by analyzing the energy flow values involved within the power train during the same cycle (R40 cycle). In Fig. 6.31a, the electric energy profiles instantaneously exchanged by electric drive, battery pack, and FCS with the electric bus are reported versus cycle length for a hard hybrid configuration, on the assumption that the energy at the beginning of the driving cycle is zero. In this test, the value of power fixed at the DC–DC converter output is selected corresponding to the average power of R40 cycle (about 300 W).

Up to 150 s, the energy flow provided by FCS is always higher than the electric drive requirements, implying that the battery SOC remains always higher than its initial value, while after 150 s the storage system compensates the difference between electric drive requirements and the energy provided by the FCS. In Fig. 6.31a, the negative derivative for battery energy indicates that energy is entering into the storage system, coming mainly from FCS and also from electric drive during braking phases of the cycle, when the motor operates as generator.

In Fig. 6.31b, the histogram corresponding to the monitoring of individual cell voltages during the test is reported, evidencing the very uniform cell working expectable for a stack managed in steady-state conditions (most cells showed voltages comprised between 0.77 and 0.79 V).

In Fig. 6.32, the results of the experiment on the scooter power train in soft hybrid configuration are reported. The power at the DC–DC converter output is controlled in order to supply the electric drive with all the power instantaneously required during the R40 cycle. In Fig. 6.32a, the electric energy profiles instantaneously exchanged by electric drive, battery pack, and FCS with the electric bus are reported versus cycle length. The FCS profile follows almost completely the electric drive energy requirements, and the limited contribution of batteries is evident during all the cycle length. The dynamic performance of the stack is

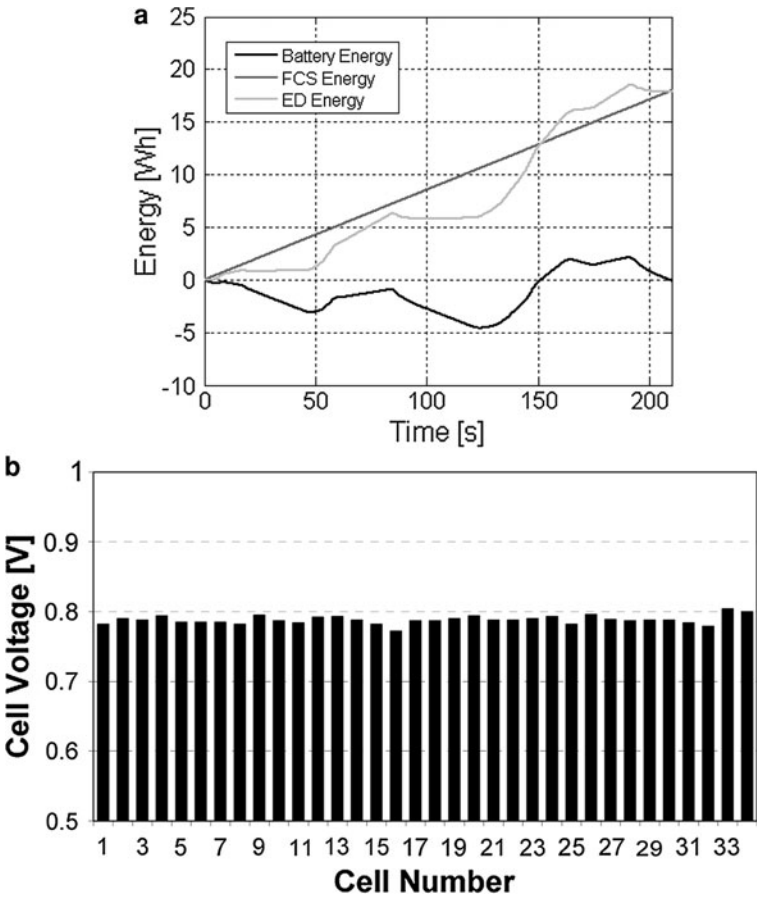

Fig. 6.31 Hard hybrid procedure during R40 cycle on fuel cell scooter. **a** electric energy profiles instantaneously exchanged by electric drive, battery pack, and FCS with the electric bus versus cycle length. **b** histogram of individual cell voltage during the steady-state FCS working

analyzed by monitoring of individual cell voltages during all the R40 cycle length. In Fig. 6.32b, three acquisitions corresponding to three instants of the third acceleration phase of the R40 cycle are shown. Only at the end of the acceleration phase (about 2 kW) an appreciable but not dangerous cell working irregularity is observed, while a very good dynamic performance is provided by the stack during all the other phases of the cycle. This management strategy appears to be particularly suitable for a scooter application, where weight and size issues of on board electric energy storage systems are more stringent, suggesting to satisfy driving range demands mainly by the fuel.

The values of efficiency obtained for the main components of the power drive by experimental measurements are reported in Table 6.6 for R40 cycle in soft and hard hybrid configurations. The evaluation of power train total efficiency takes

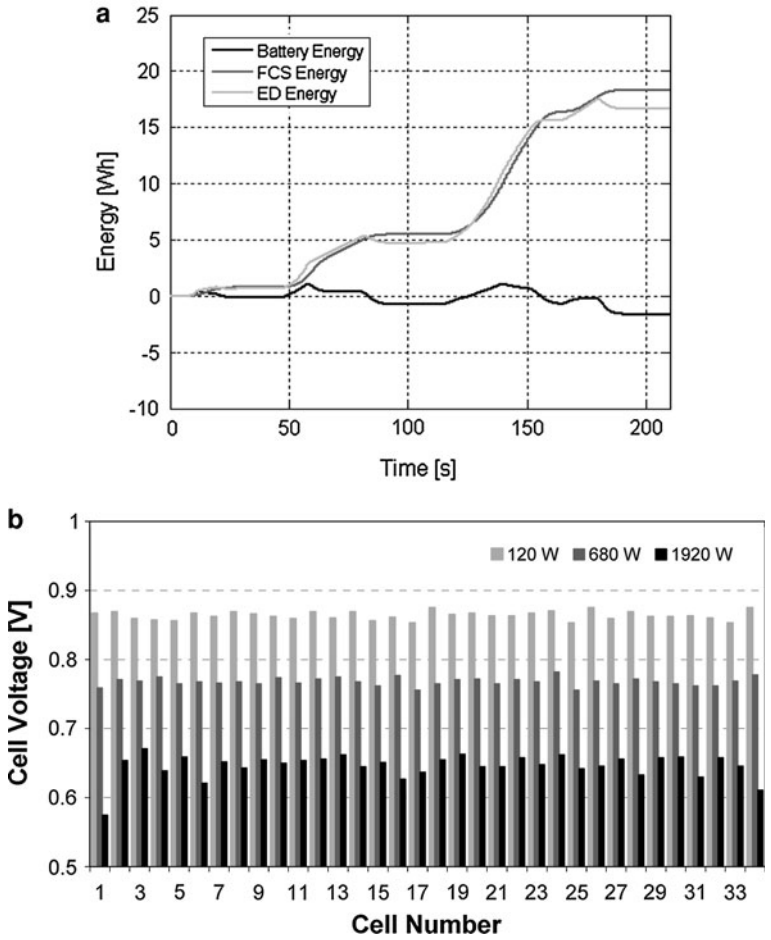

Fig. 6.32 Soft hybrid procedure during R40 cycle on fuel cell scooter. **a** electric energy profiles instantaneously exchanged by electric drive, battery pack, and FCS with the electric bus versus cycle length. **b** histogram of individual cell voltage at three instants during the third acceleration phase of the R40 cycle

into account the amount of energy needed to level the initial and final SOC for both the tests.

The fuel cell system efficiency results slightly higher for the hard hybrid procedure ($\eta_{FCS} = 0.51$) than soft hybrid ($\eta_{FCS} = 0.48$). According to the above discussion, during the hard hybrid test the stack is controlled to operate in a fixed working point, corresponding to the highest FCS efficiency, whereas during the soft hybrid experiment the stack is left free to follow the load variations, then the fuel cell system for some periods of the cycle works in a condition of low efficiency. The DC–DC converter efficiency in hard hybrid results slightly higher ($\eta_{DC} = 0.87$) than the value obtained for soft hybrid ($\eta_{DC} = 0.80$), because of

dissipations involved during the transient and low load phases of the load following configuration. The data of Table 6.6 show that the power train efficiency can be mainly affected by the operation of the fuel cell system, through the values of η_{FCS} and η_{DC}.

It is necessary to specify that the above efficiency values are evaluated assuming a value of battery efficiency equals to 100%, and this is justified by the fact that the use of the batteries to satisfy the power demands is quite limited in both the cycles, in particular it is practically negligible for the soft hybrid approach.

A comparison with the commercial scooters powered by 50 cm^3 spark ignition engines, made in terms of energy consumption per unit of traveled distance on the same standard driving cycle, evidences that a very strong reduction of consumed kJ km^{-1} is possible for the fuel cell power train, in particular its overall efficiency results about 2.5 times better than conventional propulsion systems.

References

1. Corbo P, Corcione FE, Migliardini F, Veneri O (2005) Experimental study of a fuel cell power train for road transport application. J Power Sources 145:610–619
2. Corbo P, Corcione FE, Migliardini F, Veneri O (2006) Experimental assessment of energy-management strategies in fuel-cell propulsion systems. J Power Sources 157:799–808
3. Corbo P, Migliardini F, Veneri O (2007) Performance investigation of 2.4 kW PEM fuel cell stack in vehicles. Int J Hydrogen Energ 32:4340–4349

Chapter 7
Case Study B: Fuel Cell Power Train for Cars

7.1 Description of the 30 kW Fuel Cell Power Train

Figure 7.1a–c shows the three main sections of a laboratory plant specifically designed for characterization of a 20 kW PEM stack, which was chosen to supply the electric drive for road vehicles analyzed in this chapter.

These sections include: hydrogen feeding, air feeding with humidification, and stack cooling systems. The stack specifications and detailed technical characteristics of the auxiliary components, with all the mechanical and electric devices necessary for stack operation, are reported in Table 7.1.

The fuel feeding system is reported in Fig. 7.1a. High purity hydrogen or nitrogen, necessary for the cell and hydrogen pipeline purge, are fed by high pressure cylinders (200 bar), while a pressure reduction stage (7 bar maximum) is installed at the hydrogen inlet.

For all the experimental tests the PEM stack operates in dead end configuration, i.e., the anodic compartment is maintained closed and pressurized. A purge electric valve is placed at the hydrogen line outlet to drain the excess of water diffusing zfrom the cathode to the anode side through the polymeric membrane (see Sect. 4.2). Hydrogen flow rate is calculated by the current drawn, taking into account the amount of hydrogen purged. Defining a fuel utilization coefficient (η_{util}) as ratio between the mass of fuel reacted in the stack and the mass of fuel entering the stack, it was preliminary fixed at 0.90 according to indications of the stack manufacturer. This value can be experimentally set by pre-defining the opening time and frequency of the anode purge valve, and measuring the purged volume.

The air management system is shown in Fig. 7.1b. A side channel compressor is used for low pressure experiments (below 130 kPa), while a centralized air compression plant is used to study the effect of air pressure on stack performance (between 130 and 250 kPa). An important issue to be considered is the cell humidification to guarantee that the stack works properly, since the electrolyte membrane needs to be continuously hydrated (see Sects. 3.2 and 4.5). That humidification is

P. Corbo et al., *Hydrogen Fuel Cells for Road Vehicles*,
Green Energy and Technology, DOI: 10.1007/978-0-85729-136-3_7,

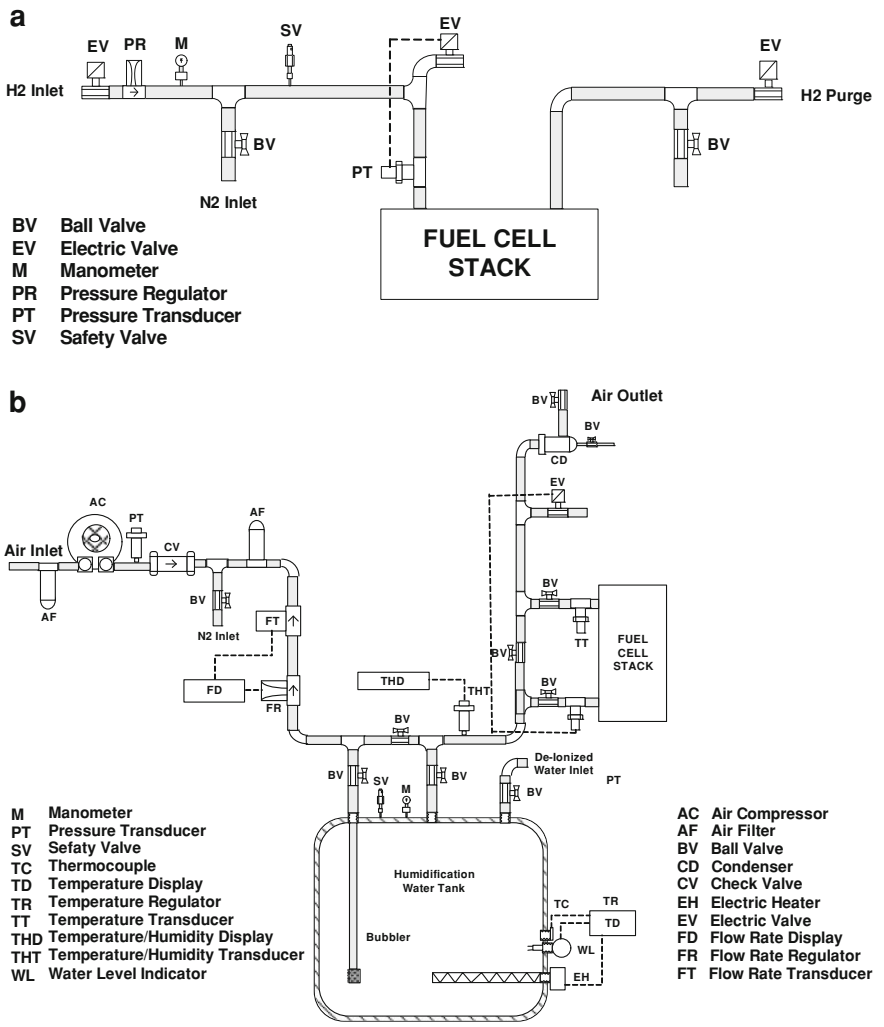

Fig. 7.1 The three sections of the fuel cell system experimental apparatus: **a** hydrogen feeding, **b** air feeding and humidification, and **c** stack cooling

realized by flowing air through a bubbler filled with de-ionized water, which is heated at different temperatures by an electric resistance before feeding the cathode side. Air relative humidity is controlled by humidity and temperature sensors at the cathode inlet. Stack temperature is measured by a thermocouple placed at the outlet of the cathode side. During experiments at low pressure, the air flow rate is measured by a variable area flow meter and regulated by acting on the compressor motor controller in order to assure the necessary stoichiometric ratio. Two pressure transducers are placed upstream of the stack to monitor the anode and cathode pressure during the experimental runs (Fig. 7.1a, b). During all the experimental tests, the inlet

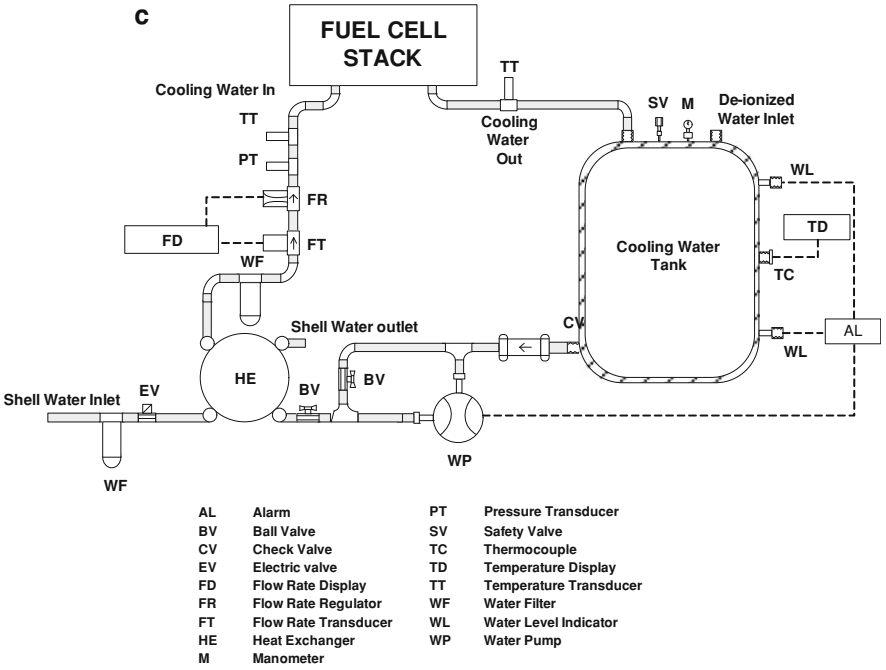

Fig. 7.1 (continued)

hydrogen pressure is set higher than 30 kPa with respect to inlet air pressure. A water condenser is located at the stack outlets before venting to verify the water balance in the system. A cooling system, shown in Fig. 7.1c, is adopted to control the temperature in the range 290–346 K and is composed by a de-ionized water circuit equipped with a pump and sensors to measure pressure, temperatures, and flow rate. In order to guarantee a sufficient uniform temperature through the cells, a difference of temperature not higher than 5 K is accepted between inlet and outlet cooling water temperatures. This is achieved by imposing the cooling water flow rate at the value required by the maximum stack power (4 $m^3\ h^{-1}$) and using a spiral heat exchanger fed with external water to control the cooling water temperature.

Two tanks of 50 l are used as water containers, respectively, for the humidification and cooling circuits. On–off, three way and tuning valves permit pressures and gas flow rates to be regulated.

The stack characterization is carried out by connecting it to a variable resistive load able to control the discharge current electronically, making possible the evaluation of different operative conditions with different values of constant current (Table 7.1).

A dedicated acquisition system able to monitor and register the voltages of the individual cells during the different runs is adopted. Moreover a *d*-space board is used for the acquisition and control of all signals associated with the FCS system components (valves, sensors, and transducers).

Table 7.1 Technical specifications of the PEM fuel cell system

PEM fuel cell stack	
Number of cells	80 cells
Maximum power	20 kW
Stack voltage range	50–80 V
Stack maximum current	360 A
Auxiliary components	
Air supply compressor	Side channel compressor, max flow rate 95 Nm^3/h, max pressure 320 mbar, 1.1 kW
Water pump	Centrifugal pump C090, flanged to 24 VDC motor, max pressure 40 kPa, max flow rate 100 l/min
Heat exchanger	Spiral heat exchanger, eight tubes (size 9.53 mm), shell diameter 273.05 × 263.6 mm
Acquisition and control system	
d-Space board	Sampling time of 0.01 s
Sensors	
Air mass flow meter	Variable area flow meter, 0–60 Nm^3/h, accuracy 1.6% of full scale
Water flow meter	Variable area flow meter, 0–5 Nm^3/h, accuracy 1.6% of full scale
Temperature sensors	Resistance thermometer, 0–100 °C, accuracy 0.5% of full scale
Pressure transducers	Pressure range 0–500 kPa, accuracy 0.5% of full scale
Humidity transducer	Testo Hygrotest 600/650 humidity temperature; accuracy of up to ±1% RH
Current transducer	Closed loop, Hall effect, accuracy 0.65% @ 300 A
Voltage transducer	Closed loop, Hall effect, accuracy 0.7% @ 100 V
Electric load	
Type	IGBT electronic converter connected to electrical resistances
Rated power	20 kW
Input current	0–300 ADC
Input voltage	0–100 VDC
Remote control of stack current	0–10 VDC
Electrical resistances	4 kW modules

A DC–DC converter of 20 kW based on IGBT technology is interconnected between the fuel cell system (FCS) and the electric load in order to adapt the variable stack voltage to the electric load voltage. For the fuel cell dynamic characterization, the DC–DC converter outlet is first connected to a resistive load, then to the power train. The resistive load can dissipate electric energy up to a maximum of 20 kW controlling electronically the discharge current. The DC–DC converter is equipped with current and voltage sensors to evaluate instantaneously the electric power flow between the FCS and the electric load or the power train. It is controlled by the *d*-space board, which is programmed to follow the desired stack current reference during the tests.

The test bench for the power train characterization is realized by using a 120 kW dynamic electric brake composed by a three-phase asynchronous machine

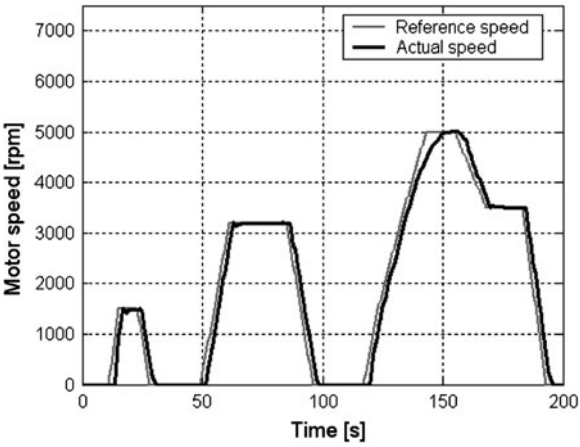

Fig. 7.2 Profile of motor speed versus time for the European R40 driving cycle (same cycle of Fig. 6.21b)

and converters providing a bidirectional flow of the energy with respect to the electric network. The power train test bench can be easily reconfigured by software using different sets of data for testing different types of vehicles, driving cycles, rolling resistances, and aerodynamic drags.

The 30 kW electric drive for road applications is composed by an asynchronous machine and IGBT inverter, both of them using the same water cooling system. The 6,000 rpm maximum motor speed is reduced by means a gear box which only provided the forward and reverse gear. A lead-acid battery pack composed by 24 batteries connected in series is used as storage system, with each battery having a nominal voltage of 12 V and an electric capacity of 50 Ah. The battery pack is also equipped with an electric switch for its connection or disconnection to the power train.

The electric drive, DC–DC converter and Pb battery pack are equipped with sensors able to monitor all the main parameters of the electric power train during the tests. All the analogic and digital signals are connected to a *d*-space prototyping system, programmed by means of MathWorks MATLAB development tools.

The experiments on the overall power train (see Sect. 7.5) refer to the European R40 driving cycle, shown in Fig. 7.2 and already described in Sect. 6.5 (Fig. 6.21b). It is composed by three phases, the first two being characterized by a sequence of acceleration, constant speed and deceleration steps, while the last one presents two steps at constant speed, before returning to zero speed. This driving cycle is used in this chapter to evaluate the performance of the fuel cell power train on a road mission typical of urban areas.

7.2 FCS Characterization: Effect of Operative Parameters

The experimental characterization of the FCS described in the previous paragraph is first performed using the operative conditions recommended by the manufacturer for maximum stack performance.

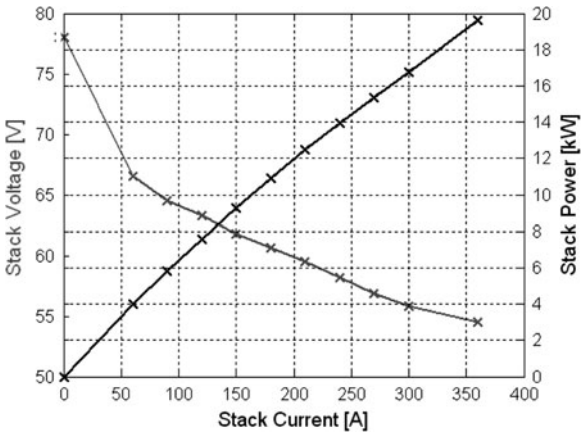

Fig. 7.3 Characteristic curves of the 20 kW PEM stack. Stack voltage and power versus current at $T = 346$ K and $P_{air} = 250$ kPa

The tests are run at the temperature of 346 K and reactant pressures of 250 kPa. The air flow rate is set for each load value in order to assure the correct stack operation and minimize air compressor power consumption and water flow rate necessary for the humidification. This regulation of oxidant flow rate determines a value of R ranging from 6 at low load to 2 at full load. An excess of air with respect to the stoichiometric requirement is always necessary due to the mass transport limitations on the cathode side (see Sect. 4.3). The stack humidification is performed by saturating the inlet air stream at the temperature value approximately equal to the measured one at the cathode outlet.

In Fig. 7.3, the characteristic of the 20 kW PEM stack is reported in terms of voltage and electric power as a function of stack current. The voltage versus current diagram represents the polarization curve, which describes the stack behavior for different loads (see Sect. 3.3). The stack output voltage decreases from 78 V at open circuit to about 55 V at the highest load tested (360 A), while the power increases with current and the highest power value (20 kW) is reached at the current value of 360 A. It can be noted that in a wide range of load conditions (60–300 A), the voltage is essentially linearly dependent on current, indicating that the voltage drop in this range is mainly due to resistive losses. For higher currents, a phenomenon of mass transfer limits the stack performance, while the voltage drop observed at low loads is due to the slow activation of the electro-catalysts (see Sect. 3.3).

In Figs. 7.4 and 7.5, the voltages of the individual cells are reported for the open circuit and full load, respectively. It can be noted that a rather uniform distribution of voltage is obtained also in severe operative conditions when the stack works at maximum power, with no endangering of the optimal stack operation.

The different terms involved in the generation of power are reported in Fig. 7.6 as a function of stack current. In this figure, P_{stack} is the electric power produced by the stack, P_{comp} is the power absorbed by the air supply device, P_{pump} is the power consumption of the cooling water pump, P_{hum} is the power necessary to

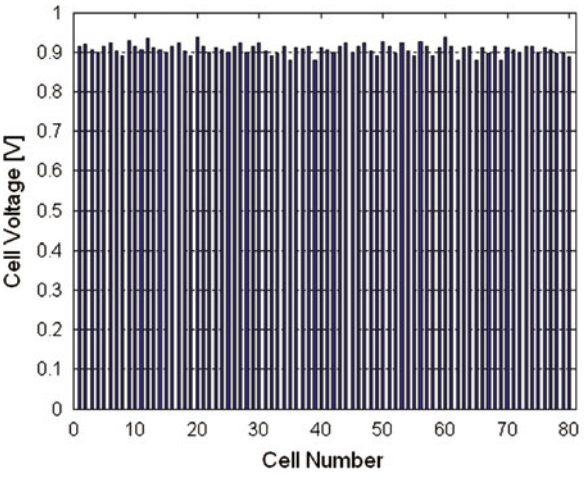

Fig. 7.4 Individual cell voltage for the 20 kW PEM stack at open circuit, $T = 346$ K and $P_{air} = 250$ kPa

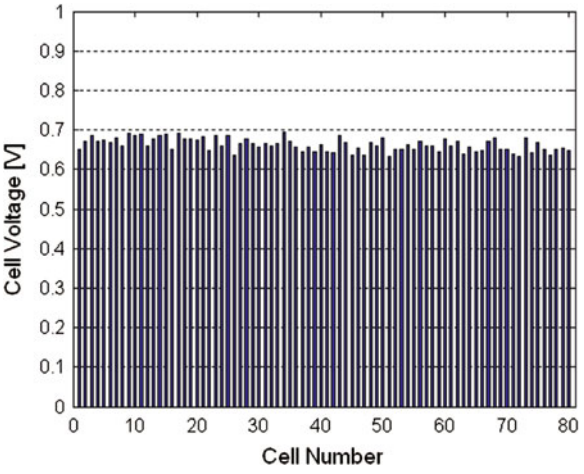

Fig. 7.5 Individual cell voltage for the 20 kW PEM stack at full load, $T = 346$ K and $P_{air} = 250$ kPa

humidify the inlet air at 70°C, P_{cool} refers to the heat absorbed by water cooling, P_{airout} is associated with the enthalpy of the cathode outlet stream, and P_{H_2} is the power related to the fuel fed to the stack, calculated by hydrogen high heating value, taking into account the fuel utilization coefficient (see Sect. 7.2). All the above power terms are calculated from experimental measurements, except for the air supply consumption, since a centralized compression plant is used for all tests conducted at higher pressure. For this reason, the compression consumption is estimated from the literature [1, 2]. It can be noticed that the power entering the stack as fuel (P_{H_2}) is recovered as stack electric power (P_{stack}), cooling heat (P_{cool}) and as part of the heat flowing from cathode side (P_{airout}). Whereas, the main energy losses are due to the humidification and compression devices (8.5 kW at

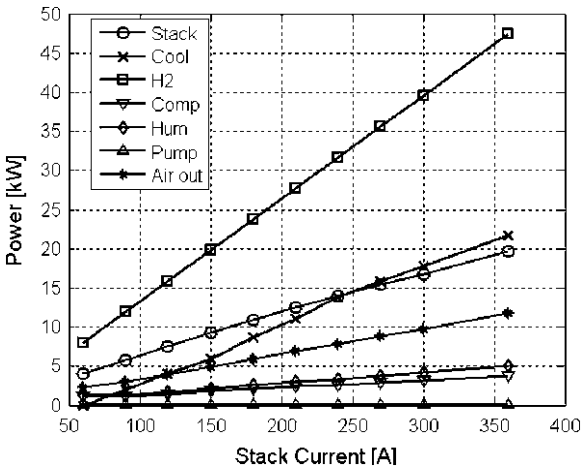

Fig. 7.6 Powers provided or absorbed by the different components of the FCS versus stack current at $T = 346$ K and $P_{air} = 250$ kPa

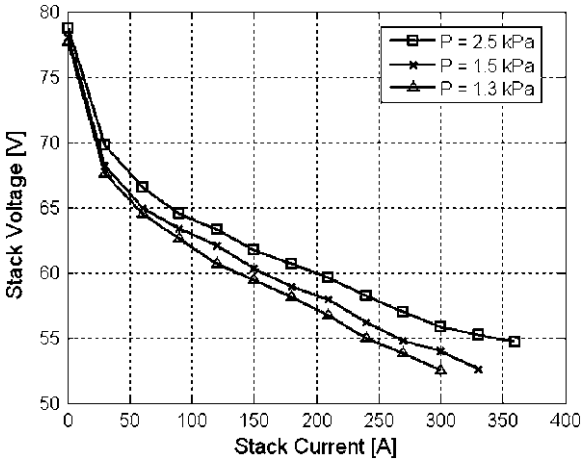

Fig. 7.7 Effect of air pressure on characteristic curves of the 20 kW PEM stack at 346 K

360 A, which corresponds to maximum load), and the constant and negligible consumption of 110 W is due to the cooling water pump.

The effect of the main operative parameters on both stack performance and electric consumptions of the auxiliary devices is shown in Figs. 7.7, 7.8, 7.9, and 7.10, whose results can be utilized to select the working conditions suitable for automotive application. The effect of the reactant pressure on the fuel cell performance is shown in Fig. 7.7, where the stack voltage is reported versus current for three values of the air pressure obtained with the centralized compression plant at the temperature of 346 K, minimizing the air flow rate for each load and setting the humidification temperature equal to stack temperature for each current value. Decreasing the pressure from 250 to 130 kPa, the stack performance is not significantly reduced. In fact, the maximum effect is observed at 300 A when the stack voltage decreases from 56 V at 250 kPa to 52 V at 130 kPa (see Sect. 3.3).

The experimental evaluation of other effects associated with the operative temperatures and stoichiometric ratio is performed in a range of pressure around 130 kPa, using the side channel air compressor whose characteristics are described in Table 7.1. The effect of the stack temperature on the voltage measured at the stack terminals is shown in Fig. 7.8. In this case, the temperature is controlled by varying the water flow rate in the heat exchanger shell while the air flow rate and humidification conditions are the same as those of Fig. 7.7. It can be observed that a decrease in temperature from 346 to 305 K determines a voltage reduction <10% up to 70% of load (200 A), while a satisfactory stack behavior at 313 K is detected in almost all load conditions (see Sect. 3.3). Then, the effect of the stoichiometric ratio is verified for three different loads at the stack and humidification temperature of 313 K. From Fig. 7.9, it can be noted that values of R higher than 2 are

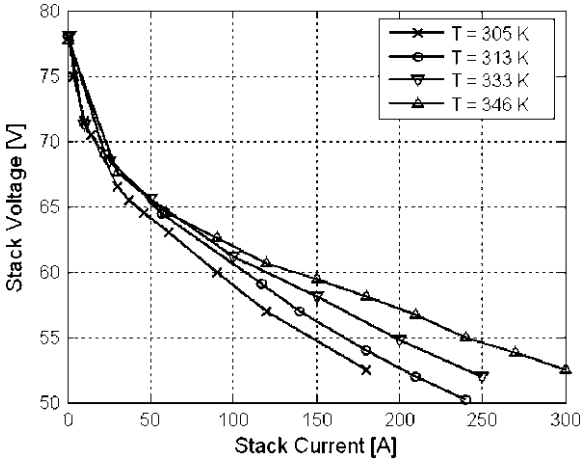

Fig. 7.8 Effect of stack temperature on characteristic curves of the 20 kW PEM stack at 130 kPa

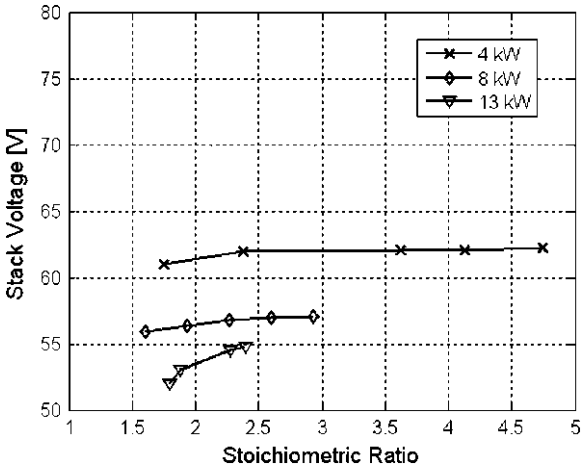

Fig. 7.9 Effect of the stoichiometric ratio on stack voltage of the 20 kW PEM stack for three different load conditions at 313 K and 130 kPa

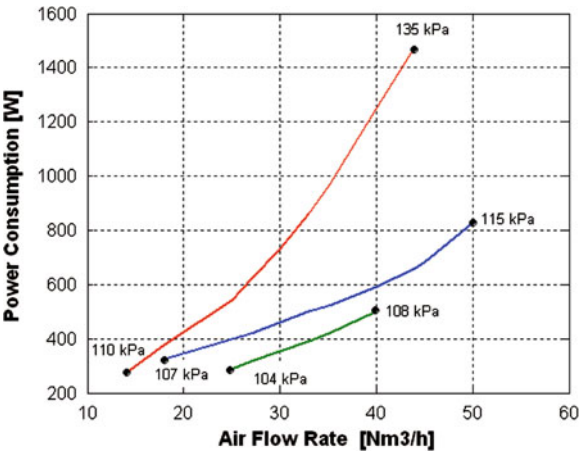

Fig. 7.10 Air compressor power consumption versus air flow rate for different pressure drop conditions

always convenient, in particular when increasing the load. Moreover, no significant effect is observed for $R > 2.5$ for all loads.

In Fig. 7.10, the behavior of the side channel air compressor is reported in terms of power consumption as a function of air flow rate for three different settings of pressure drop at the outlet of the device. The air flow rate can be varied by regulating the compressor motor speed and controlling the motor reference voltage. It can be noted that a value of 135 kPa of pressure drop permits the air flow rate necessary for the stack maximum load (about 45 $Nm^3\ h^{-1}$) to be reached with a power consumption of about 1.4 kW. This consumption decreases at partial load, which is a condition which frequently occurs for a FCS operating on a vehicle. Another consumption reduction can be achieved by choosing the minimum humidification temperature to maintain a correct stack membrane functionality. A specific experiment is performed humidifying the stack at room temperature (287 K) and allowing the stack temperature to reach 313 K with reactant pressures derived from the compressor characteristics shown in Fig. 7.10. The acquisition of stack voltage and current versus time is reported in Fig. 7.11a, while the stack and humidification temperatures are presented in Fig. 7.11b. After 3,500 s, the stack temperature reaches 313 K with a voltage of 62 V at 60 A, only 5% less than the value measured when humidifying at the same stack temperature (Fig. 7.8). In this case, the correct membrane operation is verified by monitoring the individual cell voltage at the end of the test as shown in Fig. 7.12. A similar regular behavior is observed also at higher loads, in particular for a stack power up to 12 kW.

The whole characterization of the FCS in the experimental conditions of Fig. 7.11 allows the stack and FCS electric efficiency to be calculated (see Sect. 6.4) and reported in Fig. 7.13 as a function of the stack power. The FCS efficiency is about 47% in a wide range of load conditions, with a slight decrease after 8 kW of stack power.

For a vehicle application, the humidification system at room temperature should be designed taking into account criteria of constructive simplicity and reliability.

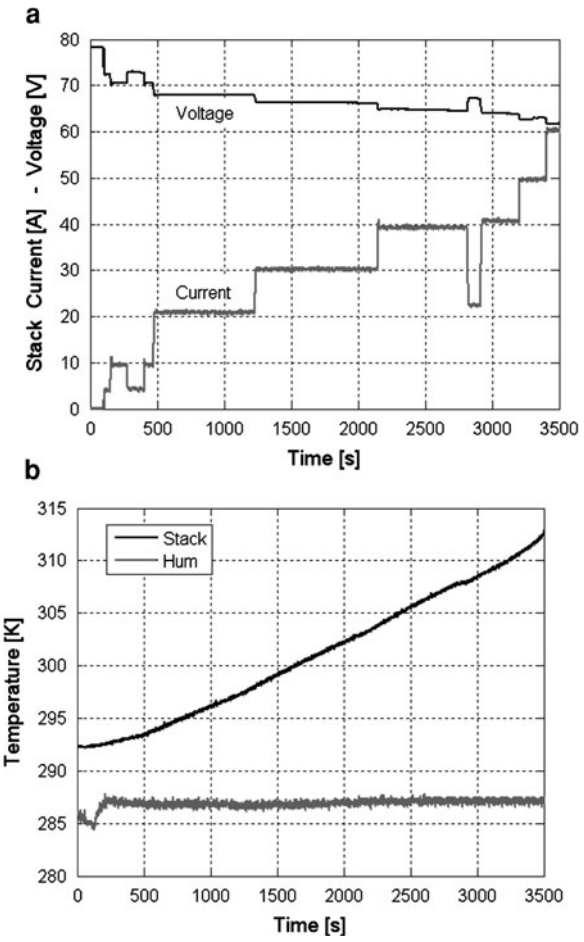

Fig. 7.11 Start-up performance of the 20 kW PEM stack humidified at room temperature (287 K) up to 4 kW. Acquisition during time of: **a** stack current and voltage and **b** stack and humidification temperatures

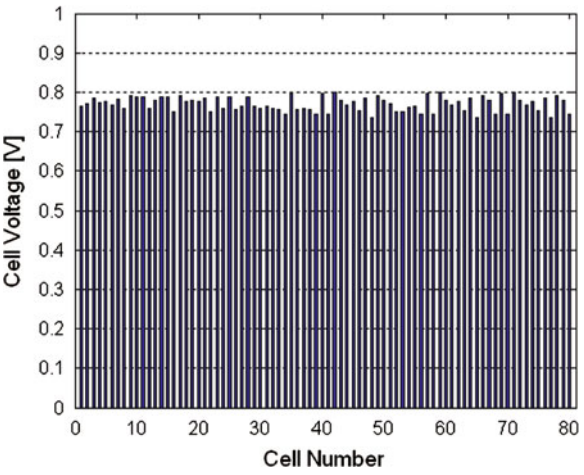

Fig. 7.12 Individual cell voltage for the 20 kW PEM stack at the end of test of Fig. 7.11

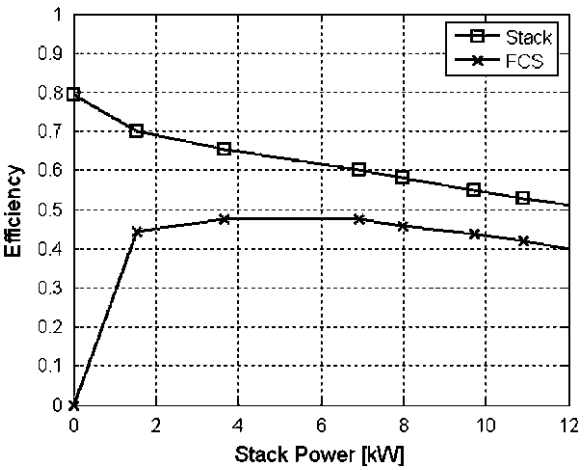

Fig. 7.13 Stack and FCS electric efficiencies versus stack current at $T = 313$ K

Then, the system based on the bubbler does not appear as the most convenient solution. A system based on electronic injection of water into the cathode inlet manifold, whose action depends on the uniformity of the individual cell voltages, could be the most effective technique for automotive applications. This solution would involve the use of an injection pump, which, however, would not affect significantly the FCS electric efficiency shown in Fig. 7.12. Another not predominant contribution to the energy losses due to the FCS auxiliary components can be identified in the electric consumption of the fan/radiator, which is useful to control the cooling water temperature on board of a vehicle [3].

7.3 Analysis of the Dynamic Behavior of the FCS

The interaction between stack and its auxiliary components in dynamic conditions has to be investigated to obtain indications about the possibility to adopt hybrid configurations that require fast load variations of the FCS (up to 6 kW/s). The hydrogen purge, external humidification, stack temperature, and stoichiometric ratio have to selected with the aim of individuating working strategies able to assure reliable operation in dynamic conditions. Moreover, the transient performance of the FCS have to be analyzed during warm-up phases, which are characterized by similar acceleration slopes (6 kW/s).

This experimental analysis can be carried out on the FCS connected to a variable resistive load by means of the DC–DC converter, which is controlled to simulate the instantaneous current requests of electric drive. The tests described in the following are performed varying the slope of the acceleration phases, between 5 and 50 A s^{-1}, on the base of the stack current requirements. For each working condition, the uniformity of individual cell voltage during the transient step is assumed as indicator of stack operation reliability.

The results obtained from this investigation can be utilized to design the power train control strategies on the same R40 driving cycle.

7.3.1 Performance of the FCS During Load Variations

For the following tests, the fuel utilization coefficient is set at the constant value of 0.90, the stoichiometric ratio ranges between 6 and 1.8, for a stack power from 700 W to 12 kW. With regard to the stack humidification, the inlet air is saturated at room temperature (290–300 K) to minimize the amount of energy required for the best membrane hydration and reduce the electric consumption of the humidifier and the purge frequency [4]. As a consequence, the stack temperature is controlled at about 315 K, to avoid any dehydration of the membranes.

The first test on the FCS connected to the resistive load is run utilizing a simplified R40 test cycle, with just three neat peaks, in order to obtain accelerations phases in terms of current requirements of 5 A s^{-1} and maximum power of about 10 kW. The values of the air flow rate are preliminarily set in steady state conditions for the whole load range comprised in the test cycle, in order to guarantee a minimum power consumption of the air compressor compatible with satisfactory values of the cell voltages. In particular, a control strategy for the compressor was adopted choosing R values equal to 1.8 in the range 100–240 A, and making them drop from 6 to 2 from open circuit to 100 A. In Fig. 7.14, the stack current and voltage measured during this test are reported as function of the cycle length. The stack voltage reaches the minimum values of 63, 52, and 48 V for the three current peaks of 80, 180, and 240 A, respectively. The R values reproduce the steady state settings with minimum $R = 1.8$, while air flow rate reaches 35 m^3 h^{-1} at 240 A. The stack voltage profiles in Fig. 7.14 are in agreement with data of the polarization curve obtained on the same stack, suggesting that the dynamic of 5 A s^{-1} does not compromise the regular stack operation, as confirmed by the distribution of the individual cell voltages, shown in

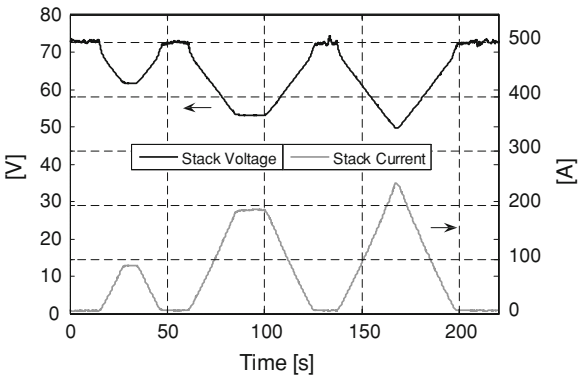

Fig. 7.14 Stack voltage and current versus time for a dynamic test at 5 A s^{-1} based on the R40 cycle

Fig. 7.15 for the instant corresponding to 240 A. In particular, it can be noticed that the voltage of most cells is close to 0.6 V, while only a voltage decreases between the first cell (about 0.4 V) and the last group of 20 cells (values of voltage comprised between 0.45 and 0.55 V for few cells is measured). As expected, the behavior of these cells results better for all the other values of current. Since no cell decreased under 0.4 V during the test, it means that the dynamic considered is satisfactorily supported by the FCS for the cycle utilized.

The data for the R40 cycle is then modified to obtain acceleration phases of 10 A s^{-1}, and another experiment is carried out on this cycle according to the target of minimizing the compressor consumption. The results of this test are

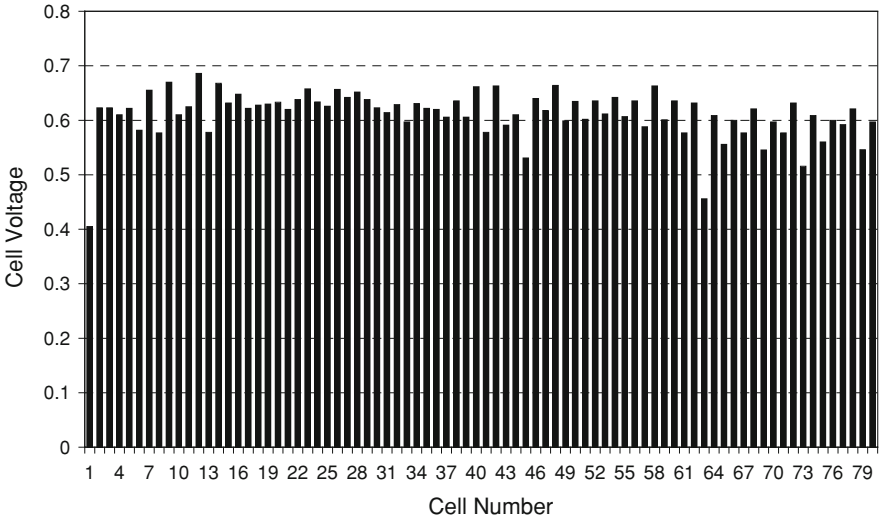

Fig. 7.15 Individual cell voltage acquisition during the experiment of Fig. 7.14 at $t = 170$ s (240 A)

Fig. 7.16 Stack voltage and current versus time for a dynamic test at 10 A s^{-1} based on the R40 cycle

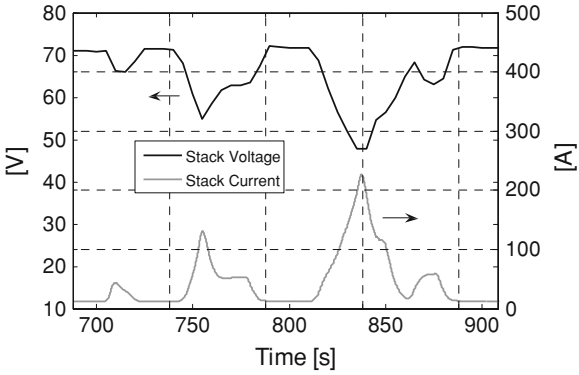

reported in Fig. 7.16, showing the stack current and voltage as function of cycle length, while R and air flow profiles are plotted in Fig. 7.17. Only a slight voltage decrease is measured in correspondence of the main current peaks (130 and 230 A) compared with the steady state values. The control law of the compressor makes possible R values only slightly lower than 1.8 for a short transient time at the end of acceleration phases, with air flow rate up to 35 $m^3\ h^{-1}$ at about 230 A. In fact, Fig. 7.18, which shows the individual cell voltage acquisition plotted as function of cycle length, evidences a general slight decrease of all cell voltages, with the first one under 0.5 V already for the second peak current (130 A) and under 0.4 V in correspondence of the highest current peak (230 A). The FCS behavior at 10 A s^{-1} suggests that the dynamic performance requires some modification in management strategies for higher current rising rates. This is confirmed by the experiment reported in Figs. 7.19, 7.20, 7.21, and 7.22, where a simple dynamic cycle of current is tested with the same compressor management strategy of the experiment of Fig. 7.17. This cycle is characterized by an acceleration ramp of 50 A s^{-1}, a short stationary phase at 220 A and a deceleration step at the same rate of acceleration. In Fig. 7.19, the acquisition data for the current cycle is reported

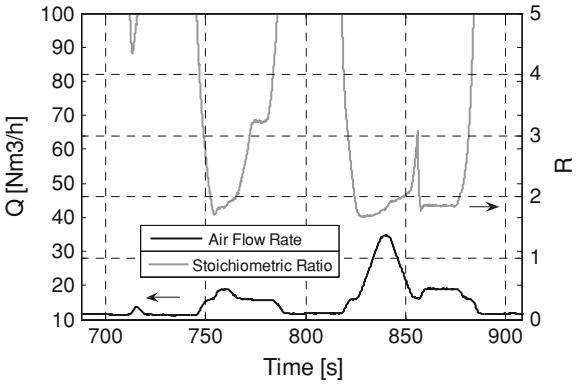

Fig. 7.17 Stoichiometric ratio and air flow rate versus time for the experiment of Fig. 7.16

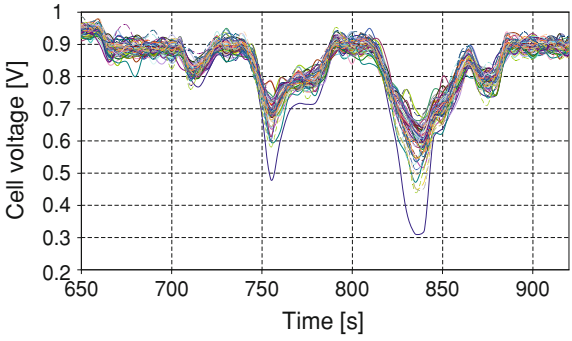

Fig. 7.18 Individual cell voltage acquisition versus cycle length during the experiment of Fig. 7.16

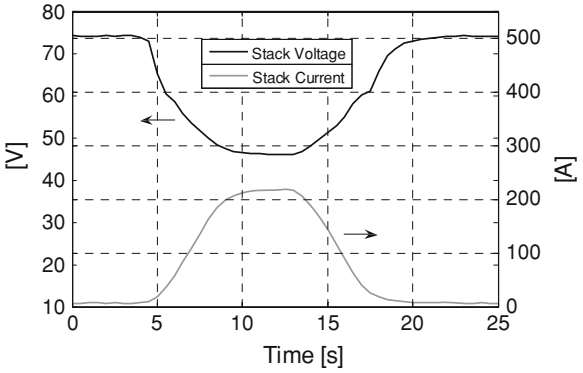

Fig. 7.19 Stack voltage and current versus time for a dynamic test at 50 A s^{-1}

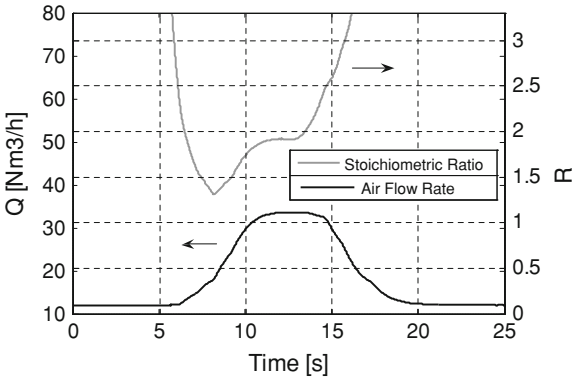

Fig. 7.20 Stoichiometric ratio and air flow rate versus time for the experiment of Fig. 7.19

together with the total stack voltage. This voltage drops down from 71 to about 45 V at the end of the acceleration step, then remains constant during the stationary phase (5 s), and rise again during the deceleration step. The *R* and air flow rate profiles, reported in Fig. 7.20, evidences that the compressor operation is stressed by the high dynamic adopted, in particular the faster dynamic of this test determines an appreciable effect on the stoichiometric ratio, whose profile decreases below 1.5 at the end of the acceleration phase. This behavior is further evidenced in Figs. 7.21 and 7.22, where the individual cell voltages are plotted as function of cycle length and as histogram acquired at the instant corresponding to the highest current peak, respectively. A problem of stack malfunctioning is clearly evidenced for several cells, in particular the first one dropped under 0.3 V, while the other three cells among the last 20 did not reached 0.4 V. The reason for this behavior is attributed to difficulties of the air compressor in supplying the right values of stoichiometric ratio (Fig. 7.20), and this suggests to change the air compressor strategy in order to increase *R* values during the fastest dynamic phases. Figures 7.23, 7.24, 7.25, and 7.26 show the results of a test on the R40 cycle operating at 50 A s^{-1} during the acceleration phases, but modified regarding the maximum power, which is limited to the optimal power obtainable by the stack

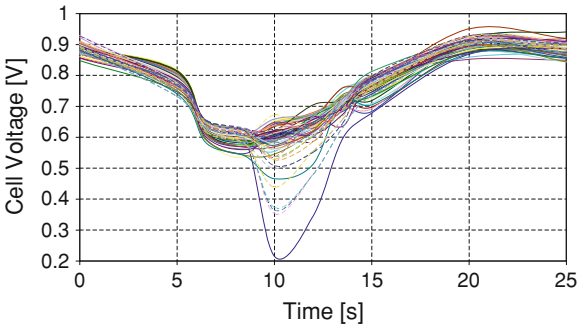

Fig. 7.21 Individual cell voltage acquisition versus cycle length during the experiment of Fig. 7.19

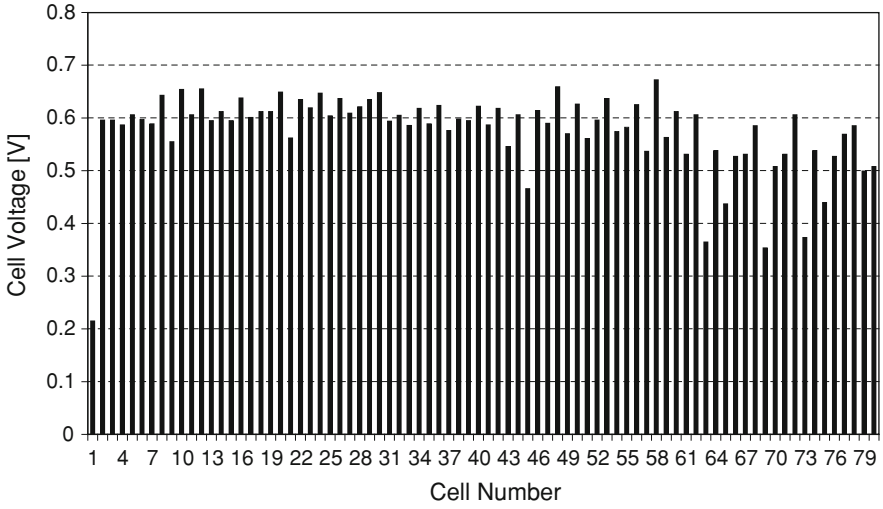

Fig. 7.22 Individual cell voltage acquisition during the experiment of Fig. 7.19 at the instant of maximum acceleration ($t = 10$ s, 220 A)

in the experimental condition adopted (12 kW with respect to 25 kW required by the cycle). For this test the air management strategy is modified, increasing the air flow rate in the range 0–200 A (see Sect. 7.4).

In Fig. 7.23, the stack current and voltage is reported as function of cycle length, while Fig. 7.24 shows the corresponding R and air flow rate for the modified air management strategy. The voltage profile results acceptable for the whole cycle, with values never lower than 47 V, while R values does not decrease under 1.8 also during the fastest acceleration phases.

The analysis of the results obtained for the individual cells (Figs. 7.25 and 7.26) confirms the benefit of the new air management strategy on the stack dynamic behavior, in particular most cells show a regular operation in the whole load range, while only for some cells a significant voltage reduction is observed at the end of the acceleration phases, with a partial voltage recovery during the stationary

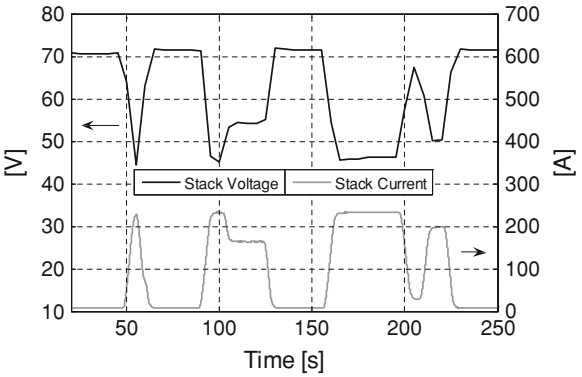

Fig. 7.23 Stack voltage and current versus time for a dynamic test at 50 A s^{-1} based on the R40 cycle

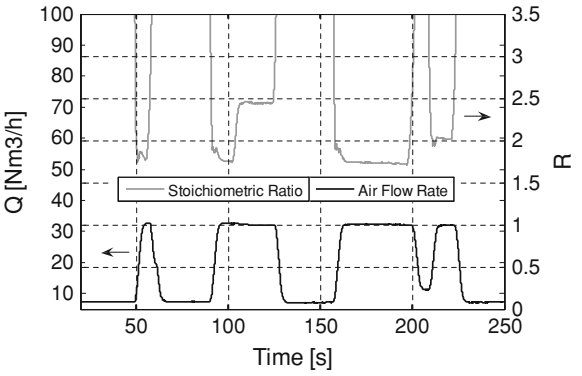

Fig. 7.24 Stoichiometric ratio and air flow rate versus time for the experiment of Fig. 7.23

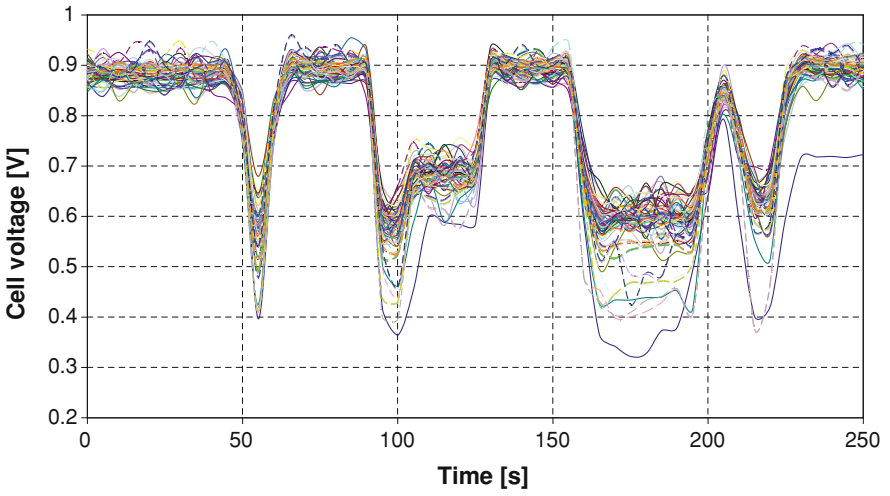

Fig. 7.25 Individual cell voltage acquisition versus cycle length during the experiment of Fig. 7.23

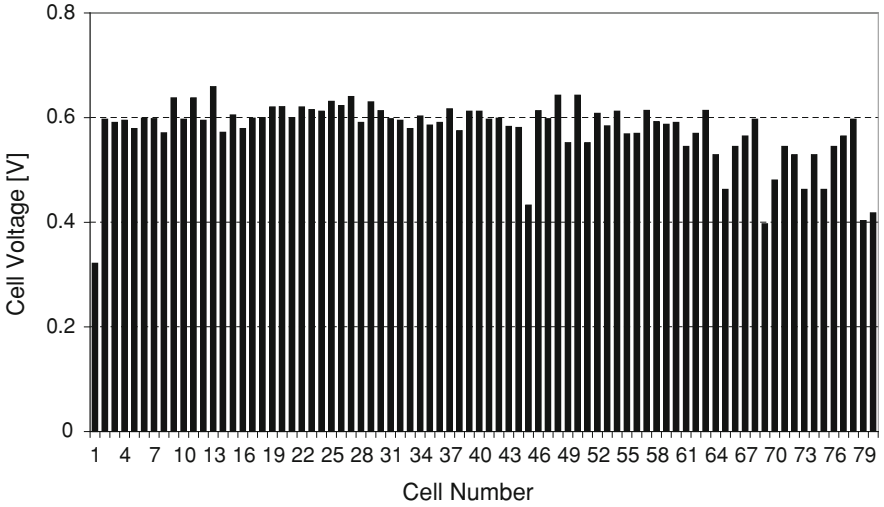

Fig. 7.26 Individual cell voltage acquisition during the experiment of Fig. 7.23 at the instant of maximum acceleration ($t = 175$ s, 230 A)

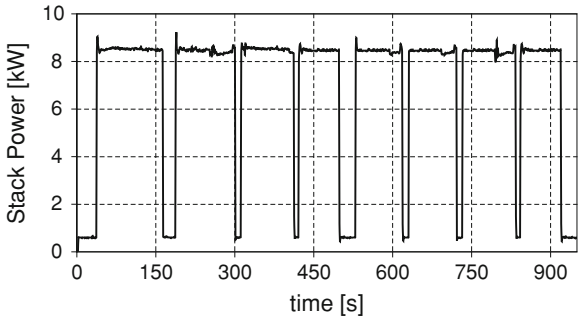

Fig. 7.27 Stack power versus time during a sequence of eight fast load variations from 0.7 to 8.5 kW

phases. No cell drops under 0.4 V, except for the first one whose voltage decreased at about 0.3 V, confirming the same trend already observed at 10 A s^{-1} [5].

The results of the FCS characterization performed with faster load variations, composed by a sequence of eight fast load variations from 0.7 to 8.5 kW, are reported in Figs. 7.27, 7.28, 7.29, 7.30, and 7.31. In Fig. 7.27, the stack power versus test length, with an acceleration slope of about 6 kW/s, is shown. The value of about 47°C is selected as initial stack temperature to overcome the limitations due to the electrochemical reaction and diffusion kinetics with respect to warm-up conditions. The inlet air is humidified at the same temperature, while the cooling system is controlled to maintain the stack temperature in the range 50–55°C. The hydrogen purge and air feeding strategies are evidenced by the acquisitions of hydrogen pressure and stoichiometric ratio during the test length (Figs. 7.28 and 7.29, respectively). Hydrogen pressure drops every 45 s according to the

frequency fixed for the purge strategy described in the previous paragraphs. Its pressure changes from 40 kPa at minimum power (0.7 kW) to 34 kPa at maximum constant power (8.5 kW) and drops to 28 kPa for each purge action.

The profile of the stoichiometric ratio, plotted in Fig. 7.29, evidences that R decreases below 1.5 throughout all the fast acceleration phases, indicating limitations of the compressor to supply enough air in the transient phases, while resulted 1.9 during steady state phases.

The function of the hydrogen purge and stoichiometric ratio control is highlighted in Figs. 7.30, 7.31, showing the C_v values and the individual cell voltages

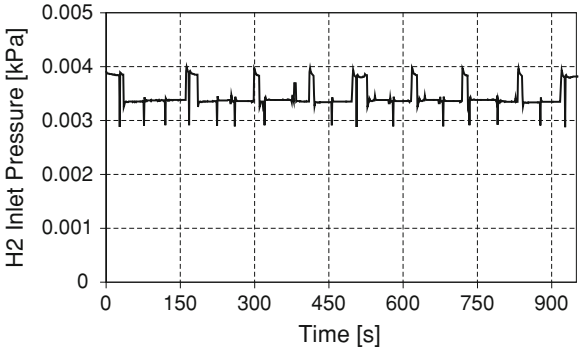

Fig. 7.28 Hydrogen inlet pressure versus time during a sequence of eight fast load variations from 0.7 to 8.5 kW

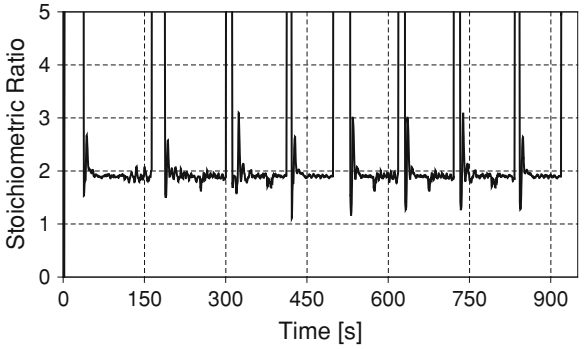

Fig. 7.29 Stoichiometric ratio versus time during a sequence of eight fast load variations from 0.7 to 8.5 kW

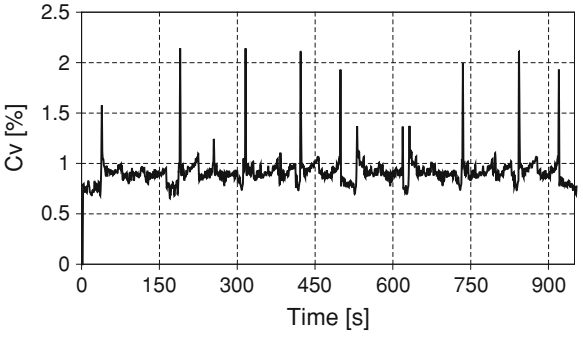

Fig. 7.30 Coefficient of variation (C_v%) versus time during a sequence of eight fast load variations from 0.7 to 8.5 kW

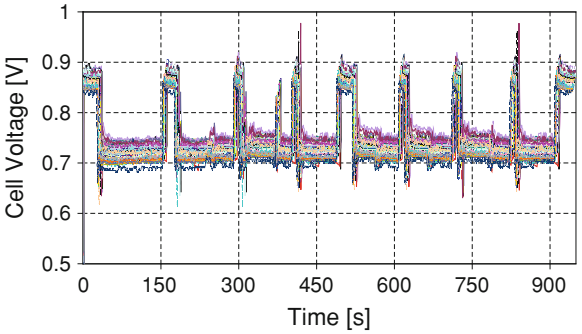

Fig. 7.31 Individual cell voltage versus time during a sequence of eight fast load variations from 0.7 to 8.5 kW

reported for the entire acquisition time, respectively. The coefficient of variation C_v is mostly lower than 1% for the entire range of time considered, while few sharp peaks up to 2.2% are observed during the acceleration phases ($R < 1.5$), evidencing an acceptable regularity of stack working. Moreover, a slight voltage recovery is observed for those cells more affected by incoming flooding phenomena (Fig. 7.31), specifically when the hydrogen pressure drops due to the purge intervention.

7.3.2 Behavior of the FCS During Warm-up

In this section, the experimental results regarding the analysis of the FCS during the warm-up phase are presented. The tests are carried out starting from 18°C, for two different acceleration values (150 and 1,500 W/s). Regarding the stack humidification, the inlet air is saturated at the same temperature adopted for the stack at the beginning of the tests, to avoid membrane de-hydration.

The individual cell uniformity is monitored by using the coefficient of percentage variation C_v as statistical indicator already introduced in Sect. 6.3. For the analysis reported in this paragraph a value of C_v equals 2.5% is considered acceptable for a regular working of the stack.

In order to study transient response of the stack during the warm-up phases the following experiments are carried out connecting the FCS to a resistive load electronically controlled. Starting from the temperature of 18°C the stack power is gradually increased up to about 8 kW by using two power accelerations (150 and 1,500 W/s). After each acceleration the system is left in steady state condition until the temperature of about 45°C is reached for the stack.

In Fig. 7.32, the stack current, voltage, and temperature are shown versus time for the test at 150 W/s, while Fig. 7.33 shows a magnification of the stack power and stoichiometric ratio during the acceleration phase. It can be observed that the stack temperature reaches its final value in about 10 min, while the stack voltage reaches the minimum value of 53 V at the end of acceleration slope (55 s), then increases up to about 60 V at 45°C. The stack current reaches the pick value of

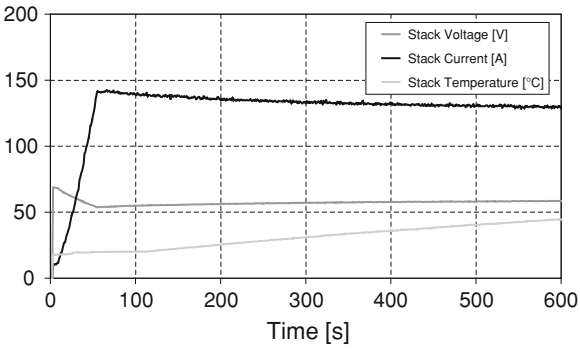

Fig. 7.32 Stack voltage, current, and temperature versus time during warm-up test at 150 W/s

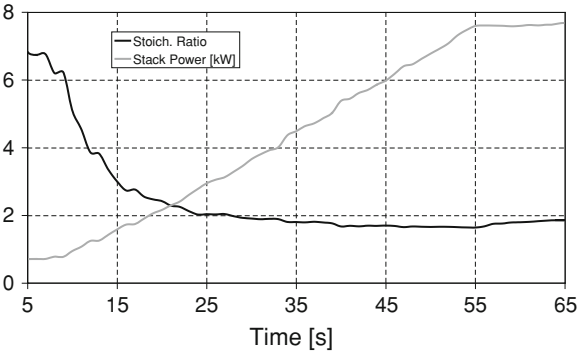

Fig. 7.33 Stoichiometric ratio and stack power versus time during the acceleration phase in warm-up test at 150 W/s

140 A at the of the acceleration phase, then slowly decreases to 130 A as the system is controlled to maintain the constant power of 7.8 kW. The stoichiometric ratio profile (Fig. 7.23) evidences a regular variation passing from the highest value at low load ($R = 6.7$) to the final value of $R = 1.9$ at the power level of 7.8 kW. The data shown in Figs. 7.32, 7.33 suggest that the operative conditions selected for this tests satisfy a acceptable dynamic behavior of the FCS, as the total stack voltage results comparable to that obtained in steady state conditions. This is confirmed by the analysis of the individual cell voltages acquired during the whole experiment, whose results are reported in Figs. 7.34, 7.35, where C_v versus time and individual cell voltages at the moment corresponding to the maximum C_v are shown, respectively. In particular, C_v resulted always lower than 1.2% and almost constant during the test (Fig. 7.34), evidencing a uniform distribution of cell voltages (Fig. 7.35), with the minimum voltage (0.63 V) for the cell N.1 at the end of the acceleration phase (maximum C_v) and most cell voltages comprised between 0.65 and 0.67 V.

The warm-up phase is also studied using a slope of acceleration 10 times higher (1,500 W/s). The results are shown in Figs. 7.36, 7.37, 7.38, and 7.39 evidencing the tendency of the FCS to operate with irregularity only at the end of acceleration phase, in particular the total stack voltage decreases to about 50 V for

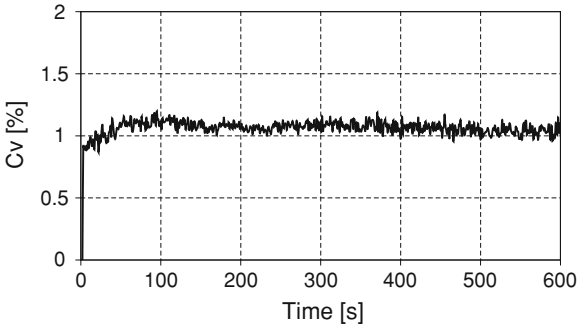

Fig. 7.34 Coefficient of variation (C_v%) versus time during warm-up test at 150 W/s

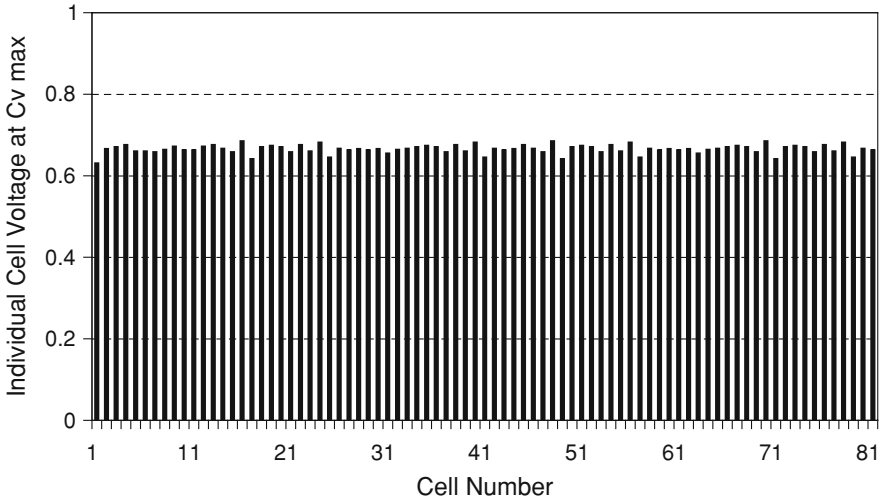

Fig. 7.35 Individual cell voltage acquisition during warm-up test at 150 W/s at the instant corresponding to maximum C_v (90 s)

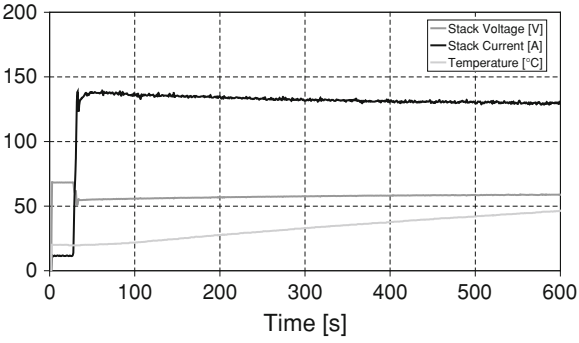

Fig. 7.36 Stack voltage, current, and temperature versus time during warm-up test at 1,500 W/s

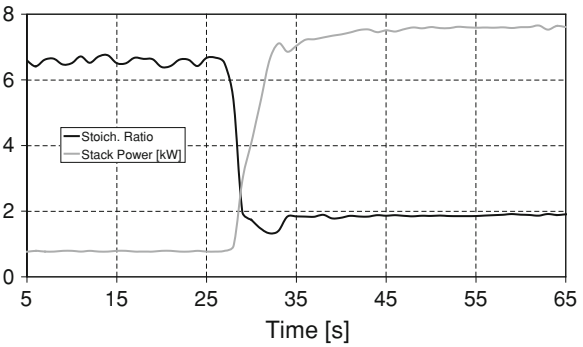

Fig. 7.37 Stoichiometric ratio and stack power versus time during the acceleration phase in warm-up test at 1,500 W/s

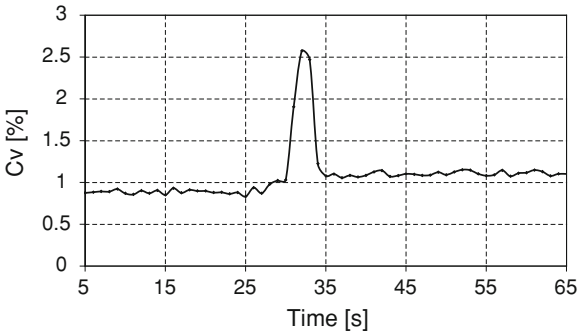

Fig. 7.38 Coefficient of variation (C_v%) versus time during the acceleration phase in warm-up test at 1,500 W/s

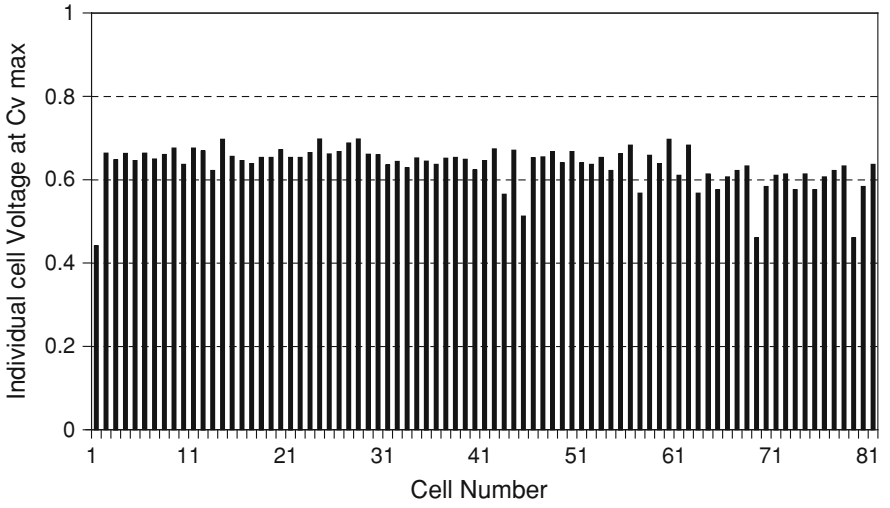

Fig. 7.39 Individual cell voltage acquisition during warm-up test at 1,500 W/s at the instant corresponding to maximum C_v (32 s)

a short-transient period (about 5 s, Fig. 7.36), R decreases below 1.5 at 7 kW (time = 32 s in Fig. 7.37), C_v profile shows a sharp peak of about 2.5% at the same instant (Fig. 7.38). The stack dynamic behavior is better detailed in Fig. 7.39 reporting the individual cell voltages at the moment corresponding to the end of the acceleration phase (maximum C_v). It can be observed that the cell voltage distribution significantly worsens compared to results of Fig. 7.35, but no cell voltage drops below 0.4 V, which can represent a limit value for a reliable stack operation, endurable only for few seconds. The results of Figs. 7.36, 7.37, 7.38, and 7.39 represent the acceptable limit for the stack tolerance to dynamic conditions of warm-up, and provide useful quantitative indications of the power ratio between the fuel cell generator and the battery during the start up [6].

7.4 Effect of Different Air Management Strategies

The results shown in previous sections suggest the crucial role of the oxidant supply system, in particular the effect of the stoichiometric ratio (air flow rate) on FCS efficiency and dynamic performance. In order to give further information about this issue, in this paragraph different air management strategies are closely examined, with particular reference to their influence on cell voltage uniformity and air compressor parasitic losses.

The behavior of the subsystem composed by stack and air compressor is studied using four different management strategies, which allows different profiles of stoichiometric ratio versus stack current to be obtained, as discussed in the following analysis.

If the stack efficiency is calculated using the equation already shown in Sect. 6.4:

$$\eta_{stack} = \frac{V}{V_{id}}, \tag{7.1}$$

the following coefficient (η_{SC}) can be used to evaluate the effect of air compressor power consumption on the net power provided by the stack:

$$\gamma_{SC} = \frac{P_{stack} - P_{comp}}{P_{stack}}, \tag{7.2}$$

then the efficiency of the sub-system composed by stack and compressor (SC) is calculated by:

$$\eta_{SC} = \eta_{stack} \cdot \gamma_{SC}. \tag{7.3}$$

The individual cell uniformity during the dynamic tests is evaluated by using the coefficient of percentage variation C_v.

In Table 7.2, the relative uncertainties of the calculated experimental parameters are reported. The results are analyzed focusing the attention on effects that air

Table 7.2 Relative uncertainties of calculated experimental parameters

Parameter	Uncertainty (%)
R	3.8
P_{comp}	1.4
P_{stack}	1.4
η_{stack}	0.7
γ_{SC}	4.0
η_{SC}	4.7

Calculated starting from the sensor accuracies reported in reference [3]

compressor management strategies have on the stack performance, for different power variation rates. The dynamic tests of the FCS are conducted on different working cycles, changing the stack current variation rate from 2 to 50 A/s. These values are selected with the aim of simulating the acceleration requirements of a fuel cell vehicle of size and power compatible with the 20 kW FCS, for instance, the power requirements of a city car or an urban minibus equipped with a nominal 30 kW electric drive running on the European R40 driving cycle are considered [7]. During the dynamic phases of this cycle, which lasts about 20 s with accelerations of about 1 m/s^2, peak power requirement of about 50 kW for the vehicle selected are certainly expected. Evaluating an average efficiency for the electric drives and DC–DC converters of about 0.8 and FCS average total voltage of about 55 V, the above value of engine peak power means a stack current derivative of about 50 A/s.

During experiments all the main parameters characteristic of stack operation, such as stack current and individual cell voltage, reactant pressure, air and cooling water temperature, and humidification level are continuously monitored. Stack temperature and reactant pressure during the tests are maintained below 330 K and 150 kPa, respectively.

Figure 7.40a shows the profiles of stoichiometric ratio versus stack current for different compressor management strategies, which can be obtained by imposing different references of the compressor motor speeds as function of stack current, while Fig. 7.40b reports the air flow rate values corresponding to the different strategies. The curves 1 and 2 of Fig. 7.40a refer to compressor motor speed regulations which determine two constant air flow rates of 33 and 24 Nm^3/h, respectively, and are obtained with constant voltage reference of the motor speed (4 and 3 V). The other curves in Fig. 7.40b refer to variable air flow rates, in particular the curve 3 is related to R values comprised between 2 and 3 in the range of 100–200 A, obtained with a linear voltage reference increase up to 4 V (140 A as stack current), corresponding to an air flow rate almost linearly increasing from 12 to 33 Nm^3/h in the range 0–150 A, and constant at this value up to 200 A. Finally, the curve 4 is obtained with a control which allowed the compressor to reach $R = 2$ already at 100 A and to keep it constant at higher loads, with an linear flow rate increase from 16 to 33 Nm^3/h in the range 100–200 A (Fig. 7.40b). This management is realized imposing a first increase of compressor voltage reference

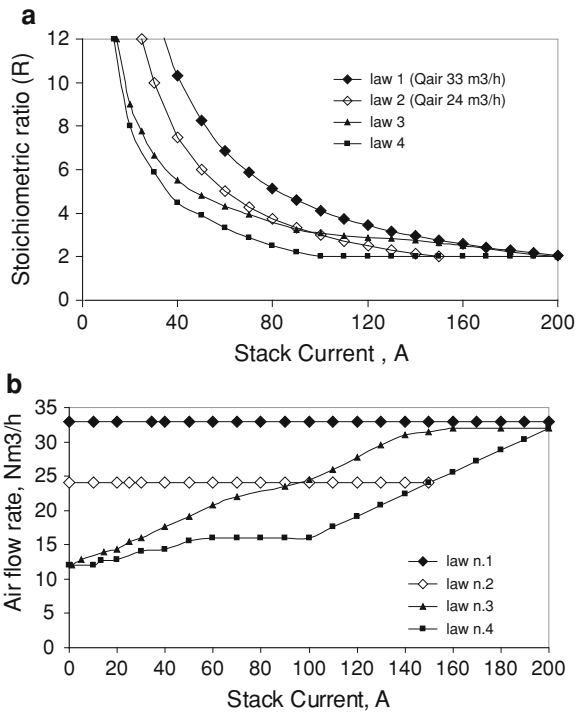

Fig. 7.40 **a** Stoichiometric ratio versus stack current for four different management strategies. **b** Air flow rate versus stack current for the management strategies (**a**)

from 1.5 to 2 V (60 A as stack current), then after a constant phase at 2 V the voltage reference is linearly increased up to 4 V in the range 110–200 A of the stack current. This last management strategy allows the compressor consumption to be minimized with R values such as to guarantee a regular stack operation in steady state operations.

The study of the effects of compressor management strategy on the efficiencies of stack and subsystem (SC) composed by stack and compressor is preliminarily carried out in steady state conditions. In particular, the stack efficiency (η_{stack}) is calculated by using the Eq. 7.1 starting from the data obtained at 313 K with the compressor management curve 4 (Fig. 7.40a, b) and reported in Fig. 7.41 as function of stack current. A linear trend can be observed in the range 30–200 A corresponding to an efficiency decrease from 0.7 to 0.5. The η_{stack} curves for the other management strategies are not reported because they are not significantly affected by $R > 2$. In Fig. 7.41, η_{SC} (Eq. 7.3) is also reported for all the different compressor management strategies of Fig. 7.40a.

Differently from stack efficiency the η_{SC} values are clearly dependent on the profile of R utilized, due to compressor consumptions connected to different motor speed regulations. In particular, highest η_{SC} values decrease from 0.60 to 0.53 passing from management curve 4 to 1, with major differences in the field of lower loads (under 100 A).

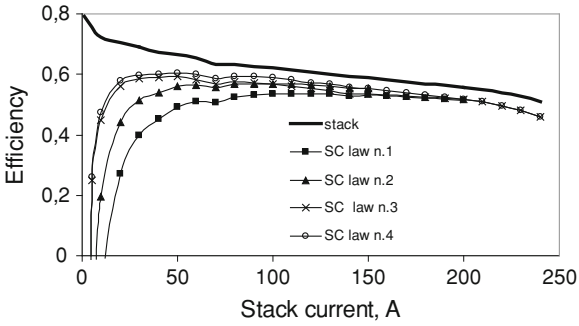

Fig. 7.41 Stack and stack + compressor system (SC) efficiencies as function of stack current, for the four strategies of Fig. 7.40a

For the tests carried out with the compressor management strategy N.4 a simple current cycle is used, whose dynamic is characterized by an acceleration ramp (2, 10, and 25 A/s), a stationary phase at 160 A and a deceleration step at the same rate of acceleration. In Fig. 7.42a–c, the acquisitions of the main operative parameters during cycle length are shown for the test at 2 A/s. In Fig. 7.42a, the current cycle is reported together with the total stack voltage. This drops down from 71 to about 49 V at the end of the acceleration step, then slowly increases up to 51 V during the stationary phase (110 s), and rises again during the deceleration step. The R and air flow rate profiles (Fig. 7.42b) show that the compressor working is not stressed for the slow dynamic adopted, as their values are exactly corresponding to those expected by the imposed management strategy for every instant of the cycle. The slight voltage increase, observed in Fig. 7.42a during the stationary phase, can be correlated with the stack temperature increase, which is possible to observe in Fig. 7.42c. However, the initial phase of this voltage increase (between 80 and 100 s) can be also related to the thermal management strategy adopted during the test. In particular, the flow of the external water through the heat exchanger is stopped just before the beginning of the cycle, when the stack output temperature is decreasing. This justifies the initial stack cooling shown in Fig. 7.42c, and the voltage behavior between 80 and 100 s. Figure 7.42c also evidences the constant values of inlet air humidity and temperature (100% and 303 K, respectively).

The results obtained at 10 A/s are shown in Fig. 7.43, in particular the voltage profile reported in Fig. 7.43a is practically coincident with that related to 2 A/s, with a more regular behavior also at the beginning of the stationary phase, because during this test the stack is not previously cooled by external water through the heat exchanger.

The temperature profiles are reported in Fig. 7.43c, where it is evidenced that output air and cooling water temperatures slightly increase during the test following almost the same values. The imposed values of air humidity and inlet temperatures are also reported in Fig. 7.43c. The faster dynamic of this test determines an appreciable effect on the stoichiometric ratio (Fig. 7.43b), whose profile decreases below $R = 2$ in the range 15–20 s at the end of the acceleration phase. These effects are more evident in the test effected at 25 A/s (Fig. 7.44b),

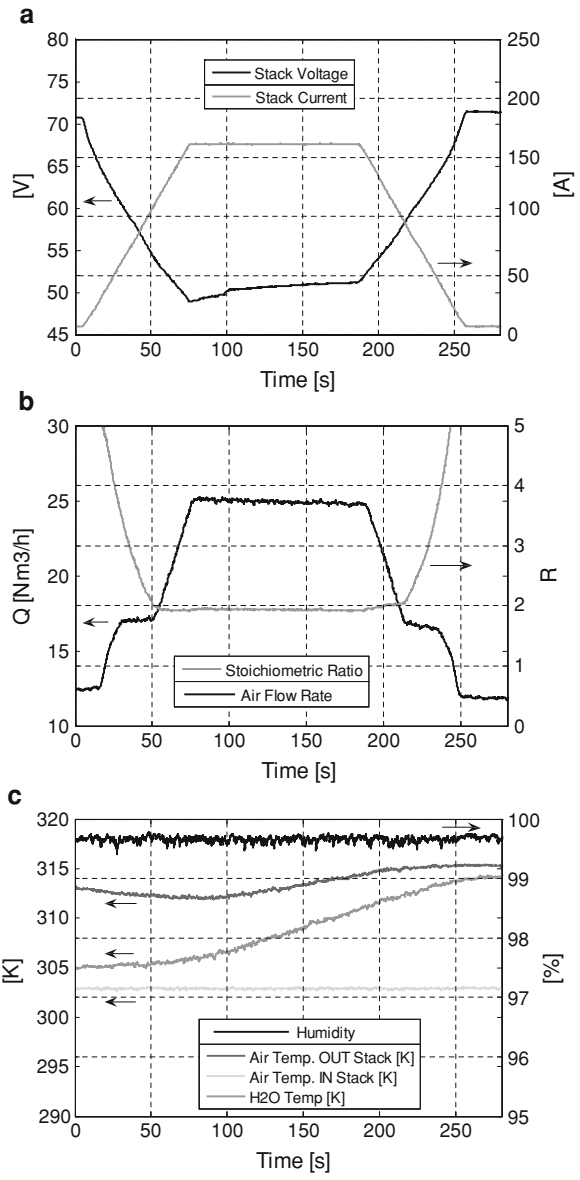

Fig. 7.42 **a** Stack voltage and current acquisition versus time during the dynamic cycle characterized by the maximum stack current variation of 2 A/s. Air management strategy N.4. **b** Stoichiometric ratio and air flow rate acquisition versus time for the experiment (**a**). **c** Stack temperature (measured at the outlet of cathode side), water temperature (measured in the cooling circuit at the outlet of the stack), inlet air relative humidity and temperature acquisition versus time for the experiment (**a**)

with the same thermal management of Fig. 7.43c. In addition, also the voltage profile results affected by the faster dynamic, as stack voltage reaches lower values (47 V) for about 10 s just after the acceleration phase (Fig. 7.44a).

A further indication of the effect of the load variation rate on the stack working regularity is obtained by the calculation of C_v values, carried out on the base of the acquisition versus time of the individual cell voltages. The C_v profile referred to

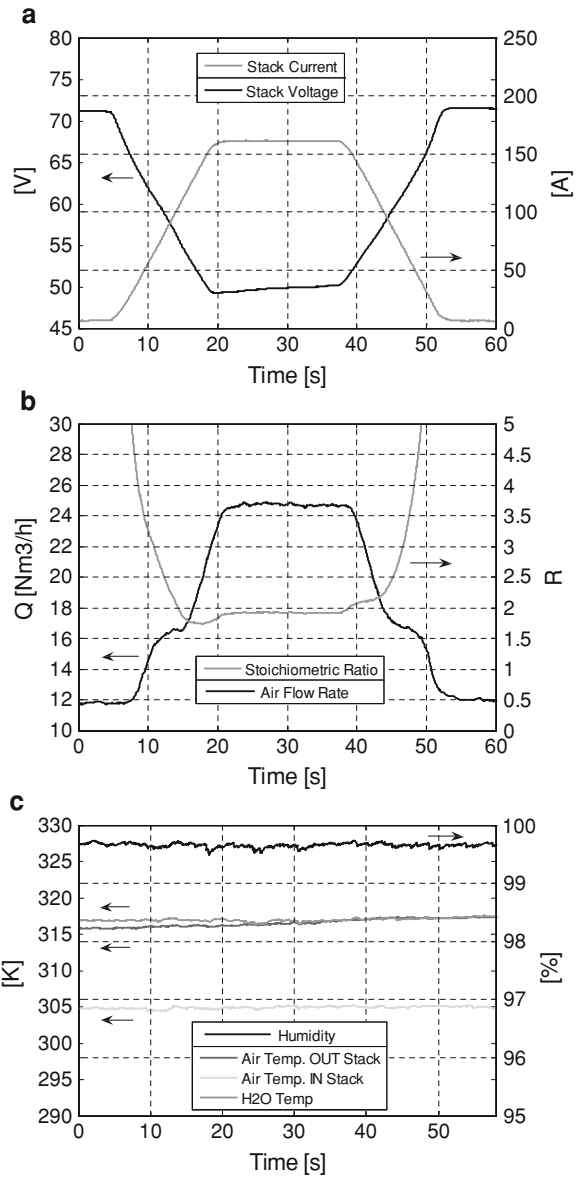

Fig. 7.43 **a** Stack voltage and current acquisition versus time during the dynamic cycle characterized by the maximum stack current variation of 10 A/s. Air management strategy N.4. **b** Stoichiometric ratio and air flow rate acquisition versus time for the experiment (**a**). **c** Stack temperature (measured at the outlet of cathode side), water temperature (measured in the cooling circuit at the outlet of the stack), inlet air relative humidity and temperature acquisition versus time for the experiment (**a**)

tests of Figs. 7.42, 7.43, and 7.44 are reported versus cycle length in Fig. 7.45, where the differences between the C_v values for the three current ramps (2, 10, and 25 A/s) are evidenced. While at 2 and 10 A/s the C_v profiles show a regular behavior associated with stack power values rather than dynamic ramps, at 25 A/s a strong effect of dynamic requirements is observed on C_v, as this coefficient reaches almost 3.5 at the end of the acceleration step.

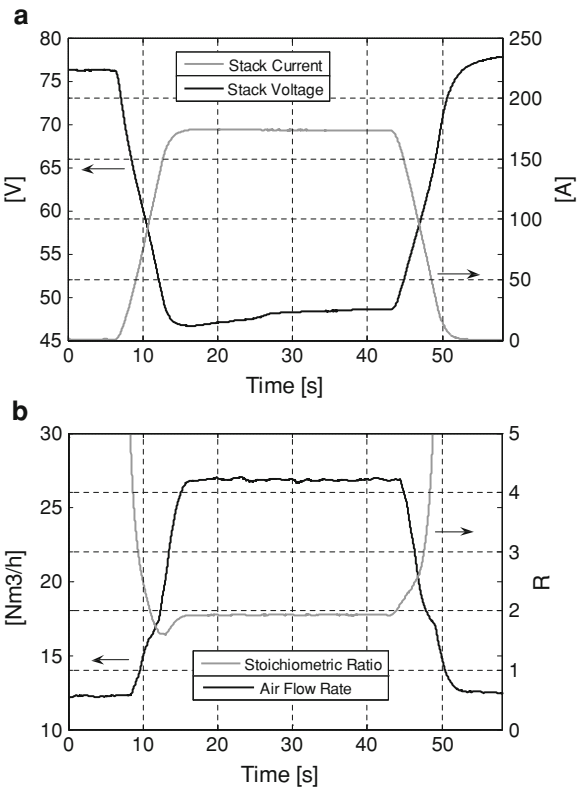

Fig. 7.44 **a** Stack voltage and current acquisition versus time during the dynamic cycle characterized by the maximum stack current variation of 25 A/s. Air management strategy N.4. **b** Stoichiometric ratio and air flow rate acquisition versus time for the experiment (**a**)

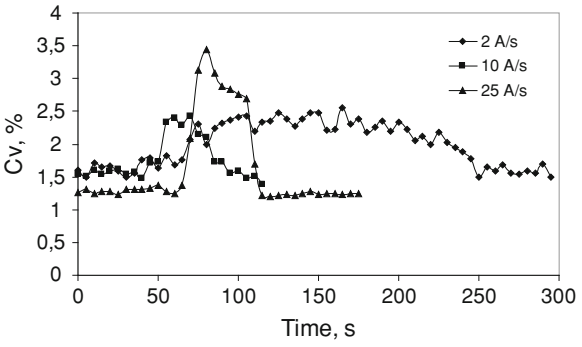

Fig. 7.45 C_v profiles versus cycle length for the experiments of Figs. 7.42, 7.43, and 7.44

This behavior is evidenced in Fig. 7.46, where the individual cell voltages corresponding to five significant instants of the cycle are reported, in particular just before acceleration ($t = 0$ s), just after acceleration ($t = 10$ s), two instants of the stationary phase ($t = 20$ and 34 s), and at the end of deceleration step ($t = 45$ s). An evident problem of stack malfunctioning is observed at $t = 10$ s, especially for the last 10 cells, due to difficulties of air compressor in assuring the necessary

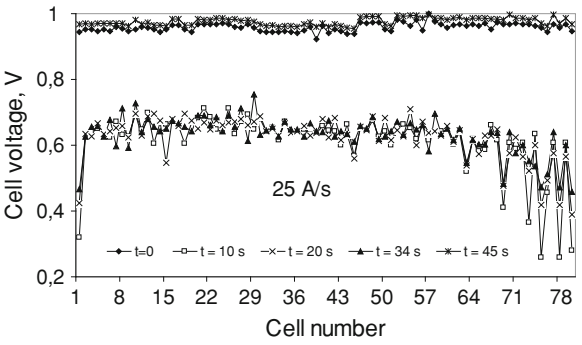

Fig. 7.46 Individual cell voltage for five significant instants of the experiment of Fig. 7.44

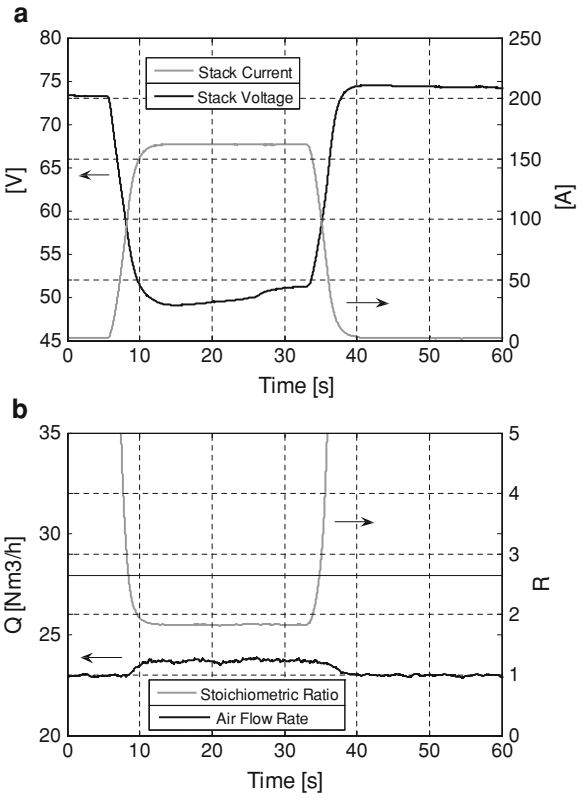

Fig. 7.47 **a** Stack voltage and current acquisition versus time during the dynamic cycle characterized by the maximum stack current variation of 50 A/s. Air management strategy N.2. **b** Stoichiometric ratio and air flow rate acquisition versus time for the experiment (**a**)

stoichiometric ratio values (Fig. 7.44b), while the cell voltage recovery at $t > 10$ s indicates the correlation between R values and voltage behavior.

The current cycle of Figs. 7.42, 7.43, and 7.44 can be utilized to verify the stack–compressor interaction in higher dynamic conditions. Figure 7.47a, b reports the results obtained with a ramp of 50 A/s and the compressor management strategy N.2 (Fig. 7.40), corresponding to a constant air flow rate of 24 Nm^3/h,

which allows the reaching during the stationary phase of the cycle R values similar to those obtained with the management strategy N.4. During this test, the output cathode temperature is maintained constant at 315 K, with 303 K and 100% of relative humidity at the inlet. In Fig. 7.47a, the voltage profile reaches the minimum value of about 48 V at the end of the acceleration step, with a partial recovery up to 51 V at the end of steady state phase. This behavior shows a stack working irregularity, not evidenced by the R profile reported in Fig. 7.47b, which follows the values reported in Fig. 7.40.

The utilization of the management strategy N.1 provides the results shown in Fig. 7.48 (same thermal management of Figs. 7.43, 7.44, and 7.47), in particular stack voltage does not decrease under 53 V maintaining this value almost constant during the stationary phase, while R follows the values expected by Fig. 7.40 and reaches about 2.5 at 160 A. The difference in stack performance observed between the management strategies N.1 and 2 is confirmed by the C_v values reported in Fig. 7.49, which evidences that the statistical indicator of cell voltage regularity does not reach the value 2.5 for the highest flow rate (33 Nm^3/h) while it overcomes the value 3.5 for 24 Nm^3/h at the end of the acceleration phase. This confirms that during the fastest dynamic phases the necessity to preserve stack

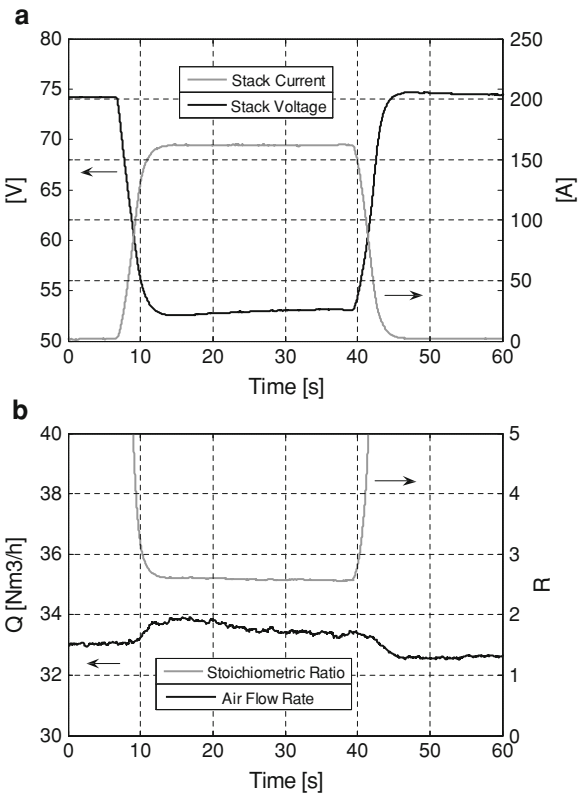

Fig. 7.48 **a** Stack voltage and current acquisition versus time during the dynamic cycle characterized by the maximum stack current variation of 50 A/s. Air management strategy N.1. **b** Stoichiometric ratio and air flow rate acquisition versus time for the experiment of (**a**)

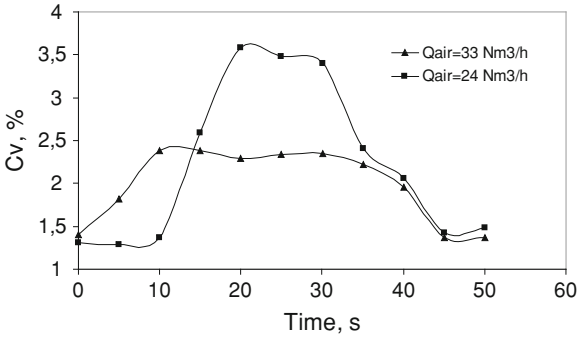

Fig. 7.49 C_v profiles versus cycle length for the experiments of Figs. 7.47 and 7.48

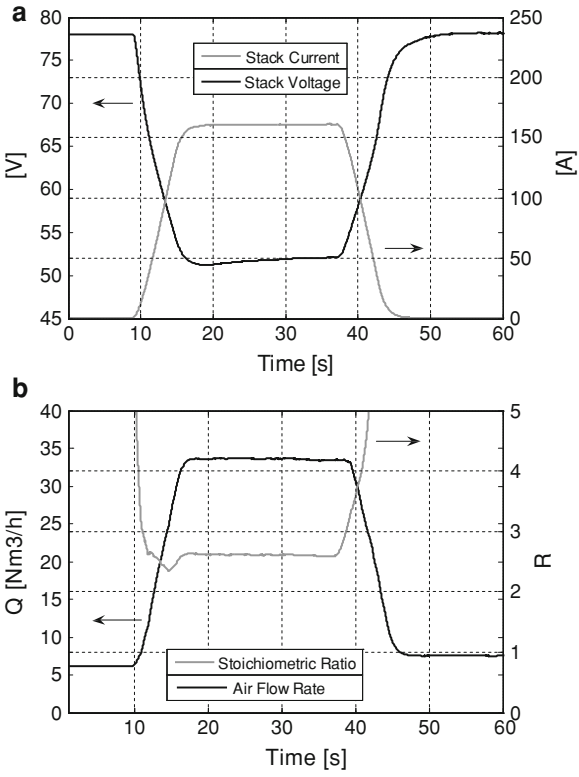

Fig. 7.50 **a** Stack voltage and current acquisition versus time during the dynamic cycle characterized by the maximum stack current variation of 25 A/s. Air management strategy N.3.
b Stoichiometric ratio and air flow rate acquisition versus time for the experiment (**a**)

durability requires stoichiometric ratio values higher than those optimized for stationary operations or for very slow dynamics.

In order to identify the best compromise between compressor consumption and stack dynamic performance the management strategy N.3 is verified for two different current variation rates, 25 and 50 A/s (Figs. 7.50 and 7.51, respectively). This management strategy allows R values higher with respect to the strategy N.4 to be realized, in particular reaching $R = 2.5$ (33 Nm^3/h) at 160 A. For both dynamic

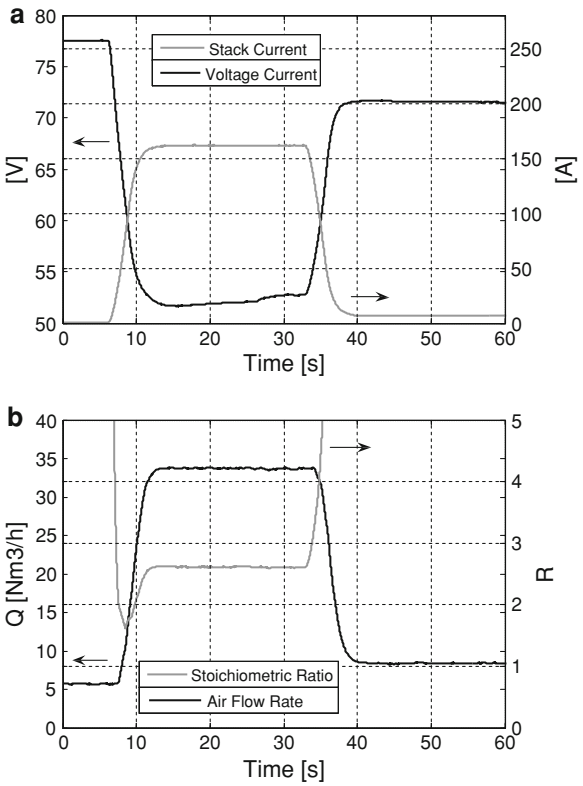

Fig. 7.51 **a** Stack voltage and current acquisition versus time during the dynamic cycle characterized by the maximum stack current variation of 50 A/s. Air management strategy N.3. **b** Stoichiometric ratio and air flow rate acquisition versus time for the experiment of (**a**)

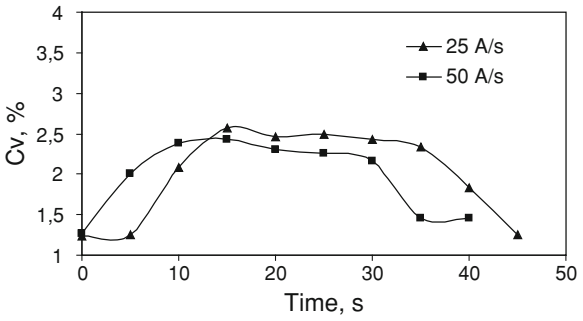

Fig. 7.52 C_v profiles versus cycle length for the experiments of Figs. 7.50 and 7.51

ramps the voltage profiles suggest a regular stack operation, with minimum voltage values always higher than 52 V (Figs. 7.50a and 7.51a). Regarding R profiles the steady state values are reached after <5 s from the beginning of the stationary phase for both ramps, while an appreciable difference is observed only at the end of the acceleration step, in particular at 50 A/s a slight and fast reduction ($R < 2$) is evidenced (Fig. 7.51b). The calculation of C_v evidences that this management strategy makes possible the regular stack working also for 50 A/s, as shown in Fig. 7.52, in fact the C_v values never overcome 2.5 also during the fastest acceleration phase.

The compressor management issues discussed above are finally verified in the range of high loads utilizing a cycle of current characterized by two successive acceleration steps at 50 A/s, each one followed by a steady state phase, the first one at 160 A and the second one at 240 A. A final deceleration step at 50 A/s takes back the stack to the initial current value. The compressor management strategy N.3 is adopted for the entire cycle length, with the aim to limit compressor consumptions and check stack operation regularity in more severe conditions.

In Fig. 7.53a, the stack current variation during the cycle and the corresponding voltage values are reported versus time. As expected the first acceleration step reproduces the same results shown in Fig. 7.51 in terms of stack voltage, as well as regarding stoichiometric ratio values (Figs. 7.51b and 7.53b), while during the second acceleration step a voltage decrease is observed from 52 to 45 V, with the corresponding R diminution from 2.5 to 2 (Fig. 7.53). Figure 7.53b also reports the air flow rate profile evidencing the different values imposed by the selected management strategy during the cycle, 33 Nm^3/h after the first acceleration phase and 38 Nm^3/h during the second one.

Some acceptable individual cell irregularities during the second acceleration phase are evidenced by the C_v values shown in Fig. 7.54, where the statistical

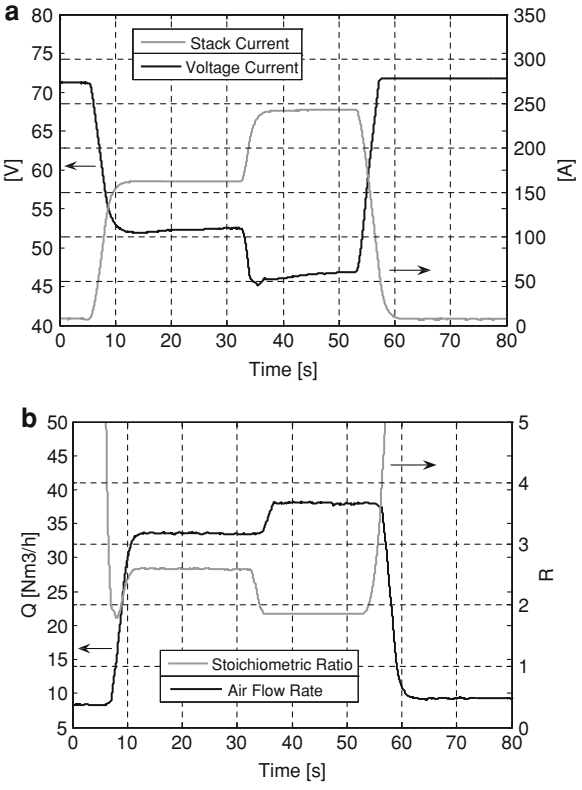

Fig. 7.53 **a** Stack voltage and current acquisition versus time during the dynamic cycle characterized by two stack current steady state levels (160 and 240 A) and the maximum stack current variation of 50 A/s. Air management strategy N.3. **b** Stoichiometric ratio and air flow rate acquisition versus time during the dynamic cycle characterized by two stack current steady state levels (160 and 240 A) and the maximum stack current variation of 50 A/s. Air management strategy N.3

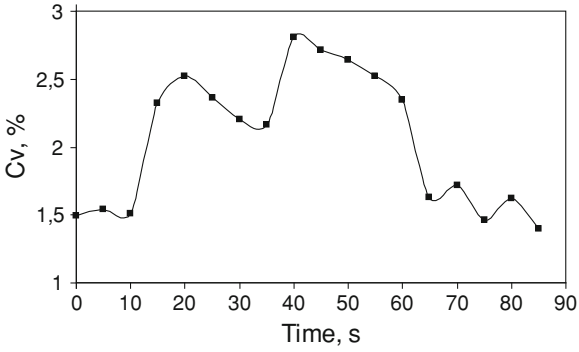

Fig. 7.54 C_v profiles versus cycle length for the experiment of Fig. 7.53

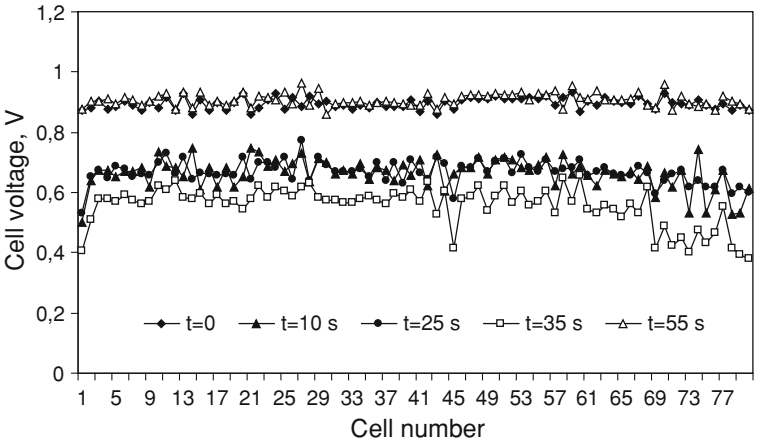

Fig. 7.55 Individual cell voltage for five significant instants of the experiment of Figs. 7.53 and 7.54

indicator is reported versus time for the entire cycle. The first peak at about 2.5 reproduces that observed in Fig. 7.52, while the second peak at about 2.8% is due to the second acceleration step, and is associated with incoming difficulties of air feeding encountered by some cells. This is better evidenced by the results of Fig. 7.55, where the acquisitions of all individual cells are reported for initial and final instants ($t = 0$ and $t = 55$ s), for the two C_v peaks ($t = 10$ and $t = 35$ s) and for the relative minimum between the two C_v peaks ($t = 25$ s) which corresponds to the initial instant of the second acceleration step. It is evident that the problem of the last section of the stack regarding the air feeding capabilities, in particular at $t = 10$ and $t = 35$ s, while at $t = 25$ s a partial voltage recovery is observed, due to the major oxygen availability during the first stationary phase.

The results reported above show that the compressor management strategy adopted during the dynamic operations tested clearly affects both individual cell voltage regularity (and then stack reliability) and FCS efficiency. In fact, although

the strategy N.4 allows the minimum compressor consumption to be assured, especially in the field of low powers, it does not guarantee the reliable stack operation in more elevated dynamic conditions (starting from 25 A/s). On the other hand, the strategies N.1 and 2, based on the regular operation of the air compressor, evidences the necessity of higher air flow rates during dynamic phases, in particular at 50 A/s, but implies a strong efficiency loss, as indicated by the steady state results of Fig. 7.41. The best balance between efficiency optimization and dynamic response of the FCS is then reached by the management strategy N.3 characterized by R values only slightly higher with respect to the strategy N.4 up to 200 A. This strategy allows a regular stack voltage to be maintained up to 50 A/s also in the field of high powers, while the overall efficiency decrease with respect to the strategy N.4 could be considered not significant, as suggested by the results obtained in stationary conditions (Fig. 7.41).

A further improvement of efficiency and regular stack working in conditions of high loads could be reached by increasing the reactant pressure, in particular this could prevent too low cell voltages at the highest loads (<0.5 V), which are observed in Fig. 7.55 [3].

7.5 Fuel Cell Power Train Tested on the R40 Driving Cycle

The propulsion system is powered in a hybrid configuration by using lead batteries and the 20 kW PEM stack described in the above paragraphs. The experimental tests in dynamic operation are carried out on a laboratory test bench utilizing the European R40 driving cycle, varying both dynamics and maximum power of the test cycle for different hybridization levels between FCS and batteries.

As previously discussed (Sect. 5.5), the battery pack of a fuel cell power train can be either minimized assigning the role of generating most energy required by the load to the fuel cell stack (soft hybrid), or sized in order to provide all dynamic requirements of the vehicle allowing the utilization of a smaller FCS (hard hybrid).

The first experiment on the fuel cell power train is carried out imposing to the R40 cycle an acceleration slope corresponding to the stack current the variation profile of Fig. 7.14 (5 A s^{-1}) and the air management strategy of Fig. 7.17 (minimum compressor consumption). The results obtained are shown in Fig. 7.56, where the power distribution between engine, battery pack, and DC–DC converter is reported versus cycle length. The engine power reaches three maximum values, which are 5, 10, and 15 kW, at the end of the three acceleration phases of the R40 cycle, then after the stationary phases diminishes up to negative power values during the deceleration phases, when the engine operates as generator. The control strategy adopted for this test is based on the hypothesis that the hybrid vehicle is used as pure electric vehicle at the start up and for partial loads, in particular the energy flows inside the power train are regulated to satisfy the engine requirements only by batteries up to about half of the engine maximum power. For higher loads the FCS satisfies all the engine demands following the same dynamic of the cycle,

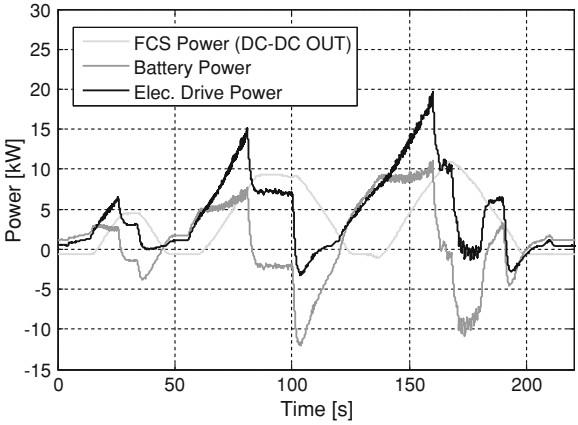

Fig. 7.56 Power distribution between FCS, electric engine, and batteries as function of cycle length for R40 cycle at 5 A s^{-1} as stack current variation rate

Table 7.3 Efficiency calculation for the 30 kW fuel cell power train on R40 driving cycle

Efficiencies (%)	Experiment of Fig. 7.56	Experiment of Fig. 7.57	Experiment of Fig. 7.58
η_{FCS}	46	45	48
η_{DC}	78	77	84
η_{ED}	74	74	75
η_{PT}	27	26	30

and recharges the batteries (Fig. 7.56). The results of the previous paragraph guarantee that no dynamic limitation can be expected during this experiment. The batteries are recharged during both deceleration phases (regenerative braking) and stationary phase when the FCS power overcomes the engine demands. The behavior of battery power affects its state of charge (SOC) during the cycle, in fact a slight decrease of battery SOC is observed (about 0.2%) at the end of a single R40 cycle managed according to Fig. 7.56. In Table 7.3, the values of efficiencies calculated for the power train and its main components on the R40 cycle are reported. The total efficiency of the FCS (η_{FCS}) is calculated as ratio between the power at DC–DC converter input and the theoretical power associated with the fuel entering the stack. The DC–DC converter (η_{DC}) and electrical drive (η_{ED}) efficiencies are calculated as ratio between outlet and inlet power of the devices. Then the total efficiency of the power train (η_{PT}) on the driving cycle is determined using the following equation, assuming a battery efficiency of 100% and taking back the final SOC to the initial level [8]:

$$\eta_{PT} = \eta_{FCS} \cdot \eta_{DC} \cdot \eta_{ED}. \tag{7.4}$$

For the test reported in Fig. 7.56, an efficiency of 46% is obtained for the FCS, which operates on the cycle mainly in conditions of partial loads, characterized by high efficiency [3]. For DC–DC converter and electric drive efficiencies of 78 and

74% are evaluated, respectively, with an overall efficiency value for the power train of about 27%.

The next experiment is performed increasing the slope of the acceleration phases of the same R40 cycle, in order to obtain current variations of 10 A s^{-1}, and maintaining the same air management strategy of Fig. 7.56. The results of this experiment are shown in Fig. 7.57, where the power distribution between engine, battery pack, and DC–DC converter is reported versus the cycle length. For this cycle a different control strategy is adopted, based in particular on the fact that all power requirements from the electric drive are mainly satisfied by the FCS already at the start up, while the contribution of batteries is limited to about 30% of the power demands during the acceleration phases. This strategy is chosen according to the soft hybrid option, aimed to minimize the intervention of the energy storage devices. The results of Fig. 7.57 clearly show that the dynamic behavior of the FCS permits the energy requirements from the engine to be instantaneously

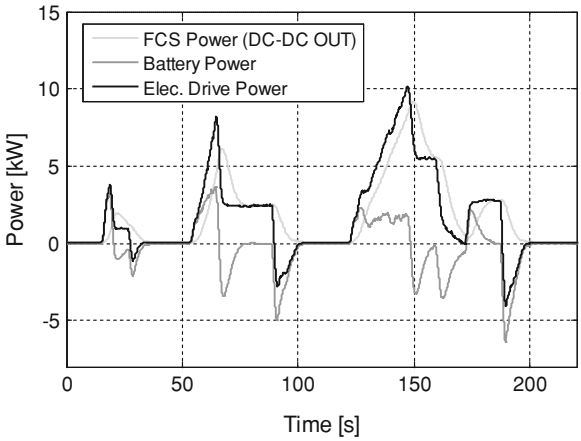

Fig. 7.57 Power distribution between FCS, electric engine, and batteries as function of cycle length for R40 cycle at 10 A s^{-1} as stack current variation rate (soft hybrid configuration)

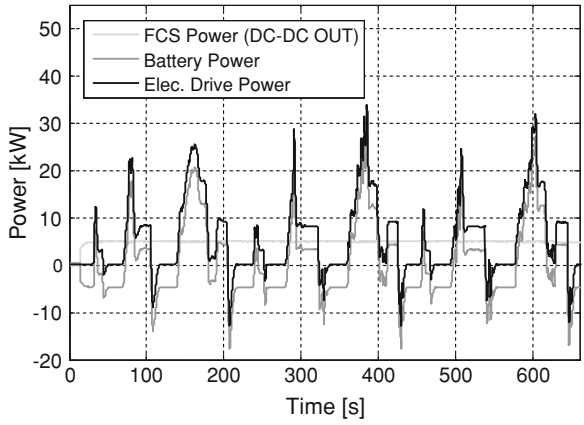

Fig. 7.58 Power distribution between FCS, electric engine, and batteries as function of cycle length for three successive R40 cycles at 50 A s^{-1} and DC–DC output power constant at 5 kW (hard hybrid configuration)

satisfied by the stack. In this test, the batteries mainly plays the role of recovering energy during the regenerative phases, as evidenced by the negative values reached by the battery and engine power curves. The energy recovered during the regenerative braking phases results about 15% of the total energy entering into the electric drive during the cycle. The data reported in Table 7.3 show that significant differences are not observed in terms of efficiency values for this test with respect to the experiment of Fig. 7.56, in particular an efficiency value of 26% is calculated for the total power train.

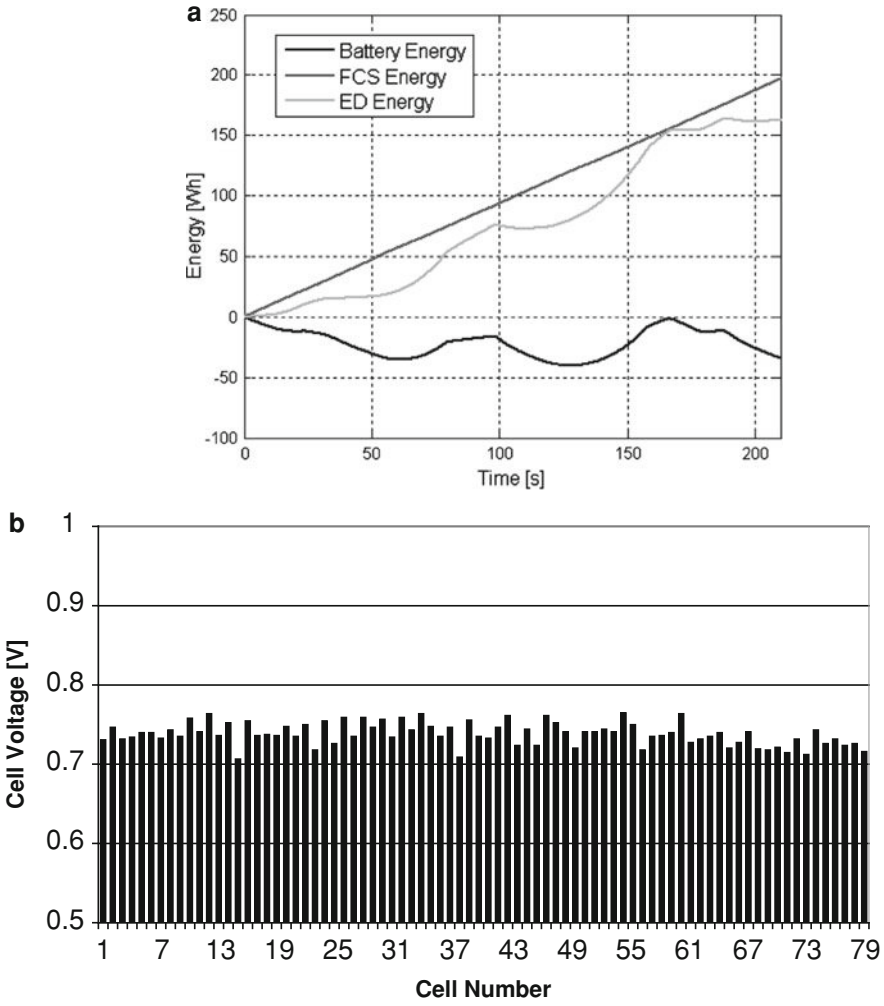

Fig. 7.59 Hard hybrid procedure during R40 cycle. **a** Electric energy profiles instantaneously exchanged by electric drive, battery pack, and FCS versus cycle length. **b** Histogram of individual cell voltage during the steady state FCS working

The hard hybrid configuration of the power train is analyzed through a test performed on the cycle R40, modified with slopes of acceleration phases corresponding to stack current variation rate of 50 A s^{-1} and a maximum power demand of 35 kW. The results of this test are shown in Fig. 7.58, where the electric power of the electric drive, batteries and FCS are reported as function of the time for a sequence of three successive cycles. The FCS operates as a power levelling source during the whole cycle (5 kW at the DC–DC converter outlet), while the dynamic requirements are provided by the batteries. Using this strategy, the FCS works in conditions of maximum efficiency, as evidenced by data of Table 7.3. In particular, the FCS efficiency resulted about 48%, and a significant increase is observed also for the DC–DC converter efficiency, which raises up to 84%, while the overall power train efficiency is about 30% [5].

The behavior of the power train in hard hybrid configuration can be also analyzed in terms of energy profiles of engine, battery pack, and FCS exchanged during the cycle (Fig. 7.59a). During this test, similarly to the experiment of Fig. 7.58, the stack power is fixed at a value corresponding to the maximum FCS efficiency, while the energy requirements from the electric drive are satisfied by both FCS and storage systems. The satisfactory working regularity of the 20 kW stack during this experiment is confirmed by the histogram of Fig. 7.59b, where the individual cell voltages are reported for a particular instant of the FCS steady state operation [9].

References

1. Larminie J, Dicks A (2000) Fuel cell systems explained. Wiley, Chichester
2. Kulp G, Nelson DJ (2000) A comparison of two fuel cell air compression systems at low load. SAE Trans J Pass Cars: Electron Electr Syst 110(7):660–669
3. Corbo P, Migliardini F, Veneri O (2007) Experimental analysis and management issues of a hydrogen fuel cell system for stationary and mobile applications. Energy Convers Manag 48:2365–2374
4. Philipps F, Simons G, Schiefer K (2006) Dynamic investigation of PEFC stacks in interaction with the air supply system. J Power Sources 154:412–419
5. Corbo P, Migliardini F, Veneri O (2008) An experimental study of a PEM fuel cell power train for urban bus application. J Power Sources 181:363–370
6. Corbo P, Migliardini F, Veneri O (2009) Dynamic behaviour of hydrogen fuel cells for automotive application. Renew Energy 34:1955–1961
7. European directive 91/441/EEC
8. Ouyang M, Xu L, Li J, Lu L, Gao D, Xie Q (2006) Performance comparison of two fuel cell hybrid buses with different powertrain and energy management strategies. J Power Sources 163:467–479
9. Corbo P, Migliardini F, Veneri O (2009) PEFC stacks as power sources for hybrid propulsion systems. Int J Hydrogen Energ 34:4635–4644

Index